SYNTHENSES, BIOLOGICAL EVALUATION, DOCKING AND ADMET PROFILING OF 4-AMINOANTIPYRINE DERIVATIVES

BY

Ehimen Annastasia **ERAZUA**
B.Tech. (FUTA), M.Sc. (Ibadan)
Matric. No.: 187560

A Thesis in the Department of Chemistry,
Submitted to the Faculty of Science
In Partial Fulfillment of the Requirement for the Degree of

DOCTOR OF PHILOSOPHY

of the

UNIVERSITY OF IBADAN

OCTOBER, 2023

CERTIFICATION

I certify that this research work was carried out by Ehimen Annastasia ERAZUA with Matric Number 187560 in the Department of Chemistry, University of Ibadan, Ibadan, Nigeria.

……

Supervisor

Folashade O. Oyedeji

B.Sc., M.Sc., Ph.D (Ibadan), PGDE (Ilorin)

Reader, Department of Chemistry,

University of Ibadan, Nigeria

……

Co-Supervisor

B. B. Adeleke

B.Sc. (Ibadan), M.Sc., Ph.D (Queens)

Professor, Department of Chemistry,

University of Ibadan, Nigeria

DEDICATION

I dedicate this work to Almighty God who kept me all through the period of this research, and to all members of my family.

ACKNOWLEDGMENTS

I acknowledge the Head of Department, Prof P. C Onianwa and the entire staff of the Chemistry department, who, through their consistency, have not only imparted knowledge to me but have also taught me how to be disciplined. God bless you all. My unfeigned gratitude and appreciation go to my supervisors Prof. B. B. Adeleke and Dr. Folashade O. Oyedeji for imparting knowledge, support, excellent guidance, motivation, unfailing patience, and advice. I deeply appreciate Third World Academy of Science (TWAS) and International Centre for Chemical and Biological Science (ICCBS) for the award of TWAS-ICCBS postgraduate fellowship, which contributed to the success of this work. My gratitude also goes to my host supervisors, Prof. M. Iqbal Choudhary, and Dr Hina Siddiqui for their hospitality, support, and impact in this work.

I express my appreciation to my beloved guardians, Mr and Mrs V. Ogedegbe, for their love, financial and moral support. They have shown me a life of love, and I am forever grateful. I am indebted to my parents, Mr and Mrs Amos Erazua for their unconditional love, encouragement, advice, and immense contributions towards my academic pursuit. I am most grateful to my late mother-inlaw, Mrs Grace Ilenikhena for her constant prayers, and encouragement. May your soul continue to rest in Peace. My deepest appreciation goes to all my siblings and in-laws whose love, friendship, financial support, and moral advice has gone a long way in my making. Your contribution towards my academics is immeasurable; I will forever remember it and promise to make you all proud. To my marvellous and treasured husband Ilenikhena Odion, and loving children (Jesse, Joachim, and Josiah), I say a big thank you for your enormous understanding, patience, sacrifice, prayers, and unending support. I could not have done this without you.

My immerse gratitude goes to my colleagues and friends, Modinat, Abel, Magaret, Josiah, Akong, Emmanuel, Micheal, Eniola, Ejike, Ufuoma, Clement, Kingsly, Fazila, Fareeda, Shahbaz, Blessing, Lola, Toke, Mayowa, Donald, Stella, Kehinde, Onyinye and Testimony. This study was worthwhile because of all your numerous contributions.

Finally, I return all glory to the Almighty God for His protection, sustenance, care, abundant grace, and love throughout my study.

ABSTRACT

Oxidative-stress, inflammation and glycation processes cause cell damages in the human body and may lead to aging and different disease conditions. Drugs that ameliorate oxidative stress can solve several disease pathologies. Drug development experiments in the early stages are expensive and time-consuming. These constraints could be minimised through computational approach. A 4-aminoantipyrine possesses biological properties including antioxidant and anti-inflammatory activities. However, information on its application as antiglycating agent is sparse. Therefore, this study was aimed at synthesising 4-aminoantipyrine derivatives and evaluating their antioxidant, anti-inflammatory, antiglycation and toxicity potentials using experimental, docking and ADMET profiling.

Synthesis of Schiff bases was carried out by condensation of 4-aminoantipyrine with different substituted benzaldehydes. Ether derivatives were prepared from 4-aminoantipyrine Schiff bases via Williamson ether synthesis. The compounds were purified by solvent extraction and characterised using Fourier Transform Infra-Red (FTIR) spectroscopy, ^{1}H and ^{13}C Nuclear Magnetic Resonance (NMR) spectroscopy, Mass Spectrometry (MS) and X-ray Diffraction (XRD) analysis. Cytotoxicity analysis was carried out using brine shrimps and 3T3 mouse fibroblast cell lines. The antioxidant, anti-inflammatory and antiglycating activities were evaluated *in vitro* using 2,2-diphenyl-1-picrylhydrazyl radical, oxidative burst assay and human serum albumin solution; and compared with gallic acid, ibuprofen and rutin (standards), respectively. Molecular descriptors were obtained from Density Functional Theory (DFT) calculations and the binding affinity determined by molecular docking. Quantitative Structure-Activity Relationship (QSAR) model was used to predict the bioactivity of the compounds. A detailed ADMET (adsorption, distribution, metabolism, excretion, and toxicity) screening was done in-silico. Data were analysed by descriptive statistics.

Fifty-eight compounds (thirty Schiff bases and twenty-eight ether derivatives) were synthesised out of which 24 were new. A newly synthesised 4-((2-chloro-4-fluorobenzylidene)amino)-1,5-dimethyl-2-phenyl-1,2-dihydro-3H-pyrazol-3-one, had characteristic FTIR $\bar{\upsilon}_{max}$ at 1593 cm^{-1} for C=N (azomethine bond). The ^{1}H-NMR spectrum showed seven methine signals at 9.91, 8.22, 7.55, 7.49, 7.40, 7.36 and 7.34 and two methyl

signals at 3.21and 2.47 ppm. The ^{13}C NMR displayed seven quaternary, nine methine and two methyl carbons. The MS showed the molecular ion at 343 *m/z* corresponding to $C_{18}H_{15}ClFN_3O$. The XRD showed a monoclinic unit cell and theta of 66.66°. None of the compounds was cytotoxic against normal cell lines (Cytotoxicity (3T3Cell-line) % inhibition $\leq$ 25%). Five of the compounds possessed antioxidant activity, with 4-((4-hydroxy-3-methoxybenzylidene)amino)-1,5-dimethyl-2-phenyl-1,2-dihydro-3H-pyraz-ol-3-one having similar activity (IC_{50} =111.10±1.80 µM) as gallic acid (IC_{50} = 111.60±2.40 µM). Four of the compounds exhibited anti-inflammatory activities with 4-((2,3-dihydroxybenzylidene)amino)-1,5-dimethyl-2-phenyl-1,2-dihydro-3H-pyrazol-3-one having a lower IC_{50} (0.01±0.02 µM) than that of ibuprofen (11.20±1.90µM). Eight of the compounds possessed moderate antiglycation activity (IC_{50} = 321.16±5.70-856.80±2.80µM) when compared to standard (IC_{50} = 282.40±0.80 µM). The DFT calculations and molecular docking confirmed compounds 4-((3,4-dihydroxybenzylidene)amino)-1,5-dimethyl-2-phenyl-1,2-dihydro-3H-pyrazol-3 one and 4-((2,3-dihydroxybenzylidene)amino)-1,5-dimethyl-2-phenyl-1,2-dihydro-3H-pyrazol-3-one with best activities among the tested compounds. The molecular descriptors (E_{HOMO}, E_{LUMO}, polarisability, dipole moment and polar surface area) were responsible for the biological activities of the compounds. All the synthesised compounds demonstrated acceptable outcome in oral bioavailability, lipophilicity, pharmacokinetics, and toxicity prediction.

The synthesised 4-aminoantipyrine derivatives were non-toxic and some possessed anti-inflammatory, antioxidant and antiglycation properties making them potential drug candidates.

Keywords: 4-Aminoantipyrine, Antiglycation, Molecular docking

Word count: 495

TABLE OF CONTENTS

LIST OF TABLES

LIST OF FIGURES

LIST OF SCHEMES

LIST OF ABBREVIATIONS AND ACRONYMS

ADMET	Absorption, Distribution, Metabolism, Elimination, and Toxicity
AGEs	Advanced Glycation End Products
BBB	Blood Brain Barrier
^{13}C NMR	Carbon 13 Nuclear Magnetic Resonance
COX-1	Cyclooxygenase 1
COX-2	Cyclooxygenase 2
CV. R^2	Cross Validation
d	Doublet
dd	Double doublet
DEPT	Distortionless Enhancement by Polarization Transfer
DFT	Density Functional Theory
δ_H	Chemical Shift of Proton
DMF	Dimethylformmide
DMSO	Dimethyl Sulfoxide
DMSO-d_6	Deuterated Dimethyl Sulphoxide
DPPH	2,2-diphenyl-1-picrylhydrazyl
EA	Ethyl Acetate
ECP	Effective Core Potential
E_{HOMO}	Energy of the HOMO
E_{LUMO}	Energy of the LUMO
EI-MS	Electron Impact Mass Spectroscopy
E_{xc}	Exchange Correlation Functional
FTIR	Fourier Transform Infrared
GGA	Generalised Gradient Approximation
GI	Gastrointestinal
GTOS	Gaussian-Type Orbitals,
^{1}H NMR	Proton Nuclear Magnetic Resonance

H	Hexane
HBBS	Hanks Balanced Salt Solution
HF	Hartree-Fock
HOMO	Highest Occupied Molecular Orbital
Hz	Hertz
IC_{50}	Half Maximum Inhibitory Concentration
IP	Ionization Potential
Kbr	Potassium Bromide
LCAO	Linear Combination of Atomic Orbitals
LDA	Local Density Approximation
LUMO	Lowest Unoccupied Molecular Orbital
m	Multiplet
MLR	Multiple Linear Regression
MeOD-d_6	Deuterated Methanol
MF	Molecular Formula
MHz	Mega Hertz
MORE	Microwave-induced Organic Reaction Enhancement
M.pt	Melting Point
MTT	3-[4,5-dimethylthiazole-2-yl]-2,5-diphenyl-tetrazolium bromide
MW	Molecular Weight
m/z	Mass to Charge Ratio
nm	nanometer
NMR	Nuclear Magnetic Resonance
NSAIDs	Nonsteroidal anti-inflammatory drugs
P-gp	Glycoprotein
ppm	parts per million
QSAR	Quantitative Structure Activity Relationship
R^2_a	Adjusted Squared Correlation

RAGE	Receptor for Advanced Glycation End Products
R*f*	Retardation Factor
RO3	Rule of Three
RO5	Rule of Five
ROS	Reactive Oxygen Species
s	Singlet
STOS	Slater-Type Orbitals
t	Triplet
TLC	Thin layer chromatography
TMS	Tetramethyl silane
TPSA	Total Polar Surface Area
UV-VIS	Ultraviolet-Visible
XRD	X-Ray Diffraction
λmax	Wavelength of Maximum Absorptions.
δ	Chemical shift
J	Coupling constant
$\bar{\upsilon}$	Absorption frequency

CHAPTER ONE
INTRODUCTION

1.1 Background to the Study

Pharmaceutical or Medicinal chemistry is a field of chemistry which involved the combination of chemistry with pharmacology to discover, design, synthesise, and develop new compounds for curative purposes (Kabir and Uzzaman, 2022). It studies their quantitative structure activity relationships (QSAR), interpretation of their interactions with different receptors, ascertainment of their absorption, transport, and distribution properties (Jia *et al.,* 2022). Medicinal chemists are currently involved with the design of synthetic compounds such as medicine, unlike in the early days when their only focus is the extraction of medicinal compounds from plants. This field of study has evolved greatly from mere organic preparation of compounds based on change of structures of known action, to the use of computer to enhance scientific procedure in drug discovery (Prajapat, 2018). Nowadays, computers are being used by chemist for storing, collecting, analyzing, manipulating, and viewing data. This have led to a more comprehensive study of molecular properties, models of biological sites, models of molecules, and even models of drug-receptor interactions (Wang, 2022).

Heterocycles form the largest group of organic chemistry and are of great importance in pharmacological, biological, industrial, inorganic, and agricultural field (Gupta *et al.,* 2017). A compound which contains one or more rings of atoms with at least one heteroatom (an element other than carbon) is known as a heterocyclic compound. The heteroatom can be either oxygen, nitrogen, or sulfur. The structures of the heterocyclic compounds may consist of either aromatic or non-aromatic rings (Mahajan and Jain, 2021). Many drugs from natural products such as codeine, morphine, atropine, emetine, and most synthetic drugs (antipyrine, metronidazole, isoniazid, azidothymidine) are all examples of heterocycles.

Recently, synthesis of heterocycles containing nitrogen atom has gained much attention due to their biological properties (Tran and Henary, 2022). Pyrazolone is an example of nitrogen containing heterocycle which have been extensively studied and reported to have great applications in various field of chemistry including their uses as therapeutic agents.

4-aminoantipyrine (4-amino-1,5-dimethyl-2-phenylpyrazole-3-one) is a heterocyclic compound containing a pyrazolone moiety and a free amino group with which it spontaneously reacts with aldehydes and ketones to form Schiff bases (Obasi *et al.,* 2016). Antipyrine was the first derivative of pyrazolone used as drug for the management of pain and inflammation (Mahmud and Rosen, 2019). 4-aminoantipyrine, due to its chelating ability, has been extensively used in inorganic chemistry to form stable metal complexes. They are very useful in catalysis. They act as corrosion inhibitors of metals in acid solution (Kashyap *et al.,* 2018), and are used in the preparation of azo dyes (Singh *et al.,* 2022). Research has been done on some Schiff bases obtained from 4-aminoantipyrine derivatives (Asiri and Khan, 2010; Murtaza *et al.,* 2017; Shoaib *et al.,* 2015; Sakthivel *et al.,* 2020; Aguilar-Llanos *et al.,* 2022).

Schiff bases are compounds containing carbon-nitrogen double bond called azomethine or imine linkage where the nitrogen atom is linked to an aryl or alkyl group. These compounds were discovered in the 19^{th} century by Hugo Joseph Schiff (Raczuk *et al.,* 2022). Schiff bases are prepared by the condensation reaction between primary amines and active carbonyl compounds (aldehydes and ketones). Schiff bases have vast application in catalysis, material science, agrochemical industry, medicinal, analytical and food chemistry (Soroceanu *et al.,* 2022). The biological activities of Schiff bases include antibacterial, antifungal, antiproliferative, antimalarial, antiviral, analgesic, and antipyretic (Mesbah *et al.,* 2018 and Raju *et al.,* 2022). Schiff base metal complexes have been investigated extensively and are found to be useful also in the preparation of medicines, industrial catalysts, analytical reagents, and agrochemicals (Ebosie *et al.,* 2021). Schiff base analogues of 4-Aminoantipyrine possess various biological properties such as anti-inflammatory, analgesic (Murtaza *et al.,* 2017), anti-microbial (Chavan and Hosamani 2018; Singh *et al.,* 2020), antioxidant (Parmar *et al.,* 2015) and anticancer (Ghorab *et al.,* 2014), antiviral, and antifungal activities (Tok *et al.,* 2019).

Research has shown that 4-aminoantipyrine Schiff bases have scavenging activity against reactive oxygen and nitrogen species (Cakmak *et al.,* 2022; Kasare *et al.,* 2022). Oxygen is a vital component of cellular metabolism. However, over consumption of oxygen can cause the production of free radicals which are referred to as reactive oxygen species (ROS). When the antioxidant system cannot efficiently remove the excessive free radicals produced, oxidative stress will occur (Forman and Zhang, 2021) and this can lead to several diseases like atherosclerosis, cataract, diabetes, cancer, aging, cardiovascular and inflammatory disease, heart diseases, neurodegenerative disorder, Alzheimer's, and Parkinson's diseases (Kumar *et al.,* 2017; Kang and Yang, 2020). To prevent these health problems, it is better to keep a good level of natural antioxidants such as N-acetylcysteine, α-lipoid acid, vitamin C, glutathione, and vitamin E in biological systems. This reduces the excess free radicals inside the cells therefore lowering oxidative stress (Kumar *et al.,* 2017; Pisoschi *et al.,* 2021). Antioxidants inhibit oxidation, prevent the formation of radicals, scavenge them, and promote their decomposition (Akbari *et al.,* 2022; Martemucci *et al.,* 2022).

4-amino antipyrine derivatives with potent anti-inflammatory activity have been recorded (Murtaza *et al.,* 2017; Yasar and Zaheer, 2021). Nonsteroidal anti-inflammatory drugs (NSAIDs) are therapeutic agents used to treat inflammation-related ailment, such as cardiovascular diseases, arthritis, and asthma (Ho and Lai-Shan, 2022). Long-term use of NSAIDs can cause adverse effect such as indigestion, renal disorders, heartburn, nausea, bleeding, vomiting, diarrhea. and gastrointestinal ulcers. These side effects are caused by the nonselective inhibition of both isoforms of the cyclooxygenase enzymes (COX-1 and COX-2) (Jahnavi *et al.,* 2020; Bindu *et al.,* 2020). The use of antipyrine Schiff bases as an antipyretic was discouraged because of its possibility to cause agranulocytosis (lowering white blood cell count) (Mahmud and Rosen, 2019).

Gylcation, oxidative stress, and inflammation are closely related. Exposure of cells to ROS induces the release of pro-inflammatory cytokines. Reactive Oxygen Species are also formed during glycation reaction (Nowotny *et al.,* 2015). Glycation is a non-enzymatic reaction that involves the attachment of a sugar molecule to a protein or lipid. It is responsible for many complications in diabetes mellitus. An increase in glucose levels

increases oxidant production which can result to chronic oxidative stress and increases the production of advanced glycation end-products (AGEs). It also escalates the expression of the receptor for AGEs (RAGE) and its activating ligands (Oguntibeju, 2019; Yuan *et al.*, 2019). Oxidative stress-related pathways can be suppressed using antioxidants and by glucose control. This will halt the progression of diabetes-related complications (Kang, and Yang, 2020; Bhatti *et al.*, 2022). The report of 4-aminoantipyrine derivatives as good anti-inflammatory and antioxidant agents is an indication that they may possess antiglycation activity, but their report as antiglycation agents is scarce in literature.

Recently, computational methods are generally used in the qualitative and quantitative evaluation of substances, which have led to transformation in almost every field of chemistry (Wu *et al.*, 2020). The application of mathematical, chemical, and computing skills to solve chemical issues is known as computational chemistry. *In silico* drug design is the chemistry which deals with the use of computer programs and efficient mathematical approximations to calculate molecular properties with a view to design and develop new drugs (Jia *et al.*, 2021).

In the early days, the process of pharmaceutical research and development was time consuming, expensive, had a high rate of failure due to poor pharmacokinetics, toxicity, and lack of efficacy (Muntha, 2016). More recently, drug discovery process has changed due to advance technologies in chemistry and bioinformatics such as virtual screening, high throughput screening, in silico absorption, distribution, metabolism, elimination, and toxicity (ADMET) screening, and structure-based drug design has improved drug discovery process. Computational techniques have help to deliver the new drug candidates, at lower cost more quickly and with less toxic waste (Bisht and Singh, 2018; Wu *et al.*, 2020; Wang, 2022). Therefore, the present study will ultilise molecular docking to investigate the interaction between synthesised compounds (ligand) and the target proteins. Evaluate theoretically the physico-chemical and structural properties of the ligands that is relevant to the desired biological activity. Adsorption distribution metabolism excretion and toxicity (ADMET) screening will be done to assess the drug-likeness, oral bioavailability, and toxicity of the compounds.

1.2 Statement of Problem

The emergence of new diseases, drug tolerance, drug resistance, and adverse effect of some existing drugs necessitates the search for new compounds with potent biological activity and little or no side effects that can be used as leads in drug discovery. 4-aminoantipyrine and its derivatives are a flexible heterocyclic scaffold for drug development due to their promising pharmacological properties. They have been used as an anti-inflammatory and antioxidant drug, but information on their antiglycation potential is very limited. Identifying these potential drug candidates can be expensive and time-consuming. However, molecular docking and ADMET profiling are important computational methods that can accelerate drug synthesis and discovery by predicting binding affinity and selectivity, guiding molecular design, expanding the search space of possible drug candidates, predicting ADMET properties, optimising drug candidates, integrating with experimental methods, and saving time and resources. The study was, therefore, designed to synthesise 4-aminoantipyrine derivatives and evaluate their anti-inflammation, antioxidant, and antiglycation potentials with less toxicity using experimental and computational approaches.

1.3 Justification of Research

The emergence of new diseases, drug tolerance, drug resistance, and adverse effect of some existing drugs necessitates the search for new compounds with potent biological activity and little or no side effects that can be used as leads in drug discovery. 4-aminoantipyrine and its derivatives are a flexible heterocyclic scaffold for drug development due to their promising pharmacological properties. They have been used as an anti-inflammatory and antioxidant drug, but information on their antiglycation potential is very limited. In addition, identifying these potential drug candidates can be expensive and time-consuming. However, molecular docking and ADMET profiling are important computational methods that can accelerate drug synthesis and discovery by predicting binding affinity and selectivity, guiding molecular design, expanding the search space of possible drug candidates, predicting ADMET properties, optimizing drug candidates, integrating with experimental methods, and saving time and resources. The study was, therefore, designed to synthesise 4-aminoantipyrine derivatives and evaluate their anti-inflammation, antioxidant, and antiglycation potentials with less toxicity using an experimental and computational approaches.

1.4 Aim and Objectives

The aim of the study is to synthesise some 4-aminoantipyrine derivatives and evaluate their biological properties by experimental and theoretical approaches.

The Specific Objectives were to:

- synthesise some Schiff bases, ether, and alkyne compounds from 4-aminoantipyrine and substituted benzaldehyde.
- elucidate structures of the synthesised compounds using standard methods.
- screen the compounds for toxicity, antioxidant, anti-inflammation and antiglycation activities.
- obtain molecular descriptors of the synthesised compounds via DFT optimisation.
- predict the biological activity of the synthesised compounds based on structural descriptors using QSAR technique.
- investigate the interaction and conformation between synthesised compounds (ligand) and target proteins using molecular docking method.
- predict the ADMET properties of the synthesised compounds in other to explore their possibility in clinical use.

CHAPTER TWO

LITERATURE REVIEW

2.1 Pyrazolone

Pyrazolone is a reduced form of pyrazole and a significant nitrogen containing five-membered heterocyclic compound. It is made up of three carbon atoms, two adjacent nitrogen atoms and one ketone group (Orabi *et al.*,2018). Pyrazolones are among the earliest synthetic medications, with antipyrine being introduced in the 1880s (Mahmud and Rosen, 2019). Ludwig Knorr first reported the synthesis of pyrazolones in 1883, using a condensation process between ethyl acetoacetate and phenyl hydrazine (Ramadan *et al.,* 2019). Pyrazolone can occur in 3 isomers, as 3-pyrazolone (1), 4-pyrazolone (2), and 5-pyrazolone (3) (Figure 2.1) (Orabi *et al.*,2018).

Due to the ease of preparation of pyrzolones, vast range of chemical reactivity, broad spectrum of biological activity and extensive industrial applications, they are used as flexible template in medicinal and combinatorial chemistry.

Pyrazolone moiety occur in many drugs which possess activities such as analgesic and antipyretic (phenazone (4), propylphenazone (5) and metamizole (6)), antirheumatic (kebuzone (7)), anti-ischemaic (edaravone (8)) and anti-cancer (TELIN (9)), (Gupta *et al.*, 2017; Abdelgawad *et al.,* 2018) (Figure 2.2). Various Pyrazolone derivatives exhibit biological properties such as antitcancer (Kshatriya, *et al.,* 2021), anti-inflammatory (Irfan, 2020), antifungi, antitubercular, antimicrobial (Parikh *et al.,* 2022) and anticonvulsant activities (Grover *et al.,* 2020). Pyrazolone derivatives are used as dyes (Qian *et al.,* 2019), optical materials (Aktan and Uyar, 2017), corrosion inhibitors (El Defrawy *et al.,* 2019), chelating agents (Bao *et al.,* 2022) and doping agents (Vasiliu *et al.,* 2016). They are employed in analytical field for determination of trace metals (Parvarinezhad *et al.,* 2022).

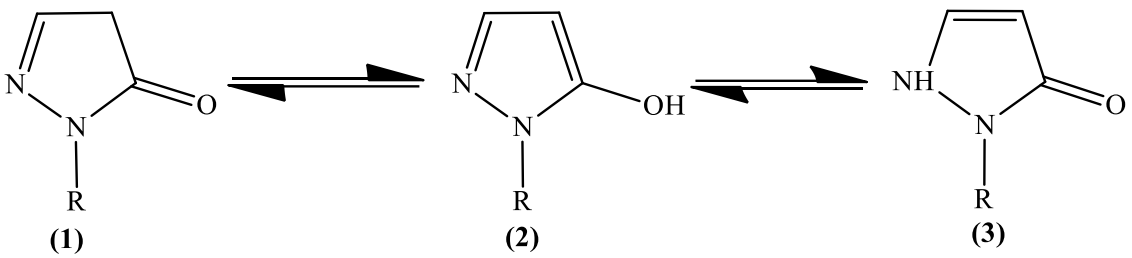

Figure 2. 1: Tautomerism in Pyrazolones

Source: Orabi *et al.*, (2018)

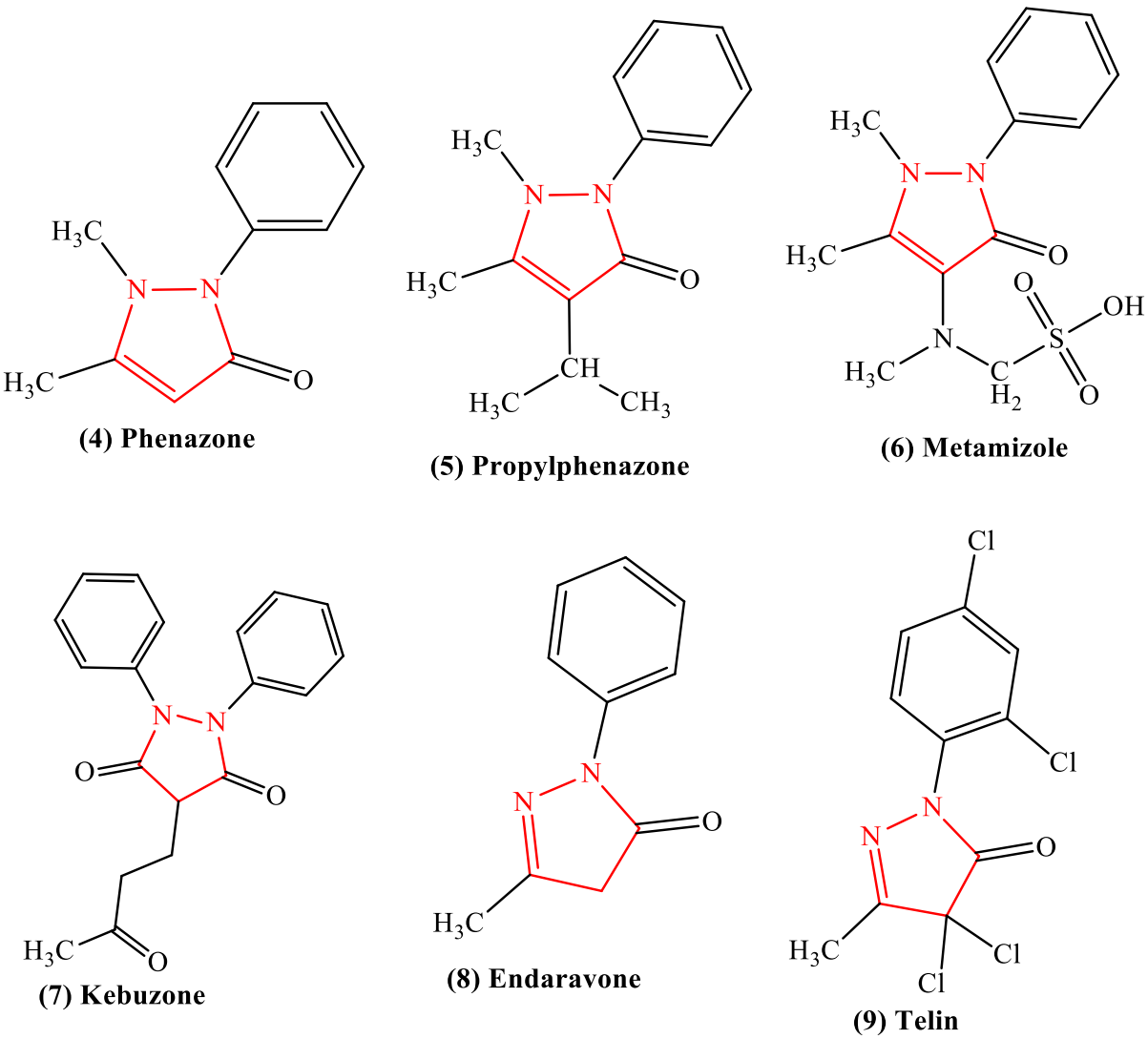

Figure 2. 2: Pyrazolone Derivatives used as Drugs.

Source: Abdelgawad *et al.*, (2018)

2.2. 4-Aminoantipyrine

Extensive research has been done on various derivatives of 4-aminoantipyrine. They have been reported to have varied application in different fields of chemistry, their uses as therapeutic agents have been reported. Research has also been done on some Schiff bases derived from 4-aminoantipyrine derivatives (Sakthivel *et al.,* 2020; Aguilar-Llanos *et al.,* 2022). Schiff base analogues of 4-Aminoantipyrine are reported to exhibit minimal protein binding, to be rapidly absorbed in the gastrointestinal tract, and to be extensively metabolised by cytochrome P450 (Alam and Lee, 2016). They possess various biological properties (Chavan and Hosamani, 2018; Tok *et al.,* 2019; Singh *et al.,* 2020). 4-aminoantipyrine has played a significant role in inorganic chemistry, due to its ability to form stable complexes with many transition metal ions. They are very useful in catalysis. They act as corrosion inhibitors of metals in acid solution and are also used in the preparation of azo dyes (Kashyap *et al.,* 2018).

2.2.1 Anti-Inflammatory Activity of 4-Aminoantipyrine

Nonsteroidal anti-inflammatory drugs (NSAIDs) are therapeutics agent used to treat acute and chronic pains, stiffness, swelling, arthritis, and fever (Bally *et al.,* 2017; Bello *et al.,* 2020). NSAIDs possesses three main therapeutic effect such as anti-inflammatory effects (lower inflammation), analgesic effect (decrease pain), antipyretic effect (reduce high body temperature and fever). Most NSAIDs act as nonselective inhibitors of the cyclooxygenase (COX) enzymes, (COX-1 and COX-2 iso enzymes). COX enzymes catalyses the synthesis of prostaglandins and thromboxane from arachidonic acid. Pyrexia and pain in the body can be caused by prostaglandins and other inflammation mediators). Inflammation can be reduced by decreasing the amount of prostaglandins that are produced by tissue damage (Rensburg and Reuter, 2019).

Use of NSAIDs can result to mild or severe side effects. The most frequently seen side effects of NSAIDs are gastrointestinal symptoms, such as gas, indigestion, heartburn, stomach pain, nausea, vomiting, diarrhea and gastric ulceration or bleeding. Other side effects include dizziness, difficulty in concentrating, headaches, drowsiness, kidney disease and adverse cardiovascular events (Wong, 2019; Sinniah *et al.,* 2021).

Aryl and heteroaryl substituted compounds such as Diclofenac, Lumiracoxib, Lonazolac, Etodolac, have been commercialised as nonsteroidal anti-inflammatory drugs. Scientists became interested on pyrazolone derivatives as potent anti-inflammatory, analgesic, and antipyretic agents since 1884, when antipyrine was marketed as drug used in management of pain, inflammation, and fever (Mahmud and Rosen, 2019). This led to the development of different pyrazolone derivatives, and some have been successfully used as drugs (NSAIDS). Examples of such drugs are, Celecoxib, phenylbutazone, oxyphenbutazone, dipyrone, and ramifenazone (Figure 2.3) (Yasar and Zaheer, 2021). The use of Antipyrine as an antipyretic (NSAID) was discouraged, due to the risk of agranulocytosis (lowering white blood cell count) (Raman Jahnavi *et al.*, 2020). Hence, there is need to study other compounds of antipyrine that may be more potent NSAID with lesser or no side effect. Recently Schiff bases of 4-aminoantipyrine have been studied as an anti-inflammatory agent (Yasar and Zaheer, 2021).

Arshad *et al.*, 2014, reported the anti-inflammatory activities of four Schiff bases from 4-aminophenazone using the carrageenan-induced hind paw edema method and their results showed that the chloro-substituted derivative (10) possesses greater percentage anti-inflammatory activities compared to standard drug. Murtaza *et al.*, 2017, also reported the synthesis of Schiff base derivatives of 4-aminophenazone and screened the compounds for anti-inflammatory activities. They reported that the tested compounds had significant anti-inflammatory analgesic and antipyretic activities with compound (11) exhibiting the highest anti-inflammatory activity.

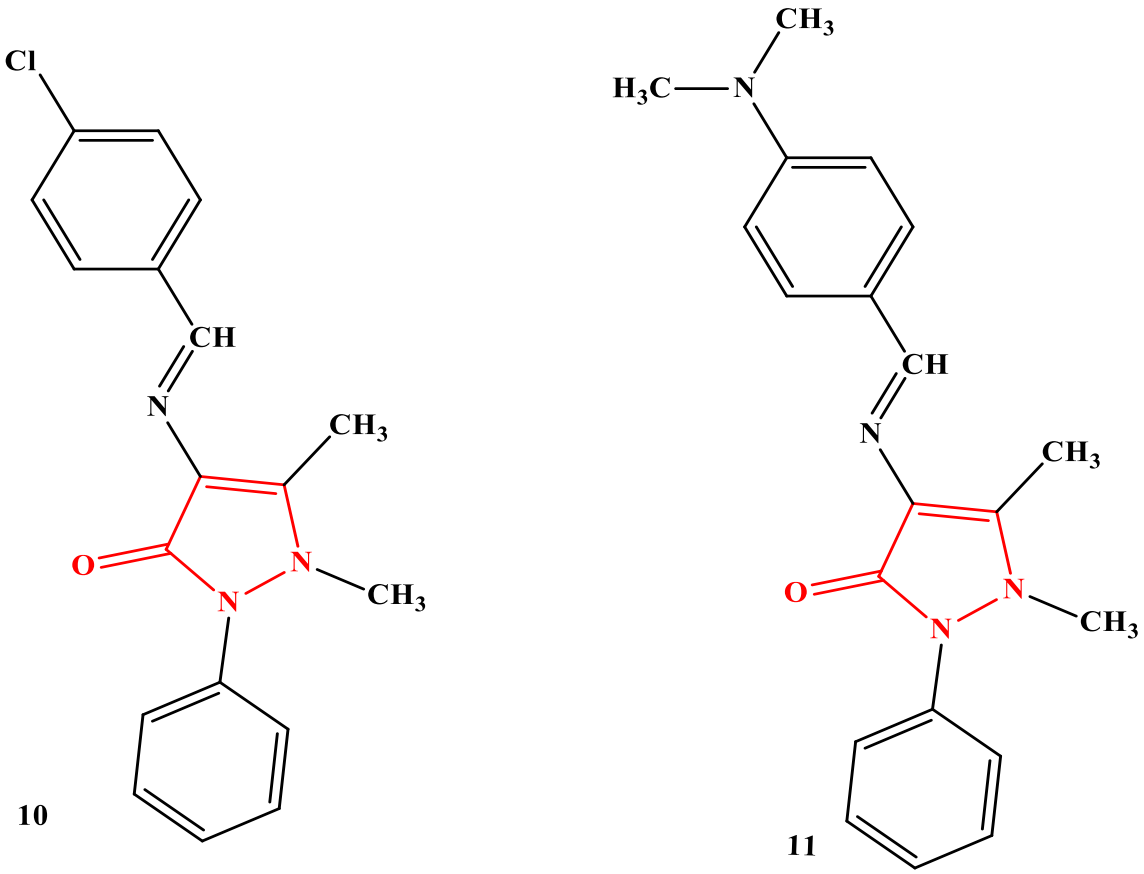

Figure 2. 3: 4-aminoantipyrine Derivatives with Anti-Inflammatory Activity

Source: Yasar and Zaheer, (2021)

2.2.2. Antioxidant Activity of 4-Aminoantipyrine Derivatives

In the new age of medicinal chemistry, the knowledge of free radicals and reactive oxygen species is very vital for diseases control. As part of regular cellular function, all cells produce free radicals continuously. Nevertheless, excess generation of free radicals can lead to chain reactions that may damage the cell of the organism and this might cause severe health issues like cataract, cardiovascular and inflammatory disease, and cancer (Kasare *et al.,* 2022). Antioxidants are compounds that inhibit oxidation. They help to prevent tissue damage caused by free radicals by inhibiting their production, scavenging them, or boosting their decomposition (Martemucci *et al.,* 2022). Research has shown that 4- aminoantipyrine and its derivatives have scavenging activity against reactive oxygen and nitrogen species (Remes *et al.,* 2012).

Remes *et al.,* 2012 synthesised some compounds from antipyrine which were active antioxidant compounds. Compound (12), containing twice the antipyrine moiety, has good antioxidant and antimicrobial behavior with low toxicity. Alam *et al.,* 2012 evaluated some Schiff bases for antioxidant and anti-inflammatory activities. They reported that the hydroxylated compounds showed the highest antioxidant activity, and that this activity was influenced by the nature and position of the substituted groups on the benzylidene.

Apotrosoaei *et al.,* 2013 prepared some antipyrine derivatives with hydrazone moiety and evaluated their antioxidant and antimicrobial activities. They reported that the derivatives from 2-methoxybenzaldehyde (13) and 4-hydroxy-benzaldehyde (14) were the most active compounds which had better antioxidant activity than ascorbic acid at the same concentration. Sonia *et al.,* 2013, evaluated antimicrobial and antioxidant activities of eleven benzoxazinyl pyrazolone arylidenes and reported that the fluro derivatives (15) showed excellent free radical scavenging, and that all compounds also possessed significant antimicrobial activity (Figure 2.4) (Apotrosoaei *et al.,* 2013).

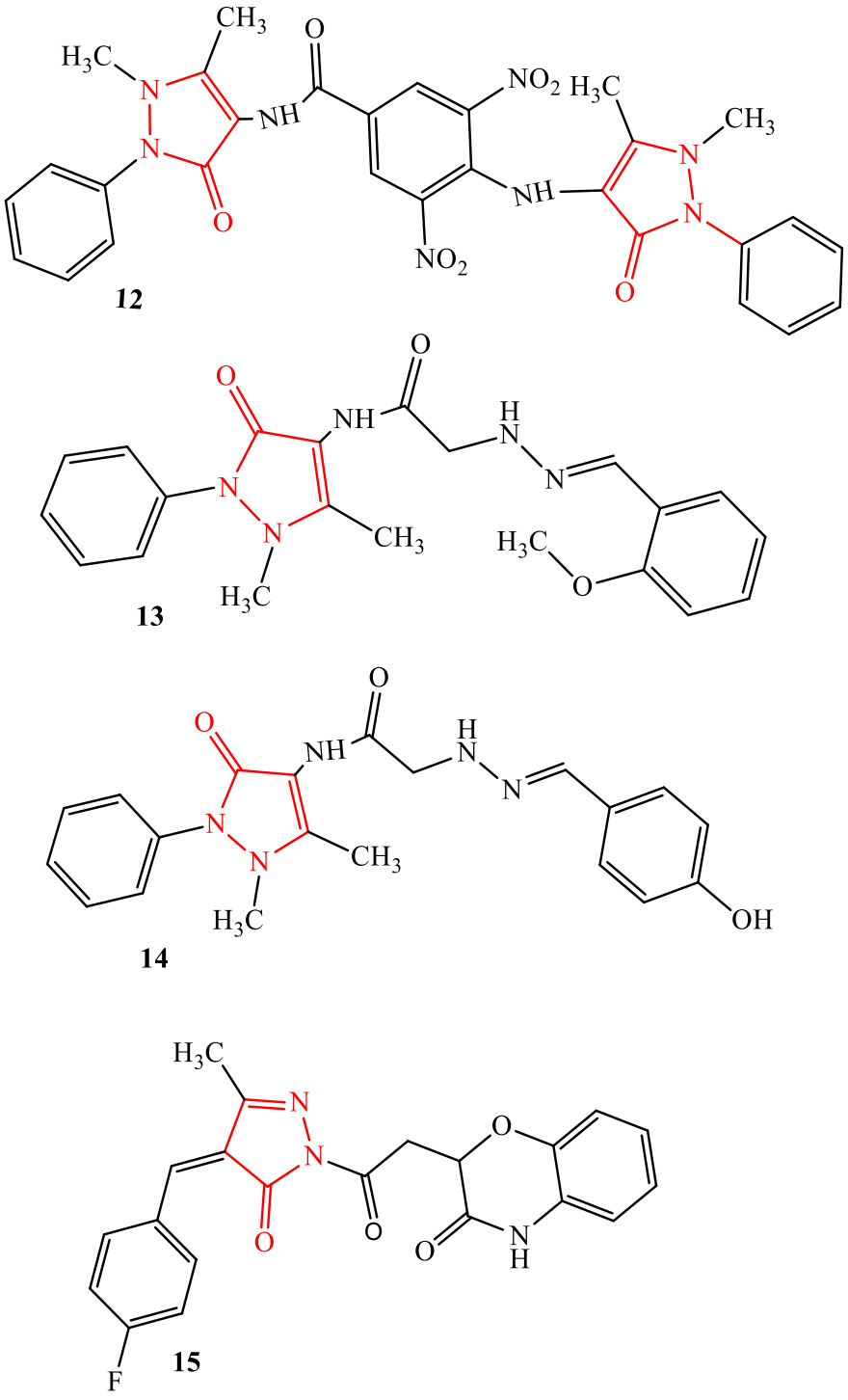

Figure 2. 4: Pyrazolone Derivatives with Antioxidant Activity

Source: Apotrosoaei *et al.*, (2013)

2.2.3 Antiglycation Activity of Schiff Bases

Researchers have explored the role that advanced glycation end products (AGEs) play in several different diseases. (Rungratanawanich *et al.,* 2021, Zgutka *et al.,* 2023). AGEs are potentially hazardous chemical compounds that are created when reducing sugars and protein Lysine side-chain amino groups interact through the Maillard reaction (Liang *et al.,* 2022, Shen *et al.,* 2020). Reactive oxygen species are produced as a by-product from maillard reaction in the presence of transition metals and oxygen molecule (Liang *et al.,* 2022). The interaction of AGEs with their receptor RAGE also contributes the generation of ROS which is believed to damage cellular mechanisms (Khalid *et al.,* 2016). These findings encouraged scientists to develop bioactive agents to halt the reaction between sugars and proteins. Studies have been done to explore antioxidant ability of 4-aminoantipyrine derivative, but studies on their antiglycation activities are scarce in literature.

Khan *et al.,* 2009 evaluated antiglycation potential of Bis-Schiff bases of isatin *in vitro*. They reported that compounds (16) (IC_{50} = 243.95 ± 4.59 lM), (17) (IC_{50} = 257.61 ± 5.63 lM), and (18) (IC_{50} = 291.14 ± 2.53 lM) showed excellent antiglycation activity better than the standard (rutin, IC_{50} = 294.46 ± 1.50 lM).

Al-Resayes *et al.,* 2014 synthesised and patented six novel heterocyclic Schiff bases consisting of pyridine, thiophene and furan. They evaluated the antiglycation potential of the compounds using bovine serum albumin-methylglyoxal assay in vitro. They observed that compound (19) possessed more antiglycating activity (IC_{50} = 397.21 ± 2.2 μM) compared to the standard (IC_{50} = 292.21 ± 1.5 μM).

Abbas *et al.,* 2017 evaluated terpenoids and alkaloids, isolated from different medicinal plants, along with their derivatives for their antiglycation activity. They observed that most of the natural products, such as terpenoids, alkaloids, and their synthetic derivatives, possessed inhibitory activity against protein glycation without any cytotoxic effect. They reported that compound gossypolidene-4-aminoantipyrine (20) (Figure 2.5) (Abbas *et al.,* 2017) had a better antiglycation activity (IC_{50} = 82.934 ± 2.924 μM) when compared to the standard rutin (IC_{50} = 98.012 ± 2.030).

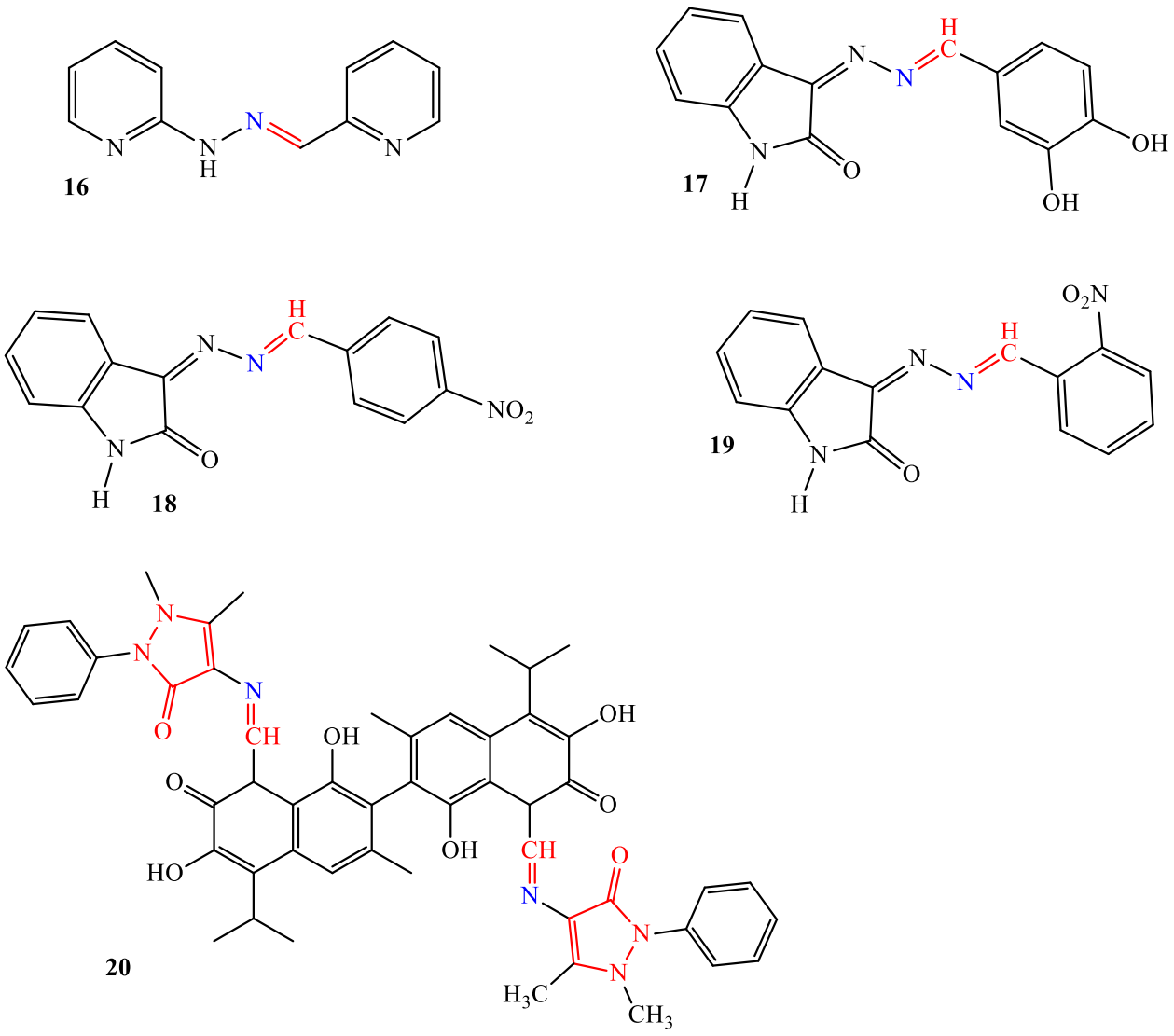

Figure 2. 5: Some Schiff Bases with Antiglycation Activity

Source: Abbas *et al.*, (2017)

2.2.4 Anticancer Activity of 4-Aminoantipyrine Derivatives

Cancers ranks as the second leading cause of death worldwide, and its toll is only becoming worse (Siegel *et al.*,2023, Arif *et al.,* 2023). A large percentage of anti-cancer drugs have been obtained from natural products and from synthesised compounds (Cakmak *et al.,* 2022). The process involved in the treatment of cancer is difficult because the medication used mostly target the human cells. Recently scientists are in search of drug molecules that can enhance efficacy and reduce adverse effects in cancer treatment (Sak, and Everaus, 2017). However, there are reports of 4-aminoantipyrine compounds that have been studied as anticancer agent in various cell lines (Figure 2.6) (Cakmak *et al.,* 2022).

Ghorab *et al.,* 2014 synthesised some heterocycles starting with 4-aminoantipyrine moiety and incorporated other biological active moieties such as pyrazole, pyrrole, pyrimidine and pyrazolopyrimidine. They evaluated their anticancer activity against human tumor breast cell line (MCF7) and observed that halogenated pyrimidine derivatives of antipyrine (**21**, **22**) had the best aticancer activities. Bensaber *et al.,* 2014, prepared some Schiff bases from pyrazol-3-one derivatives using microwave-assisted chemical method. One of the synthesised compounds (**23**) was able to cause inhibition of thymidine phosphorylase range (IC_{50} of 28 ± 2 l M) and reduce the growth of breast carcinoma cells.

2.2.5 Antibacterial Activity of 4-Aminoantipyrine Derivatives

Antibacterial resistance is a significant global health challenge and a great threat to the public health (Aljeldah, 2022, Velazquez-Meza *et al.,* 2022, Salam *et al.,* 2023). Present antibacterial drugs fail to treat many bacterial infections due to resistance (Frieri *et al.,* 2017). The search for antibacterial agents with novel mechanism is essential. To combat microbial resistance, a great deal of research is done on both natural and synthetic substances (Figure 2.7) (Choi *et al.,* 2023, Stojkovic *et al.,* 2023).

Asiri and Khan, 2010, synthesised and screened a series of 1,5-dimethyl-2-phenyl-1,2-dihydro-3H-pyrazol-3-one Schiff bases for their antibacterial activities. They observed that the compounds (**24** and **25**) with chloro and cyano substituents had better anti-bacterial activity when compared to ciprofloxacin (standard). Alam *et al.,* 2014 reported some Schiff bases from 4-aminoantipyrine which possess bactericidal and cytotoxic activities. From the report compounds (**26**) and (**27**) showed more antibacterial activity against E. coli and C.

sakazakii, respectively. Some coumarin-pyrazole hybrid compounds were recently synthesised by Microwave-assisted synthesis method (Chavan and Hosamani 2018). Among the synthesised scaffolds, compound (**28**) was reported to possess more antibacterial activities when compared to the standard (ciprofloxacin). They observed that combining coumarins with pyrazole enhanced its biological activities. Singh *et al.,* 2019, also synthesised a series of antipyrines with acetylene framework and evaluated them against protozoal pathogens (*Entamoeba histolytica and Giardia lamblia*) and bacterial strain (*Staphylococcus aureus, Vibrio cholera, E. coli, Bacillus subtillus*). They reported that two of the compounds (**29** and **30**) exhibit excellent anti-bacterial and antiparasitic activities better than approved drugs like metronidazole.

2.2.6 Antiviral Activity of 4-Aminoantipyrine Derivatives

Severe acute respiratory syndrome (SARS) is a newly emerging infectious disease caused by a novel coronavirus, SARS-coronavirus (SARS-CoV). Since the initial outbreak of SARS in Guangdong Province, China, it has been recognised as a global threat. Some of the symptoms of SARS includes high fever, chills, headache, cough, malaise rigor, and progressive radiographic changes of the chest and lymphophenia (Peiris *et al.,* 2003). There is need to explore new compounds of SARSCoV 3CLpro inhibitors that can serve as anti-SARS therapy in case the disease re-emerges.

Ramajayam *et al.,* 2010, designed, synthesised, some pyrazolone compounds and evaluated them for SARS-CoV 3CL protease inhibiting activities using fluorogenic substrate peptide. Most of the synthesised compounds showed potent inhibition against the 3CL protease. They observed that one of the inhibitors (**31**) was active against 3C protease from coxsackievirus B3. Evstropov *et al.,* (1992) also reported the antiviral activities of some derivatives of antipyrine and 4-aminoantipyrine. They discovered that nine of the studied compounds inhibited viral reproduction, and five among the nine compounds were iodinated compounds with 4-iodoantipyrine (**32**) totally inhibiting the reproduction of Coxsackie viruses (Figure 2.8) (Evstropov *et al.,* (1992).

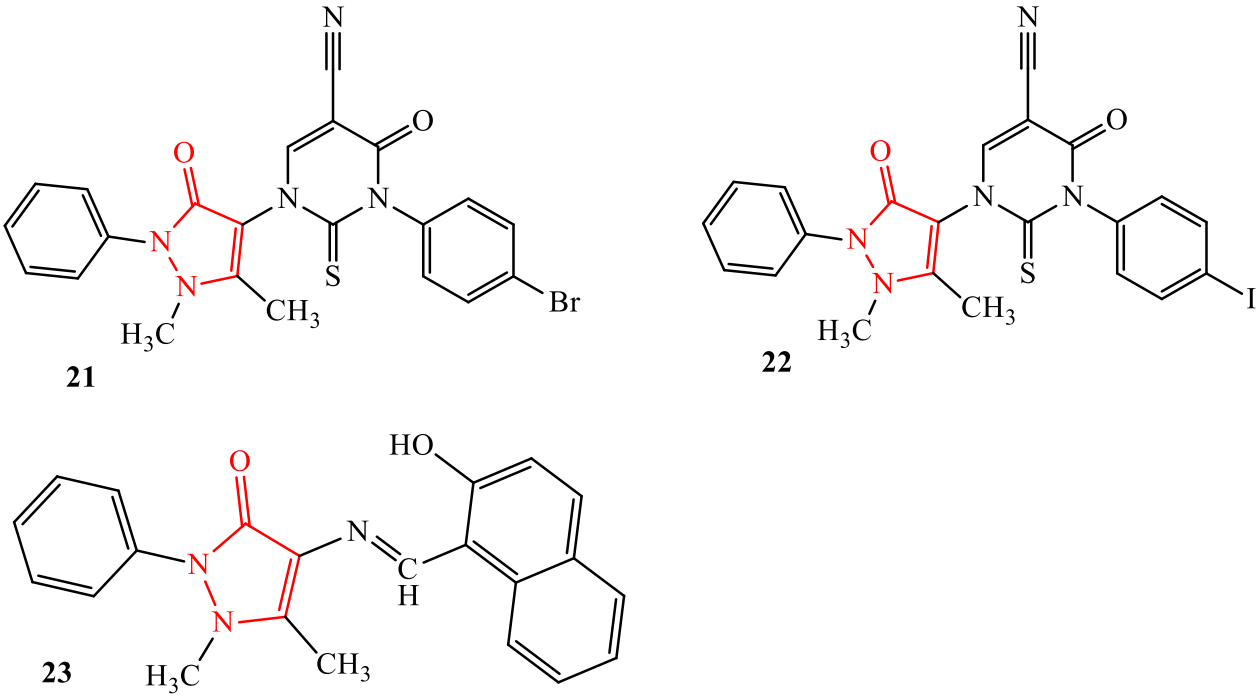

Figure 2. 6: 4-aminoantipyrine Schiff bases with Anticancer activity

Source: Bensaber *et al.*, (2014)

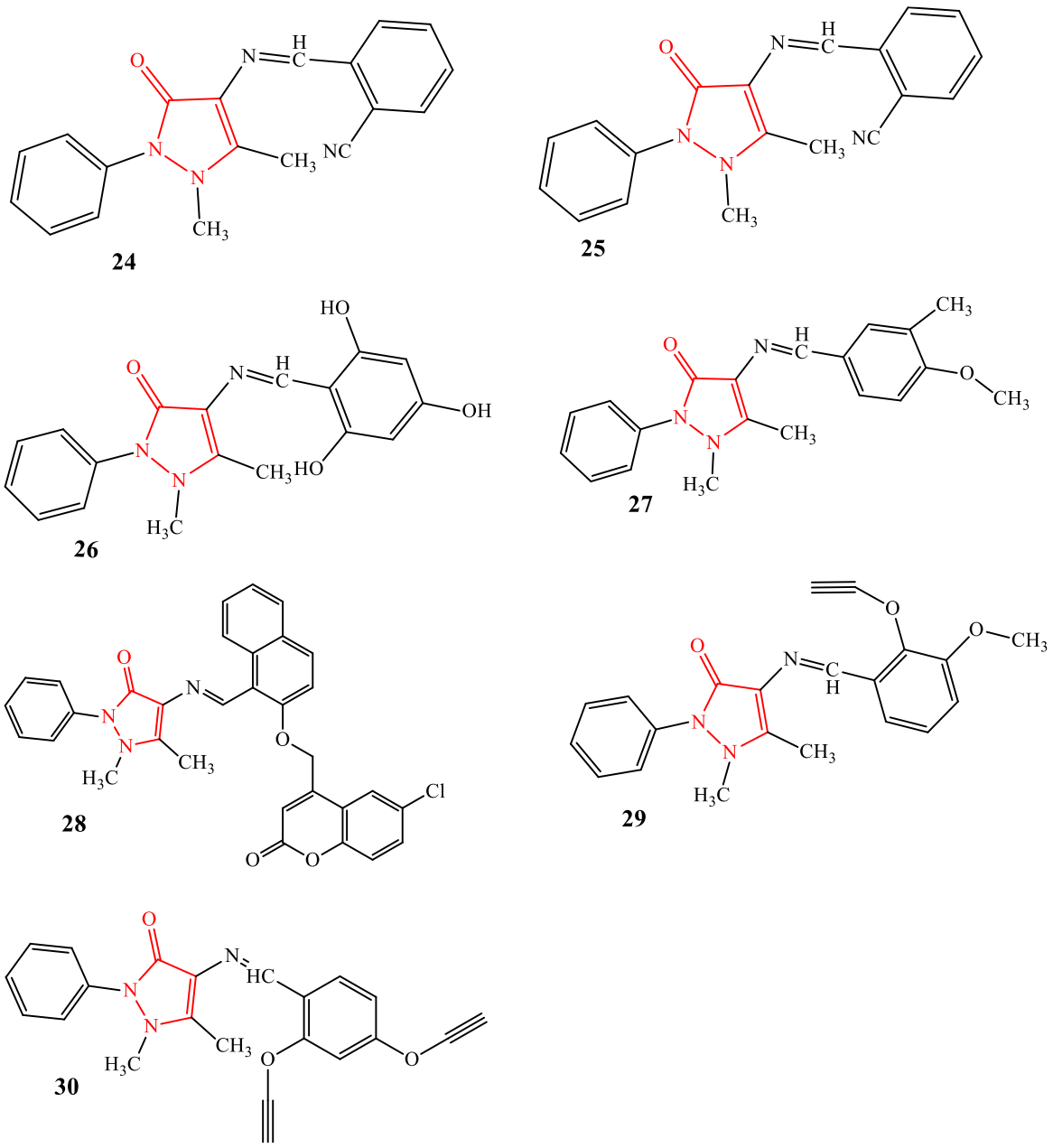

Figure 2. 7: 4-aminoantipyrine Schiff bases with Antibacterial Activity

Source: Stojkovic *et al.*, (2023)

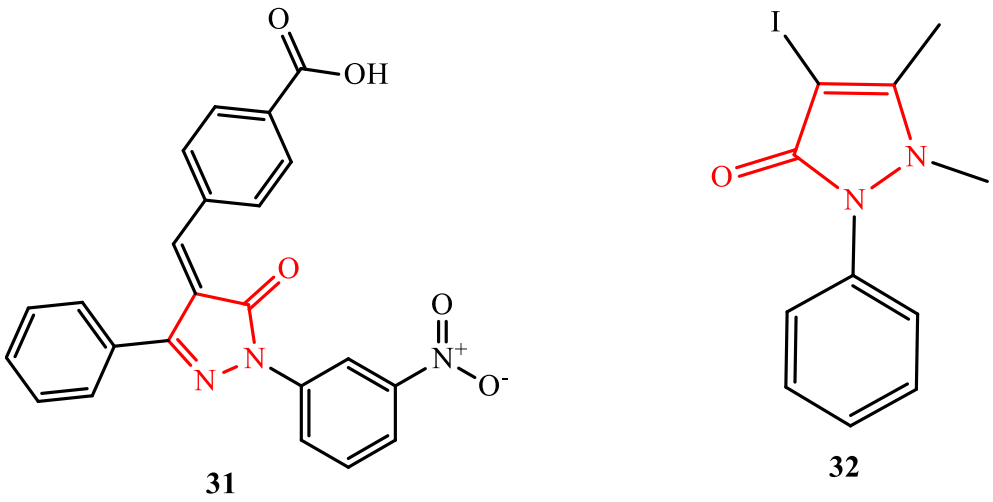

Figure 2. 8: Pyrazolone Derivatives with Antiviral Activity

Source: Evstropov *et al.*, (1992)

2.2.7 Transition Metal Complexes of 4-Aminoantipyrine Derivatives

4-aminoantipyrine readily condenses with various reagents like aldehydes, ketones, thiosemicarbazides and carbazides, thereby increasing its capacity to coordinate with metals and form various complexes (Sakthivel *et al.,* 2020). Several researchers had studied the transition metal complexes from 4-aminoantipyrine Schiff bases and had reported its numerous potential applications in analytical, biological, clinical, and pharmacological areas (Jeyasubramanian *et al.,* 2020; Ebosie *et al.,* 2021). They also reported that the activities of complexes were greater than the uncoordinated ligands due to the influence of the metal ion on the regular metabolism of cell.

Ali *et al.,* (2010) obtained metal complexes from seven different metals (Cu (II), Ni (II), Co (II), Mn (II), Zn (II), Hg (II), and Sn (II)) and 4-aminoantipyrine Schiff base, using microwave-induced organic reaction enhancement (MORE) techniques. They reported that this method of synthesis was more efficient and more environmentally friendly as compared to the traditional synthetic method. Xi *et al.,* 2009, synthesised lanthanide (III) complexes from a ligand, 1-(4-aminoantipyrine)-3-tosylurea and evaluated the DNA- binding properties. They observed that the metal complexes exhibit better scavenging activities than the ligand. Kurdekar *et al.,* 2012, synthesised some Metal complexes using ligands obtained from 4-aminoantipyrine, 2-hydroxy-3-formylquinoline, and isatin with Co (II), Ni (II), Cu (II), and Zn (II). The ligands and their metal complexes were screened for their anticonvulsant activity toward the electroshock-induced seizures in Wistar rats. They observed that all tested compounds have potential anticonvulsant activity and that the metal complexes had better activity compared to the ligands. Recently, Kashyap *et al.,* 2018, prepared Zn (II), Ni (II), Co (II) and Cu (II) metal complexes from a Schiff base of p-aminoantipyrine and m-hydroxyl benzaldehyde and evaluated their antimicrobial, anticancer and corrosion inhibitory properties. They observed that the metal complex prepared from Zn (II), exhibited more antifungal activity than the standard drug fluconazole and Ni (II) complex had excellent anticorrosion efficiency.

2.3. Theoretical Studies on 4-Aminoantipyrine

With advancements in quantum chemistry methods and computational techniques, important chemical, physical, structural, electronic and reactivity properties of molecules can be studied. Even though, numerous studies on the synthesis and biological activities of 4-aminoantipyrine and its derivatives have been reported, articles concerning the structural properties of these compounds are few in literature. Since 4-aminoantipyrine derivatives are established to be biologically active compounds, knowing their 3-dimensional structures, especially their crystal structures, will be very essential for rational drug design.

Li *et al.*, 2013, studied some compounds using single-crystal X-ray diffraction and the density functional theory (DFT) method with 6-31G to evaluate the molecular structures, molecular electrostatic potential (MEP) and the frontier molecular orbital (FMO) properties of these compounds. The results they obtained were in good agreement with experimental data. Athira *et al.*, 2017, performed DFT calculations with B3LYP/6-311G (d,p) basis set to predict the optimised geometry. They obtained a complete vibrational assignments and structural information from the study. They reported that the calculated results of the molecular geometry agreed with the X-ray diffraction parameter. Orabi *et al.*, 2018, investigated the structural and antioxidant properties of some heterocyle containing synthetic and naturally occurring pyrazole and pyrazolones derivatives. Density functional theory at the B3LYP/6-311++G(d,p) level of theory in gas phase and in methanol was used for the study. They observed that the substituents and nature of solvents influences the relative stability of pyrazolone isomers. They also predicted that the dihydroxyl derivatives are more efficient antioxidants.

2.4 Theoretical Background for Quantum Chemical Calculations

2.4.1 The Schrodinger's Wave Equation

The evolution of quantum mechanics explains molecules or atoms as interaction among electrons and nuclei while molecular geometry is described according to minimum energy arrangements of nuclei. The foundation of quantum mechanics is a product of many great contributions, the most famous and relevant for chemists is the one made by Erwin Schrdinger in 1926. He proposed that a system's state can be described as a function of particle coordinates termed a wavefunction (Ψ), which varies over time. Therefore, for one

particle, one-dimensional system, the wavefunction of the system is: $\Psi = \Psi_{(x,\ t)}$. This wavefunction contains all possible information about the system. To determine the future state of a system from the knowledge of its initial state, an equation that detailed how the wavefunction changes over time is required (Osang *et al.,* 2020). A single particle possessing an electron of mass, m, moving in field of space under the influence of a potential, V is described by a wave-function $\Psi_{(x,\ t)}$, that satisfies the Schrödinger's time dependent equation (2.1):

$$g \qquad -\frac{\hbar}{2m}\frac{\delta^2\Psi_{(x,t)}}{\delta x^2} + V_{(x)}\Psi_{(x.t)} = i\hbar\frac{\delta\Psi_{(x,t)}}{\delta t} \qquad 2.1$$

Where $i^2 = -1$, $\hbar = \frac{h}{2\pi}$; h is the Planck's constant.

Although, this time dependent Schrödinger's equation may be difficult to solve, but several applications of quantum mechanics in chemistry acquire their model from simpler Schrödinger's time-independent equation (2.2) (Paredes *et al.,* 2020).

$$-\frac{\hbar^2}{2m}\frac{\delta^2\Psi_{(x)}}{\delta x^2} + V_{(x)}\Psi_{(x)} = E\Psi_{(x)} \qquad 2.2$$

The generalised Schrödinger's equation for a multi-electron and multi-nuclear system is as shown in equation (2.3).

$$H\,\Psi = E\,\Psi \qquad 2.3$$

E is known as the energy of the system, Ψ is define as the wave-function, While H is known as the "Hamiltonian operator" which describes both kinetic energies of the electrons and nuclei that made up the molecules, together with the electrostatic interactions observe between the electrons and nuclei. There is no evident physical meaning for the wave-function., but the probability of discovering the system at a particular set of coordinates is given by the square of the wave-function multiplied by a small volume. Equation (2.4) provides the expression for H.

$$H = \frac{1}{2}\sum_i^{es}\nabla_i^2 - \frac{1}{2}\sum_A^{nu}\frac{1}{M_A}\nabla_i^2 - \sum_i^{es}\sum_A^{nu}\frac{Z_A}{r_{iA}} + \sum^{e}{}_{i<}\sum_j^{e}\frac{1}{r_{ij}} + \sum_{A<}^{n}\sum_B^{n}\frac{z_A z_B}{R_{AB}} \qquad 2.4$$

Where Z is the nuclear charge.

The mass of a nucleus A divided by the mass of an electron is expressed as M_A.

The distance between nuclei A and B is known as R_{AB}

The distance between nucleus A and electron i, is known as $r_{ij.}$

This equation yields the total energy 'E' of the system state; but finding the exact formulations of $\hat{H}$ and Ψ can be difficult and solving the equation exactly is impossible for most practically relevant chemical systems. Due to this complexity of the quantum mechanical equations, various approximations and simplifications of the equations are required (Osang *et al.*, 2020).

2.4.2 The Born-Oppenheimer Approximation

The fundamental ideas that underlie the description of the quantum states of molecules are known as the Born-Oppenheimer approximation (Federica and Basile, 2022). It separates the nuclear and electronic contributions, allowing them to be solved consecutively. It states that since electrons move in orders of magnitude faster than the heavier nuclei, they can be viewed as moving in a field of fixed nuclear potential. This is one way of simplifying the Schrödinger's equation for multi-nuclei and multi-electron systems. The Born-Oppenheimer approximation considerably decreases complexity and improves the viability of quantum chemical computations by disregarding nuclear kinetic energy (Zhao *et al.*, 2020). An electronic Schrödinger's expression results from this, as shown in (2.5) and (2.6) where the Hamiltonian operator has been collapsed:

$$\hat{H}^{ei}\Psi^{ei} = E^{ei}\Psi^{ei} \qquad 2.5$$

$$\hat{H}^{ei} = -\frac{1}{2}\sum_i^e \nabla_i^2 - \sum_i^e \sum_A^n \frac{Z_A}{r_{iA}} + \sum_{i<}^e \sum_j^e \frac{1}{r_{ij}} \qquad 2.6$$

The electronic energy, Eei, was added to the nuclear coulumbic part that is constant in equation 2.4 to obtain the total energy, E, for the system as illustrated in equation (2.7), which is absent from equation 2.6.

$$E = E^{ei} + \sum_{A<}^{nuclei} \sum_B^{nuclei} \frac{Z_A Z_B}{R_{AB}} \qquad 2.7$$

2.4.3 Hartree-Fock Models

The Hartree-Fock (HF) method was developed by Hartree and Fock soon after the birth of quantum mechanics (Chen *et al.*, 2020). The Hartree-Fock Models continues from electronic Schrodinger equation by introducing two approximations which are the Hartree-Fork approximation and the LCAO approximation.

The need to simultaneously calculate each electron's energy in the presence of all other electrons causes the Schrödinger equation to be the most challenging to solve (Osang *et al.,* 2020). The Hartree-Fock approximation, however, circumvented this issue by assuming that electrons move independently of one another and are constrained to structures known as molecular orbitals, with each electron's energy being calculated in the averaged static field of the others (Scamps *et al.,* 2020). An approximation is first made about the electron energies before the energy of each electron is then estimated in the field of the initial electron configuration.

The LCAO makes use of the idea that each one electron solutions for many-electron atoms and molecules will mirror a single electron solution for the hydrogen atom. The predominant way to approximate the total many-electron wave-function Ψ, required to solve the Schrödinger equation 2.5, is by combining some atom-centered function called basis functions Φ into molecular orbitals ψ (Goletto *et al.,* 2021):

$$\Psi_i = \sum_{\mu=1}^{Basisfunction} C_{\mu,i}\,\phi_\mu \qquad 2.8$$

In equation (2.8), *C* is the coefficient of the molecular orbital function, often named molecular orbital. The construction of N molecular orbitals from linear combination of N atomic orbitals (MO-LCAO) is a common method of gaining quantitative many-electron wave functions, where diverse quantum chemical methods are used to determine the optimal coefficients C_i. MO-LCAO is also used frequently for qualitative arguments to rationalise properties of molecules, such as the nature of bond formation, reactivities, and orbital hybridisations. This highlights how quantum chemical method can promote a general understanding of chemistry outside the purely computational domain.

2.4.4 Density Functional Theory

The Density functional theory Popularly known as DFT was established by Kohn, Sham and Hohenberg, in the mid-1960s (Herbert, 2023). The DFT method, an alternative to the HF methodology, enables more accurate findings to be acquired using calculations that need less computer effort (Qin *et al.,* 2023). This theory state that "the energy, E, of a system is a functional of the electron density $\rho(r)$ of the system written as:

$$E = F\left[\rho_{(r)}\right] \qquad 2.9$$

As a result, the electron density can be used to calculate a molecule's energy rather than the wave function that the Hartree-Fock technique requires. The benefit of utilising electron density is that since it is a three-dimensional function and scales as N^3, the integrals for Coulomb repulsion only need to be performed over the electron density. Additionally, some electron correlation can be incorporated into the computations, which makes them more precise and faster than HF calculations (which scale as N^4). There are numerous classes of density functionals according to the type of approximations that are made to the Exchange Correlation Functional (E_{XC}) (Nagai *et al.,* 2020). The simplest approximation to the complete problem is called a local density approximation (LDA) where E_{XC} depends solely on the electron density, $\rho(r)$ at each point in space.

Band structure calculations frequently involve LDA calculations. For molecular computations, where both qualitative and quantitative mistakes might occur, their performance is less outstanding since they provide less precise geometries and estimate binding energies that are drastically too high (Stohr *et al.,* 2019).

A more complex set of functional used is the generalised gradient approximation (GGA) where the functional form of E_{XC} rely on the density of the electron and the gradient of the electron density, at each point in space. There are a variety of hybrid techniques that combine Hartree Fock calculation components, often the exchange integrals, with functionals from other methods. One of the most common combinations is the B3 functional, an exchange functional, twinned with LYP to produce B3LYP. However, B3LYP has proved very successful for the study of a wide range of systems. Other examples are BLYP, BP86 and BPW91 (Garrick *et al.,* 2023).

2.4.5 Basis Sets

A basis set is a collection of functions known as basis functions, used in the Hartree-Fock method or DFT to describe the electronic wave function and convert the model's partial differential equations into algebraic equations that can be effectively implemented on a computer (Zhang and Lu, 2021). Atomic orbitals and molecular orbitals are created using basis functions, and they are frequently enlarged as a linear combination of these functions with evaluable coefficients. There are two categories into which these basis functions can be divided:

Slater type orbitals (STOs)

Gaussian type orbitals (GTOs)

The Slater type orbitals provide a detailed description of the behavior of hydrogen atomic orbitals because they have a good exponential decay for bigger values, of spherical coordinates. Due to the time-consuming nature of the four centre two electron integrals, they are challenging to process computationally. The GTOs, in contrast, decrease too quickly when using a large value of spherical coordinates. Notwithstanding, the GTOs are more acceptable since a third atom that is positioned between two other atoms that are the canters of two GTOs is created. Several GTOs can be put together to estimate an STO, and in many cases, this turns out to be more effective than utilising the STO directly (Shaw *et al.,* 2020).

Since valence electrons undergo the greatest amount of change during chemical reactions, it is crucial to have a versatile description of these electrons. Split valence basis sets are those in which the treatment of the core and valence orbitals differs. The 6-31G is an example of the most popular split valence basis set. This basis set's nomenclature, X-YZG, is as follow:

When describing a single contracted Gaussian function of the core, X is the total number of primitive GTOs employed.

The numbers Y and Z indicate how many simple GTOs are used to describe the valence orbitals. 6-31G is made up of two functions, one with three primitives and the other with just one.

- X is the total number of primitive GTOs employed when describing a single contracted Gaussian function of the core.
- Y and Z. indicate how many simple GTOs are used to describe the valence orbitals. For instance, 6-31G is made up of two functions, one with three primitives and the other with just one.

By utilising polarization functions and/or diffuse functions, the basis sets can be expanded. An atomic bond causes the electrical cloud surrounding each atom to deform, this is known as polarization. To account for this, higher angular momentum functions are added to the basis set. For instance, Polarization is enabled by adding a p-function to H. Similarly, a d-function can be inserted to a basis set containing p valence orbitals, and a f-functions for d-valence orbitals. To obtain more concise results, the given polarization functions can be described more precisely. For instance, P and d polarization functions can be applied to a hydrogen atom's 6-31G basis set to create 6-31G (p d).

When deliberating anions or diffuse electronic clouds in second or third row transition metals, the section of atomic orbitals far from the nucleus known as the diffuse functions, denoted by a "+" (for instance, 6-31+G or 6-31++G), can play a crucial role. Also note that the inner core of transition metal atoms is very massive, which means that a lot of basis functions would be needed to represent it. These basic functions can be replaced with an Effective Core Potential (ECP) to fix the issue. The ECP will represent the impact of the nucleus and the inner shell electrons on the valence electrons as a typical effect (Yeung *et al.,* 2019). This enables the minimisation of large computational calculations while also including certain relativistic impacts on the system under study, since these basis functions are produced via relativistic atomic computations. The notation 6-31G means that 6 primitive gaussians are used for each core orbital and two functions containing three and one primitives are used for each of the valence orbitals. Most basis sets start with 6-31G or 6-311G and then extend by adding diffuse (+) and/or polarisation functions (Ireland and McKemmish, 2023).

2.4.6 QSAR Studies

The properties of any molecule are a function of its molecular structure. The biological activity of a compound can be modified by modifying the chemical structure of the compound since molecules with identical structures might share comparable biological activities (Suhane *et al.,* 2019). Quantitative Structure Activity Relationship (QSAR) model establishes mathematical correlations between descriptors and biological functions or chemical reactivity of known ligands to anticipate the unknown ligands' activity or reactivity. QSAR is a technique ultilised in various field like, biology, environmental toxicology, agro-chemistry, pharmaceutical chemistry, and drug design to foresee and categorise biological activity of either virtual or synthesised molecules (Tomar, 2022; Veerasamy, 2022).

QSAR models play a crucial part in designing new chemical substances, by discerning the hit compounds and providing high quality leads to minimise the frequency of expensive experiments, speed up the drug discovery process, avoid unnecessary animal testing and prevent a lot of environmental toxicity (Fu *et al.,* 2021; Belfield *et al.,* 2023). QSAR models are utilised to choose alternate mechanisms of action, forecast new design approaches, identify pertinent structural traits, and suggest fresh hypotheses for future research (Veerasamy, 2022).

QSAR modeling is done in stages, firstly, dataset is collected, and these data must be original, accurate, reliable, and understandable. They should be robust and sufficient to maintain statistical stability of a QSAR model and uniform distribution of compound bioactivity (Czub *et al.,* 2022).

Secondly, molecular descriptors are created and selected for the dataset's ligands. A molecular descriptor is the outcome of a logical and mathematical process that converts the chemical information contained in a molecule's graphical representation into a meaningful number. Only a small number of the chemical structural descriptors accessible from various computing programs have a strong correlation with the activity. It is crucial to use descriptors that can capture the fluctuation of activity with structure to produce a statistically robust model (Belfield *et al.,* 2023).

Thirdly, a satisfactory statistical model to determine the connection between the selected descriptors and biological function is developed. Either linear or non-linear approaches can be used to construct this model. Examples of linear approaches are multiple linear regressions (MLR) (Quadri *et al.,* 2022) or partial least square (PLS) (Laise *et al.,* 2021). Non-linear methods include Polynomial Neural Network (PNN) and support vector machine (Mahdaviara *et al.,* 2020). To get more robust and biologically appropriate model, the number of descriptors should be kept minimum. Generally, the number of descriptors chosen to perform MLR is one-fifth of the number of compounds throughout the training set to keep off chance correlation.

Lastly, a subset of randomly picked compounds from a known dataset is utilised as the training dataset, and the other compounds are used as testing compounds. To maintain the statistical stability of the QSAR model, validation techniques like leave-one-out cross-validation (LOOCV) are frequently used during model training. Up till a sufficient training performance is attained, the training process is repeated. The trained model is then used to predict the activity values of those chemicals in the testing set (Kovacs *et al.,* 2021).

2.4.7 Molecular Docking

Molecular docking process is a structure-based drug design method used to stimulate molecular interaction and forecast the mechanism of binding between a tiny molecule (a ligand) and a protein (a receptor) (Pinzi and Rastelli, 2019). Docking aids in analyzing the behavior of the ligand in the binding site of the target protein, forecasting the conformation, orientation, and location of the ligand in the active site, and calculate the binding affinity. The docking process helps to explain the fundamental biochemical processes. Böhm developed the first programs and scoring functions in the 1990's (Bohm, 1992; Kumar and Kumar, 2019).

The numerous numbers of docking programs now obtainable has made it easier for docking to be done successfully in two steps. Initially, by sampling the ligand's conformation within the protein's active site and secondly, by using a scoring formula to rank these conformations (Isert *et al.,* 2023). Scoring is a forecast of the binding tightness for each ligand orientation with a physical or empirical energy function (Vemula *et al.,* 2023).

According to the theory that lower energy scores indicate better ligand-receptor interactions than higher ones, the final docked conformation (position) is chosen.

Programs frequently used for molecular docking research are Molecular Operating Environment (MOE), GOLD, FlexX, DOCK, and AutoDock (Ivanova and Karelson, 2022). More recently Autodock Vina from PyRX (Ivanova and Karelson, 2022), Prime MM-GBSA program and Glide Ligand Docking panel of Maestro 12.5 on Schrödinger Suite (Schrodinger 2020) are used for docking.

Docking techniques have been successfully used to screen millions of potential pharmacophores, to acquire fresh chemical compounds that might turn into new medicines. The advent of the reverse molecular docking technology had led to a great improvement in the prediction of drug target and in understanding molecular mechanism for drug design (Fan *et al.,* 2019). Hence docking has greatly aided in the speedy, cost-effective, and efficient discovery of new drugs.

2.4.8 In Silico ADMET Profiling

It is possible to determine whether a compound when used as a drug can be easily absorbed, transported to its specific site of action, metabolised in a way that does not immediately remove the activity, and easily removed from the body while preventing advert effects through a process called Absorption, Distribution, Metabolism, Elimination, and Toxicity (ADMET) analysis (Pradeepkiran *et al.,* 2021). The inclusion of in silico prediction of ADMET properties at earlier stages of drug discovery programs is crucial (Guan *et al.,* 2019; Wu *et al.,* 2020) for minimising the rate of pharmacokinetics related failure of drugs in the clinical phases and to lower the cost of bringing a new drug to the market. Drug-likeness is defined as the compounds that have adequate absorption, distribution, metabolism, and elimination qualities to be accepted into human Phase 1 clinical trials (Ferreira and Andricopulo, 2019). Drug-likeness analysis is a qualitative evaluation of oral bioavailability, and it is created based on structural or physicochemical investigation of compounds in the advanced phases of drug development. Drug-likeness has been successfully studied using the Rule-based filters (Daina *et al.,* 2017). The Rule-based filters is a combination of the Lipinski filter (Lipinski *et al.,* 2001), the Ghose method (Ghose *et*

al., 1999), the Veber method (Veber *et al.,* 2002), Egan ‘s method (Egan *et al.,* 2000), and Muegge’s method (Muegge *et al.,* 2001).

Christopher A. Lipenski in 1997, developed the Lipinski’s rule of five, also known as the Rule of Five (RO5), following the discovery that most medication relatively have small molecular mass and are lipohillic (Lipinski *et al.,* 2001). The RO5 was designed as an aid in filtering out regions of chemical space that are less likely to see success as an orally absorbed drug. The rule states that for a compound to be a likely successful lead candidate, orally absorbed, it must obey at least 3 of the following: less than 5 hydrogen bond donor groups, less than 10 hydrogen bond acceptor groups, a molecular mass of than 500 Da and calculated lipophilicity (clogP) of less than 5. In practice, these rules aim to get rid of substances that would be too polar, too large, or too insoluble to be effectively absorbed in the stomach following oral administration (Homayun *et al.,* 2022).

Ghose and co-workers proposed that for a compound to be a suitable drug, it should have an estimated Log P of -0.4 to 5.6, 40 to 130 molar refractivity, molecular weight of 180 to 480, number of atoms of 20 to 70 atoms. The Veber's Rule predicts that substances will have adequate oral bioavailability if they have 10 or fewer rotatable bonds and PSA no greater than 140 $Å^2$. According to the Egan rule, the Log P value, and TTPSA) should not exceed 5.88 and 131.6, respectively. Bayer Pharmaceuticals proposed the Muegge rule and according to the rule, an effective drug molecule must have MW of 200-600 D, Log P between -2 to +5, TPSA not more than 150, Number of rings ≤ 7, Number of carbon atoms ≥ 4, Number of heteroatoms more than 1, Number of rotatable bonds ≤ 15, HBD ≤ 5, HBA ≤ 10 and Abbott bioavailability F not more than 10%. These parameters relate to adequate aqueous solubility and intestinal permeability and oral bioavailability.

If a molecule breaks two or more of the rules, it would not be active when taken orally. Drug-like compounds also need to be screened against biological targets to ascertain their oral bioavailability, aqueous solubility, synthetics accessibility (SA), pharmacokinetic viability, blood-brain barrier permeability (BBB). In addition, appropriate toxicity of compounds such as hepatotoxicity, carcinogenicity, immunotoxicity, mutagenicity and cytotoxicity need to be predicted for the compounds to pass phase I clinical trials (Cavasotto and Scardino, 2022; Erazua *et al.,* 2023).

CHAPTER THREE

MATERIAL AND METHODS

3.1 Experimental Reagents, Apparatus, and Instruments

The chemicals used in synthesis were bought from commercial sources Sigma Aldrich (USA), Alfa Aesar (USA), Oakwood Chemicals (USA), Fluka (Switzerland), and were used without further purification. The reagents/chemicals used include 4-aminoantipyrine, glacial acetic acid, benzaldehyde derivatives, 2,2-Diphenyl-1-picrylhydrazyl (DPPH), opsonised zymosan, Gallic acid, N-acetyl cysteine, 3-[4,5-dimethylthiazole-2-yl]-2,5-diphenyl-tetrazoliumbromide (MTT), reactive oxygen species detecting probe and permethrin.

All solvents, including n-hexane, ethyl acetate, dichloromethane, methanol, ethanol, chloroform, and dimethylsulfoxide (DMSO) were analytical grades. Distilled water was also used. Glass wares utilised are 50 mL and 100 mL round bottom flasks, beakers, reflux condensers, glass funnels, stirring rod, Thin Layer Chromatography (TLC) developing tank, separating funnel, and vials. Magnetic stirrer/heater, electric oven, a Black and Decker electric gun heater, Germany) Precoated aluminum plates (Alugram, SIL G/UV254, Germany) and ultraviolet light (uvitec UV-254/365 nm) apparatus were also utilised. Other apparatus/materials used are chiller, spatula, retort stand, magnetic beads, magnetic rod, micro-pipette, hatching tray, Lamp, petri plates, brush, and cotton wool.

Melting Points (m.pt) were recorded in open capillaries on a Buchi M-560 (Japan) apparatus. The Fourier Transform Infrared (FT-IR) spectra of the compounds were recorded Shimadzu FTIR-8900 (Japan) spectrometer using potassium bromide disc technique to determine the vibrational frequencies, (cm^{-1}) of the IR active functional groups. Thermo scientific Evolution 300 UV-Vissible spectrophotometer was used to determine the

wavelength of maximum absorption (λmax) in chloroform and methanol. The Mass to Charge (*m/z*) ratios of ions produced were determined by Electron Ionisation-Mass Spectrometry (EI-MS) using Jeol-600H-1(Japan). Crystal structures were obtained by using Bruker APEXII CCD diffractometer. The Bruker SHELXTL Software Package was used to solve and refine the structure. ^{1}H and ^{13}C Nuclear Magnetic Resonance (NMR) spectra of the compounds, in Dueterated Dimethyl Sulphoxide (DMSO-d_6) and methanol were obtained on Bruker Avance 400 and 500 MHz spectrometers (Switzerland).

3.2. Synthesis

Schiff bases were first synthesised by condensation method. The Schiff bases with one or more hydroxyl substituent were reacted with benzyl halide to further synthesise ethers or reacted with propargyl bromide to obtain ether alkyne compounds. The percentage yield, melting point and physical appearance of each synthesised compounds, were recorded. The compounds were analysed by IR spectroscopy using potassium bromide (KBr) disc method to obtain the various characteristics vibrational frequencies $\bar{\upsilon}$ (cm^{-1}) of the functional groups present. Ultraviolet (UV) spectroscopic analysis was done in chloroform to obtain maximum absorptions, λmax (nm). Some of the synthesised compounds were dissolved in a solution of dichloromethane and methanol (1:1) and allowed to evaporate slowly at 25 to 35 ^{o}C to obtain crystals which were used for XRD. EI-MS produced ions were separated and analysed according to their *m/z* ratios. Chemical shift values, δ (ppm) were obtained using tetramethyl silane $(CH_3)_4Si$, (TMS) as internal standard and recorded in part per million (ppm) to 3 decimal places. The coupling constants (*J*) were measured in Hertz (Hz) to one decimal place. ^{13}C NMR chemical shift values were listed and assigned to specific carbon atoms.

3.2.1 Synthesis of Schiff Bases

The Schiff bases (SB1-SB19) were synthesised according to schemes 3.1 to 3.30, by the condensation of commercially available 4-aminoantipyrine with different aromatic aldehydes in ethanol, using glacial acetic acid as catalyst (Murtaza *et al.,* 2017; Borase *et al.,* 2021; Raju *et al.,* 2022).

3.2.2 Synthesis of Ether Compounds

4-aminoantipyrine Schiff bases were converted to ethers by the procedure described by Chavan and Hosamani 2018 as shown in schemes 3.31 to 3.48. A mixture ofanhydrous potassium carbonate (used as catalyst) and the synthesised Schiff bases (with hydroxyl substituent) in a ratio of 2:1 was stirred for 1h in DMF. To this, substituted benzyl bromide or benzyl chloride was introduced and the mixture stirred for 6 –18 h at 25-35 ^{o}C. TLC was used to monitor the progress of the reaction. Extraction was done using water and ethyl acetate. The ethyl acetate (organic) layer was further extracted with saturated solution of lithium chloride. Excess ethyl acetate was evaporated off and solid products were obtained as pure compounds.

3.2.3 Synthesis of Ether-Alkyne Compounds

4-aminoantipyrine Schiff bases were converted to ether-alkyne compounds by the procedure described by Chavan and Hosamani 2018 according to Schemes 3.49 to 3.58. A mixture of anhydrous potassium carbonate (used as catalyst) and the synthesised Schiff bases in a ratio of 2:1 was stirred for 1h in DMF. To this, substituted propargyl bromide was added and the mixture stirred for 6 -12 hours at 25-35 ^{o}C. The TLC was used to monitor the progress of the reaction. Extraction was done using water and ethyl acetate. The ethyl acetate (organic) layer was further extracted with saturated solution of lithium chloride. Excess ethyl acetate was evaporated off and solid products were obtained as pure compounds.

3.3.1 Synthesis of 4-(benzylideneamino)-1,5-dimethyl-2-phenyl-1,2-dihydro-3H-pyrazol-3-one (SB0)

Compound SBO was synthesised according to Scheme 3.1**.** In a round bottom flask (100 mL) fitted with a condenser and a magnetic stirrer, benzaldehyde (0.05 mL, 0.4 mmol), 4-aminoantipyrine (0.0813 g, 0.4 mmol), glacial acetic acid (2 drops) and ethanol (10 mL), were refluxed at 80 ^{o}C for 10 hours. A TLC system of n-hexane: ethyl acetate, 6:4 (*Rf* value 0.520) was used to keep track of the rection development. The resulting mixture was filtered after cooling to room temperature, recrystallised with ethanol and dried under vacuum to afford cream crystals of compound 4-(benzylideneamino)-1,5-dimethyl-2-phenyl-1,2-dihydro-3H-pyrazol-3-one (0.1062 g).

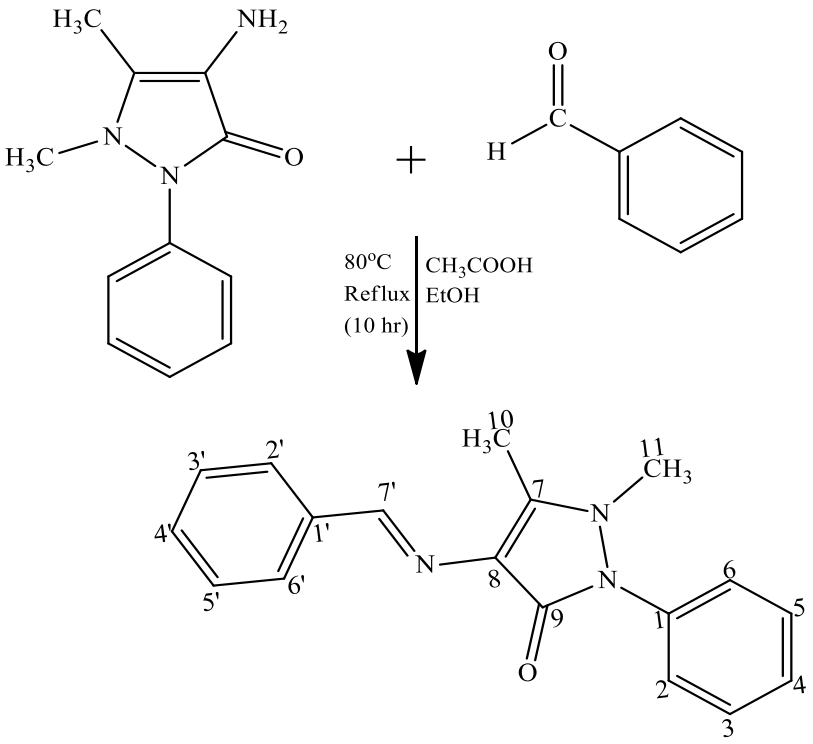

Scheme 3. 1: Synthetic Route for SB0

3.3.2 Synthesis of 1,5-dimethyl-4-((4-nitrobenzylidene)amino)-2-phenyl-1,2-dihydro-3H-pyrazol-3-one (SB1)

The synthesis of compound SB1 followed Scheme 3.2. A mixture of 4-nitrobenzaldehyde (0.0605 g, 0.4 mmol), 4-aminoantipyrine (0.0813 g, 0.4 mmol), glacial acetic acid (2 drops) and 10 mL of ethanol, in a round bottom flask (100 mL) was refluxed at 80 ^{o}C for 4 hours. A TLC system of n-hexane: ethyl acetate, 5:5 (R*f* value 0.61) was used to monitor the reaction process. The resulting mixture was cooled to room temperature, filtered, recrystallised with ethanol and dried under vacuum to afford orange crystals of compound 1,5-dimethyl-4-((4-nitrobenzylidene)amino)-2-phenyl-1,2-dihydro-3H-pyrazol-3-one (0.1097g).

3.3.3 Synthesis1,5-dimethyl-4-((2-nitrobenzylidene)amino)-2-phenyl-1,2-dihydro-3H-pyrazol-3-one (SB1A)

According to Scheme 3.3, compound SB1A was synthesised. A mixture of 2-nitrobenzaldehyde (0.0605 g, 0.4 mmol), 4-aminoantipyrine (0.0813 g, 0.4 mmol), glacial acetic acid (2 drops) and 10 mL of ethanol, was refluxed at 80 ^{o}C in a round bottom flask (100 mL) for 5 hours. The process of reaction was monitored by TLC system of n-hexane: ethyl acetate, 5:5 (R*f* value 0.63). On completion of the reaction, the temperature of the mixture was lowered to room temperature, precipitates formed were filtered out, recrystallised with ethanol, and dried. Orange crystals of compound (1,5-dimethyl-4-((2-nitrobenzylidene)amino)-2-phenyl-1,2-dihydro-3H-pyrazol-3-one (0.1179 g) was obtained.

3.3.4 Synthesis of 1,5-dimethyl-4-((3-nitrobenzylidene)amino)-2-phenyl-1,2-dihydro -3H-pyrazol-3-one (SB1B)

In accordance with Scheme 3.4, compound SB1B was synthesised. Equimolar quantity (0.4 mmol) of 3-nitrobenzaldehyde (0.0605 g), 4-aminoantipyrine (0.0813 g), in 10 mL of ethanol and with 2 drops of glacial acetic acid was refluxed at 80 ^{o}C in a round bottom flask (100 mL) for 6 hours. A TLC system of n-hexane: ethyl acetate, 5:5 (R*f* value 0.60), was used to track the reaction's progress. The resultant mixture was filtered after reaching room temperature, recrystillised with ethanol and dried to afford orange crystals of compound 1,5-dimethyl-4-((3-nitrobenzylidene)amino)-2-phenyl-1,2-dihydro-3H-pyrazol-3-one 0.1199g.

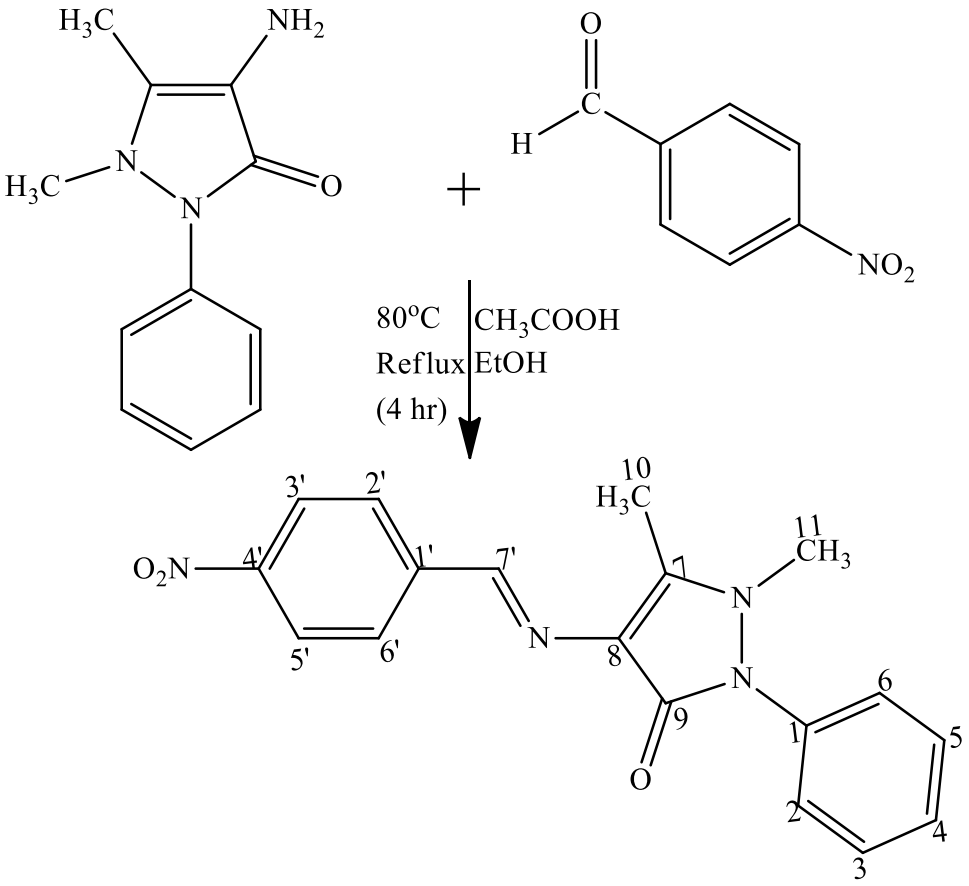

Scheme 3. 2: Synthetic Route for SB1

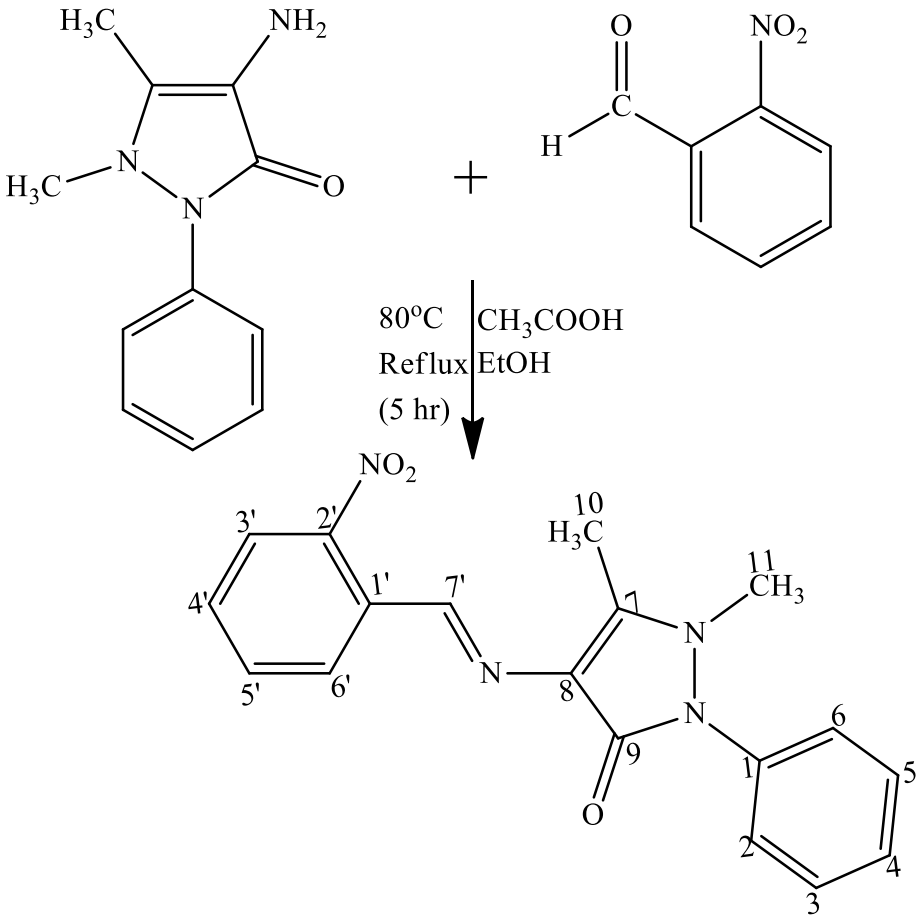

Scheme 3. 3: Synthetic Route for SB1A

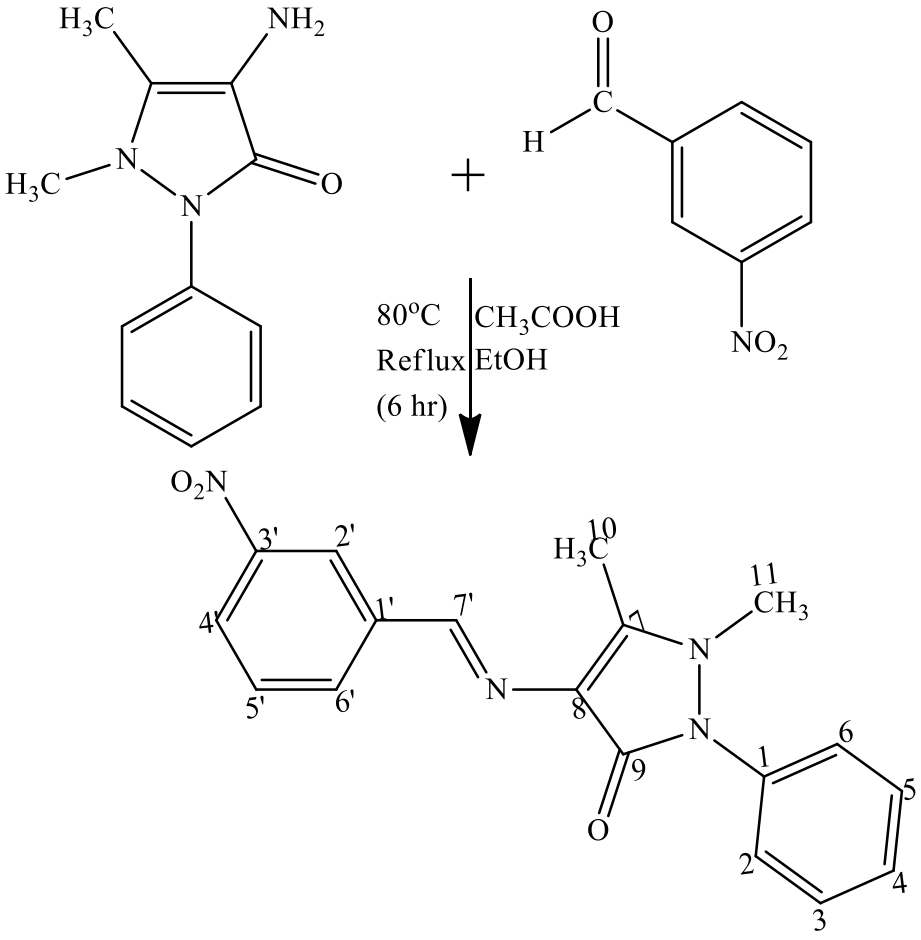

Scheme 3. 4: Synthetic Route of SB1B

3.3.5 Synthesis of 4-((4-fluorobenzylidene)amino)-1,5-dimethyl-2-phenyl-1,2-dihydro-3H-pyrazol-3-one (SB2)

The synthesis of compound SB2 followed Scheme 3.5. In a round bottom flask (100 mL) fitted with a condenser and a magnetic stirrer,4-fluorobenzaldehyde (0.043 mL, 0.4 mmol), 4-aminoantipyrine (0.0813 g, 0.4 mmol), glacial acetic acid (2 drops) and ethanol (10 mL), were refluxed at 80 ^{o}C for 4 hours. A TLC system of n-hexane: ethyl acetate, 7:3 (R*f* value 0.57) was used to monitor the progress of the reaction. The resultant mixture was cooled to room temperature, filtered, recrystillised with ethanol and dried under vacuum to afford pale yellow crystals of compound 4-((4-fluorobenzylidene)amino)-1,5-dimethyl-2-phenyl-1,2-dihydro-3H-pyrazol-3-one (0.0835 g).

3.3.6 Synthesis of 4-((2-fluorobenzylidene)amino)-1,5-dimethyl-2-phenyl-1,2-dihydro-3H-pyrazol-3-one (SB2A)

The synthesis of compound SB2A followed Scheme 3.1. In a round bottom flask (100 mL) fitted with a condenser and a magnetic stirrer, 2-fluoro benzaldehyde (1.178 g, 0.4 mmol), 4-aminoantipyrine (0.0813 g, 0.4 mmol), glacial acetic acid (2 drops) and ethanol (10 mL), were refluxed at 80 ^{o}C for 6 hours. A TLC system of (n-hexane: ethylacetate,7:3 (R*f* value 0.55) was used to keep track of the reaction progress. On completion of the reaction, the resultant mixture was lowered to room temperature, filtered, recrystillised with ethanol and dried under vacuum to obtain yellow crystals of compound 4-((2-fluorobenzylidene)amino)-1,5-dimethyl-2-phenyl-1,2-dihydro-3H-pyrazol-3-one (0.1140 g).

3.3.7 Synthesis of 4-((3-fluorobenzylidene)amino)-1,5-dimethyl-2-phenyl-1,2-dihydro-3H-pyrazol-3-one (SB2B)

Compound SB2B was synthesised according to Scheme 3.7. In a round bottom flask (100 mL) fitted with a condenser and a magnetic stirrer, 3-fluoro benzaldehyde (0.424 mL, 0.4 mmol), 4-aminoantipyrine (0.0813 g, 0.4 mmol), glacial acetic acid (2 drops) and ethanol (10 mL), were refluxed at 80 ^{o}C for 3 hours. A TLC system of n-hexane: ethyl acetate,7:3 (R*f* value 0.43) was used to keep track of the reaction progress. On completion of the reaction, the resultant mixture was lowered to room temperature, filtered, recrystillised with ethanol and dried under vacuum. Pale yellow crystals of compound 4-((2-fluorobenzylide ne)amino)-1,5-dimethyl-2-phenyl-1,2-dihydro-3H-pyrazol-3-one (0.1059 g) was obtained.

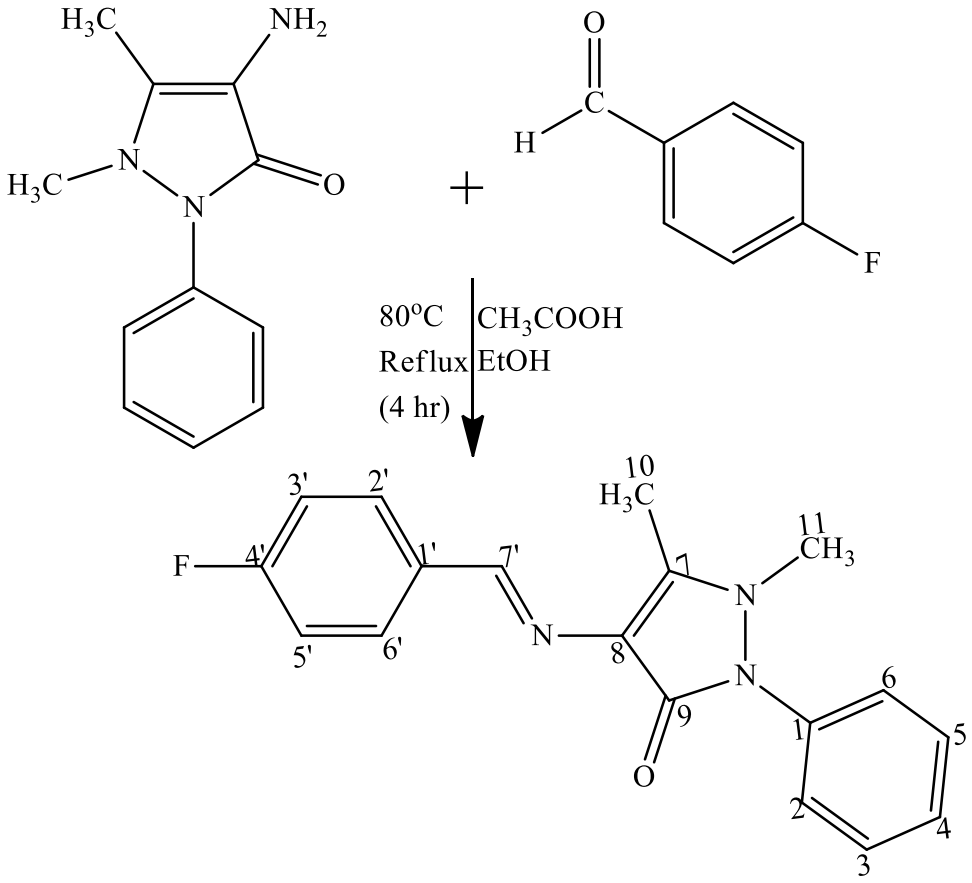

Scheme 3. 5: Synthetic Route of SB2

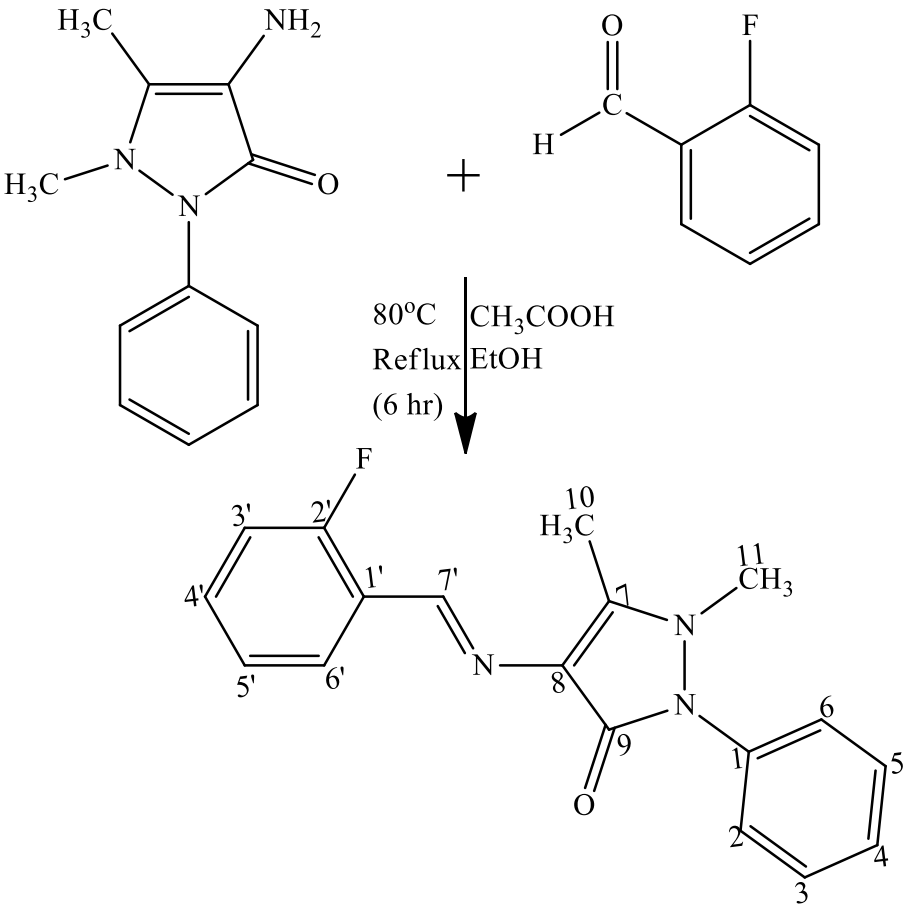

Scheme 3. 6: Synthetic Route of SB2A

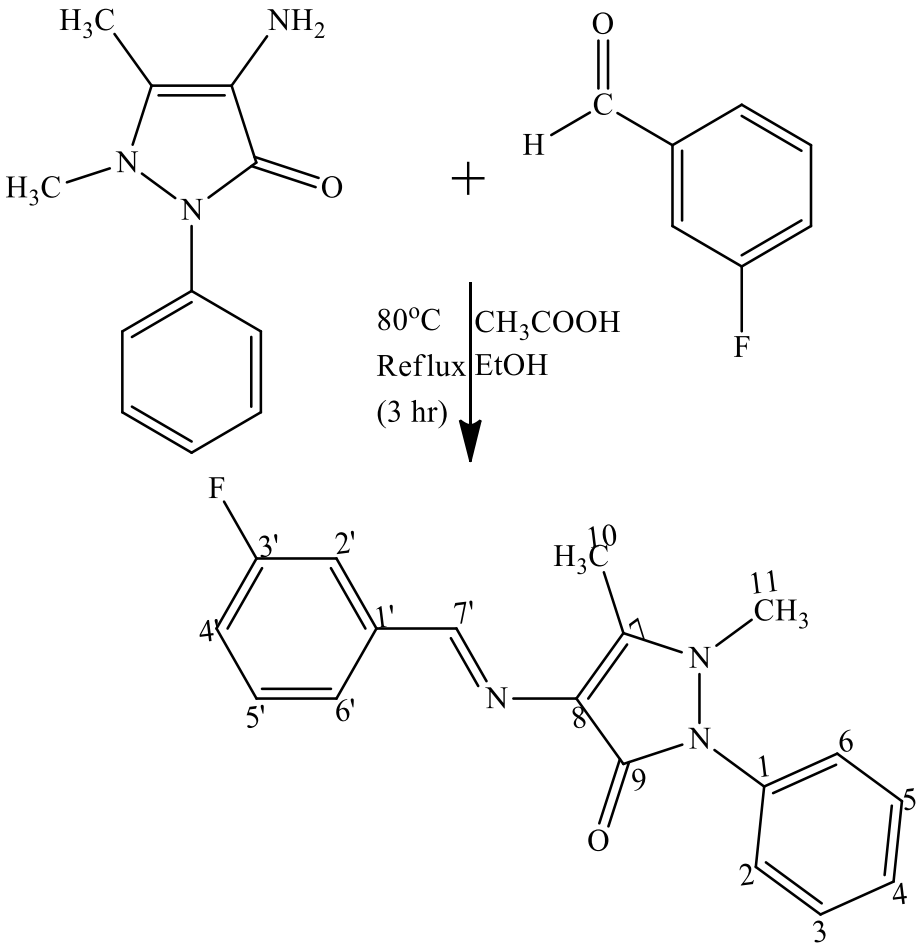

Scheme 3. 7: Synthetic Route of SB2B

3.3.8 Synthesis of (Z)-4-((4-chlorobenzylidene)amino)-1,5-dimethyl-2-phenyl-1,2-dihydro-3H-pyrazol-3-one (SB3)

Compound SB3 was synthesised according to Scheme 3.8. An equimolar amount (0.4 mmol) of 4-chlorobenzaldehyde (0.0523 g), 4-aminoantipyrine (0.0813 g), in 10 mL of ethanol and with 2 drops of glacial acetic acid was refluxed at 80 ^{o}C in around bottom flask (100 mL) for 5 hours. Using a TLC system with a 7:3 n-hexane: ethyl acetate ratio (R*f* value 0.55), the reaction's progress was monitored. The resulting mixture after cooling was filtered, recrystillised with ethanol and dried under vacuum to afford pale yellow crystals of compound (Z)-4-((4-chlorobenzylidene)amino)-1,5-dimethyl-2-phenyl-1,2-dihydro-3H-pyrazol-3-one (0.1174 g).

3.3.9 Synthesis of (Z)-4-((2-chlorobenzylidene)amino)-1,5-dimethyl-2-phenyl-1,2-dihydro-3H-pyrazol-3-one (SB3A)

The synthesis of compound SB3A followed Scheme 3.9. An equimolar amount (0.4 mmol) of 2-chlorobenzaldehyde (0.045mL), 4-aminoantipyrine (0.0813 g), in 10 mL of ethanol and with 2 drops of glacial acetic acid was refluxed at 80 ^{o}C in around bottom flask (100 mL) for 5 hours. The TLC system of n-hexane: ethyl acetate, 7:3 (R*f* value 0.55), was used to track the reaction's progress. The resulting mixture after cooling to room temperature was filtered, recrystillised with ethanol and dried under vacuum to afford a pale yellow crystals of compound (Z)-4-((2-chlorobenzylidene)amino)-1,5-dimethyl-2-phenyl-1,2-dihydro-3H-pyrazol-3-one (0.1195 g).

3.3.10 Synthesis of 4-((4-bromobenzylidene)amino)-1,5-dimethyl-2-phenyl-1,2-dihydro-3H-pyrazol-3-one (SB4)

The synthesis of compound SB4 followed Scheme 3.10. A mixture of 4-bromobenzaldehyde (0.0740 g, 0.4 mmol), 4-aminoantipyrine (0.0813 g, 0.4 mmol), glacial acetic acid (2 drops) and 10 mL of ethanol, was refluxed at 80 ^{o}C in a round bottom flask (100 mL) for 4 hours. The reaction progress was monitored by TLC system of n-hexane: ethyl acetate, 7:3 (R*f* value 0.49). On completion of the reaction, the mixture was cooled to room temperature and the precipitate filtered, recrystillised with ethanol and dried under vacuum. Pale yellow crystals of compound 4-((4 bromobenzylidene)amino)-1,5-dimethyl-2-phenyl-1,2-dihydro-3H-pyrazol-3-one (0.139 g) was obtained.

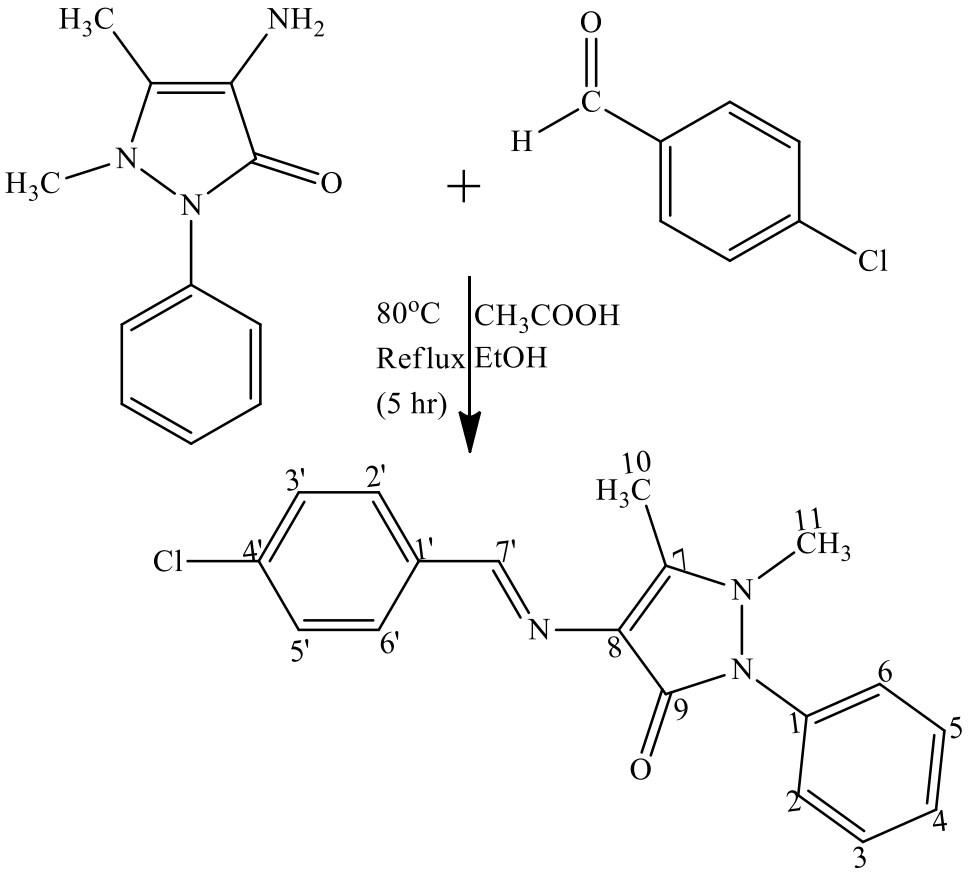

Scheme 3. 8: Synthetic Route of SB3

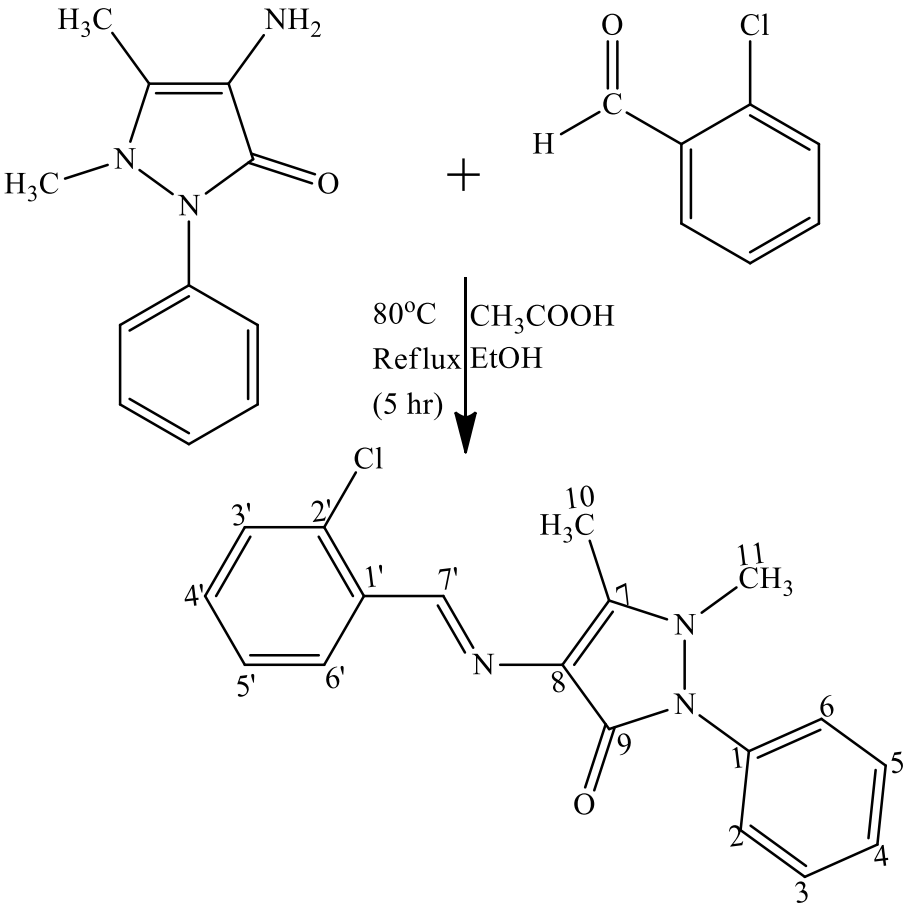

Scheme 3. 9: Synthetic Route of SB3A

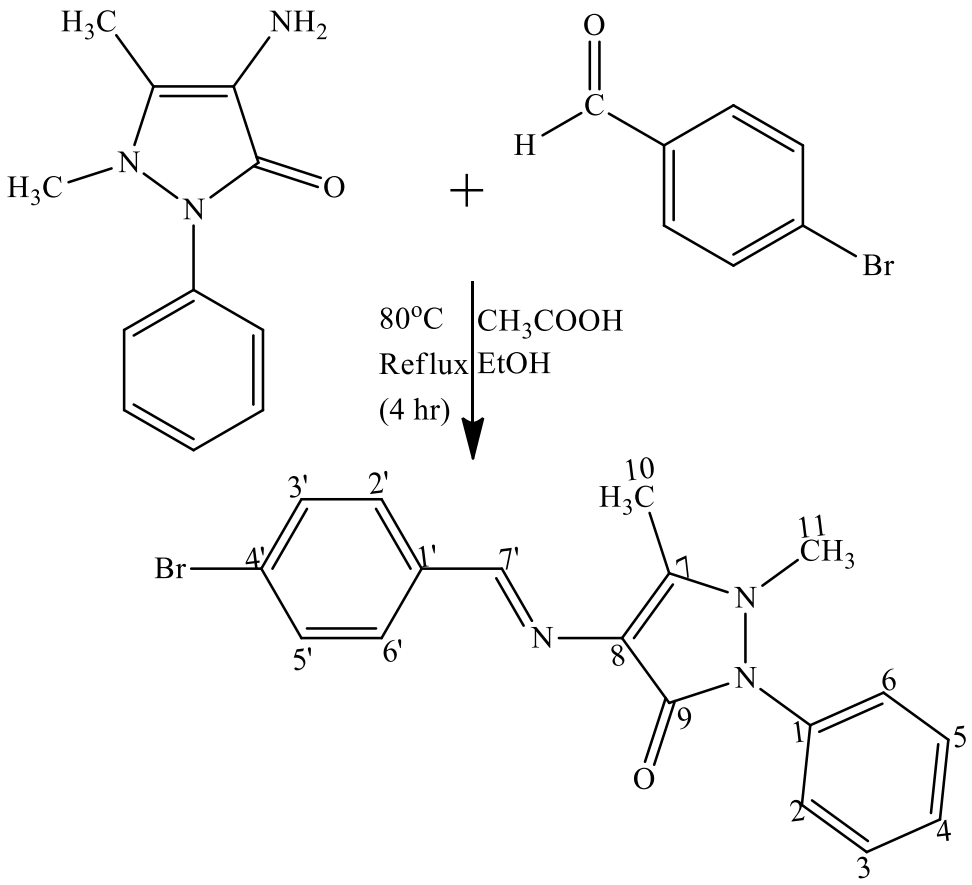

Scheme 3. 10: Synthetic Route of SB4

3.3.11 Synthesis of 4-((2-bromobenzylidene)amino)-1,5-dimethyl-2-phenyl-1,2-dihydro-3H-pyrazol-3-one (SB4A)

Compound SB4A was synthesised according to Scheme 3.11.A mixture of 2-bromobenzaldehyde (0.047 mL, 0.4 mmol), 4-aminoantipyrine (0.0813 g, 0.4 mmol), glacial acetic acid (2 drops) and 10 mL of ethanol, was refluxed at 80 ^{o}C in a round bottom flask (100 mL) for 8 hours. The reaction progress was monitored by TLC system of n-hexane: ethyl acetate, 7:3 (R*f* value 0.52). On completion of the reaction, the mixture was cooled to room temperature, filtered, recrystillised with ethanol and dried under vacuum to afford yellow crystals of compound 4-((2-bromobenzylidene)amino)-1,5-dimethyl-2-phenyl-1,2-dihydro-3H-pyrazol-3-one (0.130 g).

3.3.12 Synthesis of 4-((3-bromobenzylidene)amino)-1,5-dimethyl-2-phenyl-1,2-dihydro-3H-pyrazol-3-one(SB4B)

Compound SB4B was synthesised according to Scheme 3.12. A mixture of 3-bromobenzaldehyde (0.047 mL, 0.4 mmol), 4-aminoantipyrine (0.0813 g, 0.4 mmol), glacial acetic acid (2 drops) and 10 mL of ethanol, was refluxed at 80 ^{o}C in a round bottom flask (100 mL) for 9 hours. The reaction progress was monitored by TLC system of n-hexane: ethyl acetate, 7:3 (R_f value 0.45). On completion of the reaction, the mixture was cooled to room temperature and the precipitate filtered, recrystillised with ethanol and dried under vacuum to afford yellow crystals of compound 4-((3-bromobenzylidene)amino)-1,5-dimethyl-2-phenyl-1,2-dihydro-3H-pyrazol-3-one (0.1205 g).

3.3.13 Synthesis of 4-((4-hydroxyl-3-methoxybenzylidene)amino)-1,5-dimethy-2-phenyl-1,2-dihydrox-3H-pyraz-ol-3-one (SB5)

According to Scheme 3.13, compound SB5 was synthesised. An equimolar amount (0.4 mmol) of 4-hydroxy-3-methoxybenzaldehyde (0.0609 g) and 4-aminoantipyrine (0.0813 g), in 10 mL of ethanol and with 2 drops of glacial acetic acid was refluxed at 80 ^{o}C in around bottom flask (100 mL) for 10 hours. Progress of reaction was track by TLC system of n-hexane: ethyl acetate, 5:5 (R*f* value 0.55). The resulting mixture after cooling to room temperature was filtered, recrystillised with ethanol and dried under vacuum. Pale yellow crystals of compound 4-((4-hydroxy-3-methoxybenzylidene)amino)-1,5-dimethyl-2-phenyl-1,2-dihydro-3H-pyraz- ol-3-one (0.1205 g), was obtained.

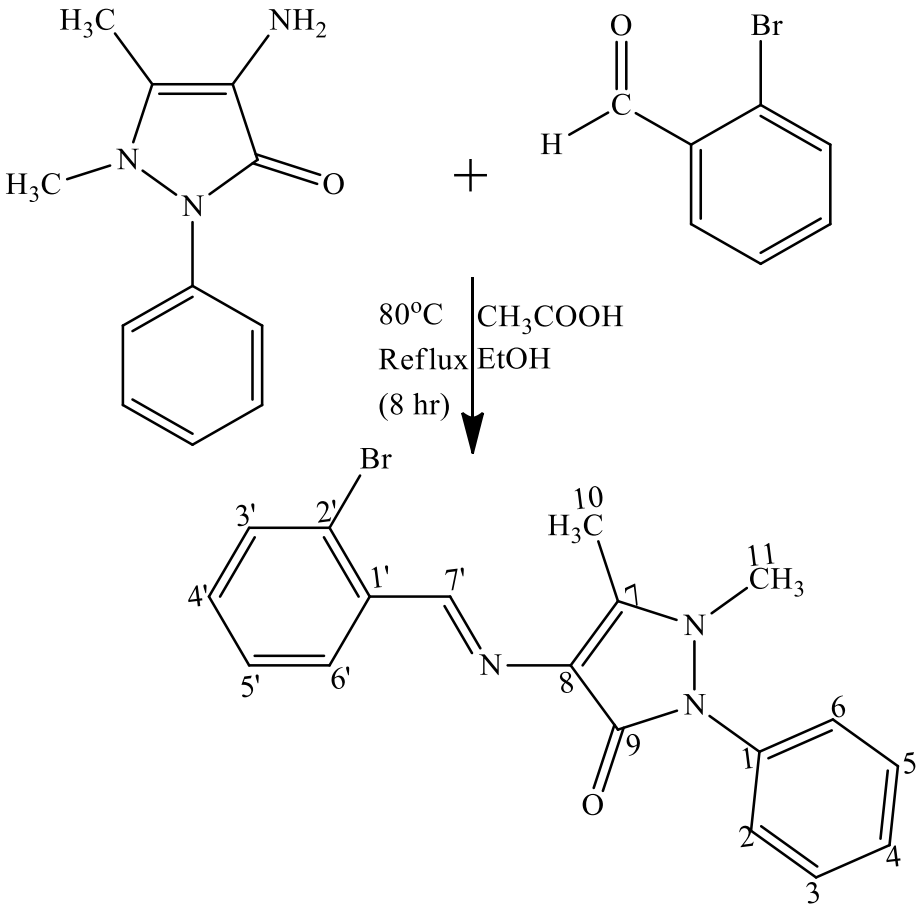

Scheme 3. 11: Synthetic Route of SB4A

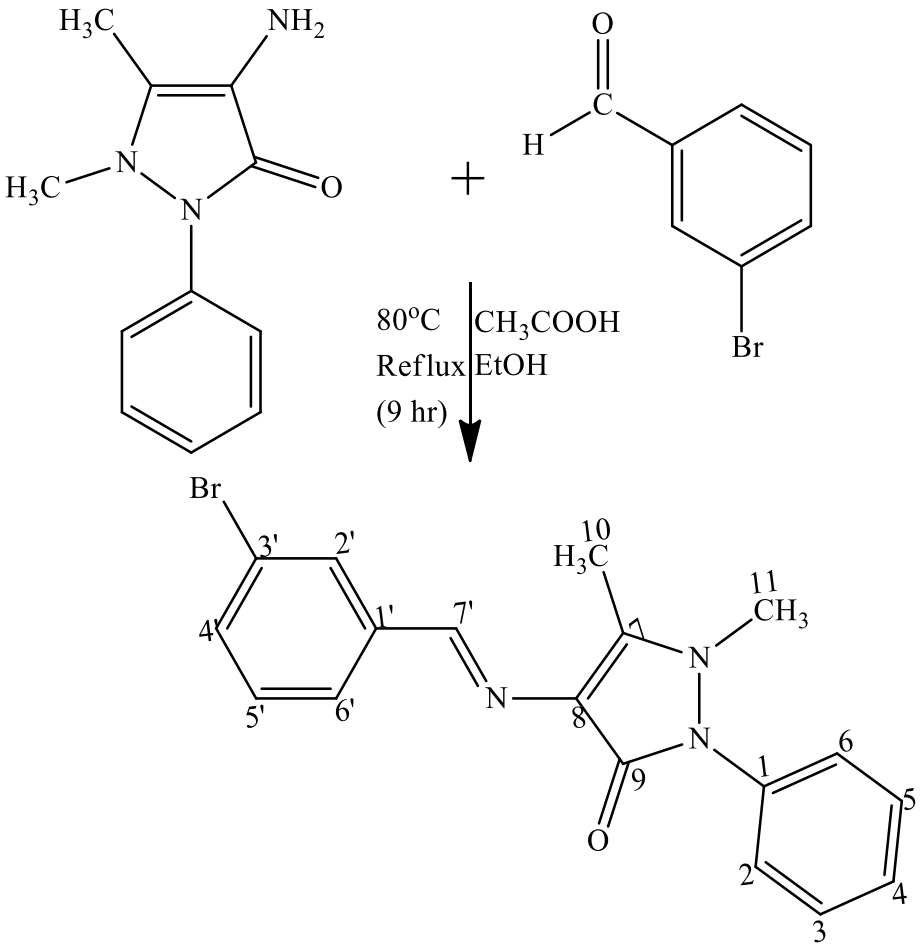

Scheme 3. 12: Synthetic Route of SB4B

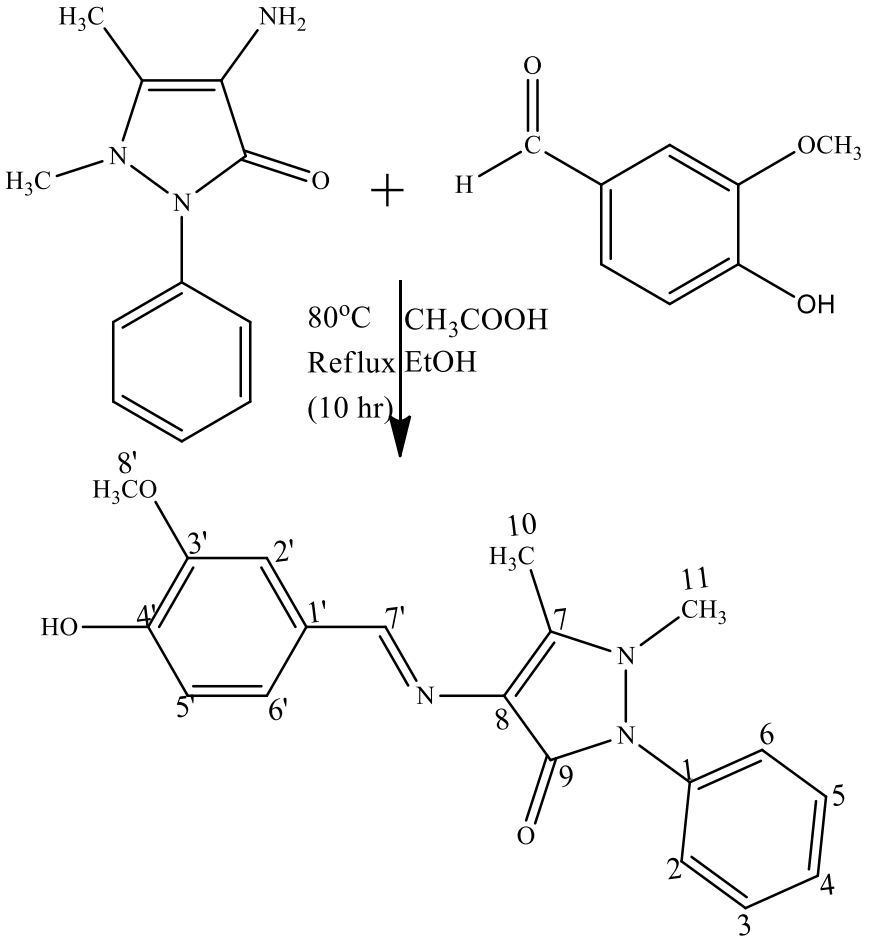

Scheme 3. 13: Synthetic Route of SB5

3.3.14 Synthesis of 4-((2-hydroxy-3-methoxybenzylidene)amino)-1,5-dimethyl-2-phenyl-1,2-dihydro-3H-pyrazol-3-one (SB5A)

According to Scheme 3.14, compound SB5A was synthesised an equimolar amount (0.4 mmol) of 2-hydroxy-3-methoxybenzaldehyde (0.0609 g) and 4-aminoantipyrine (0.0813 g), in 10 mL of ethanol and with 2 drops of glacial acetic acid was Arefluxed at 80 ^{o}C in around bottom flask (100 mL) for 4 hours. The Progress of reaction was tracked by a TLC system of n-hexane: ethyl acetate, 5:5 (R*f* value 0.61). The resultant mixture was lowered to room temperature, filtered, recrystillised with ethanol and dried under vacuum. Yellow crystals of compound 4-((2-hydroxy-3-methoxybenzylidene) amino)-1,5-dimethyl-2-phenyl-1,2-dihydro-3H-pyrazol-3-one (0.1198 g) was obtained.

3.3.15 Synthesis of 4-((3-hydroxy-4-methoxybenzylidene)amino)-1,5-dimethyl-2-phenyl-1,2-dihydro-3H-pyrazol-3-one (SB5B)

The synthesis of compound SB5B followed Scheme 3.15. An equimolar amount (0.4 mmol) of 3-hydroxy-4-methoxybenzaldehyde (0.0609 g) and 4-aminoantipyrine (0.0813 g), in 10 mL of ethanol and with 2 drops of glacial acetic acid was refluxed at 80^{o}C in around bottom flask (100 mL) for 12 hours. The reaction progress was tracked by TLC system of n-hexane: ethyl acetate, 5:5 (R*f* value 0.52). On completion of the reaction, the resultant mixture was cooled to room temperature, filtered, recrystillised with ethanol and dried. Pale yellow crystals of compound 4-((3-hydroxy-4-methoxybenzylidene)amino)-1,5- dimethyl-2-phenyl-1,2-dihydro-3H-pyrazol-3-one (0.124 g) was obtained.

3.3.16 Synthesis of 4-((4-methoxybenzylidene)amino)-1,5-dimethyl-2-phenyl-1,2-dihydro-3H-pyrazol-3-one (SB6)

The synthesis of compound SB6 followed Scheme 3.16. In a 100 mL round bottom flask fitted with a condenser and a magnetic stirrer, 4-methoxybenzaldehyde (0.049 mL, 0.4 mmol), 4-aminoantipyrine (0.0813 g, 0.4 mmol), glacial acetic acid (2 drops) and ethanol (10 mL), were refluxed at 80 ^{o}C for 16 hours. The reaction's progress was monitored with a TLC system n-hexane: ethyl acetate, 7:3 (R*f* value 0.53). On completion of the reaction the resultant mixture was lowered to room temperature, filtered, recrystallised with ethanol and dried to obtain dark cream crystals of compound 4-((4-methoxybenzylidene)amino)-1,5-dimethyl-2-phenyl-1,2-dihydro-3H-pyrazol-3-one (0.9995 g).

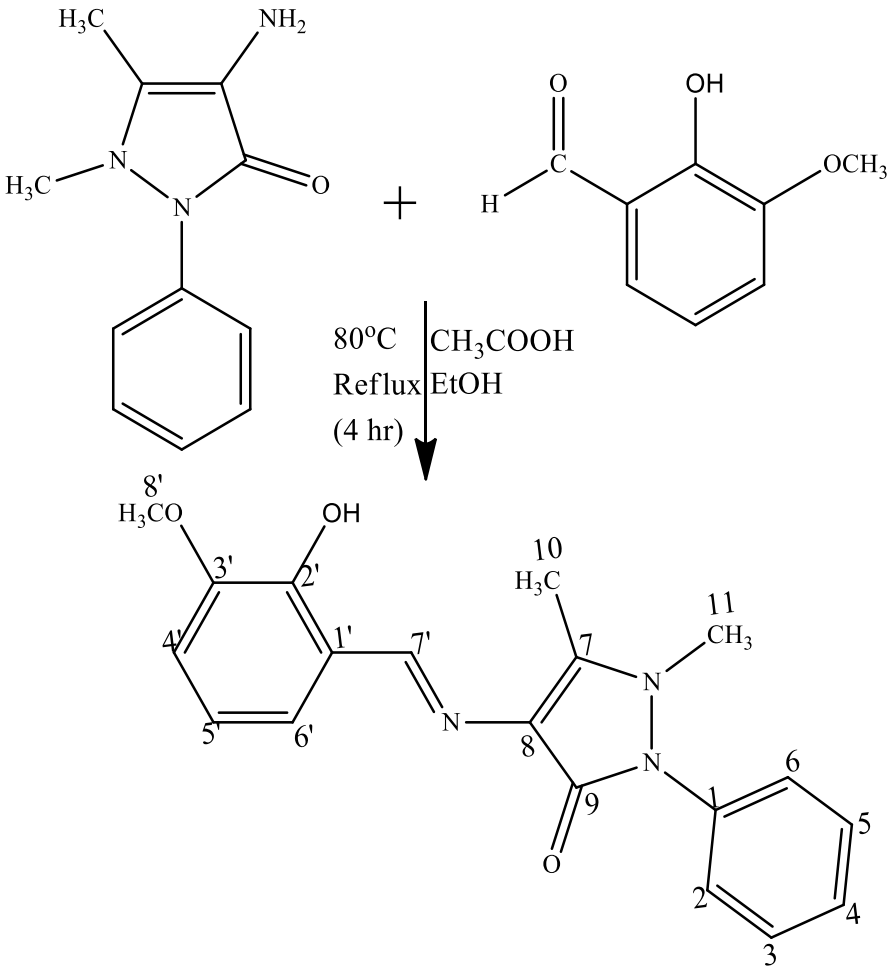

Scheme 3. 14: Synthetic Route of SB5A

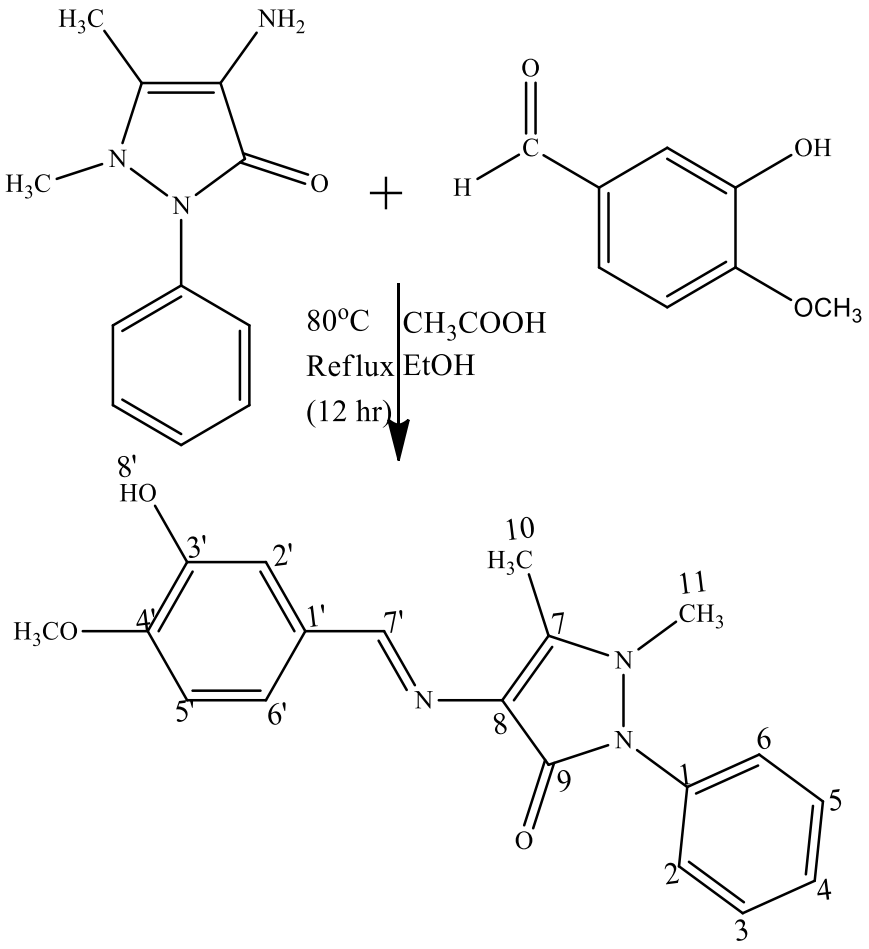

Scheme 3. 15: Synthetic Route of SB5B

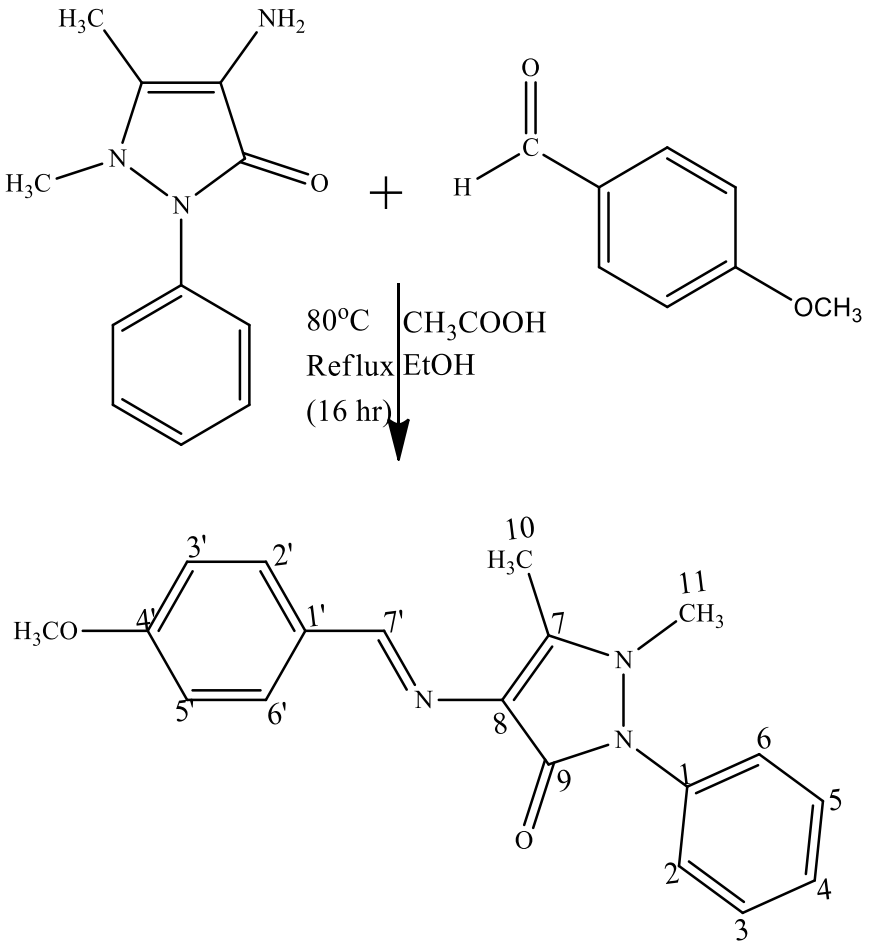

Scheme 3. 16: Synthetic Route of SB6

3.3.17 Synthesis of 4-((2-methoxybenzylidene)amino)-1,5-dimethyl-2-phenyl-1,2-dihydro-3H-pyrazol-3-one (SB6A)

The synthesis of compound SB6A followed Scheme 3.17. In a 100 mL round bottom flask fitted with a condenser and a magnetic stirrer, 2-methoxybenzaldehyde (0.048 mL, 0.4 mmol), 4-aminoantipyrine (0.0813 g, 0.4 mmol), glacial acetic acid (2 drops) and ethanol (10 mL), were refluxed at 80 ^{o}C for 18 hours. The reaction's progress was monitored with a TLC system n-hexane: ethyl acetate, 7:3 (Rf value 0.56). On completion of the reaction, the resulting mixture was lowered to room temperature, filtered, recrystillised with ethanol and dried to obtain yellow crystal of compound 4-((2-methoxybenzylidene)amino)-1,5-dimethyl-2-phenyl-1,2-dihydro-3H-pyrazol-3-one (0.1120 g).

3.3.18 Synthesis of 4-((3-methoxybenzylidene)amino)-1,5-dimethyl-2-phenyl-1,2-dihydro-3H-pyrazol-3-one (SB6B)

The synthesis of compound SB6B followed Scheme 3.18. In a 100 mL round bottom flask fitted with a condenser and a magnetic stirrer, 3-methoxybenzaldehyde (0.049 mL, 0.4 mmol), 4-aminoantipyrine (0.0813 g, 0.4 mmol), glacial acetic acid (2 drops) and ethanol (10 mL), were refluxed at 80 ^{o}C for 6 hours. The Progress of reaction was tracked by a TLC system of n-hexane: ethyl acetate, 7:3 (Rf value 0.45). On completion of the reaction, the resulting mixture was lowered to room temperature, filtered, recrystillised with ethanol and dried under vacuum to obtain pale yellow crystals of compound 4-((3-methoxybenzylidene) amino)-1,5-dimethyl-2-phenyl-1,2-dihydro-3H-pyrazol-3-one (0.1152 g).

3.3.19 Synthesis of 1,5-dimethyl-4-((4-methylbenzylidene)amino)-2-phenyl-1,2-dihydro-3H-pyrazol-3-one (SB7)

Compound SB7 was synthesised according to Scheme 3.19. A mixture of 4-methylbenzaldehyde (0.047 mL, 0.4 mmol), 4-aminoantipyrine (0.0813 g, 0.4 mmol), glacial acetic acid (2 drops) and 10 mL of ethanol, was refluxed at 80 ^{o}C in a round bottom flask (100 mL) for 11 hours. The reaction progress was tracked by TLC system of n-hexane: ethyl acetate, 8:2 (Rf value 0.46). On completion of the reaction, the mixture was cooled to room temperature and the precipitate filtered, recrystillised with ethanol and dried under vacuum to afford yellow crystals of compound 1,5-dimethyl-4-((4-methylbenzylidene) amino)-2-phenyl-1,2-dihydro-3H-pyrazol-3-one (0.0899 g).

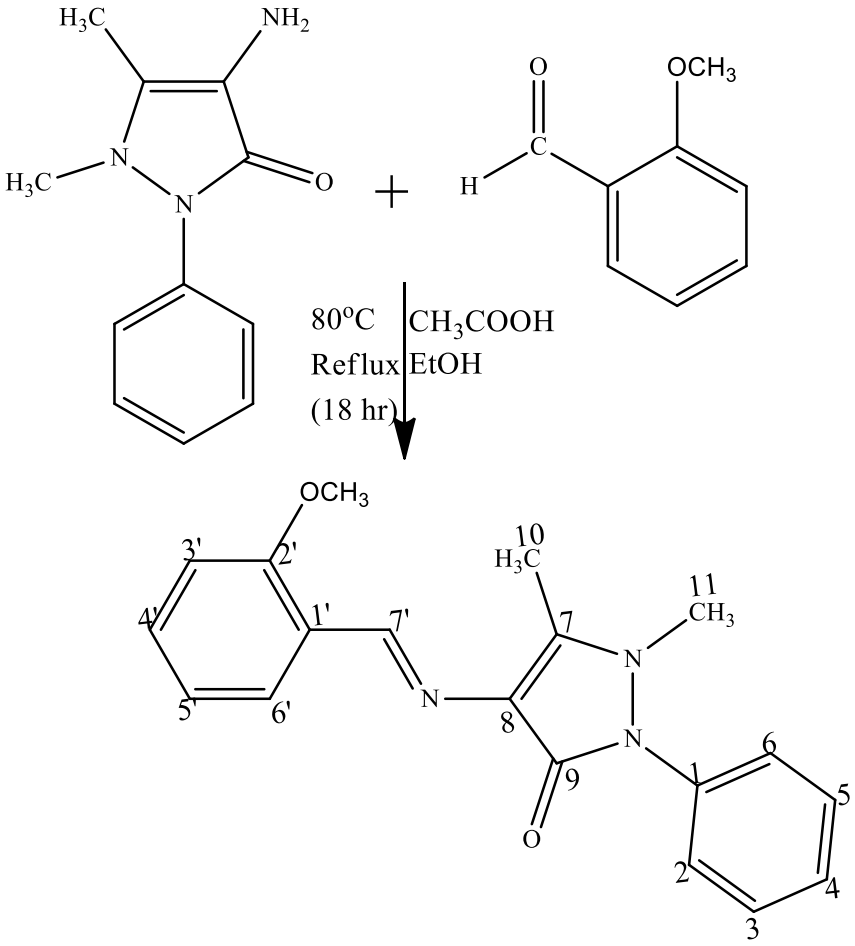

Scheme 3. 17: Synthetic Route of SB6A

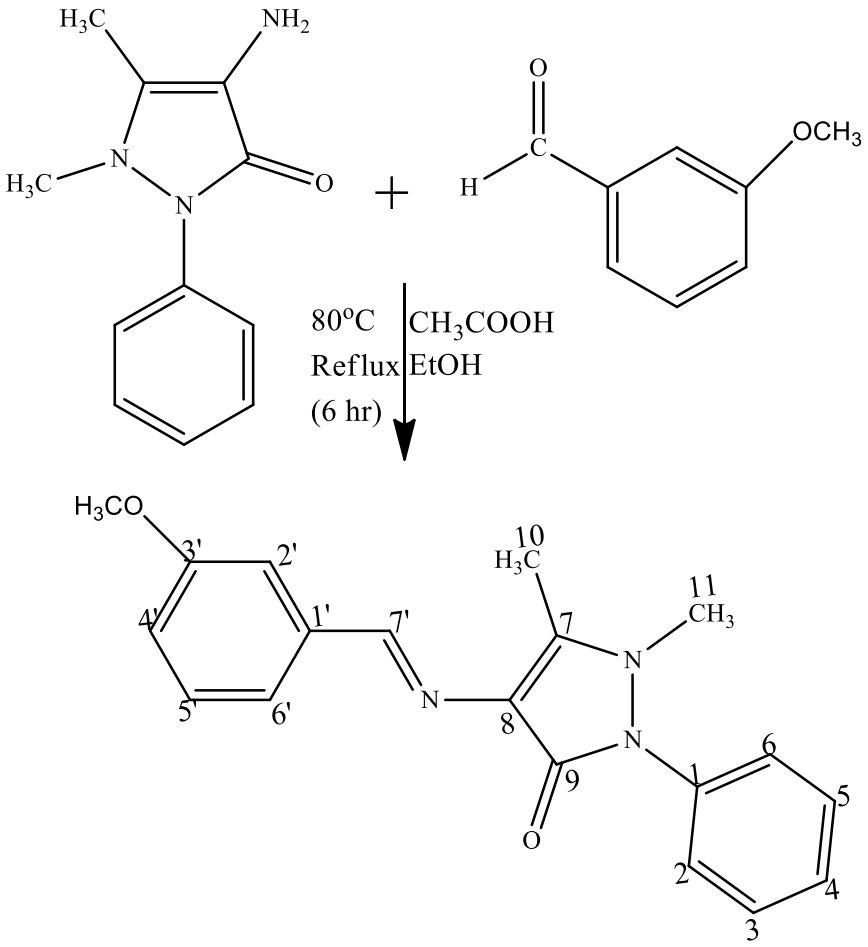

Scheme 3. 18: Synthetic Route of SB6B

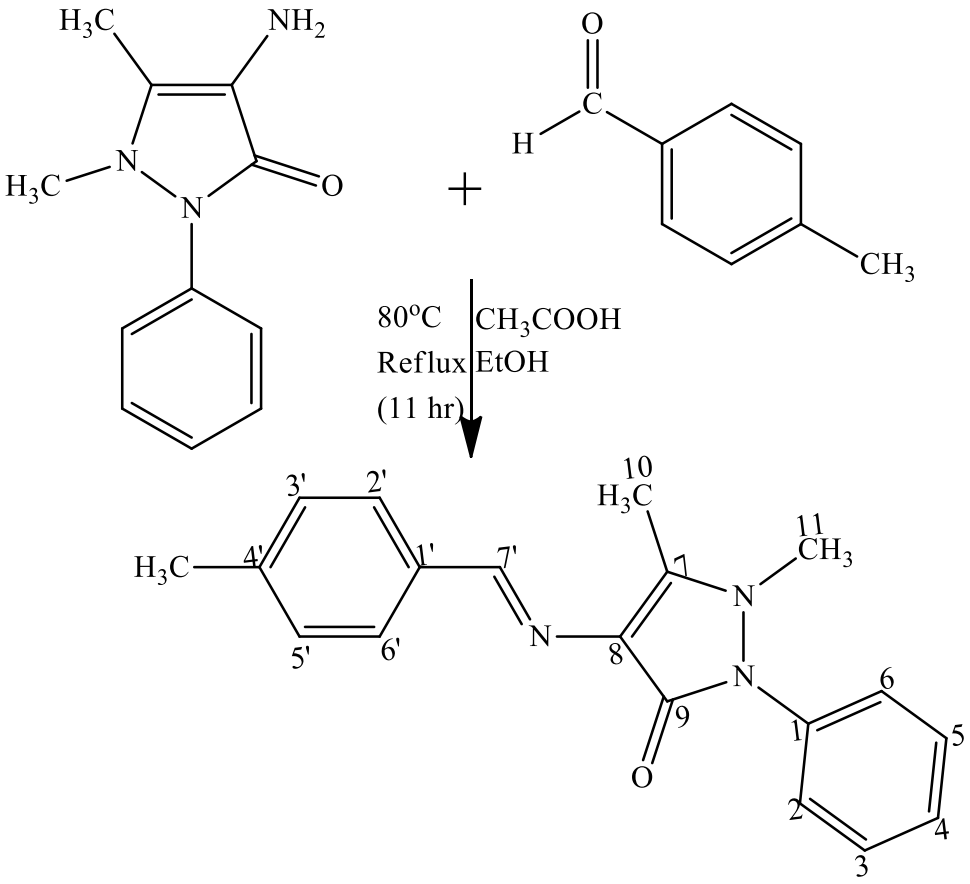

Scheme 3. 19: Synthetic Route of SB7

3.3.20 Synthesis of 4-(((1,5-dimethyl-3-oxo-2-phenyl-2,3-dihydro-1H-pyrazol-4-yl)imino) methyl) benzonitrile (SB8)

Compound SB8 was synthesised according to Scheme 3.20. A mixture of 4-cyanobenzaldehyde (0525g, 0.4 mmol), 4-aminoantipyrine (0.0813 g, 0.4 mmol), glacial acetic acid (2 drops) and 10 mL of ethanol, was refluxed at 80 ^{o}C in a100 mL round bottom flask for 4 hours. The reaction progress was monitored by TLC system of n-hexane: ethyl acetate, 5:5 (R*f* value 0.52). On completion of the reaction, the mixture was cooled to room temperature and the precipitate filtered, recrystillised with ethanol and dried under vacuum to afford a yellow powdered compound, 4-(((1,5-dimethyl-3-oxo-2-phenyl-2,3-dihydro-1H-pyrazol-4-yl)imino)methyl)benzo- nitrile (0.1080 g).

3.3.21 Synthesis of 4-(3-hydroxybenzylideneamino)-1,2-dihydro-2,3-dimethyl-1-phenyl pyrazol-5-one (SB9)

Compound SB9 was synthesised according to Scheme 3.21. A mixture of 3-hydroxybenzaldehyde (0.0488 g, 0.4 mmol), 4-aminoantipyrine (0.0813 g, 0.4 mmol), glacial acetic acid (2 drops) and 10 mL of ethanol, was refluxed at 80^{o}C in around bottom flask (100 mL) for 4 hours. The reaction progress was monitored by TLC system of n-hexane: ethyl acetate, 5:5 (R*f* value 0.51). On completion of the reaction, the mixture was cooled to room temperature and the precipitate filtered, recrystillised with ethanol and dried under vacuum to afford pale yellow crystals of compound 4-(3-hydroxybenzylideneamino)-1,2-dihydro-2,3-dimethyl-1-phenyl pyrazol-5-one (0.1058 g).

3.3.22 Synthesis of 4-(4-hydroxybenzylideneamino)-1,2-dihydro-2,3-dimethyl-1-phenyl pyrazol-5-one (SB9B)

Compound SB9B was synthesised according to Scheme 3.22. A mixture of 4-hydroxybenzaldehyde (0.04858 g, 0.4 mmol), 4-aminoantipyrine (0.0813 g, 0.4 mmol), glacial acetic acid (2 drops) and 10 mL of ethanol, was refluxed at 80 ^{o}C in a100 mL round bottom flask for 4 hours. The reaction progress was monitored by TLC system of n-hexane: ethyl acetate, 5:5 (R*f* value 0.43). On completion of the reaction, the mixture was cooled to room temperature, the precipitate filtered, recrystillised with ethanol and dried under vacuum to afford cream crystals of compound 4-(4-hydroxybenzylideneamino)-1,2-dihydro-2,3-dimethyl-1-phenylpyrazol-5-one (0.1094 g).

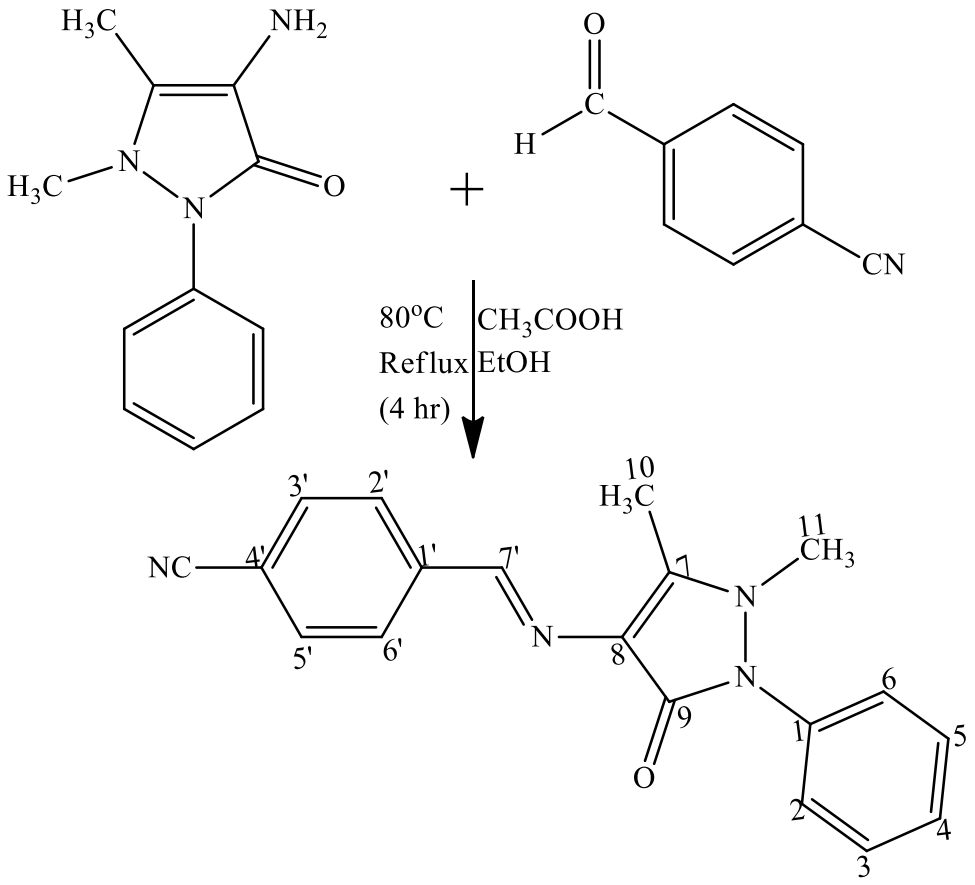

Scheme 3. 20: Synthetic Route of SB8

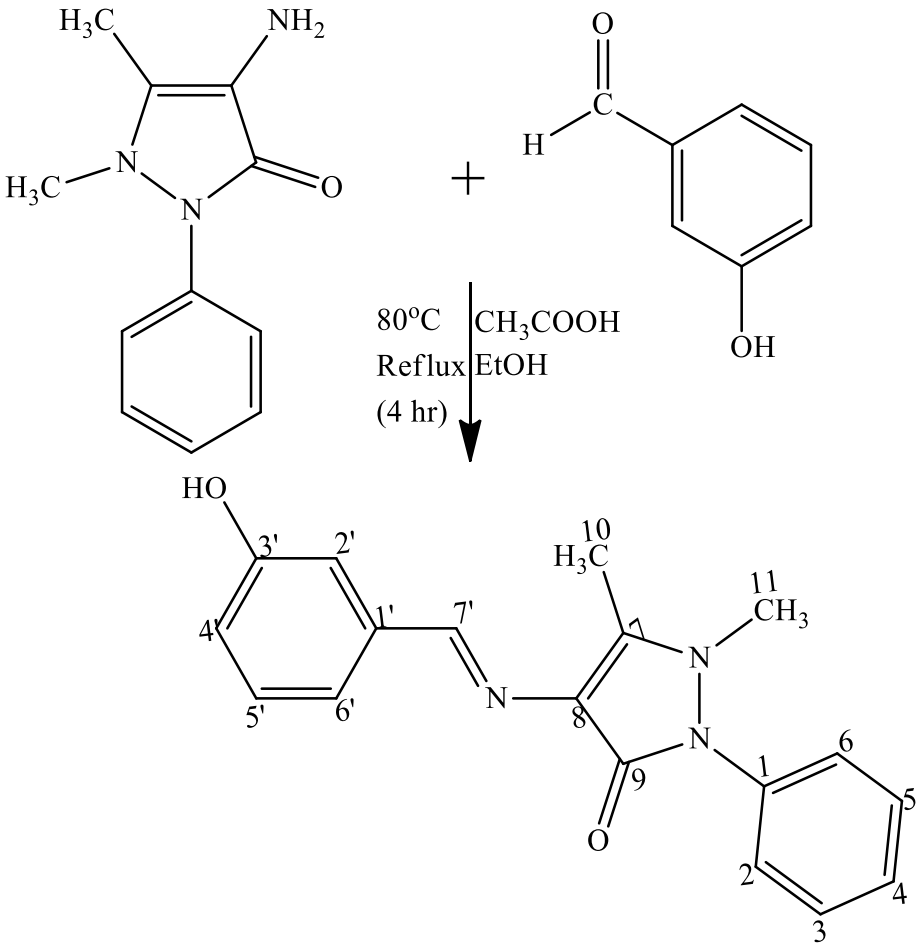

Scheme 3. 21: Synthetic Route of SB9

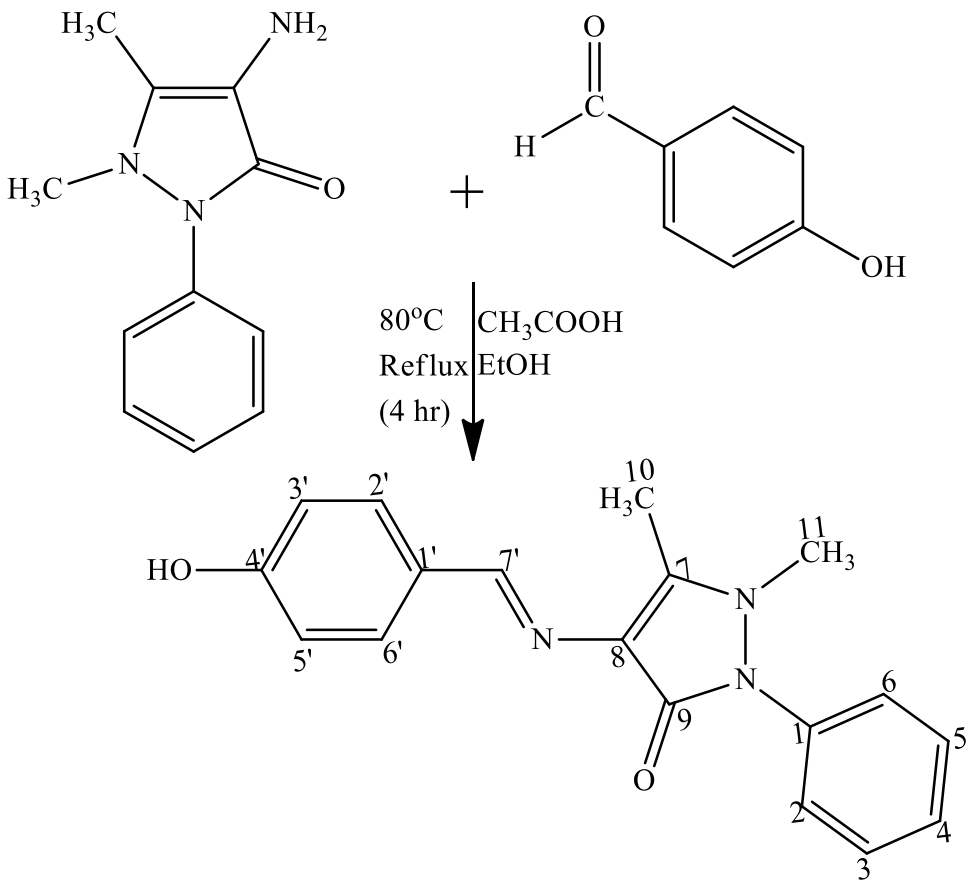

Scheme 3. 22: Synthetic Route of SB9B

3.3.23 Synthesis of 4-((3-hydroxy-4-nitrobenzylidene)amino)-1,5-dimethyl-2-phenyl-1,2-dihydro-3H-pyrazol-3-one (SB10)

Compound SB10 was synthesised according to Scheme 3.23. A mixture of 3-hydroxy-4-nitrobenzaldehyde (0.0669g, 0.4 mmol), 4-aminoantipyrine (0.0813 g, 0.4 mmol), glacial acetic acid (2 drops) and 10 mL of ethanol, was refluxed at 80^{o}C in a round bottom flask (100 mL) for 3 hours. The reaction progress was monitored by TLC system of n-hexane: ethyl acetate, 5:5 (R*f* value 0.52). On completion of the reaction, the mixture was cooled to room temperature, filtered, recrystillised with ethanol and dried under vacuum to afford bright orange crystals of compound 4-((3,4-dihydroxybenzylidene)amino)-1,5-dimethyl-2-phenyl-1,2-dihydro-3H-pyrazol-3-one (0.118 g).

3.3.24 Synthesis of 4-((3,4-dihydroxybenzylidene)amino)-1,5-dimethyl-2-phenyl-1,2-dihydro-3H-pyrazol-3-one (SB11)

Compound SB11 was synthesised according to Scheme 3.24. A mixture of 3,4-dihydroxybenzaldehyde (0.0553 g, 0.4 mmol), 4-aminoantipyrine (0.0813 g, 0.4 mmol), glacial acetic acid (2 drops) and 10 mL of ethanol, was refluxed at 80^{o}C in a round bottom flask (100 mL) for 8 hours. A TLC system of n-hexane: ethyl acetate, 5:5 (R*f* value 0.55) was used to track the progress of the reaction. On completion of the reaction, the mixture was cooled to room temperature, filtered, recrystillised with ethanol and dried under vacuum to afford light brown crystals of compound 4-((3,4-dihydroxybenzylidene)amino)-1,5-dimethyl-2-phenyl-1,2-dihydro-3H-pyrazol -3-one (0.118 g).

3.3.25 Synthesis 4-((2,4-dihydroxybenzylidene)amino)-1,5-dimethyl-2-phenyl-1,2-dihydro-3H-pyrazol-3-one (SB11A)

Compound SB11A was synthesised according to Scheme 3.25. A mixture of 2,4-dihydroxybenzaldehyde (0.0553 g, 0.4 mmol), 4-aminoantipyrine (0.0813 g, 0.4 mmol), glacial acetic acid (2 drops) and 10 mL of ethanol, was refluxed at 80^{o}C in a round bottom flask (100 mL) for 8 hours. A TLC system of n-hexane: ethyl acetate, 5:5 (R*f* value 0.47) was used to monitor the progress of the reaction. On completion of the reaction, the mixture was cooled to room temperature, filtered, recrystillised with ethanol and dried under vacuum to afford yellow crystals of compound 4-((2,4-dihydroxybenzylidene)amino)-1,5-dimethyl-2phenyl-1,2-dihydro-3H-pyra zol-3-one (0.1160 g).

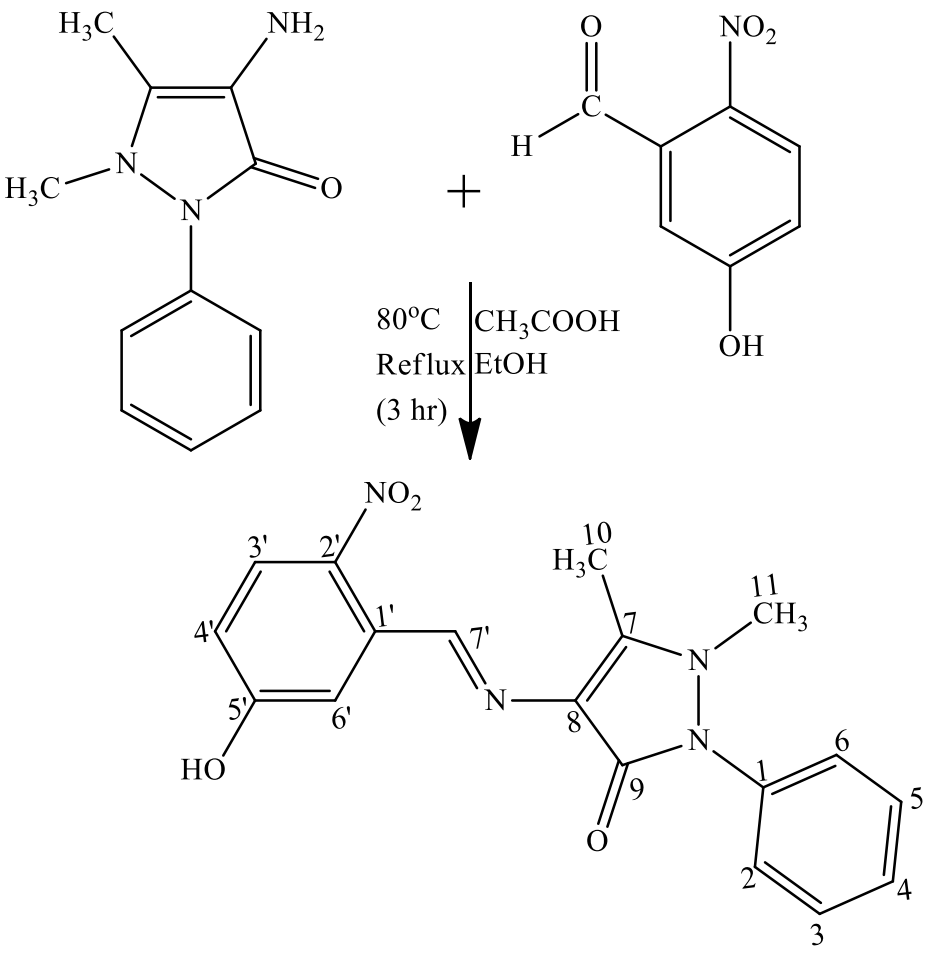

Scheme 3. 23: Synthetic Route of SB10

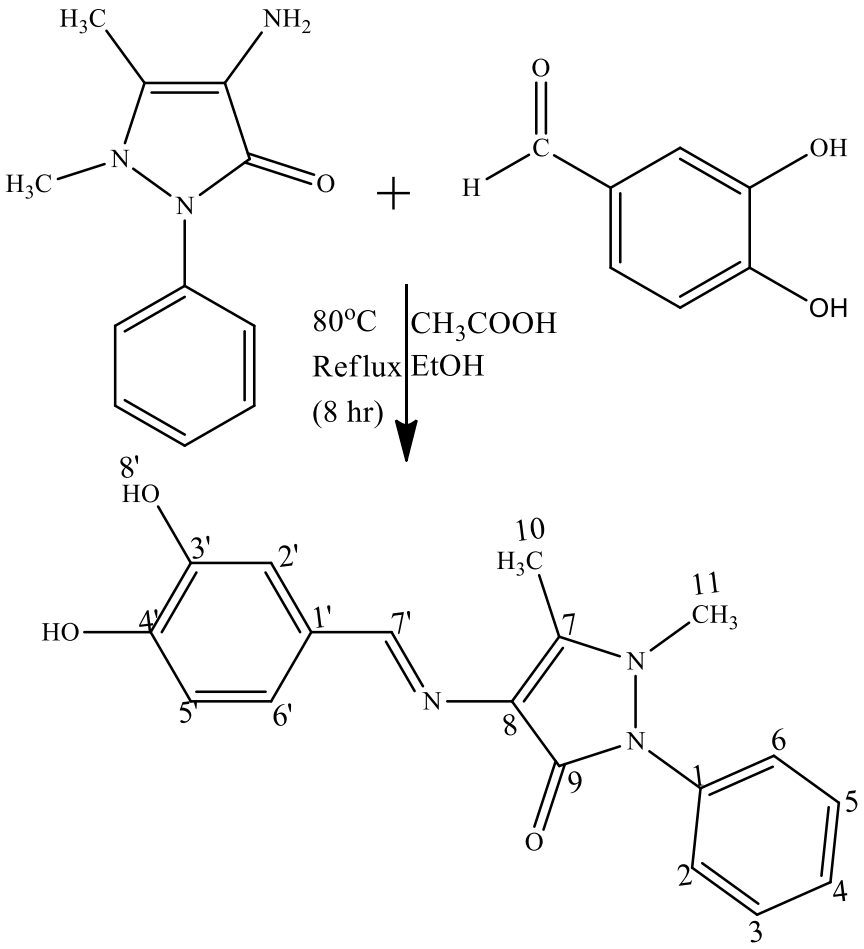

Scheme 3. 24: Synthetic Route of SB11

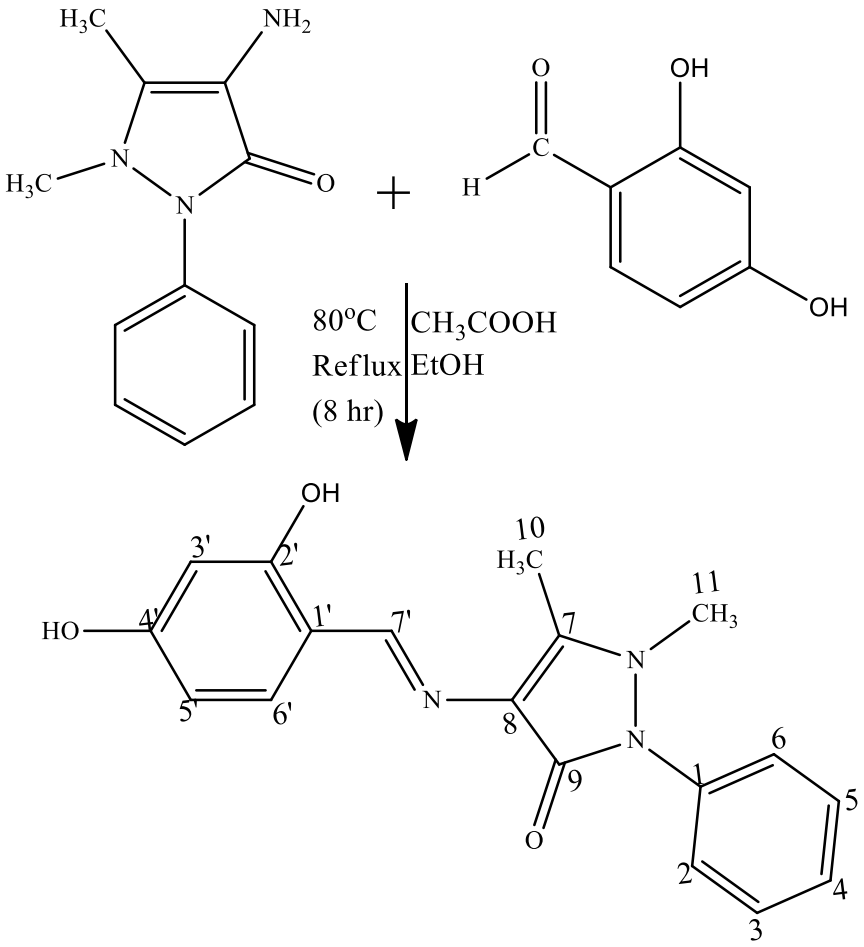

Scheme 3. 25: Synthetic Route of SB11A

3.3.26 Synthesis 4-((2,3-dihydroxybenzylidene)amino)-1,5-dimethyl-2-phenyl-1,2-dihydro-3H-pyrazol-3-one (SB11B)

Compound SB11B was synthesised according to Scheme 3.26. A mixture of 2,3-dihydroxybenzaldehyde (0.0553 g, 0.4 mmol), 4-aminoantipyrine (0.0813 g, 0.4 mmol), glacial acetic acid (2 drops) and 10 mL of ethanol, was refluxed at 80 ^{o}C in a round bottom flask (100 mL) for 6 hours. The progress of the reaction was tracked by TLC system of n-hexane/ethyl acetate, 5:5 (Rf value 0.56). On completion of the reaction, the mixture was cooled to room temperature, filtered, recrystillised with ethanol and dried under vacuum to afford light orange crystals of compound 4-((2,3-dihydroxybenzylidene) amino)-1,5-dimethyl-2-phenyl-1,2-dihydro-3H-pyrazol-3-one (0.1189 g).

3.3.27 Synthesis of 4-((2-chloro-4-fluorobenzylidene)amino)-1,5-dimethyl-2-phenyl-1,2-dihydro-3H-pyrazol-3-one (SB12)

Compound SB12 was synthesised according to Scheme 3.27. In a 100 mL round bottom flask fitted with a condenser and a magnetic stirrer, 2-chloro-4-fluorobenzaldehyde (0.0634g, 0.4 mol), 4-aminoantipyrine (0.0813 g, 0.4 mmol), glacial acetic acid (2 drops) and ethanol (10 mL), were refluxed at 80^{o}C for 3 hours. A TLC system of n-hexane: ethyl acetate, 7:3 (Rf value 0.61) was used to monitor the reaction. On completion of the reaction, the mixture was cooled to room temperature, filtered, recrystillised with ethanol and dried to obtain yellow crystals of compound 4-((2-chloro-4-fluorobenzylidene)amino)-1,5-dimethyl-2-phenyl-1,2-dihydro-3H-pyrazol-3-one (0.1290 g).

3.3.28 Synthesis of 4-((3,4-dimethylbenzylidene)amino)-1,5-dimethyl-2-phenyl-1,2-dihydro-3H-pyrazol-3-one (SB13)

Compound SB13 was synthesised according to Scheme 3.28. In a 100 mL round bottom flask fitted with a condenser and a magnetic stirrer, 3,4-dimethylbenzaldehyde (0.0537 g, 0.4 mmol), 4-aminoantipyrine (0.0813 g, 0.4 mmol), glacial acetic acid (2 drops) and ethanol (10 mL), were refluxed at 80^{o}C for 18 hours. A TLC system of n-hexane: ethyl acetate, 7:3 (Rf value 0.56) was used to track the progress of the reaction. On completion of the reaction, the resulting mixture was cooled to room temperature, filtered, recrystillised with ethanol and dried to obtain pale yellow crystals of compound 4-((3,4-dimethyl benzylidene)amino)-1,5-dimethyl-2-phenyl-1,2-dihydro-3H-pyrazol-3-one (0.1140 g).

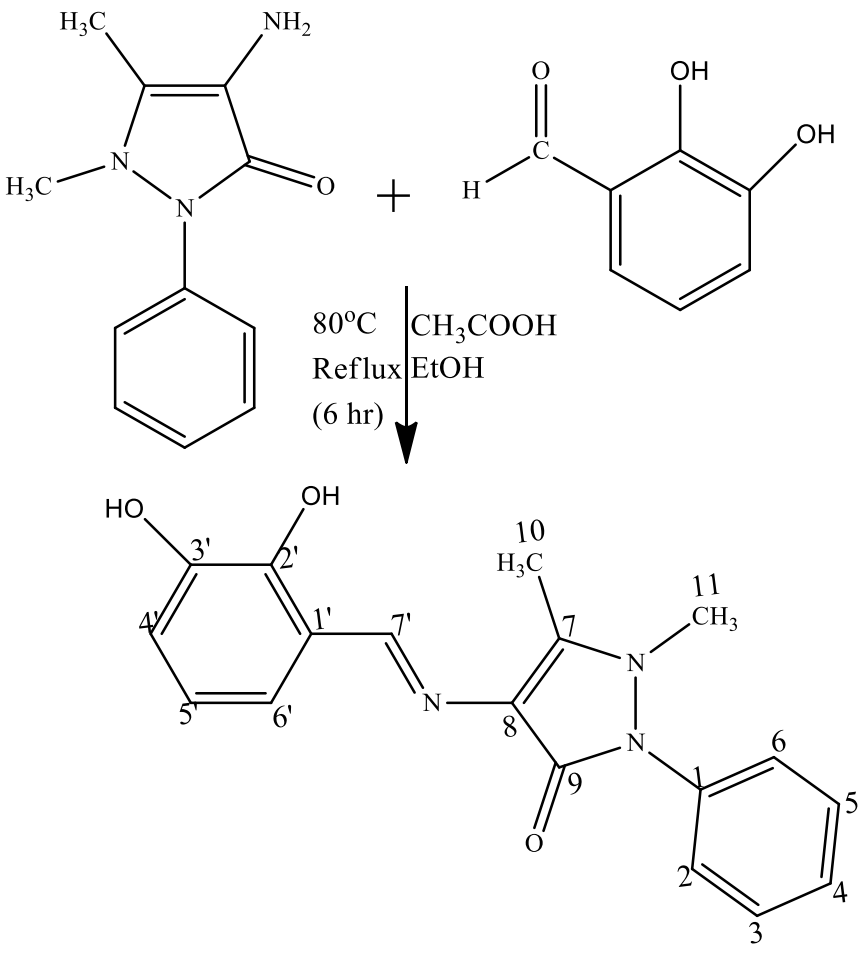

Scheme 3. 26: Synthetic Route of SB11B

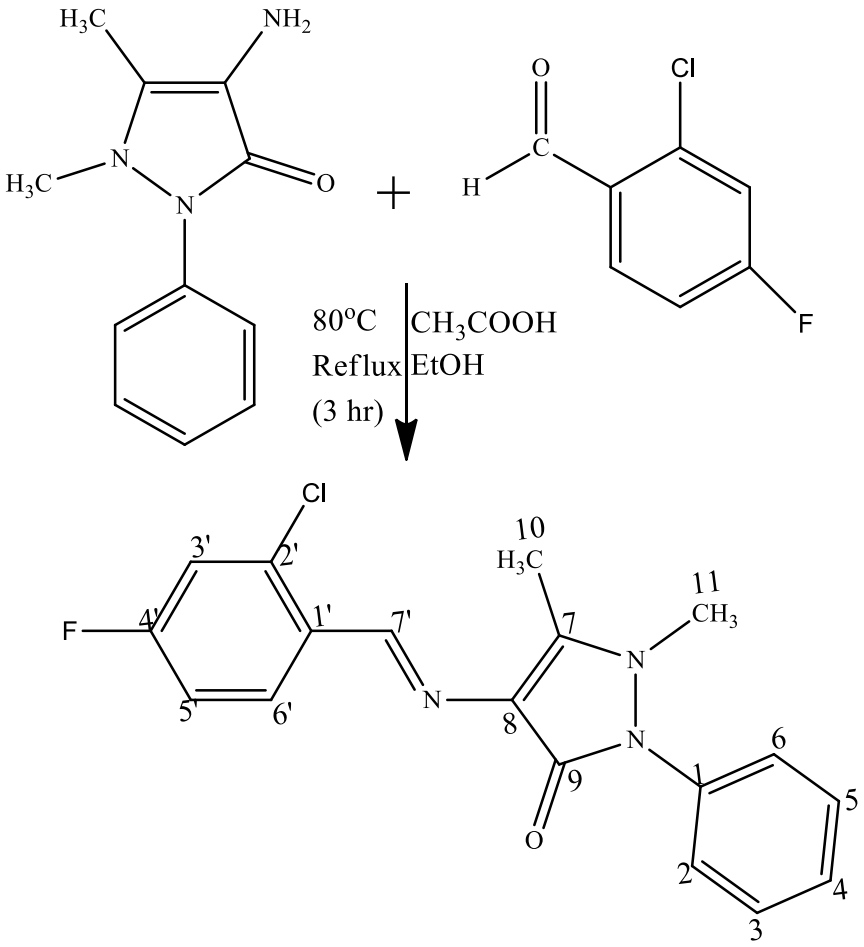

Scheme 3. 27: Synthetic Route of SB12

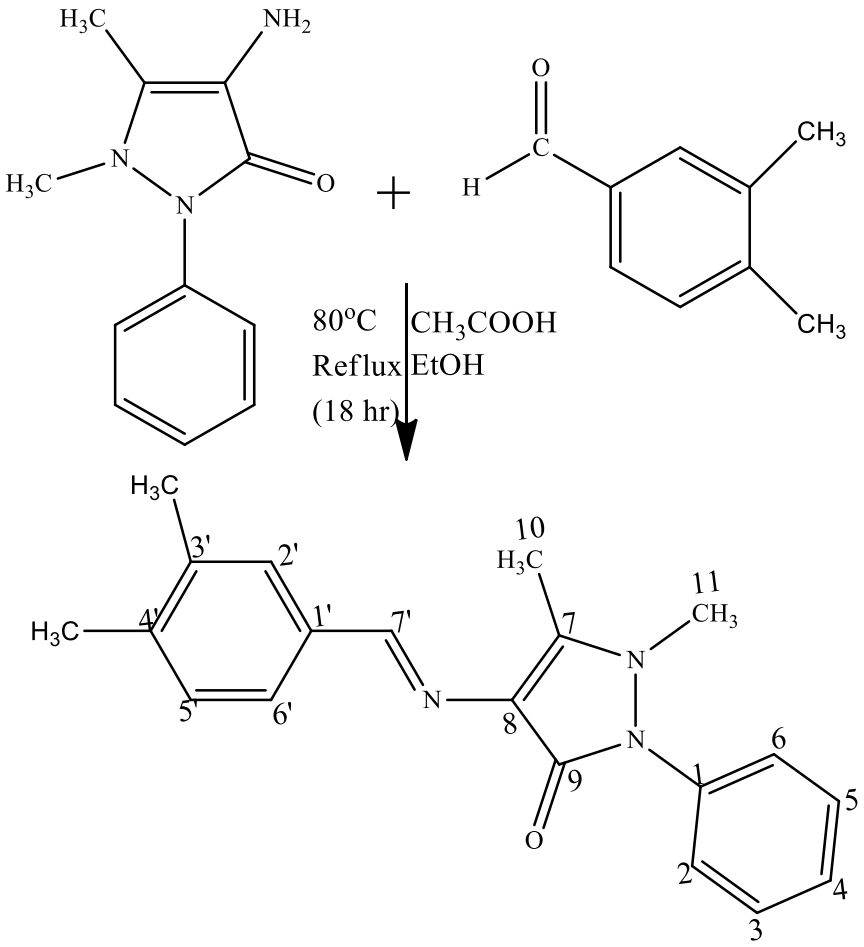

Scheme 3. 28: Synthetic Route of SB13

3.3.29 Synthesis of 4-((2,3,4-triahydroxybenzylidene)amino)-1,5-dimethyl-2-phenyl-1,2- dihydro-3H-pyrazol-3-one (SB17)

Compound SB17 was synthesised according to Scheme 3.29. In a 100 mL round bottom flask fitted with a condenser and a magnetic stirrer, 3,4-dimethylbenzaldehyde (0.0618 g, 0.4 mmol), 4-aminoantipyrine (0.0813 g, 0.4 mmol), glacial acetic acid (2 drops) and ethanol (10 mL), were refluxed at 80^{o}C for 5 hours. A TLC system of n-hexane: ethyl acetate, 5:5 (R*f* value 0.54) was used to track the progress of the reaction. On completion of the reaction, the resulting mixture was cooled to room temperature, the precipitate was filtered, recrystallised with ethanol and dried under vacuum to obtain dark yellow crystals of compound 4-((2,3,4-trihydroxybenzylidene)amino)-1,5-dimethyl-2-phenyl-1,2-dihydro-3H-pyrazol-3-one (0.1149 g).

3.3.30 Synthesis of 4-((-4hydroxyl-3,5-dimethoxybenzylidene)amino)-1,5-dimethy-2-phenyl-1,2-dihydrox-3H-pyraz-ol-3-one (SB19)

Compound SB19 was synthesised according to Scheme 3. 30. In a 100 mL round bottom flask fitted with a condenser and a magnetic stirrer, 3,4-dimethylbenzaldehyde (0.0729 g, 0.4 mmol), 4-aminoantipyrine (0.0813 g, 0.4 mM), glacial acetic acid (2 drops) and ethanol (10 mL), were refluxed at 80^{o}C for 2 hours. A TLC system of n-hexane: ethyl acetate, 5:5 (R*f* value 0.43) was used to monitor the progress of the reaction. On completion of the reaction, the resulting mixture was cooled to room temperature, the precipitate was filtered, recrystillised with ethanol and dried under vacuum to obtain an off white powdered compound 4-((4-hydroxy-3,5-dimethoxybenzylidene)amino)-1,5-dimethyl-2-phenyl-1,2-dihydro-3H-pyrazol-3-one (0.1381 g).

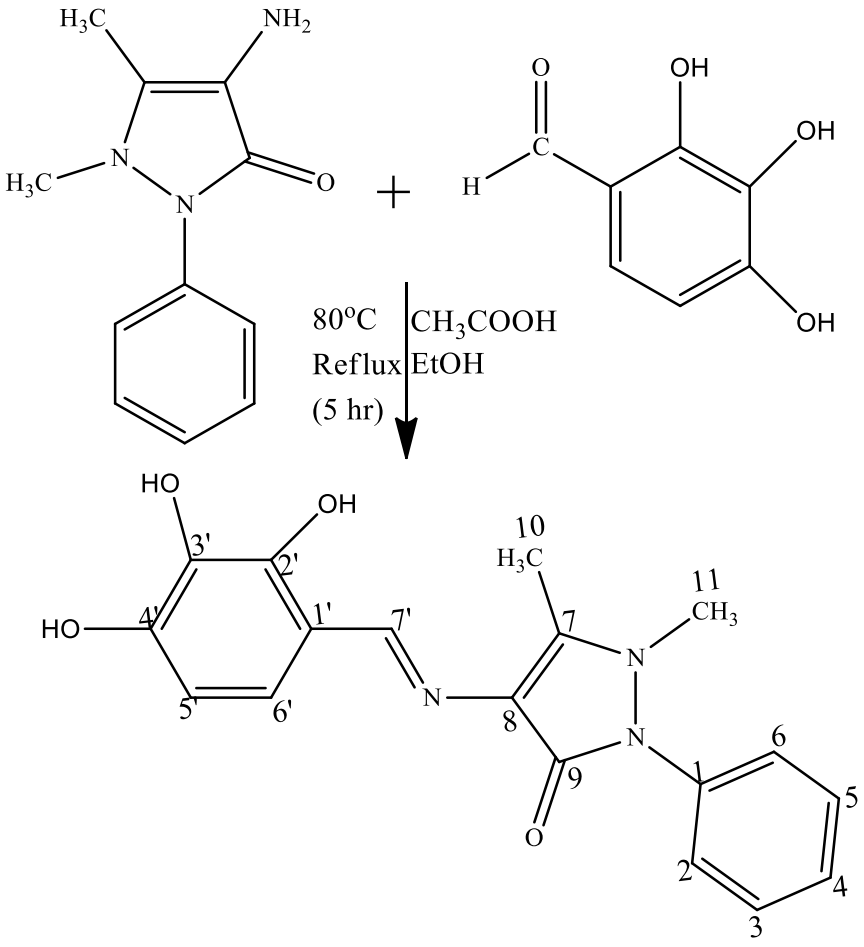

Scheme 3. 29: Synthetic Route of SB17

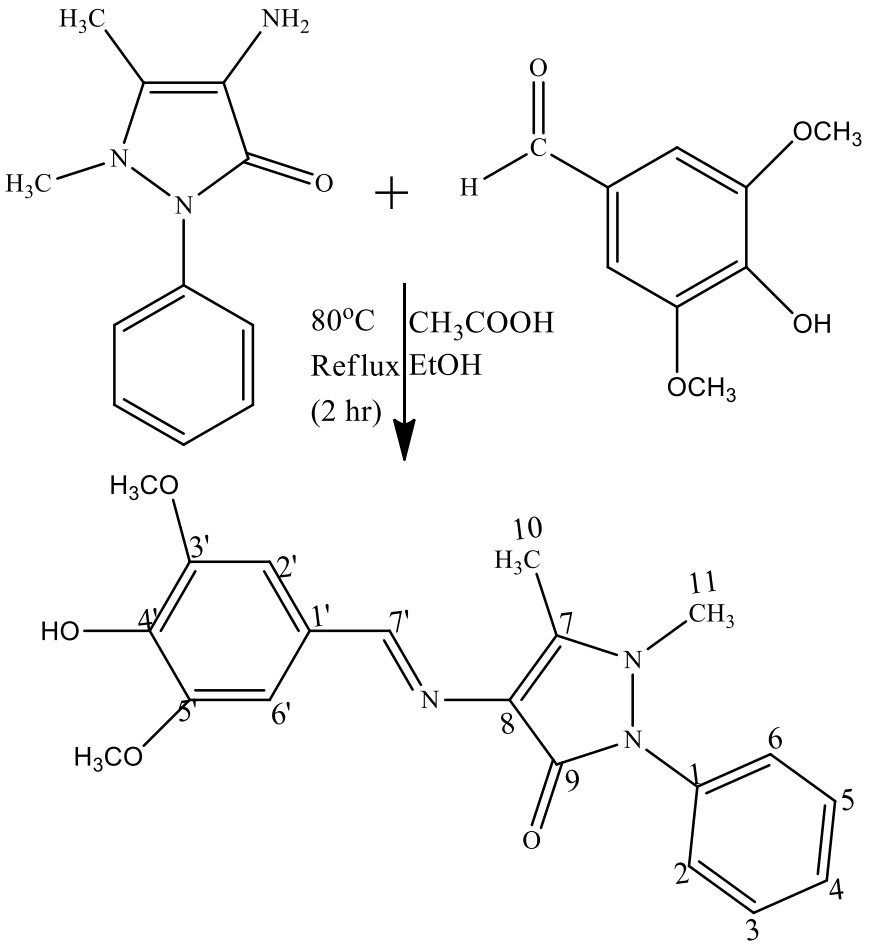

Scheme 3. 30: Synthetic Route of SB19

3.3.31 4-((3-methoxy-2-((4-(methylthio)benzyl)oxy)benzylidene)amino)-1,5-dimethyl -2-phenyl-1,2-dihydro-3H-pyrazol-3-one(5A-1)

The synthesis of compound 5A-1 followed Scheme 3.31. In a 100 mL round bottom flask, a mixture of anhydrous potassium carbonate (0.0691 g, 0.5 mmol), 4-((2-hydroxy-3-methoxybenzylidene)amino)-1,5-dimethyl-2-phenyl-1,2-dihydro-3H-pyrazol-3-one (SB5A) (0.0843 g, 0.25 mmol) and 5 mL of DMF was stirred for one hour. To this mixture, 4-methylthiobenzylchloride (0.0368 mL, 0.25mmol) was added and the mixture was stirred further for 15 hours at room temperature. A TLC system of n-hexane: ethyl acetate, 6:4 (R*f* value 0.47) was employed to track the reaction's progression. When the reaction is complete, the organic layer of the mixture was extracted using ethyl acetate. Further extraction was done with saturated solution of lithium chloride. After evaporation of excess solvent a pure brown solid compound 4-((3-methoxy-2-((4-(methylthio)benzyl)oxy) benzylidene)amino)-1,5-dimethyl-2-phenyl-1,2-dihydro-3H-pyrazol-3-one (0.0796 g) was obtained.

3.3.32 4-((3-methoxy-2-((4-(trifluoromethyl)benzyl)oxy)benzylidene)amino)-1,5-dimethyl-2-phenyl-1,2-dihydro-3H-pyrazol-3-one (5A-2)

The synthesis of compound 5A-2 followed Scheme 3.32. A mixture of anhydrous potassium carbonate (0.0691g, 0.5 mmol), 4-((2-hydroxy-3-methoxybenzylidene)amino)-1,5-dimethyl-2-phenyl-1,2-dihydro-3H-pyrazol-3-one (SB5A) (0.0843 g, 0.25 mmol) and 5 mL of DMF was stirred at room temperature. After 1 hour of stirring, 4-trifluoromethylbenzylchloride (0.0369 mL, 0.25mmol) was introduced and stirred further for 12 hours. A TLC system of n-hexane: ethyl acetate, 6:4 (R*f* value 0.56) was used to track the progress of the reaction. On completion of the reaction, the organic layer of the reaction mixture was extracted with ethyl acetate. Further extraction was done using saturated solution of lithium chloride. After evaporation of excess solvent a pale yellow solid compound 4-((3-methoxy-2-((4-(trifluoromethyl)benzyl)oxy)benzylidene)amino)-1,5-dimethyl-2-phenyl-1,2-dihydro-3H-pyrazol-3-one (0.0961 g) was obtained.

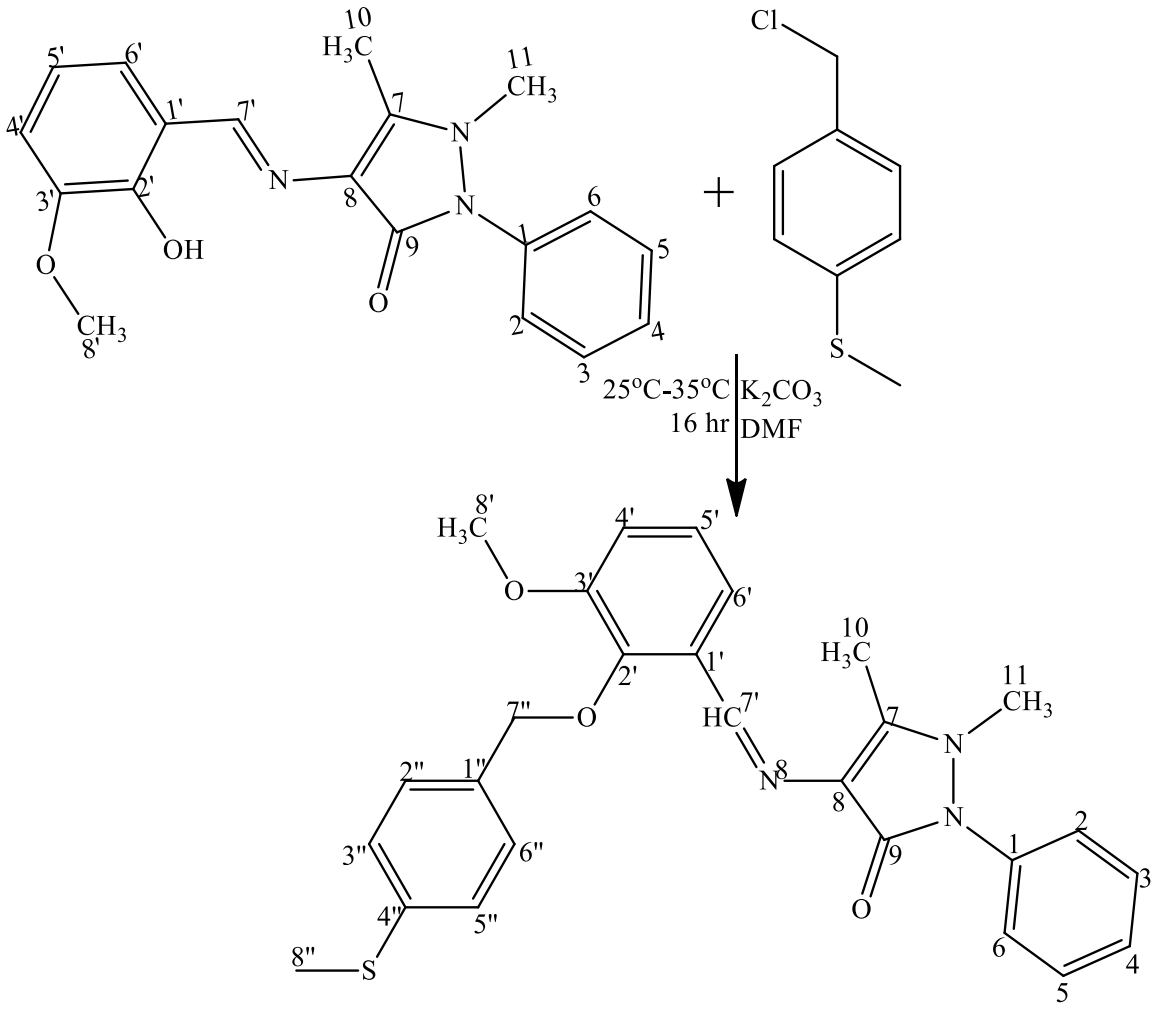

Scheme 3. 31: Synthetic Route of 5A-1

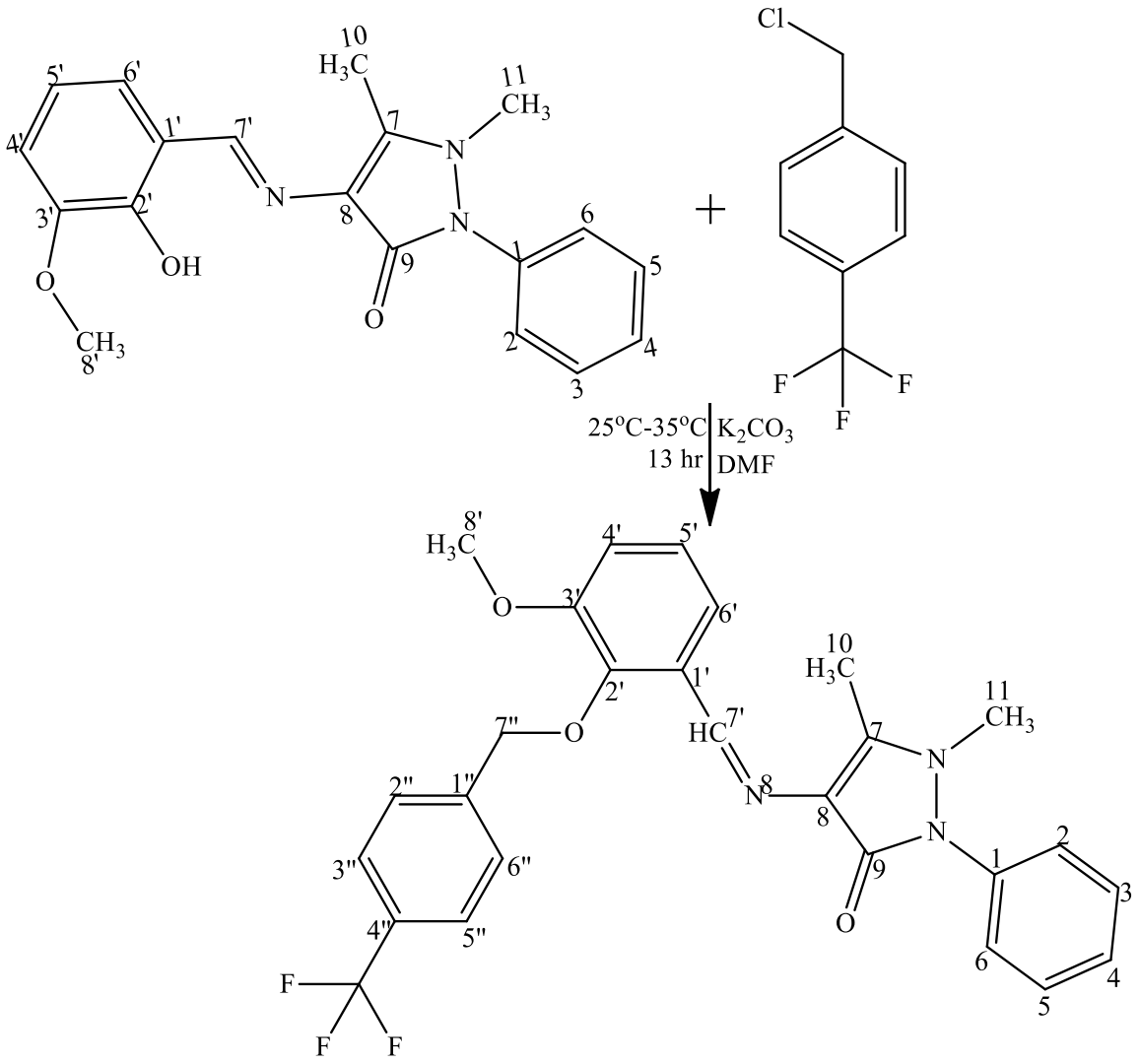

Scheme 3. 32: Synthetic Route of 5A-2

3.3.33 4-((2-((3-chlorobenzyl)oxy)-3-methoxybenzylidene)amino)-1,5-dimethyl-2-phenyl-1,2-dihydro-3H-pyrazol-3-one (5A-5)

The synthesis of compound 5A-5 followed Scheme 3.33. In a 100 mL round bottom flask, a mixture of anhydrous potassium carbonate (0.0691 g, 0.5 mmol), 4-((2-hydroxy-3-metho xybenzylidene)amino)-1,5-dimethyl-2-phenyl-1,2-dihydro-3H-pyrazol-3-one (SB5A) (0.0843 g, 0.25 mmol) and 5 mL of DMF was stirred for one hour. 3-chlorobenzylbromide (0.0328 mL, 0.25mmol) was introduced and the mixture was stirred further for 8 hours at room temperature. A TLC system of n-hexane: ethyl acetate, 6:4 (R*f* value 0.54) was used to track the progress of the reaction. On completion of the reaction, the organic layer of the reaction mixture was extracted with ethyl acetate. Further extraction was done using saturated solution of lithium chloride. After evaporation of excess solvent, a pure brown solid compound 4-((2-((3-chlorobenzyl)oxy)-3-methoxybenzylidene)amino)-1,5-dimethyl-2-phenyl-1,2-dihydro-3H-pyrazol-3-one (0.085 g) was obtained.

3.3.34 4-((2-((2-bromobenzyl)oxy)-3-methoxybenzylidene)amino)-1,5-dimethyl-2-phenyl-1,2-dihydro-3H-pyrazol-3-one (5A-6)

The synthesis of compound 5A-6 followed Scheme 3.34. In a 100 mL round bottom flask, a mixture of anhydrous potassium carbonate (0.0691 g, 0.5 mmol), 4-((2-hydroxy-3-metho xybenzylidene)amino)-1,5-dimethyl-2-phenyl-1,2-dihydro-3H-pyrazol-3-one (SB5A) (0.0843 g, 0.25 mmol) and 5 mL of DMF was stirred for one hour. 2-bromobenzylbromide (0.0625 g, 0.25mmol) was added and the mixture was stirred further for 6 hours at room temperature. A TLC system of n-hexane: ethyl acetate, 6:4 (R*f* value 0.55) was employed to track the reaction's progression. On completion of the reaction, the organic layer of the reaction mixture was extracted using ethyl acetate. Further extraction was done with saturated solution of lithium chloride. After evapouration of excess solvent, a pale yellow solid compound 4-((2-((2-bromobenzyl)oxy)-3-methoxybenzylidene)amino)-1,5-dimethyl-2-phenyl-1,2-dihydro-3H-pyrazol-3-one (0.1160 g) was obtained.

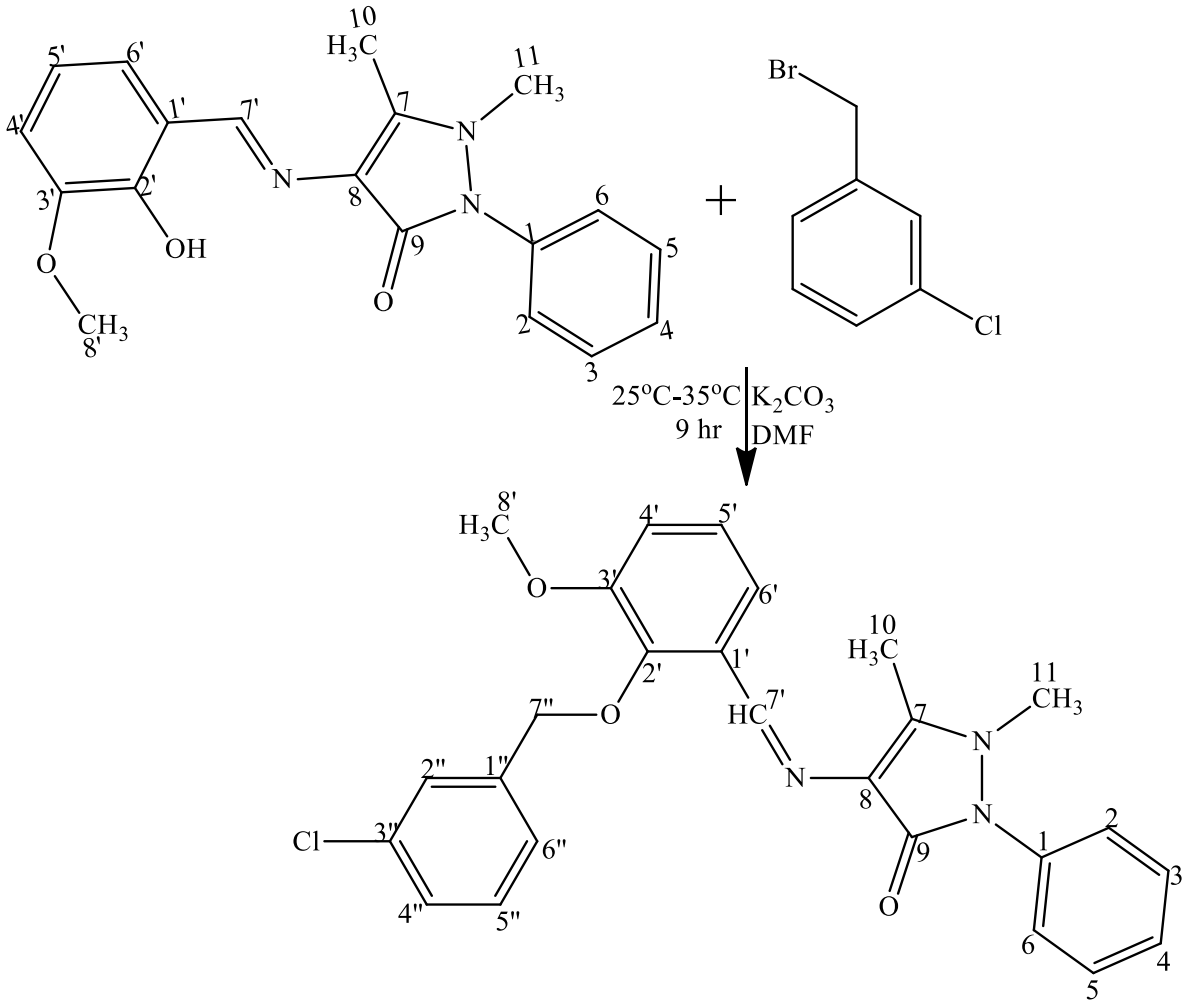

Scheme 3. 33: Synthetic Route of 5A-5

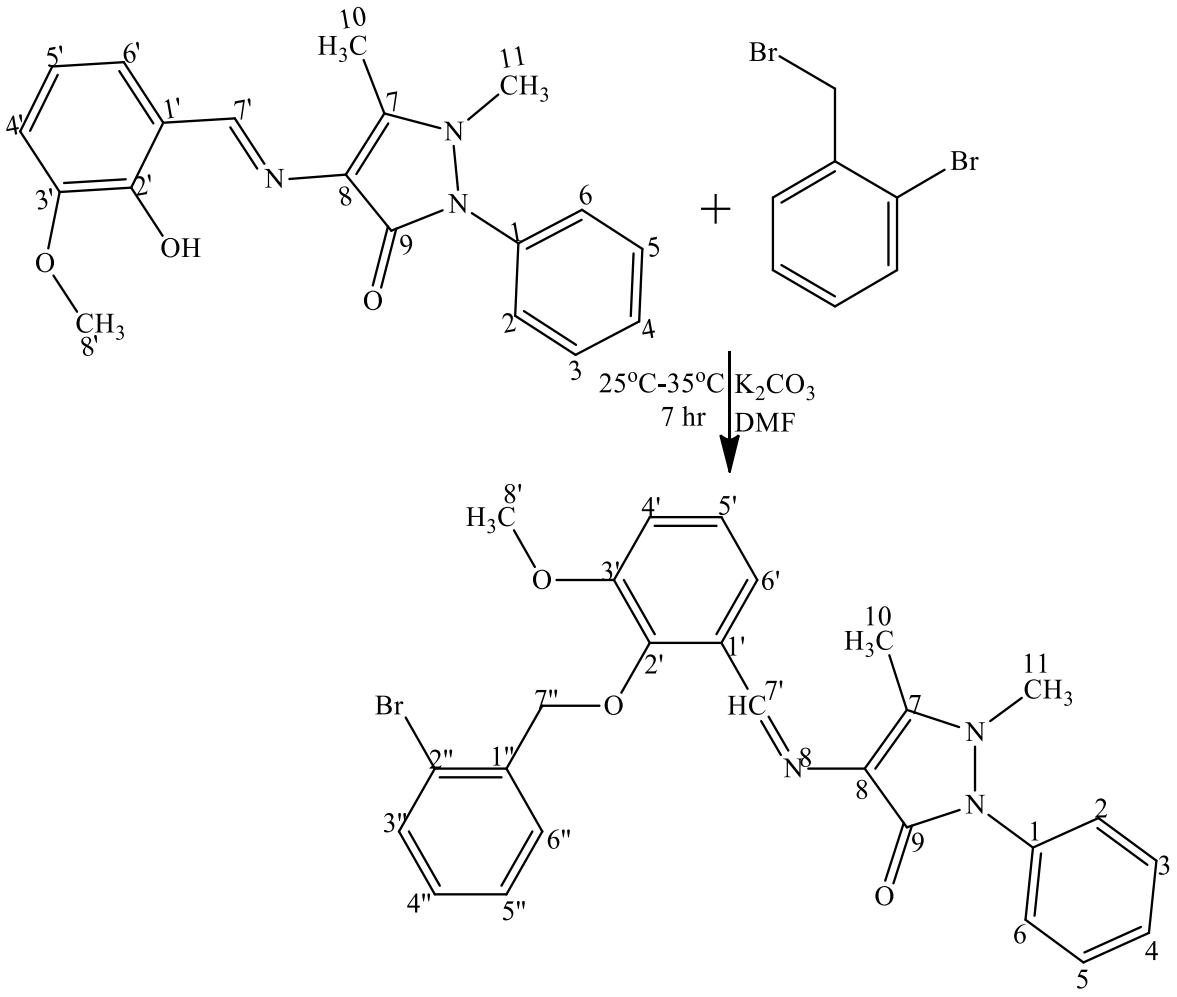

Scheme 3. 34: Synthetic Route of 5A-6

3.3.35 4-((3-methoxy-2-((3-nitrobenzyl)oxy)benzylidene)amino)-1,5-dimethyl-2-phenyl-1,2-dihydro-3H-pyrazol-3-one(5A-8)

The synthesis of compound 5A-8 followed Scheme 3.35. A mixture of anhydrous potassium carbonate (0.0691 g, 0.5 mmol), 4-((2-hydroxy-3-methoxybenzylidene)amino)-1,5-dimethyl-2-phenyl-1,2-dihydro-3H-pyrazol-3-one (SB5A) (0.0843 g, 0.25 mmol) and 5 mL of DMF was stirred for one hour. To this mixture, 3-nitrobenzylbromide (0.0540g 0.25mmol) was introduced and the mixture was stirred further for 12 hours at room temperature. A TLC system of n-hexane: ethyl acetate, 6:4 (R*f* value 0.48) was employed to track the reaction's progression. On completion of the reaction, the organic layer of the reaction mixture was extracted using ethyl acetate. Further extraction was done with saturated solution of lithium chloride. After evaporation of excess solvent a pure golden yellow solid compound 4-((3-methoxy-2-((3-nitrobenzyl)oxy)benzylidene)amino)-1,5-dimethyl-2-phenyl-1,2-dihydro-3H-pyrazol-3-one (0.0915 g) was obtained.

3.3.36 4-((3-methoxy-2-((3-methoxybenzyl)oxy)benzylidene)amino)-1,5-dimethyl-2-phenyl-1,2-dihydro-3H-pyrazol-3-one (5A-9)

The synthesis of compound 5A-9 followed Scheme 3.36. In a 100 mL round bottom flask, a mixture of anhydrous potassium carbonate (0.0636 g, 0.46 mmol), 4-((2-hydroxy-3-methoxybenzylidene)amino)-1,5-dimethyl-2-phenyl-1,2-dihydro-3H-pyrazol-3-one (SB5A) (0.0776 g, 0.23 mmol) and 5 mL of DMF was stirred for one hour. To this mixture, 3-methoxylbenzylbromide (0.033 mL, 0.23mmol) was introduced and the mixture was stirred further for 8 hours at room temperature. The progress of the reaction was tracked with TLC system of n-hexane: ethyl acetate, 5:5 (R*f* value of 0.48). On completion of the reaction, the organic layer of the reaction mixture was extracted using ethyl acetate. Further extraction was done with saturated solution of lithium chloride. After evaporation of excess solvent, a pure light brown solid compound 4-((3-methoxy-2-((3-methoxybenzyl) oxy)benzylidene)amino)-1,5-dimethyl-2-phenyl-1,2-dihydro-3H-pyrazol-3-one (0.0920 g) was obtained.

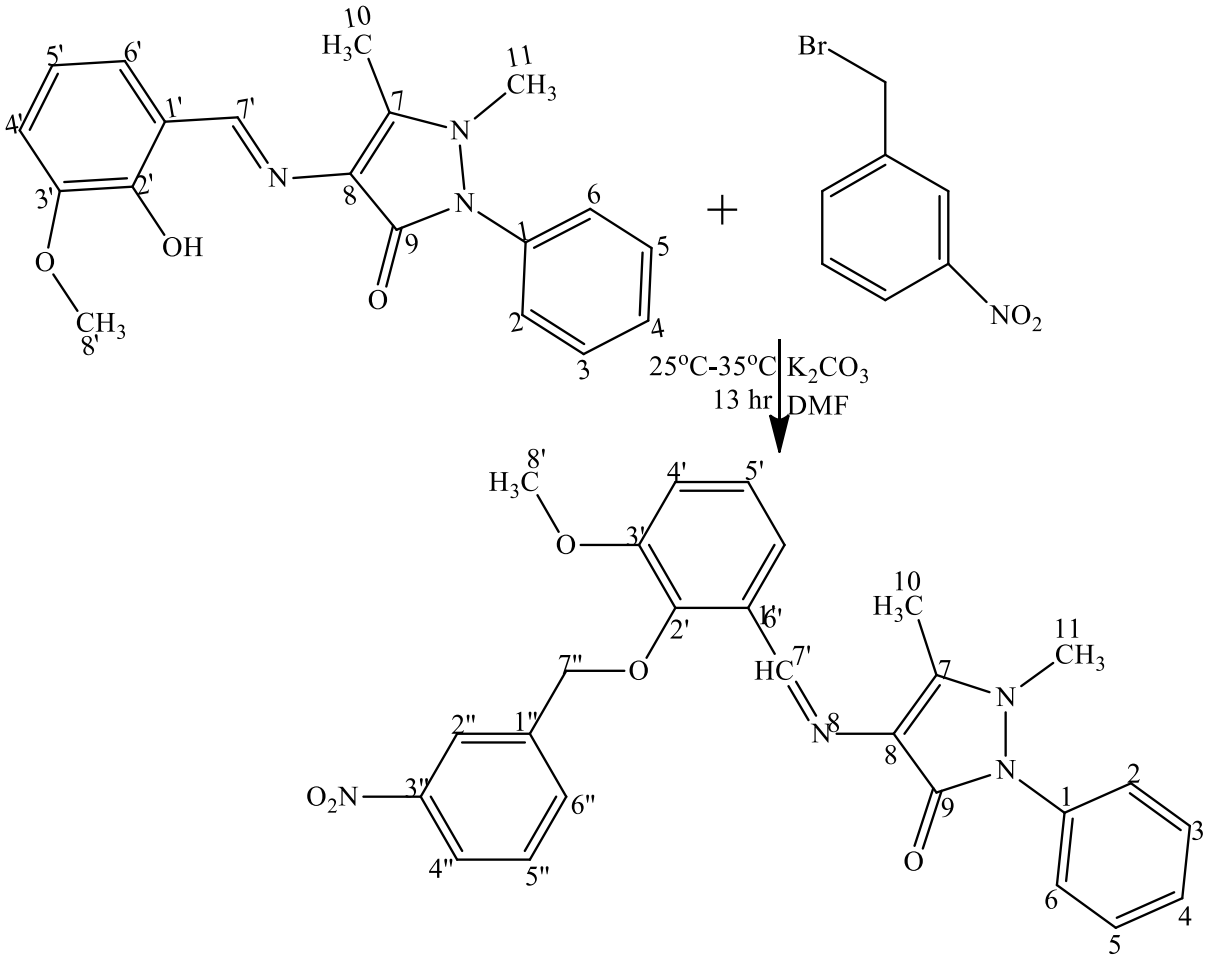

Scheme 3. 35: Synthetic Route of 5A-8

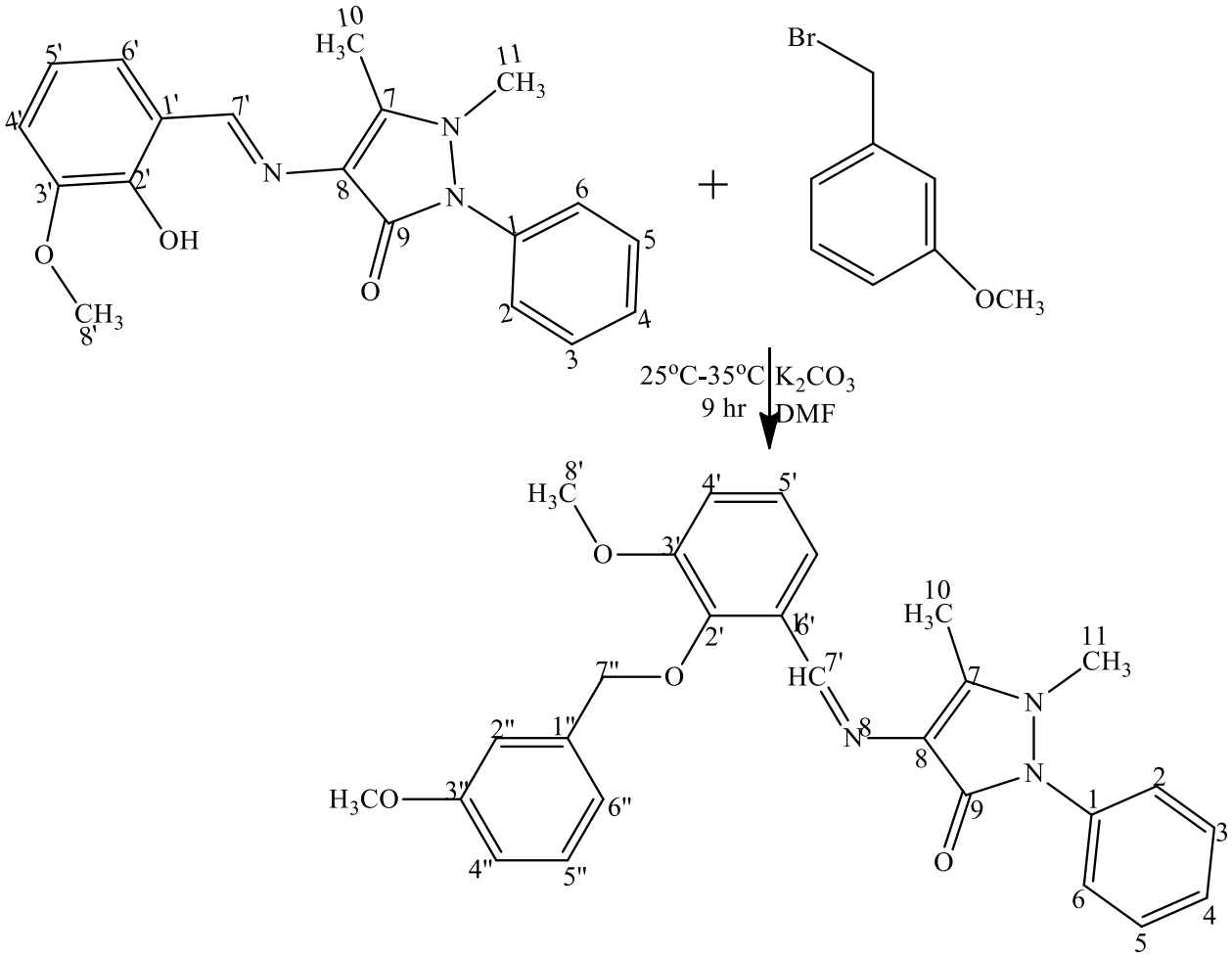

Scheme 3. 36: Synthetic Route of 5A-9

3.3.37 Synthesis of 1,5-dimethyl-4-((4-((4-(methylthio)benzyl)oxy)benzylidene) amino)-2-phenyl-1,2-dihydro-3H-pyrazol-3-one (9B-1)

Compound 9B-1 was synthesised according to Scheme 3.37. 0.0553 g (0.4 mmol) of anhydrous potassium carbonate and 0.0615 g (0.2 mmol) of 4-(4-hydroxybenzylideneamino)-1,2-dihydro-2,3-dimethyl-1-phenylpyrazol-5-one (SB9B) were dissolved in 5 mL of DMF in a 100 mL round bottom flask and stirred at room temperature. After 1 hour of stirring 4-methylthiobenzylchloride (0.0295 mL, 0.2 mmol) was added and the reaction mixture was stirred further for 12 hours. The progress of the reaction was tracked with TLC system of n-hexane: ethyl acetate, 5:5 (R*f* value of 0.58). On completion of the reaction, the organic layer of the reaction mixture was extracted using ethyl acetate. Further extraction was done with saturated solution of lithium chloride. After evaporation of excess solvent a pure brown solid compound 1,5-dimethyl-4-((4-((4-(methylthio)benzyl)oxy)benzylidene)amino)-2-phenyl-1,2-dihydro-3H-pyrazol-3-one (9B- 1) (0.0720 g) was obtained.

3.3.38 Synthesis of 1,5-dimethyl-2-phenyl-4-((4-((4-(trifluoromethyl)benzyl)oxy) benzylidene)amino)-1,2-dihydro-3H-pyrazol-3-one (9B-2)

Compound 9B-2 was synthesised in accordance with Scheme 3.38. 0.O691 g (0.5 mmol) of anhydrous potassium carbonate and 0.0768 g (0.2 mmol) of 4-(4-hydroxybenzyliden e-amino)-1,2-dihydro-2,3-dimethyl-1-phenyl pyrazol-5-one (SB9B) were dissolved in 5 mL of DMF in a 100 mL round bottom flask and stirred at room temperature. After 1 hour of stirring, 4-trifluoromethylbenzylchloride (0.0369 mL, 0.25mmol) was added and the reaction mixture was stirred further for 6 hours. The reaction progress was monitored by TLC system of n-hexane: ethyl acetate, 5:5 (R*f* value of 0.54). On completion of the reaction, the organic layer of the reaction mixture was extracted using ethyl acetate. Further extraction was done with saturated solution of lithium chloride. A pure brown solid compound 1,5-dimethyl-2-phenyl-4-((4-((4-(trifluoromethyl)benzyl)oxy) benzylidene)amino)-1,2-dihydro-3H-pyrazol-3-one (9B-2) (0.0801 g) was obtained after evaporation of excess solvent.

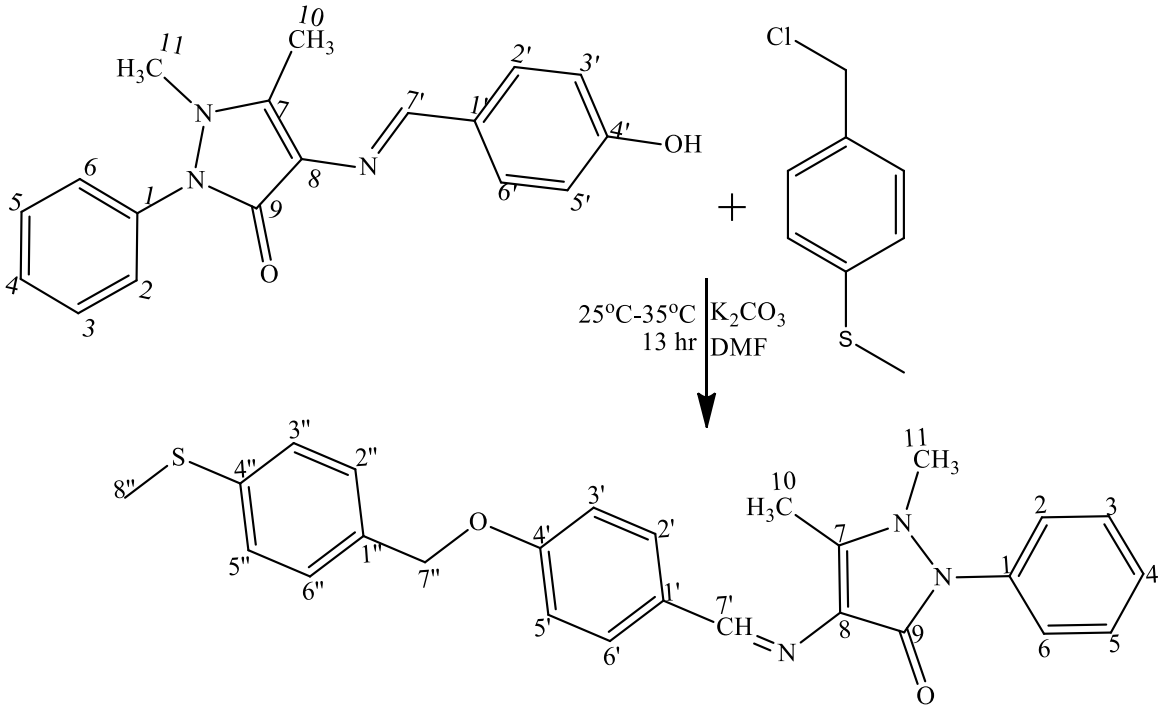

Scheme 3. 37: Synthetic Route of 9B-1

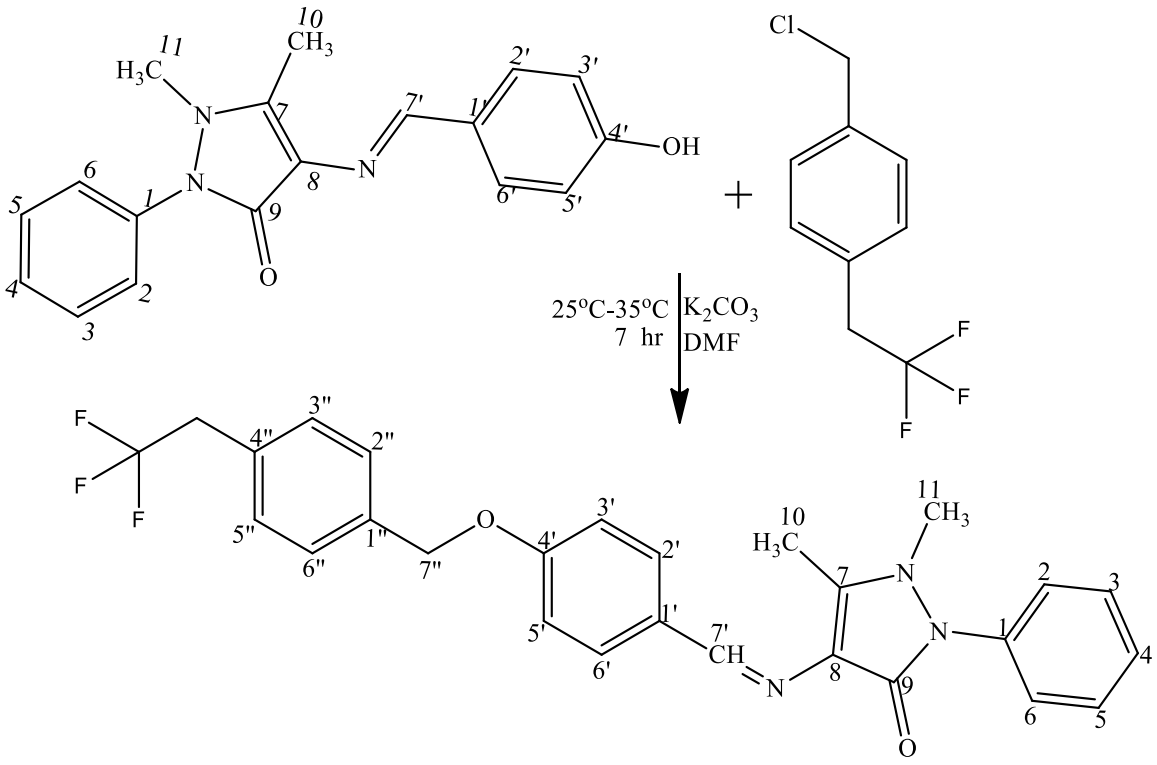

Scheme 3. 38: Synthetic Route of 9B-2

3.3.39 Synthesis of 1,5-dimethyl-4-((4-((3-chlorobenzyl)oxy)benzylidene)amino)-2-phenyl-1,2-dihydro-3H-pyrazol-3-one (9B-5)

Compound 9B-5 was synthesised in accordance with Scheme 3.39. 0.0610 g (0.5 mmol) of anhydrous potassium carbonate and 0.0768 g (0.25 mmol) of 4-(4-hydroxybenzylidene amino)-1,2-dihydro-2,3-dimethyl-1-phenylpyrazol-5-one (SB9B) were dissolved in 5 mL of DMF in a 100 mL round bottom flask and stirred at room temperature. After 1 hour of stirring 3-chlorobenzylbromide (0.032 mL, 0.25mmol) was introduced and the reaction mixture was stirred further for 24 hours. The progress of the reaction was tracked with TLC system of n-hexane: ethyl acetate, 5:5 (R*f* value of 0.54). On completion of the reaction, the organic layer of the reaction mixture was extracted using ethyl acetate. Further extraction was done with saturated solution of lithium chloride. A pure brown solid compound 1,5-dimethyl-4-((4-((3-chlorobenzyl)oxy)benzylidene)amino)-2-phenyl-1,2-dihydro-3H-pyrazol-3-one (0.092 g) was obtained after evaporation of excess solvent.

3.3.40 Synthesis of 4-((4-((2-bromobenzyl)oxy)benzylidene)amino)-1,5-dimethyl-2-phenyl-1,2-dihydro-3H-pyrazol-3-one (9B-6)

Compound 9B-6 was synthesised in accordance to Scheme 3.40. 0.0829 g (0.6 mmol) of anhydrous potassium carbonate and 0.0922g (0.3 mmol) of 4-(4-hydroxybenzylideneamino)-1,2-dihydro-2,3-dimethyl-1-phenylpyrazol-5-one (SB9B) were dissolved in 5 mL of DMF in a 100 mL round bottom flask and stirred at room temperature. After 1 hour of stirring 2-bromobenzylbromide (0.0744 g, 0.3 mmol) was added and the reaction mixture was stirred further for 12 hours. The progress of the reaction was tracked with TLC system of n-hexane: ethyl acetate, 5:5 (R*f* value of 0.55). On completion of the reaction, the organic layer of the reaction mixture was extracted using ethyl acetate. Further extraction was done with saturated solution of lithium chloride. A pale yellow solid compound 4-((4-((2-bromobenzyl)oxy)benzylidene)amino)-1,5-dimethyl-2-phenyl-1,2-dihydro-3H-pyrazol-3-one (0.1401 g) was obtained after evaporation of excess solvent.

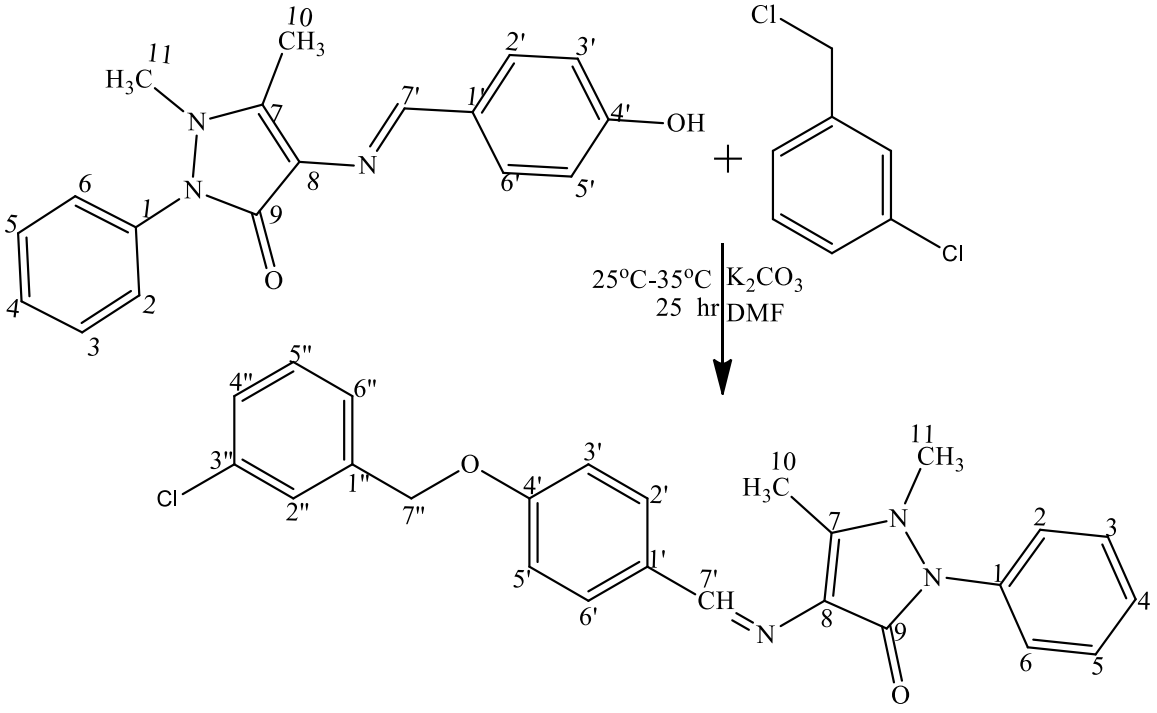

Scheme 3. 39: Synthetic Route of 9B-5

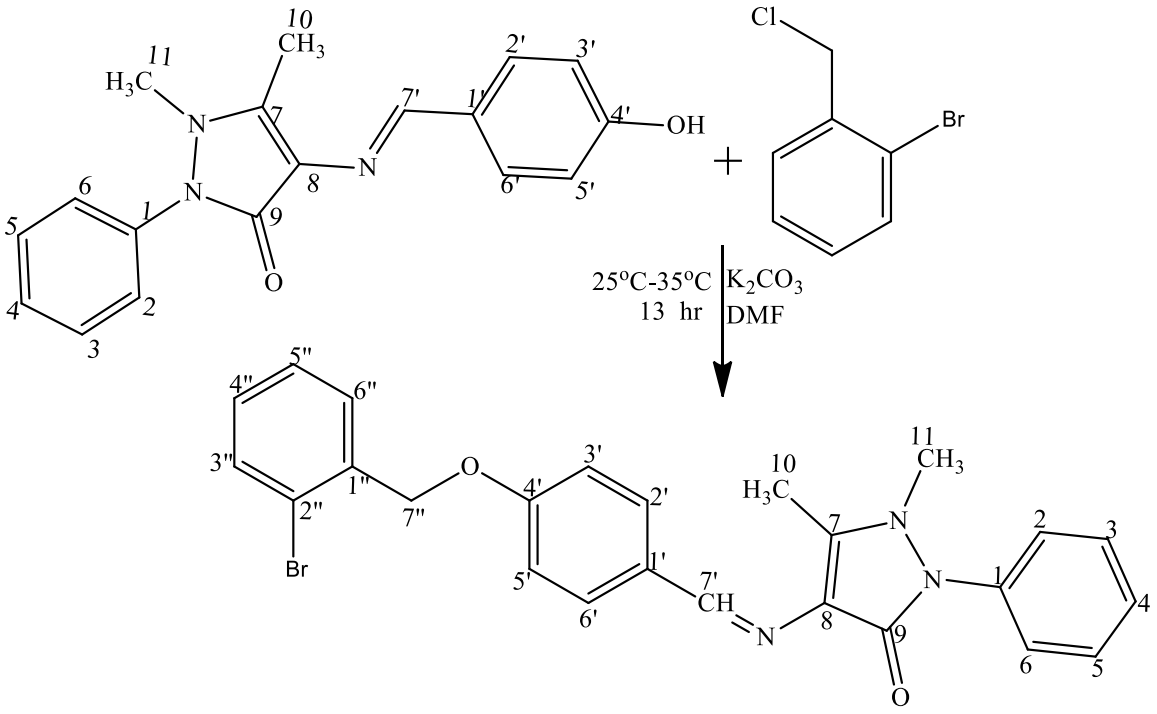

Scheme 3. 40: Synthetic Route of 9B-6

3.3.41 Synthesis of 1,5-dimethyl-4-((4-((3-nitrobenzyl)oxy)benzylidene)amino)-2-phenyl-1,2-dihydro-3H-pyrazol-3-one (9B-8)

Compound 9B-2 was synthesised in accordance with Scheme 3.41. 0.0610 g (0.5 mmol) of anhydrous potassium carbonate and 0.0768 g (0.25 mmol) of 4-(4-hydroxybenzylidene-amino)-1,2-dihydro-2,3-dimethyl-1-phenyl pyrazol-5-one (SB9B) were dissolved in 5 mL of DMF in a 100 mL round bottom flask and stirred at room temperature. After 1 hour of stirring 3-nitrobenzylbromide (0.0540 g, 0.25 mmol) was added and the reaction mixture was stirred further for 10 hours. The progress of the reaction was tracked with TLC system of n-hexane/ethyl acetate, 5:5 (R*f* value of 0.56). On completion of the reaction, the organic layer of the reaction mixture was extracted using ethyl acetate. Further extraction was done with saturated solution of lithium chloride. A pure yellow solid compound 1,5-dimethyl-4-((4-((3-nitrobenzyl)oxy)benzylidene)amino)-2-phenyl-1,2-dihydro-3H-pyrazol-3-one (9B-8) (0.1029 g) was obtained after evaporation of excess solvent.

3.3.42 Synthesis of 4-((4-((3-methoxybenzyl)oxy)benzylidene)amino)-1,5-dimethyl-2-phenyl-1,2-dihydro-3H-pyrazol-3-one (9B-9)

Compound 9B-9 was synthesised in accordance with Scheme 3.42. 0.0816 g (0.58 mmol) of anhydrous potassium carbonate and 0.0891 g (0.29 mmol) of 4-(4-hydroxybenzyli deneamino)-1,2-dihydro-2,3-dimethyl-1-phenyl pyrazol-5-one (SB9B) were dissolved in 5 mL of DMF in a 100 mL round bottom flask and stirred at room temperature. After 1 hour of stirring 3-methoxylbenzylbromide (0.042 mL, 0.29mmol) was added and the reaction mixture was stirred further for 10 hours. The reaction progress was monitored by TLC system of n-hexane: ethyl acetate, 5:5 (R*f* value of 0.56). On completion of the reaction, the organic layer of the reaction mixture was extracted using ethyl acetate. Further extraction was done with saturated solution of lithium chloride. After evaporation of excess solvent, a pale yellow solid compound 4-((4-((3-methoxybenzyl)oxy)benzyli dene)amino)-1,5-dimethyl-2-phenyl-1,2-dihydro-3H-pyrazol-3-one (9B-9) (0.0698 g) was obtained.

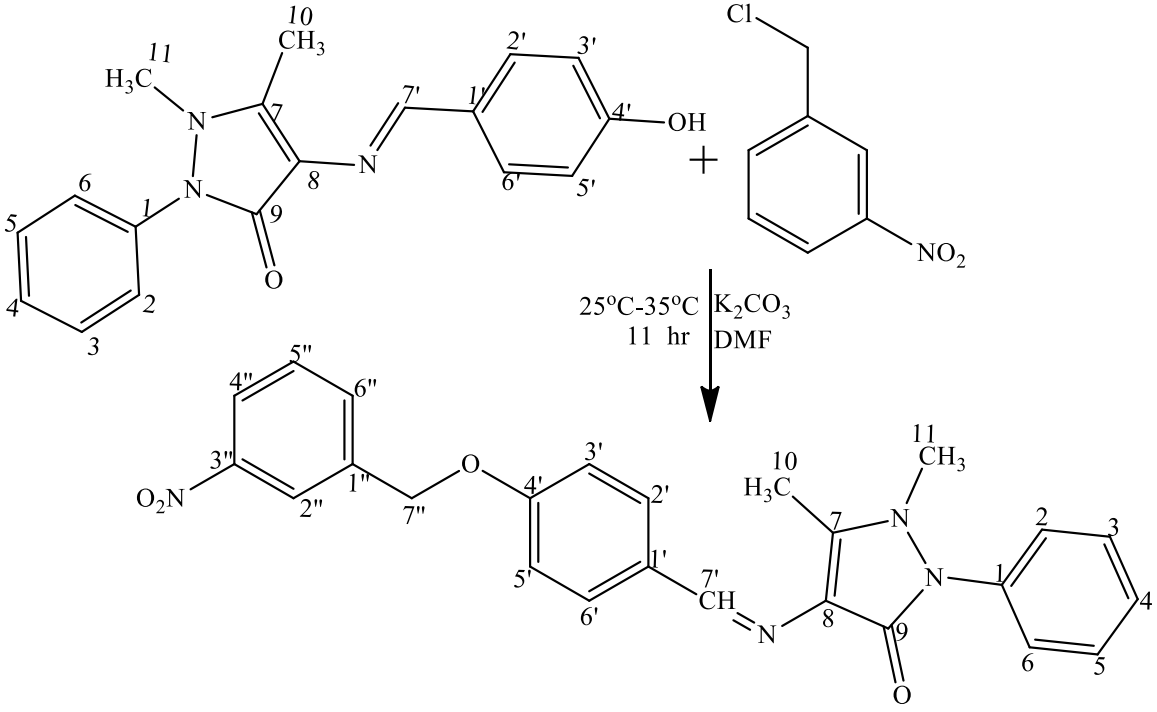

Scheme 3. 41: Synthetic Route of 9B-8

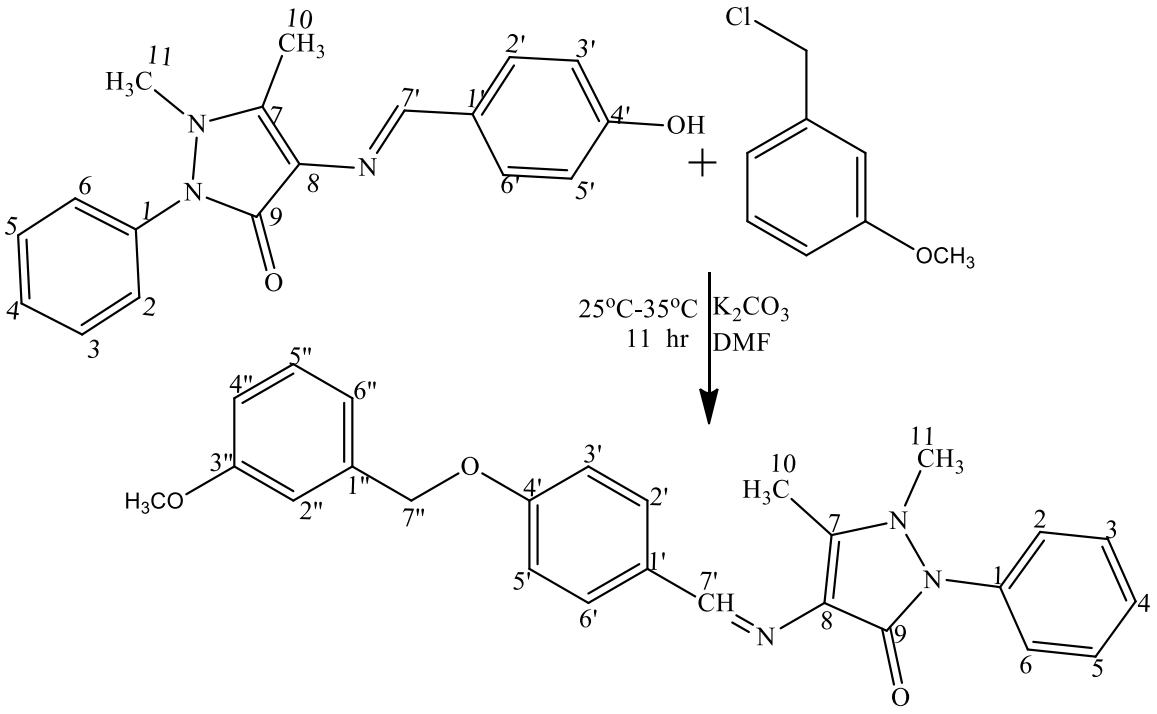

Scheme 3. 42: Synthetic Route of 9B-9

3.3.43 Synthesis of 1,5-dimethyl-4-((5-((4-(methylthio)benzyl)oxy)-2-nitrobenzylidene)amino)-2-phenyl-1,2-dihydro-3H-pyrazol-3-one (10-1)

The synthesis of compound 10-1 followed Scheme 3.43. A mixture of 0.0392 g (0.284 mmol) of anhydrous potassium carbonate, 0.050 g (0.142 mmol) of 4-((3-hydroxy-4-nitrobenzylidene)amino)-1,5-dimethyl-2-phenyl-1,2-dihydro-3H-pyrazol-3-one (SB10), and 5 mL of DMF in a 100 mL round bottom flask was stirred at room temperature. After 1 hour of stirring, 4-methylthiobenzylchloride (0.021mL, 0.142 mmol) was added and the reaction mixture was stirred further for 8 hours. The reaction progress was tracked by TLC system of n-hexane: ethyl acetate, 6:4 (R*f* value of 0.55). On completion of the reaction, the organic layer of the reaction mixture was extracted using ethyl acetate. Further extraction was done with saturated solution of lithium chloride. After evaporation of excess solvent, compound 1,5-dimethyl-4-((5-((4-(methylthio)benzyl)oxy)-2-nitrobenzylidene)amino)-2-phenyl-1,2-dihydro-3H-pyrzol-3-one (0.0598g) was acquired as Orange solid.

3.3.44 Synthesis of 1,5-dimethyl-4-((2-nitro-5-((4-(trifluoromethyl)benzyl)oxy)benzylidene)amino)-2-phenyl-1,2-dihydro-3H-pyrazol-3-one (10-2)

The synthesis of compound 10-2 followed Scheme 3.44. A mixture of 0.0533g (0.4 mmol) of anhydrous potassium carbonate, 0.0705 g (0.2 mmol) of 4-((3-hydroxy-4-nitrobenzylidene)amino)-1,5-dimethyl-2-phenyl-1,2-dihydro-3H-pyrazol-3-one (SB10) and DMF (5 mL) in a 100 mL round bottom flask was stirred at room temperature. After 1 hour of stirring, 4-trifluoromethylbenzylchloride (0.029 mL, 0.2 mmol) was added and the reaction mixture was stirred further for 8 hours. The reaction progress was tracked by TLC system of n-hexane: ethyl acetate, 6:4 (R*f* value of 0.56). On completion of the reaction, the organic layer of the reaction mixture was extracted using ethyl acetate. Further extraction was done with saturated solution of lithium chloride. After evaporation of excess solvent, compound 1,5-dimethyl-4-((2-nitro-5-((4-(trifluoromethyl)benzyl)oxy)benzylidene)amino)-2-phenyl-1,2-dihydro-3H-pyrazol-3-one (10-2) (0.090 g) was obtained as golden yellow solid.

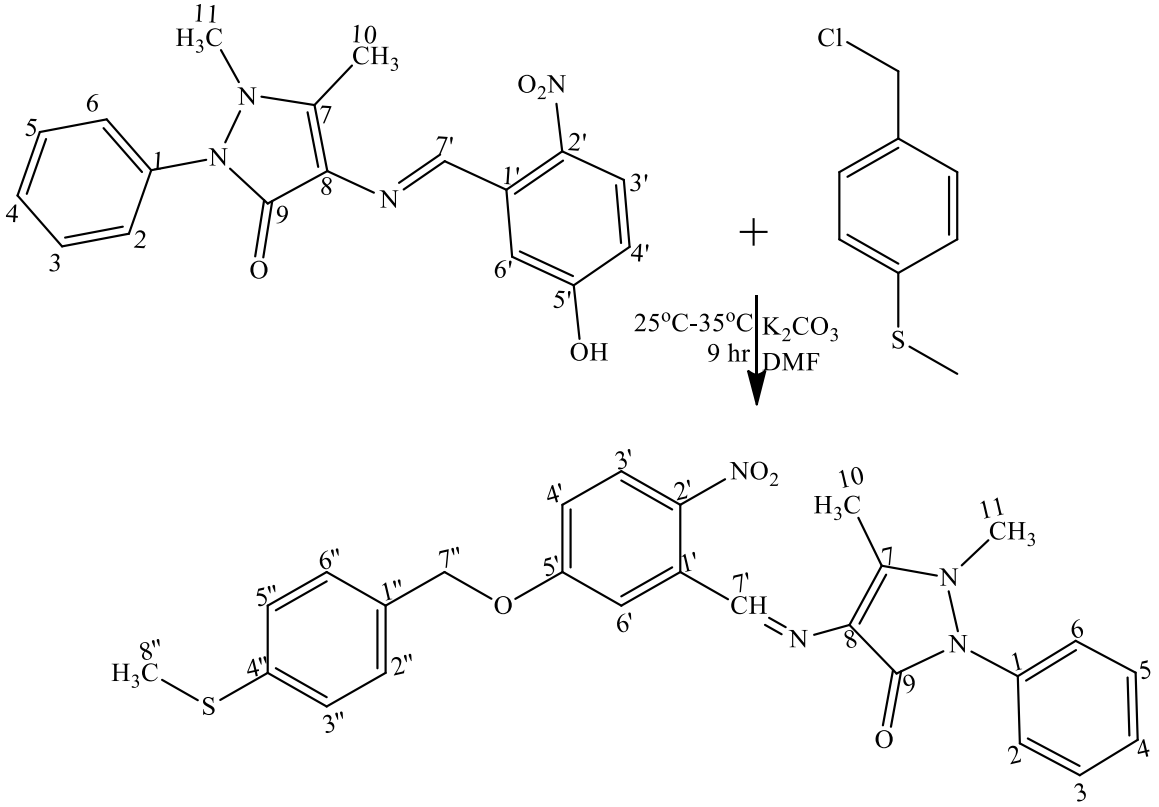

Scheme 3. 43: Synthetic Route of 10-1

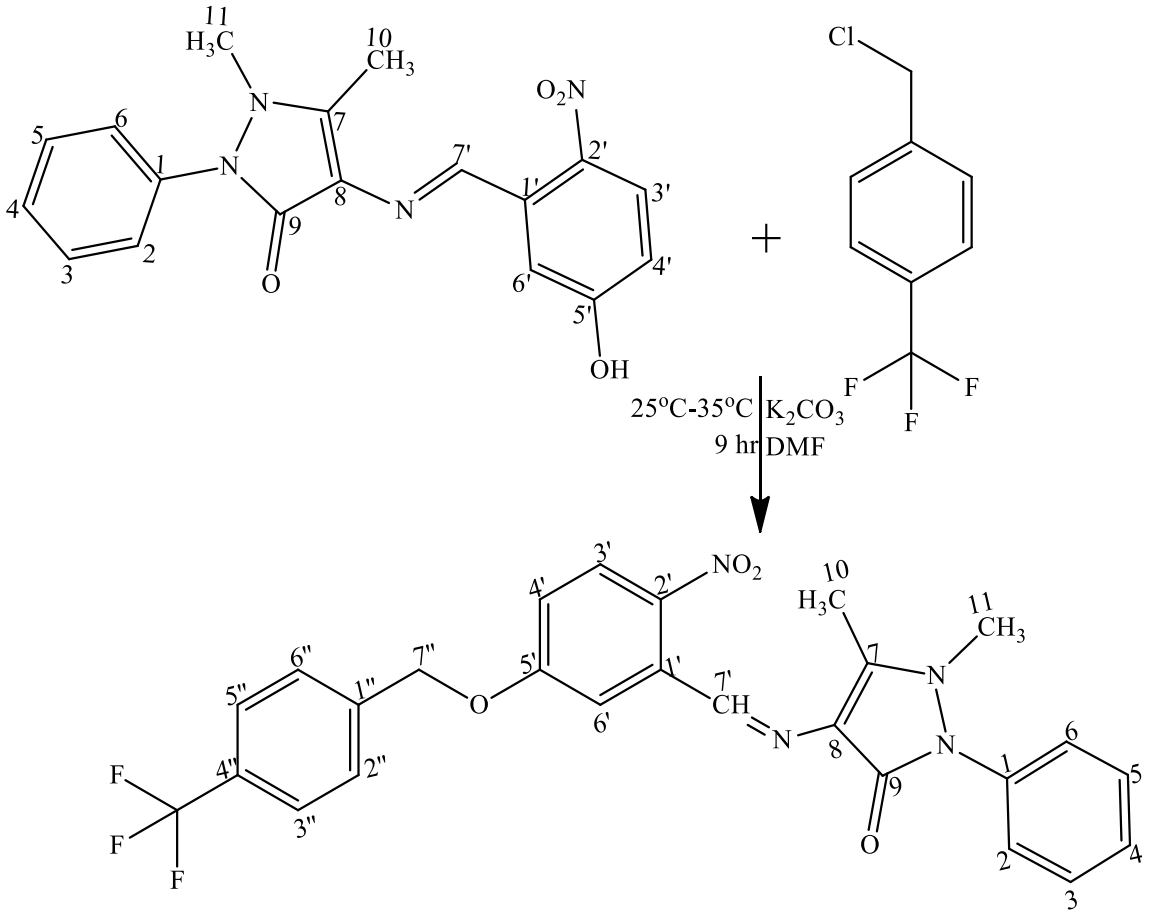

Scheme 3. 44: Synthetic Route of 10-2

3.3.45 Synthesis of 4-((5-((3-chlorobenzyl)oxy)-2-nitrobenzylidene)amino)-1,5-dimethyl -2-phenyl-1,2-dihydro-3H-pyrazol-3-one (10-5)

The synthesis of compound 10-2 followed Scheme 3.45. A mixture of 0.0533g (0.4 mmol) of anhydrous potassium carbonate, 0.0705 g (0.2 mmol) of 4-((3-hydroxy-4-nitrobenzylid ene)amino)-1,5-dimethyl-2-phenyl-1,2-dihydro-3H-pyrazol-3-one (SB10) and DMF (5 mL) in a 100 mL round bottom flask was stirred at room temperature. After 1 hour of stirring, 3-chlorobenzylbromide (0.0263 mL, 0.2 mmol) was added and the reaction mixture was stirred further for 12 hours. The reaction progress was monitored by TLC system of n-hexane: ethyl acetate, 6:4 (R*f* value of 52). On completion of the reaction, the organic layer of the reaction mixture was extracted using ethyl acetate. Further extraction was done with saturated solution of lithium chloride. After evaporation of excess solvent, compound 4-((5-((3-chlorobenzyl)oxy)-2-nitrobenzylidene)amino)-1,5-dimethyl-2-phenyl-1,2-dihydro-3H-pyrazol-3-one (10-5) (0.091 g) was obtained as orange solid.

3.3.46 Synthesis of 4-((3-((2-bromobenzyl)oxy)-4-nitrobenzylidene)amino)-1,5-dimethyl-2-phenyl-1,2-dihydro-3H-pyrazol-3-one (10-6)

The synthesis of compound 10-6 followed Scheme 4.46. A mixture of 0.0533 g (0.4 mmol) of anhydrous potassium carbonate, 0.0705 g (0.2 mmol) of 4-((3-hydroxy-4-nitrobenzylid ene)amino)-1,5-dimethyl-2-phenyl-1,2-dihydro-3H-pyrazol-3-one (SB10) and DMF (5 mL) in a 100 mL round bottom flask was stirred at room temperature. After 1 hour of stirring, 2-bromobenzylbromide (0.0494 g, 0.2 mmol) was added and the reaction mixture was stirred further for 3 hours. The reaction progress was tracked by TLC system of n-hexane: ethyl acetate, 7:3 (R*f* value of 0.52). On completion of the reaction, the organic layer of the reaction mixture was extracted using ethyl acetate. Further extraction was done with saturated solution of lithium chloride. After evaporation of excess solvent, compound 4-((3-((2-bromobenzyl)oxy)-4-nitrobenzylidene)amino)-1,5-dimethyl-2-phenyl-1,2-dihydro-3H-pyrazol-3-one (0.0931 g) was obtained as orange solid.

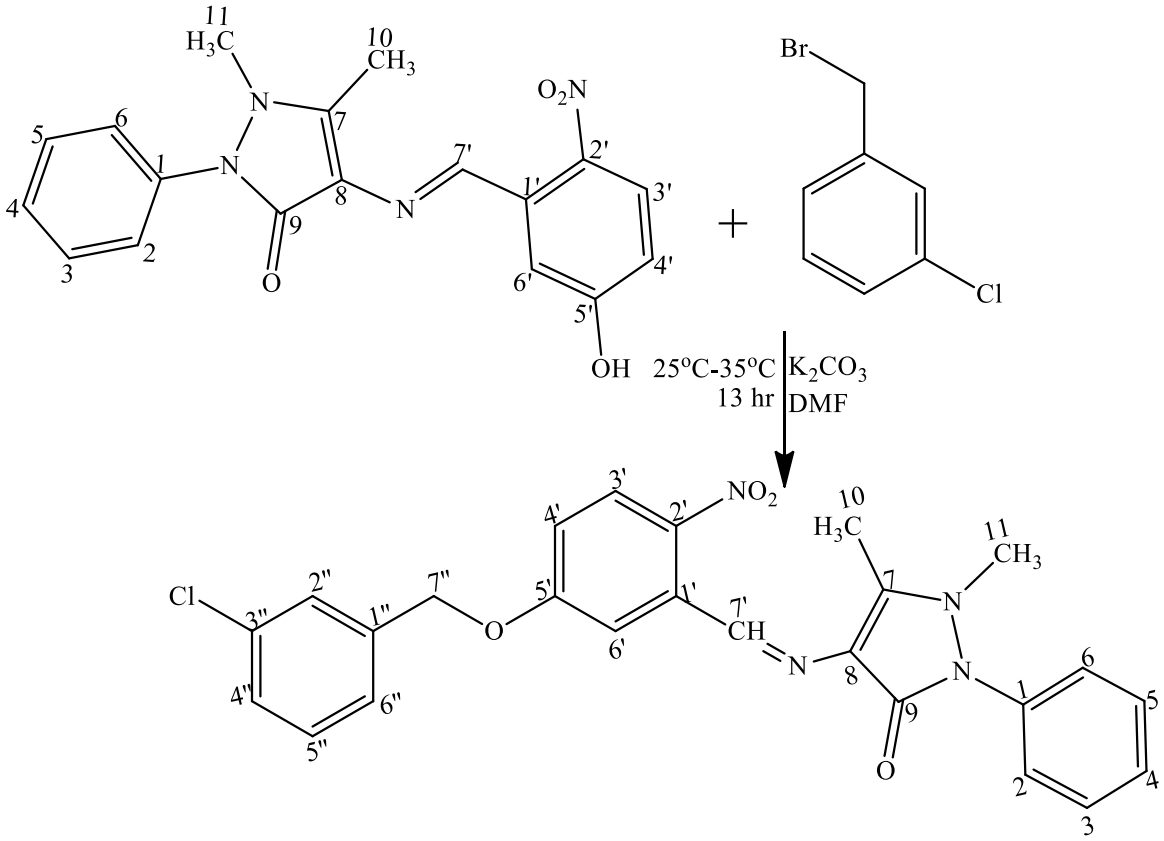

Scheme 3. 45: Synthetic Route of 10-5

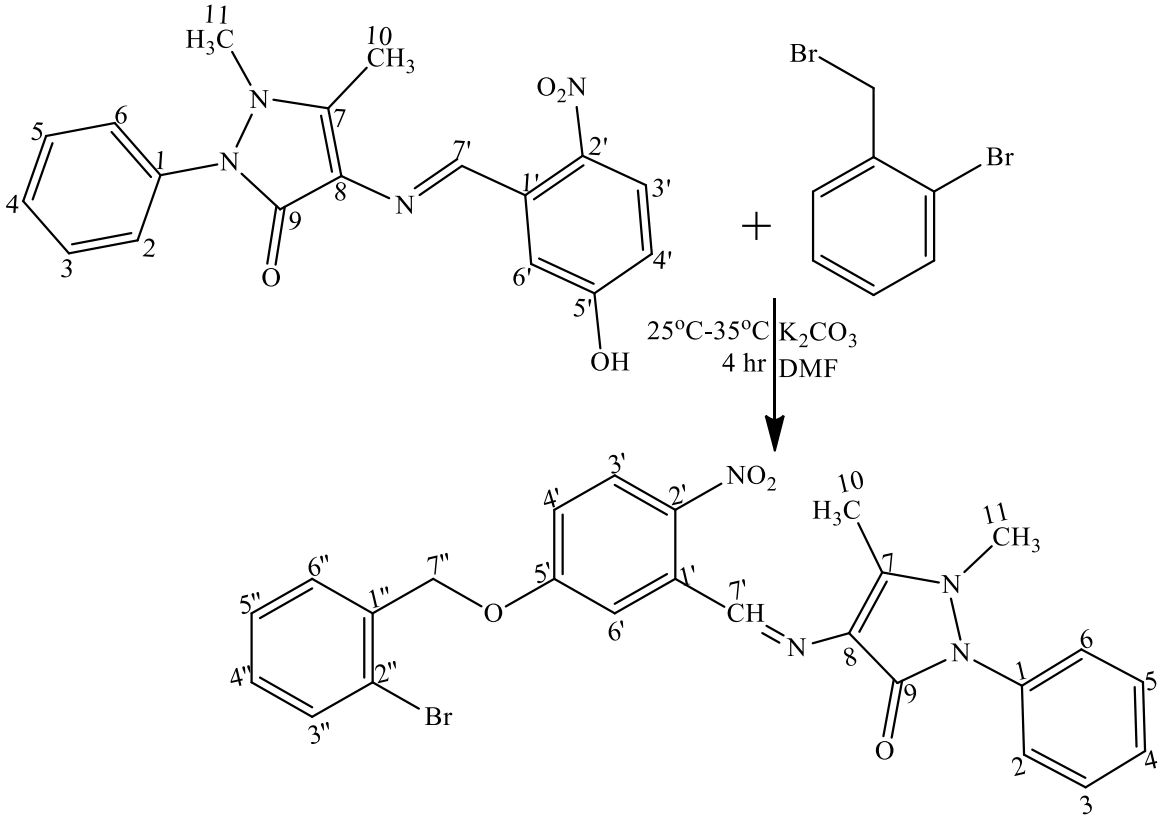

Scheme 3. 46: Synthetic Route of 10-6

3.3.47 Synthesis of 1,5-dimethyl-4-((2-nitro-5-((3-nitrobenzyl)oxy)benzylidene) amino)-2-phenyl-1,2-dihydro-3H-pyrazol-3-one (10-8)

The synthesis of compound 10-8 followed Scheme 4.47. A mixture of 0.0533 g (0.4 mmol) of anhydrous potassium carbonate, 0.0705 g (0.2 mmol) of 4-((3-hydroxy-4-nitrobenzylidene)amino)-1,5-dimethyl-2-phenyl-1,2-dihydro-3H-pyrazol-3-one (SB10) and DMF (5 mL) in a 100 mL round bottom flask was stirred at room temperature. After 1 hour of stirring, 3-nitrobenzylbromide (0.0431 mL, 0.2 mmol) was added and the reaction mixture was stirred further for 9 hours. The reaction progress was monitored by TLC system of n-hexane: ethyl acetate, 6:4 (R*f* value of 0.58). On completion of the reaction, the organic layer of the reaction mixture was extracted using ethyl acetate. Further extraction was done with saturated solution of lithium chloride. After evaporation of excess solvent, compound 1,5-dimethyl-4-((2-nitro-5-((3-nitrobenzyl)oxy)benzylidene)amino)-2-phenyl-1,2-dihydro-3H-pyrazol-3-one (10-8), (0.091 g) was obtained as orange solid.

3.3.48 Synthesis of 4-((5-((3-methoxybenzyl)oxy)-2-nitrobenzylidene)amino)-1,5-di methyl-2-phenyl-1,2-dihydro-3H-pyrazol-3-one (10-9)

The synthesis of compound 10-9 followed Scheme 4.48. A mixture of 0.0533 g (0.4 mmol) of anhydrous potassium carbonate, 0.0705 g (0.2 mmol) of 4-((3-hydroxy-4-nitrobenzylidene)amino)-1,5-dimethyl-2-phenyl-1,2-dihydro-3H-pyrazol-3-one (SB10) and DMF (5 mL) in a 100 mL round bottom flask was stirred at room temperature. After 1 hour of stirring, 3-methoxylbenzylbromide (0.028 mL, 0.2 mmol) was added and the reaction mixture was stirred further for 6 hours. The reaction progress was monitored by TLC system of n-hexane: ethyl acetate, 5:5 (R*f* value of 5.6). On completion of the reaction, the organic layer of the reaction mixture was extracted using ethyl acetate. Further extraction was done with saturated solution of lithium chloride. After evaporation of excess solvent, compound 4-((5-((3-methoxybenzyl)oxy)-2-nitrobenzylidene)amino)-1,5-dimethyl-2-phenyl-1,2- dihydro-3H-pyrazol-3-one (10-9) (0.076 g) was obtained as deep yellow solid.

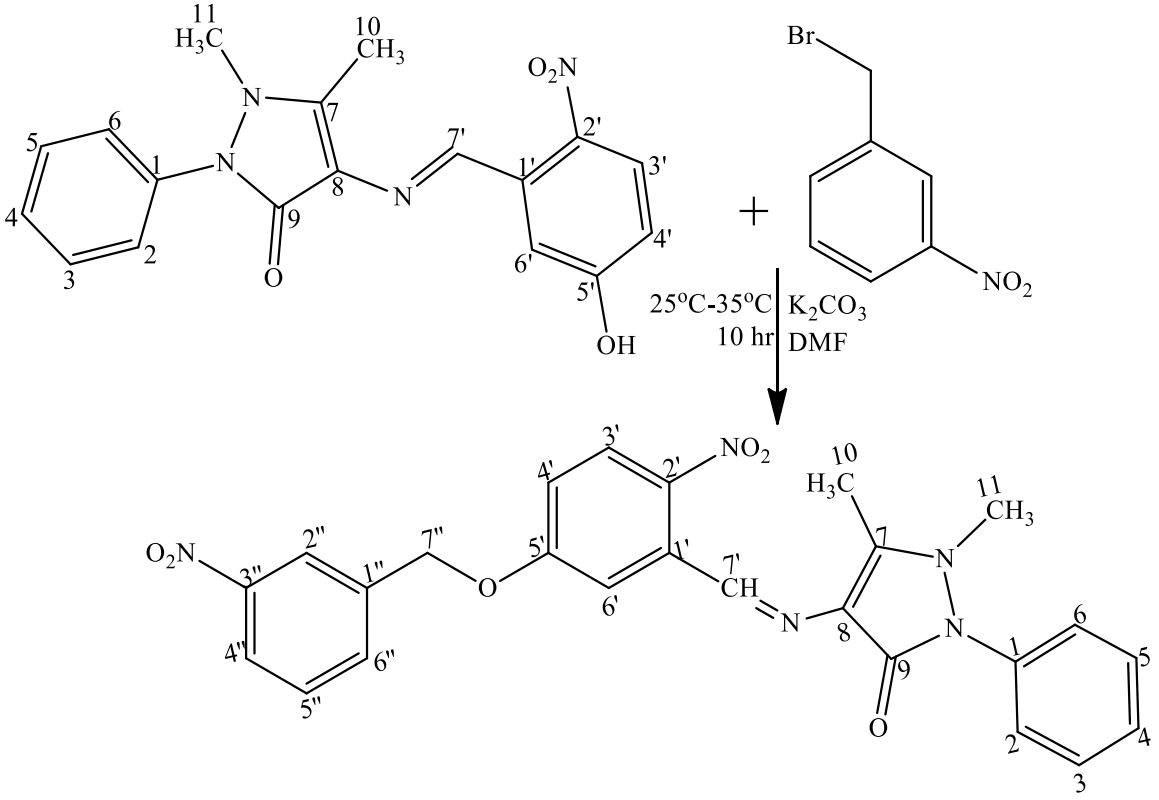

Scheme 3. 47: Synthetic Route of 10-8

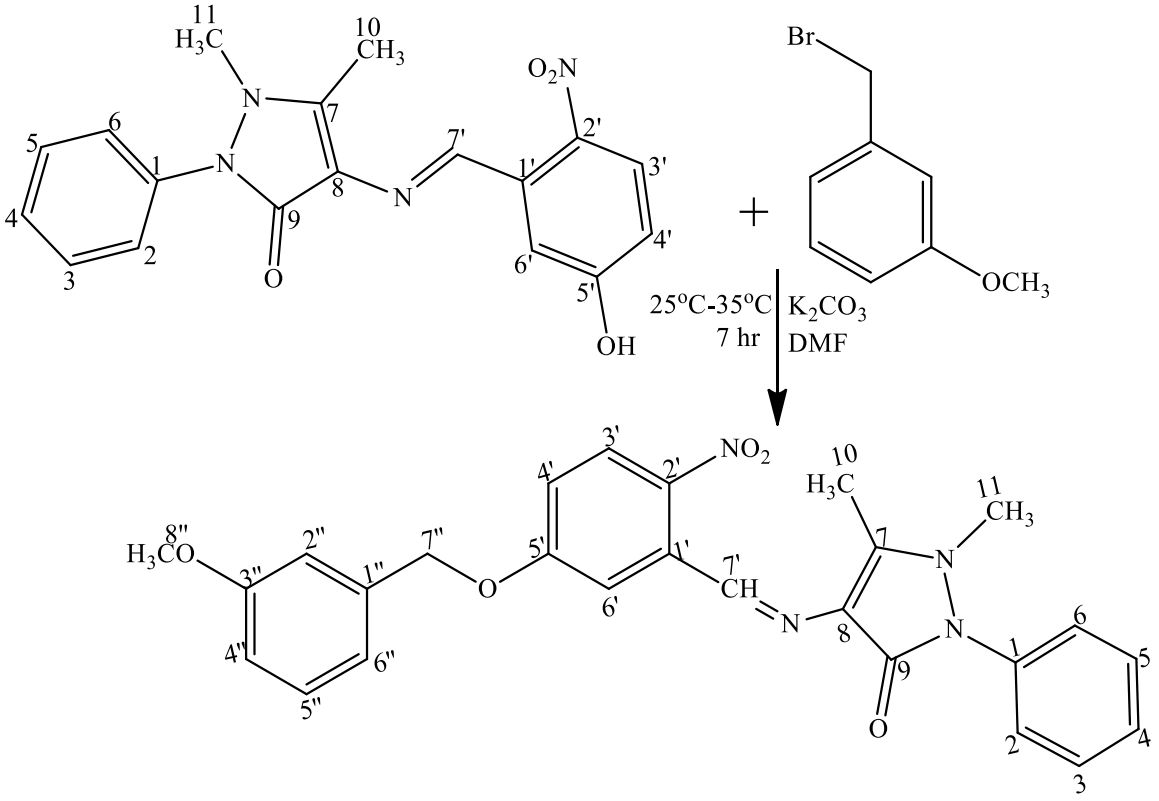

Scheme 3. 48: Synthetic Route of 10-9

3.3.49 Synthesis of 4-((3-methoxy-4-(prop-2-yn-1-yloxy)benzylidene)amino)-1,5-di methyl-2-phenyl-1,2-dihydro-3H-pyrazol-3-one (SB-A)

Compound SB-A was synthesised according to Scheme 3.49. In a 100 mL round bottom flask, a mixture of anhydrous potassium carbonate (0.0853g, 0.4 mmol), 4-((4-hydroxy-3-methoxybenzylidene)amino)-1,5-dimethyl-2-phenyl-1,2-dihydro-3H-pyraz-ol-3-one (SB5) (0.0675 g, 0.2 mmol) and DMF (5 mL) was stirred at room temperature. After 1 hour of stirring, propargyl bromide (0.015 mL, 0.2 mmol) was added and an additional six hours were spent stirring the mixture. The progress of the reaction was monitored by TLC system of n-hexane: ethyl acetate, 6:4 (R*f* value of 0.52). On completion of the reaction, the organic layer of the reaction mixture was extracted using ethyl acetate. Further extraction was done with saturated solution of lithium chloride. After evaporation of excess solvent, a pure solid of compound 4-((3-methoxy-4-(prop-2-yn-1-yloxy)benzylidene)amino)-1,5-dimethyl-2-phen yl-1,2-dihydro-3H-pyrazol-3-one (SB-A) (0.061 g) was obtained.

3.3.50 Synthesis of 4-((3-methoxy-2-(prop-2-yn-1-yloxy)benzylidene)amino)-1,5-dimethyl-2-phenyl-1,2-dihydro-3H-pyrazol-3-one (SB-B)

Compound SB-B was synthesised according to Scheme 3.50. In a 100 mL round bottom flask, a mixture of anhydrous potassium carbonate (0.0636g, 0.46 mmol), 4-((2-hydroxy-3-methoxybenzylidene)amino)-1,5-dimethyl-2-phenyl-1,2-dihydro-3H-pyrazol-3-one (SB5A) (0.0776 g, 0.23 mmol) and DMF (5 mL) was stirred at room temperature. After 1 hour of stirring, propargyl bromide (0.018 mL, 0.23 mmol) was added and an additional six hours were spent stirring the mixture. The progress of the reaction was monitored by TLC system of n-hexane: ethyl acetate, 6:4 *(Rf* value of 0.48). On completion of the reaction, the organic layer of the reaction mixture was extracted using ethyl acetate. Further extraction was done with saturated solution of lithium chloride. After evaporation of excess solvent, a cream solid compound 4-((3-methoxy-2-(prop-2-yn-1-yloxy)benzylidene)amino)-1,5- dimethyl-2-phenyl-1,2-dihydro-3H-pyrazol-3-one (SB-B) (0.0799 g) was obtained.

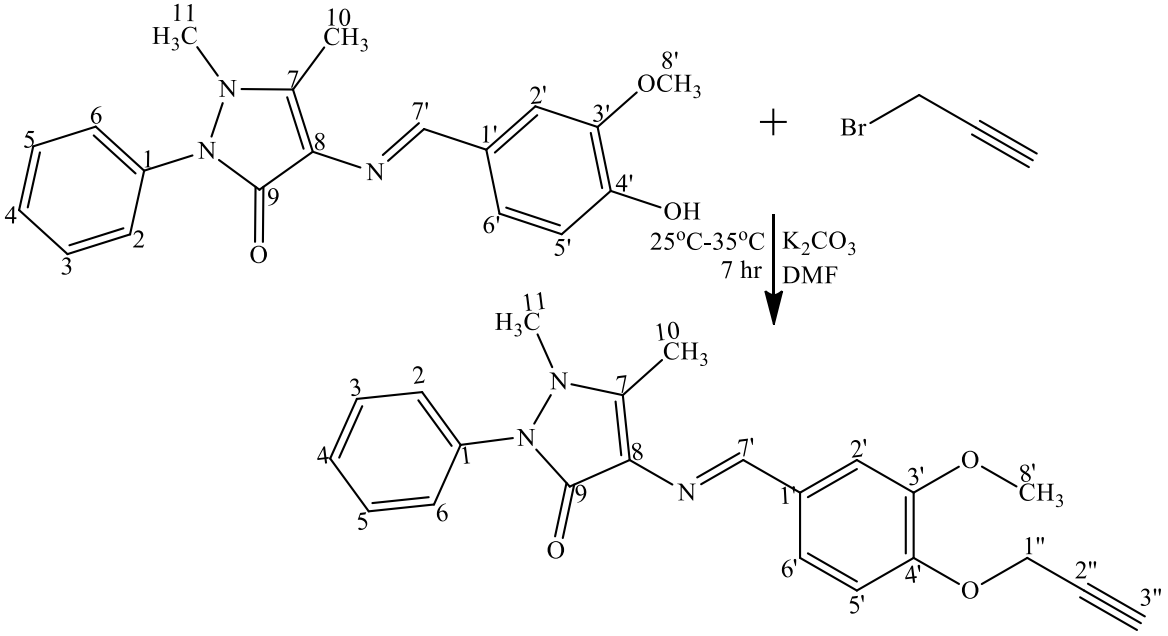

Scheme 3. 49: Synthetic Route of SB-A

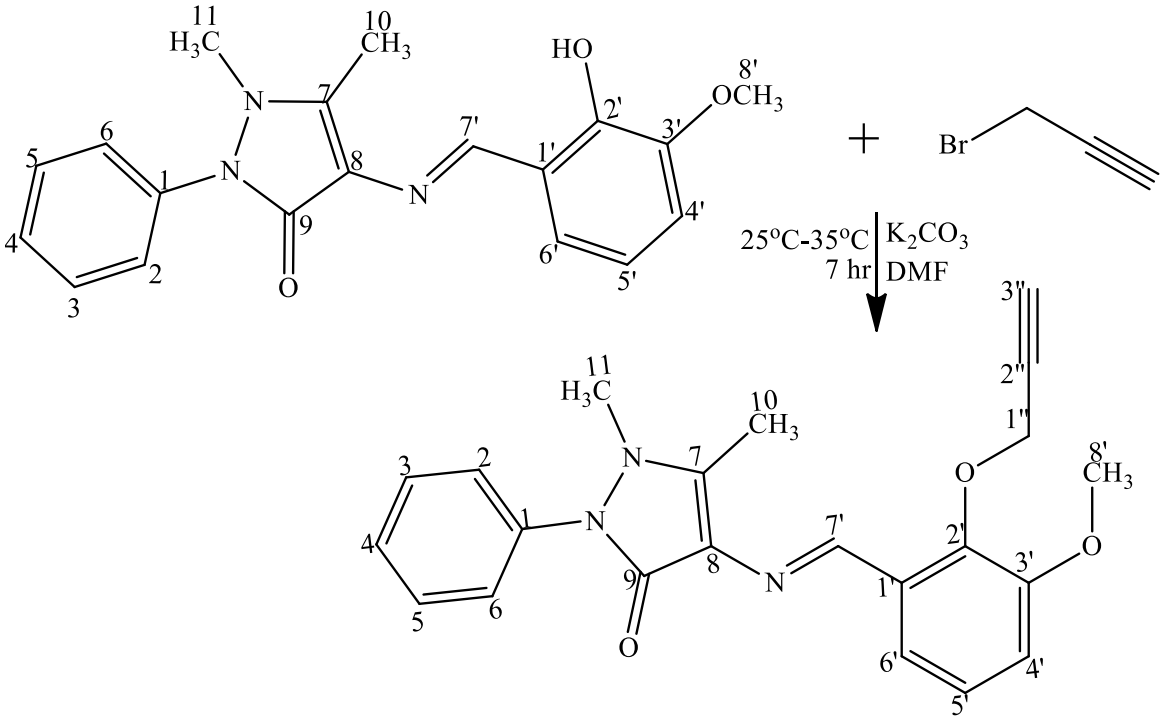

Scheme 3. 50: Synthetic Route of SB-B

3.3.51 Synthesis of 4-((4-methoxy-3-(prop-2-yn-1-yloxy)benzylidene)amino)-1,5-dimethyl-2-phenyl-1,2-dihydro-3H-pyrazol-3-one (SB-C)

Compound SB-C was synthesised according to Scheme 3.51. In a 100 mL round bottom flask, a mixture of anhydrous potassium carbonate (0.0636g, 0.46 mmol), 4-((3-hydroxy-4-methoxybenzylidene)amino)-1,5-dimethyl-2-phenyl-1,2-dihydro-3H-pyrazol-3-one (SB5B) (0.0776 g, 0.23 mmol) and DMF (5 mL) was stirred at room temperature. After 1 hour of stirring, propargyl bromide (0.018 mL, 0.2 mmol) was added and an additional seven hours were spent stirring the mixture. The progress of the reaction was monitored by a TLC system of n-hexane: ethyl acetate, 6:4. On completion of the reaction, the organic layer of the reaction mixture was extracted using ethyl acetate. Further extraction was done with saturated solution of lithium chloride. After evaporation of excess solvent, a pure brownish yellow solid of compound 4-((4-methoxy-3-(prop-2-yn-1-yloxy)benzylidene) amino)-1,5-dimethyl-2-phenyl-1,2-dihydro-3H-pyrazol-3-one (SB-C) (0.0700g) was obtained.

3.3.52 Synthesis of 1,5-dimethyl-2-phenyl-4-((3-(prop-2-yn1-yloxy)benzylidene) amino)-1,2-dihydro-3H-pyrazol-3-one (SB-D)

Compound SB-D was synthesised according to Scheme 3.52. In a 100 mL round bottom flask, a mixture of anhydrous potassium carbonate (0.0691 g, 0.5 mmol), 4-(3-hydroxybenzylideneamino)-1,2-dihydro-2,3-dimethyl-1-phenyl pyrazol-5-one (SB9) (0.0778 g, 0.25 mmol) and DMF (5 mL) was stirred at room temperature. After 1 hour of stirring, propargyl bromide (0.0189 mL, 0.25 mmol) was added and an additional nine hours were spent stirring the mixture. The progress of the reaction was monitored by a TLC system of n-hexane: ethyl acetate, 6:4 (R*f* value of 0.55). On completion of the reaction, the organic layer of the reaction mixture was extracted using ethyl acetate. Further extraction was done with saturated solution of lithium chloride. After evaporation of excess solvent, a pure, pale yellow solid of compound 1,5-dimethyl-2-phenyl-4-((3-(prop-2-yn-1-yloxy)benzylidene)amino)-1,2-dihydro-3H-pyrazol-3-one (SB-D) (0.0720g) was obtained.

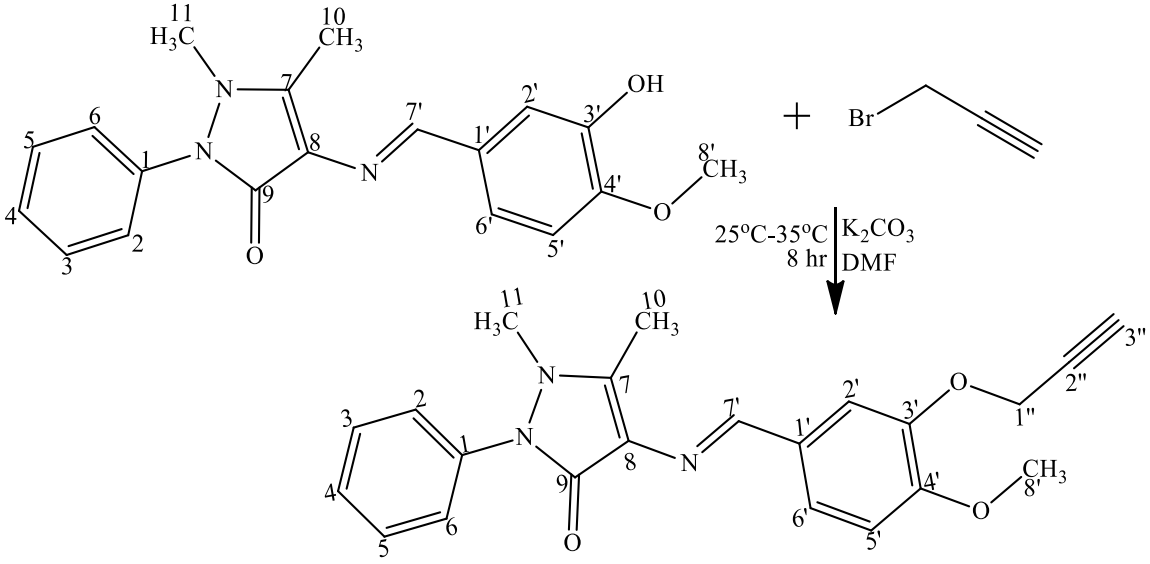

Scheme 3. 51: Synthetic Route of SB-C

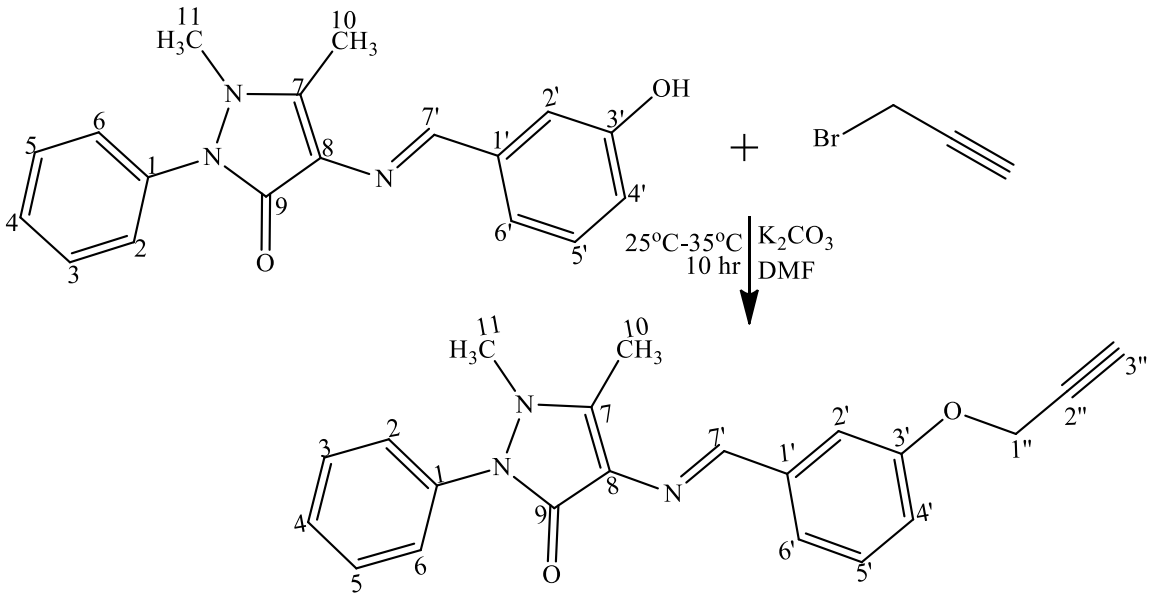

Scheme 3. 52: Synthetic Route of SB-D

3.3.53 Synthesis of 1,5-dimethyl-2-phenyl-4-((4-(prop-2-yn-1-yloxy)benzylidene) amino)-1,2-dihydro-3H-pyrazol-3-one (SB-E)

Compound SB-E was synthesised according to Scheme 3.53. In a 100 mL round bottom flask, a mixture of anhydrous potassium carbonate (0.0691g, 0.5 mmol), 4-(4-hydroxybenzylideneamino)-1,2-dihydro-2,3-dimethyl-1-phenylpyrazol-5-one (SB9B) (0.0768 g, 0.25 mmol) and DMF (5 mL) was stirred at room temperature. After 1 hour of stirring, propargyl bromide (0.0189 mL, 0.25 mmol) was added an additional twelve hours were spent stirring the mixture. The reaction progression was monitored by a TLC system of n-hexane: ethyl acetate, 6:4 (R*f* value of 0.48). On completion of the reaction, the organic layer of the reaction mixture was extracted using ethyl acetate. Further extraction was done with saturated solution of lithium chloride. After evaporation of excess solvent, a pure, pale yellow solid of compound 1,5-dimethyl-2-phenyl-4-((4-(prop-2-yn-1-yloxy)benzylidene)amino)-1,2-dihydro-3H-pyrazol-3-one (SB-E) (0.059 g) was obtained.

3.3.54 Synthesis of 4-((3-bromo-5-chloro-2-(prop-2-yn-1-yloxy)benzylidene)amino)-1,5-dimethyl-2-phenyl-1,2-dihydro-3H-pyrazol-3-one (SB-F)

Compound SB-F was synthesised according to Scheme 3.54. In a 100 mL round bottom flask, a mixture of anhydrous potassium carbonate (0.0691g, 0.5 mmol), 4-((3-bromo-5-chloro-2-hydroxybenzylidene)amino)-1,5-dimethyl-2-phenyl-1,2-dihydro-3H-pyrazol-3-one (0.0768 g, 0.25 mmol) and DMF (5 mL) was stirred at room temperature. After 1 hour of stirring, propargyl bromide (0.0189 mL, 0.2 mmol) was added and an additional five hours were spent stirring the mixture. The reaction development was monitored by a TLC system of n-hexane: ethyl acetate, 6:4 (R*f* value of 0.58). On completion of the reaction, the organic layer of the reaction mixture was extracted using ethyl acetate. Further extraction was done with saturated solution of lithium chloride. After evaporation of excess solvent, a pure, yellow solid of compound 4-((3-bromo-5-chloro-2-(prop-2-yn-1-yloxy)benzylidene)amino)-1,5-dimethyl-2-phenyl-1,2-dihydro-3H-pyrazol-3-one (SB-F) was obtained.

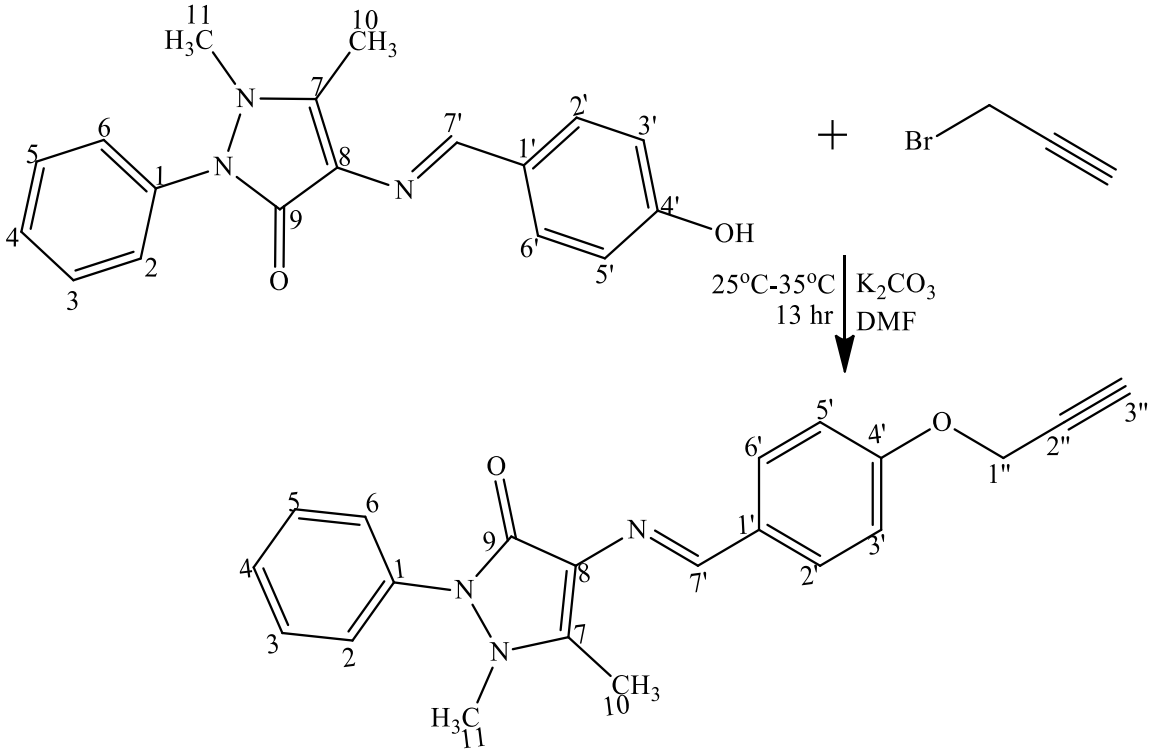

Scheme 3. 53: Synthetic Route of SB-E

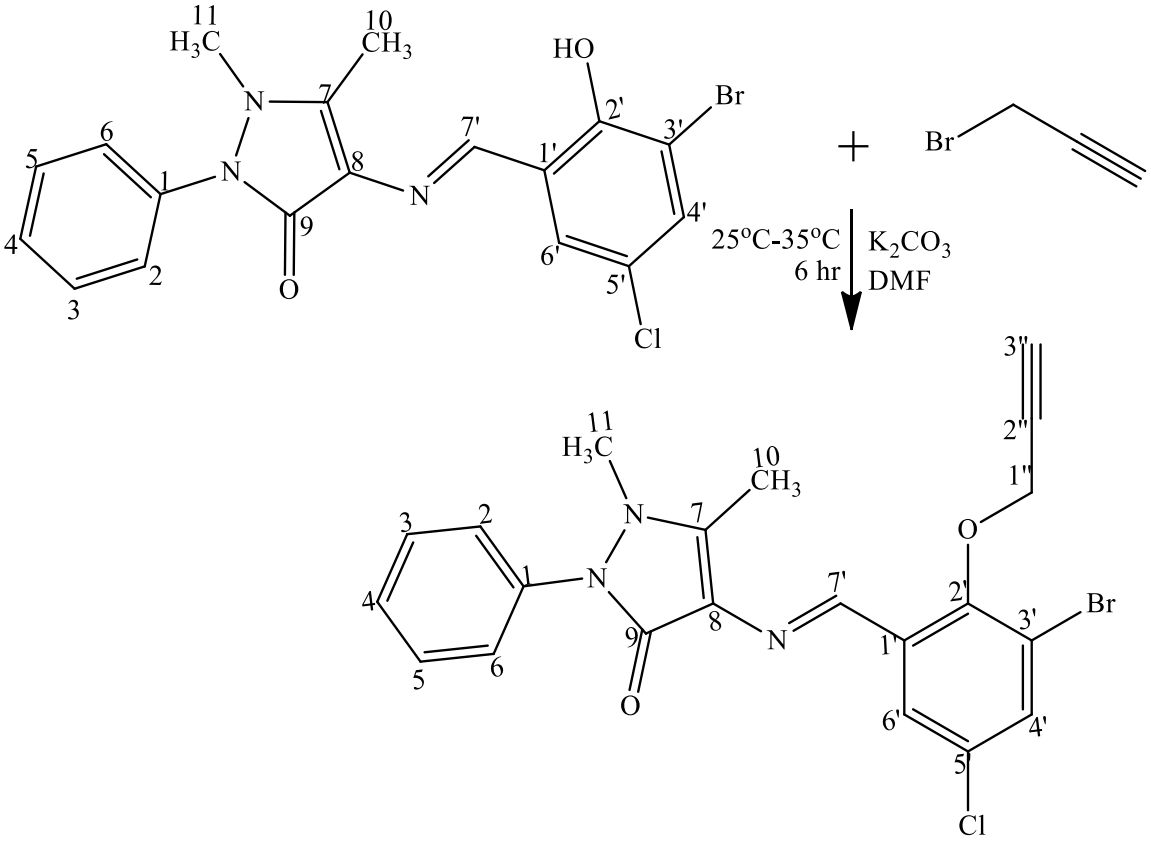

Scheme 3. 54: Synthetic Route of SB-F

3.3.55 Synthesis of 1,5-dimethyl-4-((2-nitro-5-(prop-2-yn-1-yloxy)benzylidene)amino) -2-phenyl-1,2-dihydro-3H-pyrazol-3-one (SB-G)

Compound SB-G was synthesised according to Scheme 3.55. 0.0553 g (0.4 mmol) of anhydrous potassium carbonate and 0.0705 g (0.2 mmol) of 4-((5-hydroxy-2-nitrobenzyli dene)amino)-1,5-dimethyl-2-phenyl-1,2-dihydro-3H-pyrazol-3-one (SB10) were dissolved in DMF (5 mL) in a 100 mL round bottom flask and stirred at room temperature. After 1 hour of stirring, propargyl bromide (0.0152 mL, 0.2 mmol) was added and an additional three hours were spent stirring the mixture. The reaction development was monitored by a TLC system of n-hexane: ethyl acetate, 6:4 (R*f* value of 0.48). On completion of the reaction, the organic layer of the reaction mixture was extracted using ethyl acetate. Further extraction was done with saturated solution of lithium chloride. After evaporation of excess solvent, a pure, yellow solid of compound 1,5-dimethyl-4-((2-nitro-5-(prop-2-yn-1-yloxy)benzylidene)amino)-2-phenyl-1,2-dihydro-3H-pyrazol-3-one (SB-G) (0.071 g) was obtained.

3.3.56 Synthesis of 4-((3,4-bis(prop-2-yn-1-yloxy)benzylidene)amino)-1,5-dimethyl-2-phenyl-1,2-dihydro-3H-pyrazol-3-one (SB-H)

Compound SB-H was synthesised according to Scheme 3.56. In a 100 mL round bottom flask, a mixture of anhydrous potassium carbonate (0.0691g, 0.5 mmol), 4-((3,4-dihydroxy benzylidene)amino)-1,5-dimethyl-2-phenyl-1,2-dihydro-3H-pyrazol-3-one (SB11) (0.0808 g, 0.25 mmol) and DMF (5 mL) was stirred at room temperature. After 1 hour of stirring, propargyl bromide (0.0189 mL, 0.25 mmol) was added and an additional eight hours were spent stirring the mixture. The development of the reaction was monitored by a TLC system of n-hexane: ethyl acetate, 6:4 (R*f* value of 0.52). On completion of the reaction, the organic layer of the reaction mixture was extracted using ethyl acetate. Further extraction was done with saturated solution of lithium chloride. After evaporation of excess solvent, a pure brown solid of compound of 4-((3,4-bis(prop-2-yn-1-yloxy)benzylidene)amino)-1,5-dimethyl-2-phenyl-1,2-dihydro-3H-pyrazol-3-one (0.0920 g) was obtained.

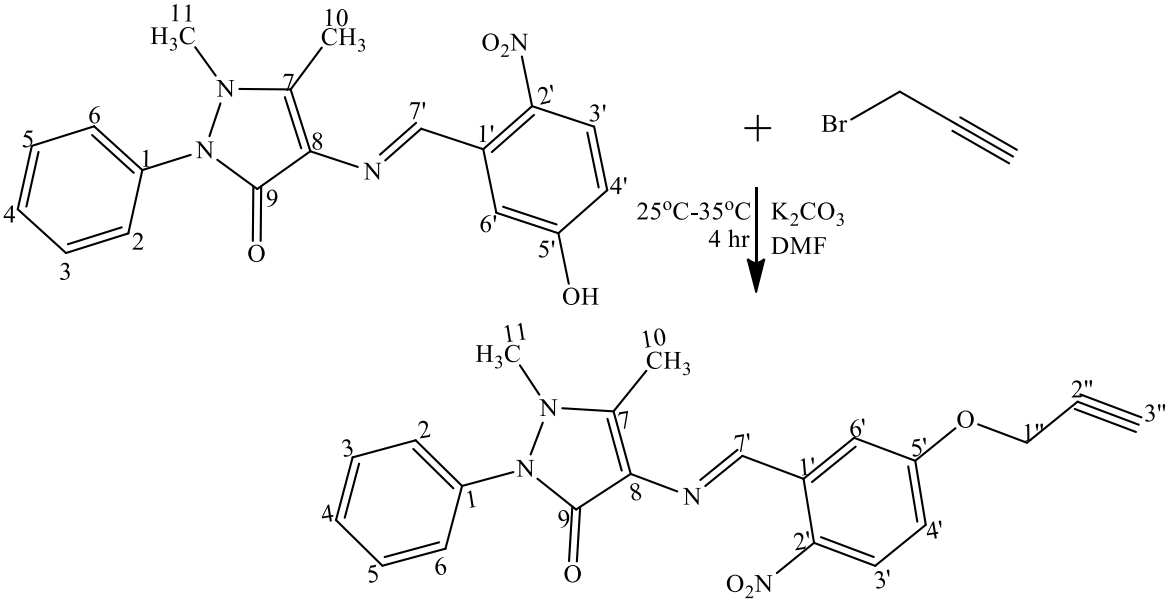

Scheme 3. 55: Synthetic Route of SB-G

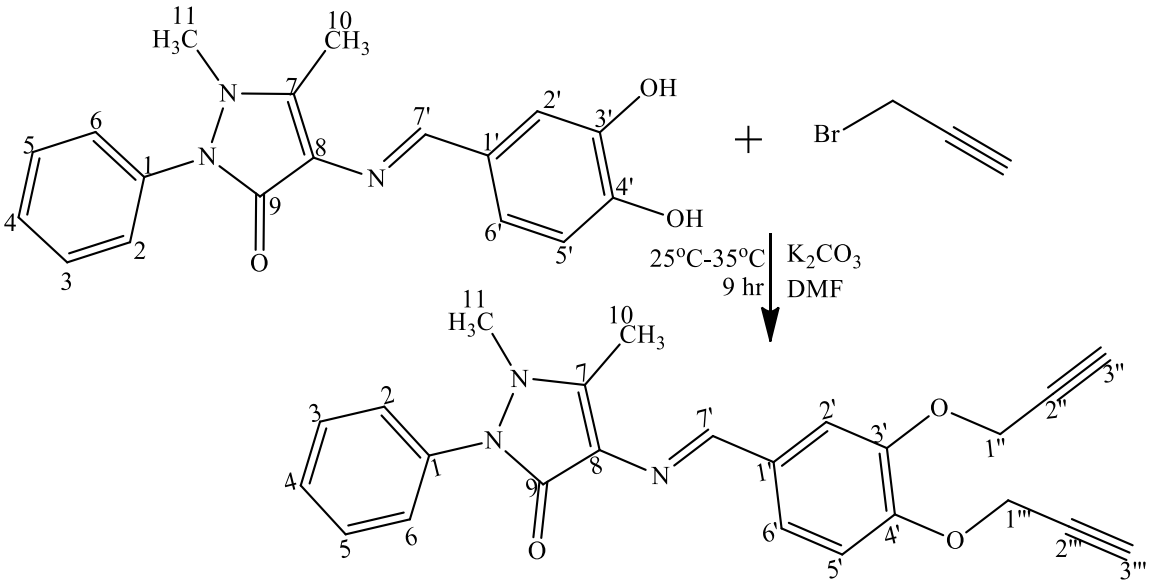

Scheme 3. 56: Synthetic Route of SB-H

3.3.57 Synthesis of 4-((2,4-bis(prop-2-yn-1-yloxy)benzylidene)amino)-1,5-dimethyl-2-phenyl-1,2-dihydro-3H-pyrazol-3-one (SB-I)

Compound SB-I was synthesised according to Scheme 3.57. 0.0691 g (0.5 mmol) of anhydrous potassium carbonate and 0.0808 g (0.25 mmol) of 4-((2,4-dihydroxybenzylidene)amino)-1,5-dimethyl-2-phenyl-1,2-dihydro-3H-pyrazol-3-one (SB11A) were dissolved in DMF (5 mL) in a 100 mL round bottom flask and stirred at room temperature. After 1 hour of stirring, propargyl bromide (0.0189 mL, 0.25 mmol) was added and an additional five hours were spent stirring the mixture. The reaction development was monitored by a TLC system of n-hexane: ethyl acetate, 6:4 (R*f value* of 0.46). On completion of the reaction, the organic layer of the reaction mixture was extracted using ethyl acetate. Further extraction was done with saturated solution of lithium chloride. After evaporation of excess solvent, a pure, yellow solid of compound 4-((2,4-bis(prop-2-yn-1-yloxy)benzylidene)amino)-1,5-dimethyl-2-phenyl-1,2-dihydro-3H-pyrazol-3-one (SB-I) (0.075g) was obtained.

3.2.58 Synthesis of 4-((3,5-dimethoxy-4-(prop-2-yn-1-yloxy)benzylidene)amino)-1,5-dimethyl-2-phenyl-1,2-dihydro-3H-pyrazol-3-one (SB-J)

Compound SB-J was synthesised according to Scheme 3.58. 0.0553 g (0.4 mmol) of anhydrous potassium carbonate and 0.0735 g (0.2 mmol) of 4-((4-hydroxy-3,5-dimethoxy benzylidene)amino)-1,5-dimethyl-2-phenyl-1,2-dihydro-3H-pyrazol-3-one (SB19) were dissolved in DMF (5 mL) in a 100 mL round bottom flask and stirred at room temperature. After 1 hour of stirring, propargyl bromide (0.015 mL, 0.2 mmol) was added and an additional four hours were spent stirring the mixture. The progress of the reaction was monitored by a TLC system of n-hexane: ethyl acetate, (5:5 R*f* value of .0.55). On completion of the reaction, the organic layer of the reaction mixture was extracted using ethyl acetate. Further extraction was done with saturated solution of lithium chloride. After evaporation of excess solvent, a pure, brown solid of compound 4-((3,5-dimethoxy-4-(prop-2-yn-1-yloxy)benzylidene)amino)-1,5-dimethyl-2-phenyl-1,2-dihydro-3H-pyrazol-3-one (SB-J) (0.0750g) was obtained.

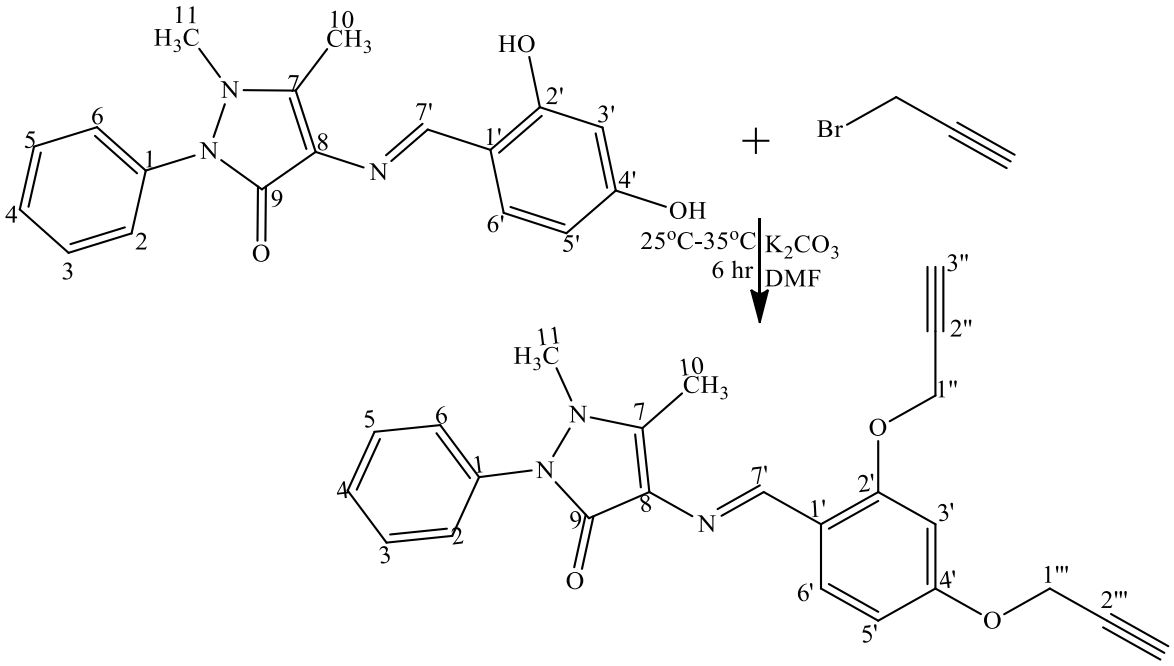

Scheme 3. 57: Synthetic Route of SB-I

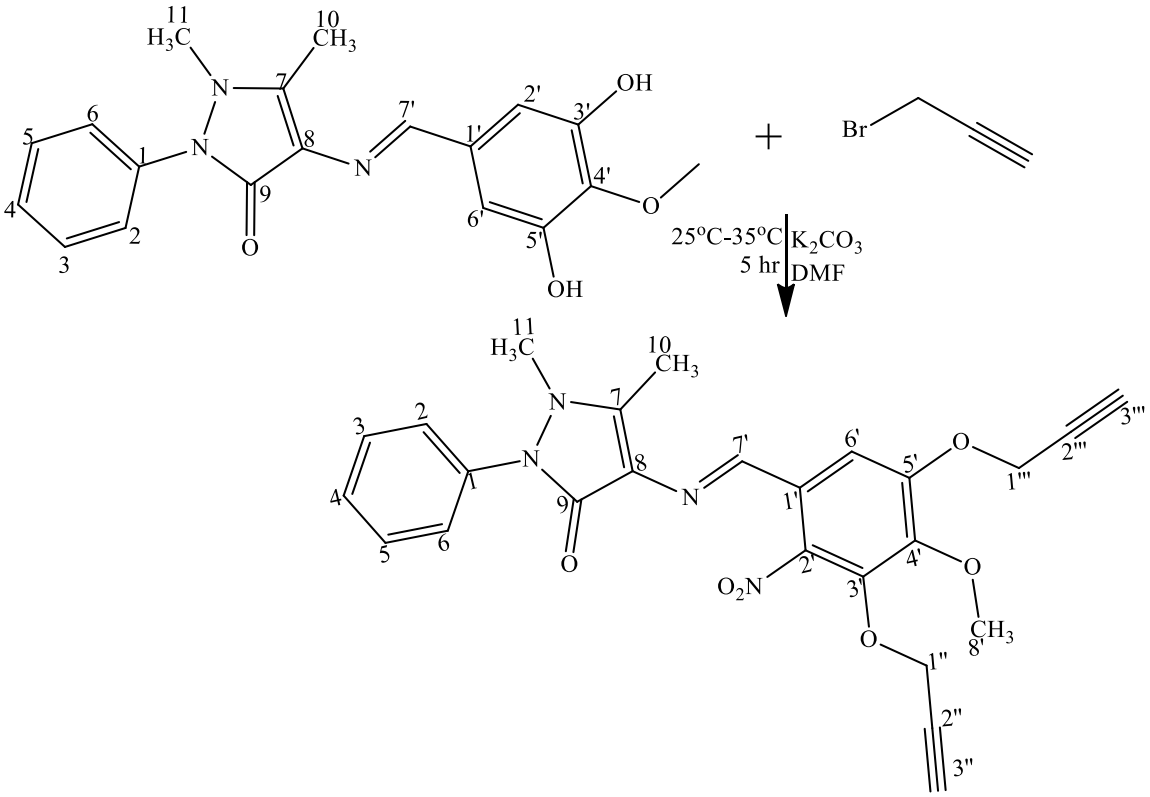

Scheme 3. 58: Synthetic Route of SB-J

3.4 Biological Evaluation

3.4.1 Determination of Cytotoxicity Using Brine Shrimp Lethality Assay

Brine shrimp lethality test is a preliminary screening technique for determining the cytotoxicity of synthesised compounds. This test was conducted as described in the literature (Banti and Hadjikakou, 2021; Suryawanshi *et al.*, 2020). Brine shrimp eggs weighing 50 mg were sprinkled into the hatching tray which was half-filled with brine solution. This was incubated at 37 ºC and the eggs hatched into larvae within two days. The test sample containing 20 mg of the compounds in 2 ml of the solvent (DMSO). A concentration of 10, 100 and 1000 µg/ml were obtained using 5, 50 and 500 µl of the test sample. After 48 hours of hatching and developing into nauplii, 10 larvae were placed per vials and 5 ml seawater was added. Each vial was placed in the incubator under illumination at 25-27º C for twenty-four hours. The reference drug, etoposide served as the positive control and the solvent served as negative control. Finney computer program was used for the analysis of the data to determine the percentage mortality with 95% confidence intervals.

3.4.2 Determination of Cytotoxicity using MTT Colorimetric Assay

Cytotoxicity was carried out using MTT (3-[4,5-dimethylthiazole-2-yl]-2,5-diphenyl-tetrazoliumbromide) colorimetric test as recorded by Karatas *et al.,* 2019. The Dulbecco's Modified Eagle Medium was used to cultivate the 3T3 (mouse fibroblast) cells. The cells in a 75 cm^2 flasks were supplemented by adding 5% of fetal bovine serum, 100 µg/ml of streptomycin and 100 IU/ml of penicillin. The flask was placed in 5% carbon(iv)oxide incubator at 37ºC. The cells exhibiting exponential growth were collected and counted using a hemocytometer. They were diluted with the same solvent. A concentration of $5x10^4$ cells per ml cell culture was prepared and was added to each well of 96-well plates (100 µL/well). After an overnight incubation, the solvent was eliminated, and new solvent (200 µL) was introduced containing the compounds in varying amounts (ranging from 1 to 30 µM). Two days after, each well plate received 200 µL of MTT (0.5 mg/ml) and 100 µL of DMSO. The plates are then placed in the incubator for 4 hrs. To determine how much MTT was converted to formazan inside of the cells, the absorbance at 540 nm was measured using a microplate reader. The cytotoxicity was obtained by calculating the percent inhibition using the formula:

$$\% \text{ inhibition} = \frac{100-((\text{mean of O.D of test sample} - \text{mean of O.D of negative control})}{(\text{mean of O.D of positive control} - \text{mean of O.D of negative control})} X\ 100 \qquad (3.1)$$

Where O.D of sample test compound is the absorbance of test sample

O.D of negative control is absorbance of negative control

O.D of positive control is absorbance of positive control

The results were analysed using Soft- Max Pro software.

3.4.3 Determination of Anti-Inflammatory Activities using Oxidative Burst Assay

As stated by Leah *et al.*, 2020, a luminol-enhanced chemiluminescence assay was conducted. 25 µL of 1, 10 and 100 µg/mL concentrations of compounds, in triplicate were incubated with 25 µL of diluted whole blood HBSS++ (Hanks balanced salt solution, comprising calcium chloride and magnesium chloride). $HBSS^{++}$ was used as the control without adding compounds. The test was conducted using white 96-well half-area plates, which were incubated using the thermostat chamber of the luminometer at 37 ºC for about 15 minutes. On completion of incubation, 25 µL of luminol an intracellular ROS detection probe with 25 µL of serum opsonised zymosan were introduced to each well apart from blank wells, which contained HBSS++ only. The ROS level was measured using a luminometer and expressed in relative light units. Ibuprofen served as the assay's control.

3.4.4 Determination of Antioxidant Activity using DPPH Radical Scavenging Assay

The antioxidant activity of the compounds was investigated using DPPH radical scavenging assay as reported by Sethi *et al.*, 2020. A free radical, 2,2-Diphenyl-1-picrylhydrazyl (DPPH), can be used to assess a compound's capacity to operate as a free radical scavenger or hydrogen donor. The DPPH free radical's odd electron produces a significant absorption maximum with a purple color at 517 nm. As the reduced DPPH-H is formed by pairing the odd electron of the DPPH radical with hydrogen from an antioxidant that scavenges free radicals, the color changes from purple to pale yellow, reducing the molar absorptivity of the DPPH radical at 515 nm. Regarding the quantity of electrons absorbed, the subsequent decolorisation is stoichiometric. 100% DMSO was used to dissolve the test samples. 95 µL of DPPH and 5 µL of sample were added to the 96-well plate after prereading at 515 nm. The 96-well plates were then covered with parafilm and incubated for 30 minutes at 37° C to prevent solvent evaporation. The ultimate absorbance was noted at 515 nm using a microplate reader at 515 nm. Control comprises of only 100% DMSO. The standard was

N-acetyl cysteine and gallic acid. Using the equation below, the percentage radical scavenging activity was determined.

$$\% \text{ Radical Scavenging Activity} = 100 - \frac{\text{O.D of sample}}{\text{O.D of control}} X\ 100 \quad (3.2)$$

Where O.D of sample is absorbance of test sample
O.D of control is absorbance of negative control.

3.4.5 Determination of Antiglycation Activity using Human Serum Albumin Solution

The inhibition of advanced glycation end products was determined according to the report of Starowicz and Zielinski (2019). 200 μL reaction mixture containing the test compound at a concentration of 1 mM (20 μL) dissolved in DMSO, Human Serum Albumin solution at a concentration of 10 mg/mL, 14 mM methylglyoxal (50 L), and a buffer of pH 7.4 which contain phosphate100 mM (80 L with 3 mM sodium azide as an antibacterial inhibitor) was prepared. The reaction mixture in triplicates in 96-well plates was incubated at 37°C for nine days. After incubation, the varioskan LUX multimode microplate reader from Thermo Scientific was used to check each sample for the emergence of a particular fluorescence (excitation 330 nm: emission 420 nm). The following formula was used to determine the percentage of inhibition of AGE production by the test sample compared to the control.

$$\% \text{ Inhibition} = 1 - \frac{\textbf{Fluorescence of test sample}}{\textbf{Fluorescence of the control group}}\ x\ 100 \quad (3.3)$$

The compounds that exhibited 50% or above percent inhibition were processed for IC_{50} calculations by using various concentrations of test compounds (ranges from 50-1000 µM). To assess the potency of each test compound, it was compared to rutin, the reference inhibitor. (IC_{50} of Rutin = 280.50±1.50µM).

3.5 Theoretical Methods

3.5.1 Optimization and Density Functional Theory Calculations

Quantum chemical calculations were done via DFT method using Spartan ’14 wavefunction Inc. 2D structures of these compounds were obtained by using Chem Draw Professional 15.0 version and were minimised to obtain good structures that are suitable for the optimisation process. Optimisation was done using DFT with the standard 6-31+G* (d)

basis set and B3LYP functional (Becke's gradient, exchange correlation (Becke, 1993), and the Lee, Yang, Parr correlation functional (Yang *et al.*, 2005). The Global reactivity descriptors that describe the bioactivities of these compounds were calculated based on EHOMO and ELUMO as reported by Koopmans' theorem (Geerlings *et al.*, 2003) using the equations 3.4-3.7. The global reactivity descriptors include global hardness (η), global softness (σ), electronegativity (χ), and global electrophilicity (ω)

Global hardness: $\eta = \frac{E_{LUMO} - E_{HOMO}}{2}$ (3.4)

Chemical softness $\sigma = \frac{1}{\eta}$ (3.5)

Electronegativity (χ) (Zhou and Navangul, 1990): $\chi = -\frac{E_{LUMO} + E_{HOMO}}{2}$ (3.6)

The electrophilicity index (Parr *et al.*,1999) $(\omega) = \frac{\mu^2}{2\eta}$ (3.7)

3.5.2 QSAR Studies

To develop a QSAR model, diverse data set and the prominent number of descriptors are needed. The DFT optimisation produced a few molecular descriptors, and a suitable set of descriptors was chosen for the investigation. Multiple linear regression method (MLR) was used to build QSAR model for biological investigation of the synthesised molecules. The linear equation that shows the relationship between a dependent and independent variable is obtained by MLR method. Least squares curve fitting method was used to estimate the regression coefficients. To obtain accurate and reliable model, the descriptors used should not be more than 1/5th the number of molecules in the training set. The selected descriptors served as the independent variable and the experimental IC_{50} obtained from antioxidant, anti-inflammatory and antiglycation analysis were used as the dependent variables. The following linear equation was used to guide the construction of the models (Puzyn *et al.*, 2010).

Predicted $IC_{50} = \alpha + \beta_1 X_1 + \beta_2 X_2 + ... + \beta_n X_n$ (3.8)

Where α and β = regression coefficients, X_1, X_2.... X_n = structural parameter of the molecules.

The cross validation (R^2) and adjusted squared correlation coefficient (Ra^2) values were used to validate the QSAR models obtained. Cross validation shows the reliability and appropriateness of a QSAR model for a given set of data. They are used to govern the predictive nature of the model and were calculated using equations (3.9) and (3.10).

$$CV.R^2 = 1 - \frac{\sum(Yobs-Ycal)^2}{\sum(Yobs-\bar{Y}obs^2)} \quad (3.9)$$

Where $Yobs$ = experimentall IC_{50}, $Ycal$ = predicted IC_{50} and $\bar{Y}obs$ = average of the experimental IC_{50}

$$R_a^2 = \frac{(N-1)\times R^2-P}{N-1-P} \quad (3.10)$$

Where N is the number of compounds observed, P is the number of molecular descriptors employed. and R^2 is the Squared coefficient correlation value obtained from the QSAR model.

3.5.3 Molecular Docking Study

The Molecular docking was done to examine the potential binding mode of the studied compounds with some antioxidant, anti-inflammatory, and antiglycation protein targets to complement the experimental results. The compounds which were synthesised and screened for biological activities were utilised as ligands. The 2D structures of the ligands were drawn with the help of Chem Professional 15.0 and saved as Structure Data File (SDF). The protein target used for antioxidant are heme-oxygenase (HO-1) (PDB ID: 1N3U) and glutathione peroxidase (PDB ID: 3KIJ). For the anti-inflammation activity, cyclooxygenase-1 (COX-1) and cyclooxygenase-2 (COX-2) proteins with PDB ID 2QGE and 1OQ5 were used, respectively. Alpha-amylase (PDB ID: 4GQR) and Receptor for Advanced Glycation End products (RAGE) (PDB ID: 4LP5) are the protein targets for anti-glycation studies.

3D Structures of these molecules were obtained from protein databank (www.rcsb.org). The possible binding sites/ active site of receptors were searched using Computed Atlas of Surface Topography of Proteins (CASTp) and UniProtKB. The proteins were prepared using Chimera 1.14. The water molecules, multiple ligands, non-protein parts, and other foreign compounds downloaded together with the proteins were removed. The ligands

saved as SDF files and treated proteins were converted to PDBQT format using Autodock 4.2. from PyRX. Grid space was set around the amino acid residues in the active site of the proteins. The Grid box size and grid center dimensions for the proteins were set and values recorded in Table 3.1. Using Autodock Vina from the PyRX workspace (Trott and Olson, 2010), the prepared ligands were docked into the active site of the proteins and the binding affinities were obtained. Finally, UCSF Chimera 1.14 was used to create 3D images of the complexes generated between proteins and ligands, while Discovery Studio 2020 was used to create 2D representations of the molecular interactions.

3.5.4 ADMET Screening

In silico predictive models were used to evaluate the ADMET properties of the test compounds. The absorption, distribution, metabolism, and excretion (ADME) characteristics of the test substances were ascertained using the Swiss ADME web server (Daina *et al.,* 2017). The LD_{50}, toxicity class, cytotoxicity, hepatotoxicity, mutagenicity, carcinogenicity, and immunotoxicity of the compounds were predicted using ProTox-II online server. Swiss ADME and ProTox-II online servers utilises a huge database to accurately forecast the physicochemical properties, pharmacokinetics, solubility, lipophilicity, drug-likeness, bioavailability score, therapeutic qualities, and toxicity of substances.

Using the rule-based filters developed by Lipinski, Ghose, Verber, Egan, and Muegge, the compounds' drug-likeness characteristic was assessed (Lipinski *et al.,* 2001 and Veber *et al.,* 2002)**.** The lipophilicity also known as the partition coefficient between n-octanol and water was assessed using WLOGP, XLOGP, iLOGP, MLOGP, and SILICOS-IT predictive models. The arithmetic mean of the five models is refer to as the consensus log P. Water solubility was calculated using log S value which is the logarithm of the molar solubility in water (Daina *et al.,* 2017). The pharmacokinetic parameters predicted are Gastrointestinal (GI) absorption permeability, Blood Brain Barrier (BBB) permeability, substrate of Glycoprotein (P-gp) permeability, inhibitor of any Cytochrome p450 (CYP), and skin permeability.

Table 3. 1: Grid box Sizes and Grid Centre Dimension for the Target Proteins

PDB ID	Grid Box Size			Grid Centre Dimension		
	x	y	z	x	Y	z
1N3U	17.98	15.37	9.36	21.34	16.81	42.53
3KIJ	13.75	14.79	14.88	8.36	-2.46	18.28
2QGE	16.27	14.78	18.54	-13.12	-4.32	-2.99
1OQ5	22.07	28.62	25.28	15.02	10.32	15.23
4LP5	26.23	26.23	35.33	51.96	-38.38	0.623
4GQR	15.91	18.02	15.50	27.89	33.73	58.19

CHAPTER FOUR

RESULTS AND DISCUSSION

4.1 Synthesis and Physical Properties of the Synthesised Compounds

Fifty-eight compounds (thirty Schiff bases and twenty-eight ether derivatives) were synthesised. The Schiff bases were made by condensing 4-aminoantipyrine with different substituted benzaldehydes as shown in schemes 3.1-3.30. The ether derivatives were formed from the Schiff bases via Williamson ether synthesis as shown in scheme 3.31-3.58. All synthesised compounds were obtained in good yield. The chemical structures of the examined compounds were elucidated by different spectroscopic techniques and the detailed structural elucidation for each compound were outlined in section 4.2. Twenty-four of the compounds are reported for the first time in literature. The known compounds were observed to be spectroscopically the same with those reported in the literature (Murtaza *et al.,* 2017; Shoaib, *et al.,* 2015; Asiri and Khan, 2010; Senbagam *et al.,* 2016; Baluja and Chanda, 2016 and Teran *et al.,* 2019). The new compounds were further elucidated by ^{13}C NMR and X- ray crystallography. Physicochemical data obtained for all the synthesised compounds are displayed on Table 4.1.

Table 4. 1: Analytical and Physical Data of the Synthesised Compounds

S/N	Code	Color	MF	MW(g mol^{-1})	M.pt. (°C)	Yield (%)	*R*f	Solvent system
1	SB0	Cream	$C_{18}H_{17}N_3O$	291.35	176.0-176.8	91	0.52	H:EA 6:4
2	SB1	Orange	$C_{18}H_{16}N_4O_3$	336.35	256.0-257.0	82	0.61	H:EA 5:5
3	SB1A	Orange	$C_{18}H_{16}N_4O_3$	336.35	211.3-212.2	88	0.63	H:EA 5:5
4	SB1B	Orange	$C_{18}H_{16}N_4O_3$	336.35	218.0-219.4	89	0.60	H:EA 5:5
5	SB2	Pale yellow	$C_{18}H_{16}FN_3O$	309.34	232.0-233.3	68	0.57	H:EA 7:3
6	SB2A	Yellow	$C_{18}H_{16}FN_3O$	309.34	174.9-176.5	92	0.55	H:EA 7:3
7	SB2B	Pale yellow	$C_{18}H_{16}FN_3O$	309.34	189.5-190.4	86	0.43	H:EA 7:3
8	SB3	Pale yellow	$C_{18}H_{16}ClN_3$	325.80	252.3-253.5	90	0.55	H:EA 7:3
9	SB3A	Pale yellow	$C_{18}H_{16}ClN_3$	325.80	192.1-193.0	92	0.59	H:EA 7:3
10	SB4	Pale Yellow	$C_{18}H_{16}BrN_3O$	370.25	251.9-252.8	75	0.49	H:EA 7:3
11	SB4A	Yellow	$C_{18}H_{16}BrN_3O$	370.25	177.3-179.9	88	0.52	H:EA 5:5
12	SB4B	Yellow	$C_{18}H_{16}BrN_3O$	370.25	195.1-196.5	81	0.45	H:EA 7:3
13	SB5	Pale yellow	$C_{19}H_{19}N_3O_3$	337.38	207.1-208.3	82	0.55	H:EA 7:3
14	SB5A	Yellow	$C_{19}H_{19}N_3O_3$	337.38	230.1-234.4	89	0.61	H:EA 5:5
15	SB5B	Pale yellow	$C_{19}H_{19}N_3O_3$	337.38	243.8-244.5	92	0.52	H:EA 5:5
16	SB6	Dark cream	$C_{19}H_{19}N_3O_2$	321.37	171.9-172.5	78	0.53	H:EA 7:3
17	SB6A	Yellow	$C_{19}H_{19}N_3O_2$	321.37	214.5-215.5	87	0.56	H:EA 7:3
18	SB6B	Pale yellow	$C_{19}H_{19}N_3O_2$	321.37	126.8-127.4	90	0.45	H:EA 7:3
19	SB7	Yellow	$C_{19}H_{19}N_3O$	305.38	184.3-184.8	74	0.46	H:EA 8:2
20	SB8	Yellow	$C_{19}H_{16}N_4O$	316.36	300-301.4	85	0.52	H:EA 5:5

MF = Molecular formula; MW = Molecular weight; M.pt = Melting point; Rf = Retardation factor; H = Hexane; EA = Ethyl acetate.

4. 1: Analytical and Physical Data of the Compounds

S/N	Code	Color	MF	MW(g mol^{-1})	M.pt. (°C)	Yield(%)	*R*f	Solvent system
21	SB9	Pale yellow	$C_{18}H_{17}N_3O_2$	307.35	270.3-271.4	86	0.51	H:EA 5:5
22	SB9B	cream	$C_{18}H_{17}N_3O_2$	307.35	229.6-230.1	89	0.43	H:EA 5:5
23	SB10	Bright orange	$C_{18}H_{16}N_4O_4$	352.24	232.8-234.5	95	0.52	H:EA 5:5
24	Sb11	Light brown	$C_{18}H_{17}N_3O_3$	323.35	275.9-276.6	91	0.55	H:EA 5:5
25	Sb11A	Yellow	$C_{18}H_{17}N_3O_3$	323.35	228.5-230.0	90	0.47	H:EA 5:5
26	SB11B	Light orange	$C_{18}H_{17}N_3O_3$	323.20	212.2-212.9	92	0.56	H:EA 5:5
27	SB12	Yellow	$C_{18}H_{15}ClFN_3O$	343.78	210.0-211.3	94	0.61	H:EA 7:3
28	SB13	Pale yellow	$C_{20}H_{21}N_3O$	319.40	179.6-180.6	89	0.56	H:EA 7:3
29	SB17	Dark yellow	$C_{18}H_{17}N_3O_4$	339.30	257.5-258.2	90	0.54	H:EA 5:5
30	SB19	Off white	$C_{20}H_{21}N_3O_4$	367.40	255.5-257.0	94	0.45	H:EA5:5
31	5A1	Brown	$C_{27}H_{27}N_3O_3S$	473.59	153.4-154.6	84	0.47	H:EA 6:4
32	5A2	Yellow	$C_{27}H_{24}F_3N_3O_3$	495.18	199.9-202.0	78	0.56	H:EA 6:4
33	5A5	Brown	$C_{26}H_{24}ClN_3O_3$	461.95	157.4-158.4	92	0.54	H:EA 6:4
34	5A6	Pale Yellow	$C_{26}H_{24}BrN_3O_3$	506.39	172.5-173.7	88	0.55	H:EA 6:4
35	5A8	Golden Yellow	$C_{26}H_{24}N_4O_5$	472.17	175.9-176.7	78	0.48	H:EA 6:4
36	5A9	Light Brown	$C_{27}H_{27}N_3O_4$	457.53	124.6-125.5	87	0.48	H:EA 5:5
37	9B1	Brown	$C_{26}H_{25}N_3O_2S$	443.57	229.6-230.1	81	0.58	H:EA 5:5
38	9B2	Brown	$C_{26}H_{22}F_3N_3O_2$	465.48	183.0-185.0	86	0.54	H:EA 5:5
39	9B5	Brown	$C_{25}H_{22}ClN_3O_2$	431.91	164.0-165.2	85	0.52	H:EA 5:5
40	9B6	Pale yellow	$C_{25}H_{22}BrN_3O_2$	476.20	205-206.9	82	0.55	H:EA 5:5
41	9B8	Yellow	$C_{25}H_{22}N_4O_4$	442.48	162.0-163.9	93	0.56	H:EA 5:5
42	9B9	Pale yellow	$C_{26}H_{25}N_3O_3$	427.50	128.7-129.9	86	0.48	H:EA 5:5

MF = Molecular formula; MW = Molecular weight; M.pt = Melting point; Rf = Retardation factor; H = Hexane; EA = Ethyl acetate

4.1: Analytical and Physical Data of the Compounds

S/N	Code	Color	MF	MW(g mol^{-1})	M.pt. (°C)	Yield (%)	*Rf*	Solvent system
43	10-1	Orange	$C_{26}H_{24}N_4O_4S$	488.56	185.0-186.7	88	0.55	H:EA 6:4
44	10-2	Golden Yellow	$C_{26}H_{21}F_3N_4O_4$	510.47	213.0-214.0	90	0.56	H:EA 6:4
45	10-5	Orange	$C_{25}H_{21}ClN_4O_4$	476.90	164.6-166.0	96	0.52	H:EA 6:4
46	10-6	Orange	$C_{25}H_{21}BrN_4O_4$	520.10	154.2-156.8	89	0.54	H:EA 6:4
47	10-8	Orange	$C_{25}H_{21}N_5O_6$	487.47	167.9-169.0	94	0.58	H:EA 6:4
48	10-9	Deep Yellow	$C_{26}H_{24}N_4O_5$	472.50	167.3-168.3	84	0.56	H:EA 5:5
49	SBA	Brown	$C_{22}H_{21}N_3O_3$	375.43	141.9-142.8	91	0.48	H:EA 6:4
50	SBB	Cream	$C_{22}H_{21}N_3O_3$	375.43	215.1-216.4	93	0.48	H:EA 6:4
51	SBC	Yellow	$C_{22}H_{21}N_3O_3$	375.43	140.6-141.9	81	0.52	H:EA 6:4
52	SBD	Pale Yellow	$C_{21}H_{19}N_3O_3$	345.40	143.9-144.3	83	0.55	H:EA 6:4
53	SBE	Pale Yellow	$C_{21}H_{19}N_3O_3$	345.40	155.9-157.0	68	0.48	H:EA 6:4
54	SBF	Yellow	$C_{21}H_{17}BrClN_3O_2$	458.74	148.5-149.9	77	0.58	H:EA 6:4
55	SBG	Yellow	$C_{21}H_{18}N_4O_4$	390.40	150.8-152.3	91	0.48	H:EA 6:4
56	SBH	Brown	$C_{24}H_{21}N_3O_3$	399.45	167.6-168.8	92	0.54	H:EA 6:4
57	SBI	Yellow	$C_{24}H_{21}N_3O_3$	399.45	169.5-170.0	75	0.46	H:EA 6:4
58	SBJ	Brown	$C_{23}H_{23}N_3O_4$	405.45	185.9-187.3	93	0.55	H:EA 5:5

MF = Molecular formula; MW = Molecular weight; M.pt = Melting point; R*f* = Retardation factor; H = Hexane; EA = Ethyl acetate.

4.2 Characterisations of the Synthesised Compounds

4.2.1 Characterisation of 4-(benzylideneamino)-1,5-dimethyl-2-phenyl-1,2-dihydro-3H-pyrazol-3-one (SB0)

Compound 4-(benzylideneamino)-1,5-dimethyl-2-phenyl-1,2-dihydro-3H-pyrazol-3-one (Scheme 4.1) appeared as cream crystals, with 91% yield, and melting point of 176.0-176.8 ^{o}C [literature: 176.8–177.2 °C (Teran *et al.,* 2019)].

The ^{1}H NMR spectrum (500 MHz, MeOD-d_6, δ_H (ppm)) showed nine signals and a total of seventeen protons. The signal at δ_H (ppm) 9.54 (s,1H, H-7', CH) was assigned to the azomethine proton. The signals at δ_H (ppm) 7.831 (dd, $J_{2',3'} = J_{6',5'} = 8$ Hz, $J_{2',4'/2',6'} = J_{6',4'/6',2'} = 1.5$ Hz 2H, H-2', H-6'), 7.467 (t, $J_{4',3'/4',5'} = 7.5$Hz, $J_{4',6'/4',2'} = 1.5$ Hz 1H, H-4') and 7.410 (d, $J_{3',2'/3',4'} = J_{5',4'/5',6'} = 6.5$Hz, 2H, H-3', H-5') were assigned to aromatic protons on the benzaldehyde ring. While signals at δ_H (ppm) 7.574 (t, $J_{3,2/3,4} = J_{5,4/5,6} = 7.5$ Hz, $J_{3,5} = J_{5,3} = 1.5$ Hz, 2H, H-3, H-5), 7.440 (t, $J_{4,2/4,6} = 1.5$ Hz, 1H, H-4) and 7.420 (d, $J_{2,4/2,6} = J_{6,4/6,2} = 2.5$ Hz, 2H, H-2, H-6) correspond to the aromatic protons on the pyrazole ring. The two upfield singlets at δ_H (ppm) 3.247 (s, 3H, H-11, CH_3) and 2.512 (s, 3H, H-10, CH_3) were assigned to the two methyl protons.

EI-MS: *m/z* (relative abundance in %), 291 [M^+] (67), 56 (100), 121 (62), 188(43), 199 (38) and182 (23). The EI-MS spectrum of SB0 showed the molecular ion peak M^+ at *m/z* 291. The Fragment $[C_3H_6N]^{3\bullet}$ with *m/z* 56 from the pyrazole moiety corresponds to the base peak. Other prominent peaks were observed at *m/z* 199 $[C_{11}H_9N_3O]^+$, 188 $[C_{11}H_{11}N_2O]^+$, and 121 $[C_6H_7N_3]^{3+}$.

The infrared absorption spectrum of SB0 showed vibrational bands with $\bar{\upsilon}$ (cm^{-1}) for =C-H anti-sym stretch of aromatic (3043), C-H anti-sym. stretch of aliphatic (2936) -C=O stretch of carbonyl (1643), C=N stretch of the azomethine bond (1594), C=C stretch of aromatic (1564), C-N stretch (1305) and N-N stretch (1211) of pyrazole moiety.

The analysis of the UV spectrum of SB0 in chloroform revealed maximum absorption bands (nm) at 326, 253, 235, 211 and 201. The longer wavelength at 253 and 326 showed n-π* transitions. The absorptions at 235, 211 and 201 showed π-π*transitions.

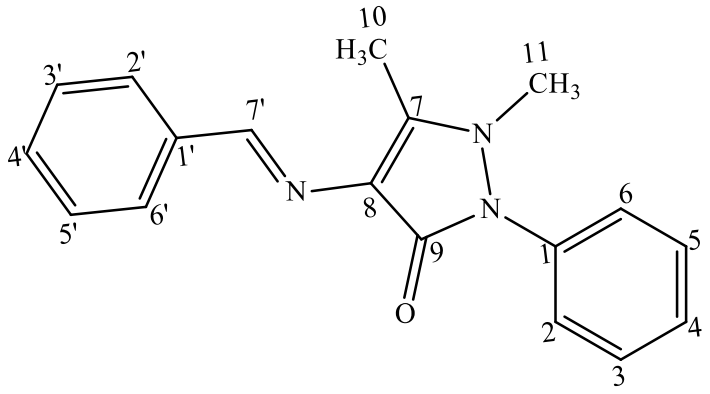

Scheme 4. 1: Structure of SB0

4.2.2 Characterisation of 1,5-dimethyl-4-((4-nitrobenzylidene)amino)-2-phenyl-1,2-dihydro-3H-pyrazol-3-one (SB1)

The compound 1,5-dimethyl-4-((4-nitrobenzylidene)amino)-2-phenyl-1,2-dihydro-3H-pyrazol-3-one (Scheme 4.2) appeared as orange crystals, with 82% yield, and melting point of 256.0-257.0 ^{o}C [literature: 254 °C (Shoaib *et al.*, 2015)].

The ^{1}H NMR spectrum (400 MHz, DMSO-$d_{6,}$ δH (ppm)) displayed ten peaks with a total of sixteen protons. The ^{1}H NMR spectrum established a signal downfield at δ_H (ppm) 9.798 (s,1H, H-7', CH) for the azomethine proton. Four peaks at δ_H (ppm) 8.188 (d, $J_{6',5'}$ = 7.2 Hz, 1H, H-6'), 7.959 (d, $J_{3',4'}$ = 8 Hz, 1H, H-3'), 7.785 (t, $J_{5',4'/5',6'}$ = 8 Hz, 1H, H-5') and 7.647 (dd, $J_{4',3'/4',5'}$ = 7.2 Hz, $J_{4',6'}$ = 2 Hz 1H, H-4') were assigned to the aromatic methine protons from the benzaldehyde ring. These bands appeared more downfield than the other aromatic methine protons at 7.551 (t, $J_{3,2/3,4}$ = $J_{5,4/5,6}$ = 8 Hz, 2H, H-3, H-5), 7.411 (d, $J_{4,3/4,5}$ = 7.6 Hz, 1H, H-4) and 7.372 (d, $J_{2,3}$ =$J_{6,5,}$= 7.6Hz, 2H, H-2, H-6) on the pyrazole moiety due to the presence of the nitro group attached to the benzaldehyde ring. The two peaks upfield at δ_H (ppm) 3.230 (s, 3H, H-11, CH_3) and 2.450 (s, 3H, H-10, CH_3) represent the methyl protons.

EI-MS: *m/z* (relative abundance in %), 336 [M^+] (26), 56 (100), 291 (25), 202 (69), 188 (17), and 77 (33). The EI-MS spectrum of SB1A showed a molecular ion, M^+ at *m/z* 336, and a base peak of *m/z* 56 corresponding to the fragment $[C_3H_6N]^{3+}$. Other prominent peaks were observed at *m/z* 291 $[C_{18}H_{16}N_3O]^+$, 202 $[C_{11}H_{11}N_3O]^+$, 188 $[C_{11}H_{11}N_2O]^+$, and 77 $[C_6H_5]^+$.

The infrared absorption spectrum of SB1A showed vibrational bands with $\bar{\upsilon}$ (cm^{-1}) for =C-H anti-sym stretch of aromatic (3069), C-H anti-sym. stretch of aliphatic (2926) -C=O stretch of carbonyl (1648), C=N stretch of the azomethine bond (1565), C=C stretch of aromatic (1518), N=O asymmetric stretch of nitro substituent (1486), N=O symmetric stretch of nitro substituent (1384). C-N stretch (1301) and N-N stretch (1128) of pyrazole.

The analysis of the UV spectrum of SB1 in chloroform revealed maximum absorption bands (nm) at 249, 260, 267, 282 and 390. The longer wavelength at 390, 282, 267 and 260 showed n-π* transitions. The absorptions at 249 showed π-π* transitions.

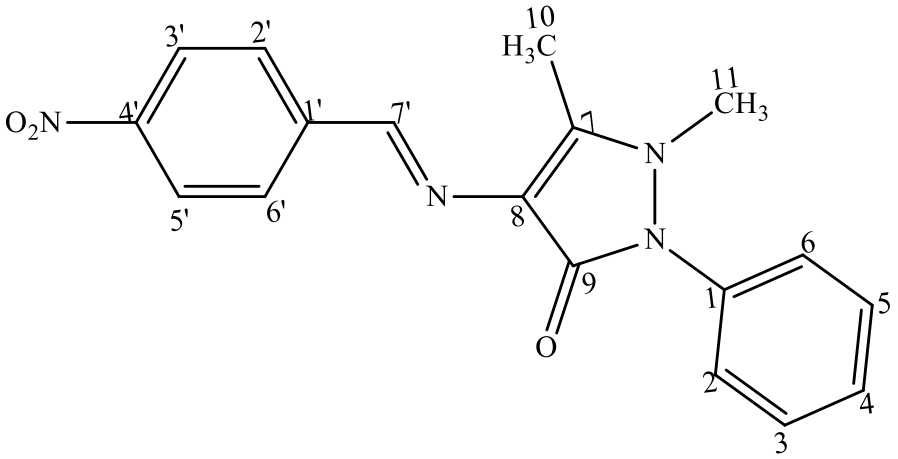

Scheme 4. 2: Structure of SB1

4.2.3 Characterisation of 1,5-dimethyl-4-((2-nitrobenzylidene)amino)-2-phenyl-1,2-di hydro-3H-pyrazol-3-one (SB1A)

The compound (1,5-dimethyl-4-((2-nitrobenzylidene)amino)-2-phenyl-1,2-dihydro-3H-pyrazol-3-one (Scheme 4.3) was obtained as orange crystals, with 88% yield, of (0.1179 g), and m.pt. of 211.3-212.2 ^{o}C [literature 212 ^{o}C (Shoaib *et al.*, 2015)].

The ^{1}H NMR spectrum (400 MHz, CD3CN-$d_{6,}$ δH (ppm)) displayed ten resonances with a total of sixteen proton. The downfield signal (a singlet) at δ_H (ppm) 9.726 (s, 1H, H-7', CH) was assigned to the azomethine proton. Four signals at δ(ppm) 8.654 (s, 1H, H-2'), 8.211(dd, $J_{6',5'}$ = 8 Hz, $J_{6',2'/6',4'}$ = 2.4 Hz 1H, H-6'), 8.185 (d, $J_{4',5'}$ = 8 Hz,1H, H-4') and 7.671(t, $J_{5',4',/5',6'}$ = 8 Hz, 1H, H-5') were assigned to the aromatic methine protons from the benzaldehyde ring. The presence of the nitro group on the benzaldehyde ring causes these protons to be more downfield. Three signals at δ_H (ppm) 7.543 (t, $J_{3,2/3,4}$ = $J_{5,4/5,6}$ =7.6 Hz, 2H, H-3, H-5),7.407 (d, $J_{4,2/4,6}$ = 1.2 Hz, 1H, H-4) and 7.404 (d, $J_{2,3}$ = $J_{6,5}$ = 8.4 Hz, 2H, H-2, H-6) were assigned to aromatic methine protons on the pyrazole moiety. The singlet peaks upfield at δ_H (ppm) 3.193 (s, 3H, H-11, CH_3), 2.480 (s, 3H, H-10, CH_3) are for the methyl proton on the pyrazole moiety.

EI-MS: *m/z* (relative abundance in %): 336 [M^+] (100), 322 (41), 244 (23), 188 (51), 121 (48), 56 (65), and 77 (13). The EI-MS spectrum of SB1B showed a molecular ion, M^+ as the base peak corresponding to *m/z* 336 and M^++1 peak at *m/z* 337. Other prominent peaks were observed at *m/z* 322 $[C_{17}H_{13}N_4O_3]^+$, 244 $[C_{11}H_8N_4O_3]^+$, 188 $[C_{11}H_{11}N_2O]^+$, 121 $[C_6H_7N_3]^{3+}$, 56 $[C_3H_6N]^{3\bullet}$ and 77 $[C_6H_5]^+$.

The infrared absorption spectrum of SB1B showed vibrational bands with characteristic vibrational frequencies $\bar{\upsilon}$ (cm^{-1}) for some functional groups assigned as =C-H anti-sym stretch of aromatic (3067), C-H anti-sym. stretch of aliphatic (2944) -C=O stretch of the carbonyl on the pyrazole moiety (1648), C=N stretch of the azomethine bond (1592), C=C stretch of aromatic (1566), N=O asymmetric stretch of nitro substituent (1522), N=O symmetric stretch of nitro substituent (1348). C-N stretch (1307) and N-N stretch (1135) pyrazole moiety.

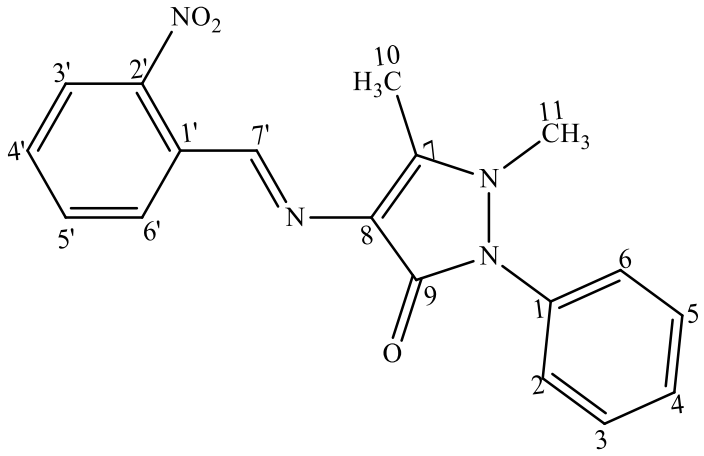

Scheme 4. 3: Structure of SB1A

4.2.4 Characterisation of 1,5-dimethyl-4-((3-nitrobenzylidene)amino)-2-phenyl-1,2-di hydro-3H-pyrazol-3-one (SB1B)

The compound 1,5-dimethyl-4-((3-nitrobenzylidene)amino)-2-phenyl-1,2-dihydro-3H-pyrazol-3-one (Scheme 4.4) was obtained as orange crystals, with 89% yield, and m.pt. of 218.0-219.4 ^{o}C [literature 218-219 ^{o}C (Senbagam *et al.*, 2016)].

The ^{1}H NMR spectrum (400 MHz, CD3CN-$d_{6,}$ δH (ppm)) displayed ten resonances with a total of sixteen proton. The downfield signal (a singlet) at δ_H (ppm) 9.726 (s, 1H, H-7', CH) was assigned to the azomethine proton. Four signals at δ(ppm) 8.654 (s, 1H, H-2'), 8.211(dd, $J_{6',5'}$ = 8 Hz, $J_{6',2'/6',4'}$ = 2.4 Hz 1H, H-6'), 8.185 (d, $J_{4',5'}$ = 8 Hz,1H, H-4') and 7.671(t, $J_{5',4',/5',6'}$ = 8 Hz, 1H, H-5') were assigned to the aromatic methine protons from the benzaldehyde ring. The presence of the nitro group on the benzaldehyde ring causes these protons to be more downfield. Three signals at δ_H (ppm) 7.543 (t, $J_{3,2/3,4}$ = $J_{5,4/5,6}$ =7.6 Hz, 2H, H-3, H-5),7.407 (d, $J_{4,2/4,6}$ = 1.2 Hz, 1H, H-4) and 7.404 (d, $J_{2,3}$ = $J_{6,5}$ = 8.4 Hz, 2H, H-2, H-6) were assigned to aromatic methine protons on the pyrazole moiety. The singlet peaks upfield at δ_H (ppm) 3.193 (s, 3H, H-11, CH_3), 2.480 (s, 3H, H-10, CH_3) are for the methyl proton on the pyrazole moiety.

EI-MS: *m/z* (relative abundance in %): 336 [M^+] (100), 322 (41), 244 (23), 188 (51), 121 (48), 56 (65), and 77 (13). The EI-MS spectrum of SB1B showed a molecular ion, M^+ as the base peak corresponding to *m/z* 336 and M^++1 peak at *m/z* 337. Other prominent peaks were observed at *m/z* 322 $[C_{17}H_{13}N_4O_3]^+$, 244 $[C_{11}H_8N_4O_3]^+$, 188 $[C_{11}H_{11}N_2O]^+$, 121 $[C_6H_7N_3]^{3+}$, 56 $[C_3H_6N]^{3\bullet}$ and 77 $[C_6H_5]^+$.

The infrared absorption spectrum of SB1B showed vibrational bands with characteristic vibrational frequencies $\bar{\upsilon}$ (cm^{-1}) for some functional groups assigned as =C-H anti-sym stretch of aromatic (3067), C-H anti-sym. stretch of aliphatic (2944) -C=O stretch of the carbonyl on the pyrazole moiety (1648), C=N stretch of the azomethine bond (1592), C=C stretch of aromatic (1566), N=O asymmetric stretch of nitro substituent (1522), N=O symmetric stretch of nitro substituent (1348). C-N stretch (1307) and N-N stretch (1135) pyrazole moiety.

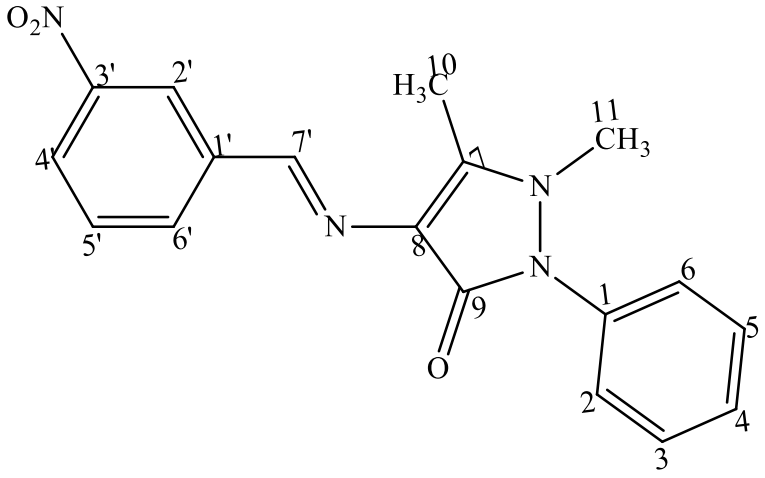

Scheme 4. 4: Structure of SB1B

4.2.5 Characterisation of 4-((4-fluorobenzylidene)amino)-1,5-dimethyl-2-phenyl-1,2-di hydro-3H-pyrazol-3-one (SB2)

The compound 4-((4-fluorobenzylidene)amino)-1,5-dimethyl-2-phenyl-1,2-dihydro-3H-pyrazol-3-one (Scheme 4.5) appeared as pale yellow crystals, with a 68% yield, and m.pt. of 232.0-233.3 ^{o}C [literature 230 ^{o}C (Baluja and Chanda, 2016)].

The ^{1}H NMR spectrum (500 MHz, DMSO-$d_{6,}$ δ_H (ppm)) displayed eight resonances with a total of sixteen protons. The downfield signal (a singlet) at δ_H (ppm) 9.542 (s, 1H, H-7', CH) was assigned to the azomethine proton. Two signals at δ_H (ppm) 7.863 (dd, $J_{2',3'} = J_{6',5'}$ = 8.5 Hz, $J_{2',6'} = J_{6',2}$ = 2 Hz, 2H, H-2', H-6') and 7.526 (dd, $J_{3',2'} = J_{5',6'}$ = 8 Hz, $J_{3',5'} = J_{5',3'}$ = 3Hz, 2H, H-3', H-5') appeared as doublet corresponding to the chemically equivalent methine protons from the benzaldehyde ring. They appeared downfield compared to other protons in the aromatic region in the spectrum due to the presence of fluorine in the ring. Three signals at δ_H (ppm) 7.369 (m, $J_{2,3} = J_{6,5}$ = 7 Hz, $J_{2,4/2,6} = J_{6,4/6,2}$ = 2 Hz, 2H, H-2, H-6), 7.359 (d, $J_{4,3/4,5}$ = 8 Hz, 1H, H-4) and 7.283 (t, $J_{3,2/3,4} = J_{5,6/5,4}$ = 9 Hz, 2H, H-3, H-5) were assigned to aromatic methine protons on the pyrazole moiety. Two singlets upfield at δ_H (ppm) 3.158 (s, 3H, H-11, CH_3) and 2.432 (s, 3H, H-10, CH_3) represent the methyl protons.

EI-MS: *m/z* (relative abundance in %), 309 [M^+] (100), 217 (28), 200 (21), 188 (34), 121 (52), and 56 (56). The EI-MS spectrum of SB2 showed a molecular ion, M^+ as the base peak corresponding to *m/z* 309. Other prominent peaks were observed at *m/z* 217 $[C_{11}H_8FN_3O]^+$, 200 $[C_{11}H_9N_3O]^+$, 188 $[C_{11}H_{11}N_2O]^+$, 121 $[C_6H_7N_3]^{3+}$, and 56 $[C_3H_6N]^{3\bullet}$.

The infrared absorption spectrum of SB2 showed vibrational bands with $\bar{\upsilon}$ (cm^{-1}) for =C-H anti-sym stretch of aromatic (3069), C-H anti-sym. stretch of aliphatic (2937) -C=O stretch of carbonyl (1651), C=N stretch of the azomethine bond (1598), C=C stretch of aromatic (1567), C-N stretch (1304) and N-N stretch (1220) of pyrazole.

The analysis of the UV spectrum of SB2 in chloroform revealed maximum absorptions bands (nm) at 249, 260, and 327. The longer wavelength at 327 and 260 suggest n-π* transitions. The absorptions at 249 indicates π-π* transitions.

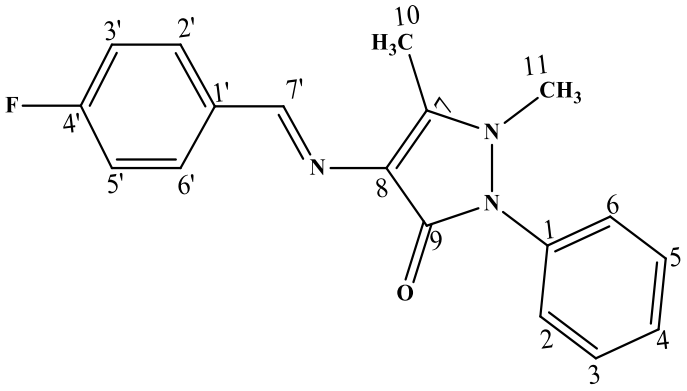

Scheme 4. 5: Structure of SB2

4.2.6 Characterisation of 4-((2-fluorobenzylidene)amino)-1,5-dimethyl-2-phenyl-1,2-dihy dro-3H-pyrazol-3-one (SB2A)

The compound 4-((2-fluorobenzylidene)amino)-1,5-dimethyl-2-phenyl-1,2-dihydro-3H-pyrazol-3-one (Scheme 4.6) appeared as yellow crystals, with 92% yield, and m.pt. of 174.9-176.5 ^{o}C.

The ^{1}H-NMR (500 MHz, MeOD-d_6 δ_H (ppm)) spectrum of SB2A displayed a total of ten signals and sixteen protons. A downfield signal at δ_H (ppm) 9.808 (s, 1H, H-7', CH) was assigned to the azomethine proton. The signals at δ_H (ppm) 8.149 (dd, $J_{6',5'}$ = 7.5 Hz, $J_{6',4'}$ = 2 Hz, 1H, H-6'), 7.470 (ddd, $J_{4',3'/4',5'}$ = 8.5 Hz, $J_{4',6'}$ = 1.5 Hz, 1H, H-4'), 7.246 (t, $J_{5',4'/5',6'}$ = 7.5 Hz, 1H, H-5') and 7.149 (ddd, $J_{3',4'}$ = 7.5 Hz, $J_{3',5'}$ = 1.5 Hz, 1H, H-3') were assigned to the aromatic methine protons on the benzaldehyde ring. Three signals at δ_H (ppm) 7.573 (dd, $J_{3,2,/3,4}$ = $J_{5,4/5,6}$ = 7.5 Hz, $J_{3,5}$ = $J_{5,3}$ = 2 Hz, 2H, H-3, H-5), 7.431 (dd, $J_{2,3}$ = $J_{6,5}$ = 8 Hz, $J_{2,4/2,6}$ = $J_{6,2/6,4}$ = 2 Hz, 2H, H-2, H-6) and 7.398 (d, $J_{4,2/4,6}$ = 3 Hz, 1H, H-4) correspond to the aromatic methine protons on the pyrazole moiety. The upfield signals at δ_H (ppm) of 3.265 (s, 3H, H-11, CH_3) and 2.523 (s, 3H, H-10, CH_3) were assigned to methyl protons.

EI-MS: *m/z* (relative abundance in %), 309 [M^+] (100), 217 (37), 200 (17), 188 (41), 121 (35), and 56 (39). The EI-MS spectrum of SB2A showed a molecular ion, M^+ as the base peak corresponding to *m/z* 309. Other prominent peaks were observed at *m/z* 217 $[C_{11}H_8FN_3O]^+$, 200 $[C_{11}H_9N_3O]^+$, 188 $[C_{11}H_{11}N_2O]^+$, 121 $[C_6H_7N_3]^{3+}$, and 56 $[C_3H_6N]^{3\bullet}$.

The infrared absorption spectrum of SB2A showed vibrational bands with $\bar{\upsilon}$ (cm^{-1}) for =C-H anti-sym stretch of aromatic (3057), C-H anti-sym. stretch of aliphatic (2938) -C=O stretch of carbonyl (1649), C=N stretch of the azomethine bond (1570), C=C stretch of aromatic (1487), C-N stretch (1305) and N-N stretch (1229) of pyrazole moiety.

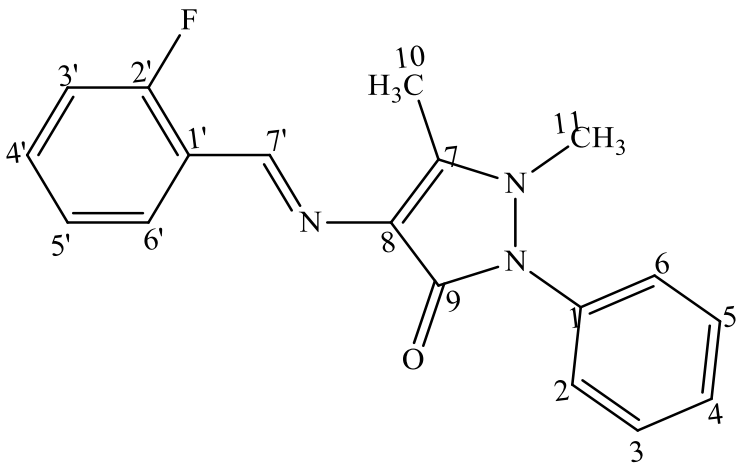

Scheme 4. 6: Structure of SB2A

4.2.7 Characterisation of 4-((3-fluorobenzylidene)amino)-1,5-dimethyl-2-phenyl-1,2-dihydro-3H-pyrazol-3-one (SB2B)

The compound 4-((3-fluorobenzylidene)amino)-1,5-dimethyl-2-phenyl-1,2-dihydro-3H-pyrazol-3-one (Scheme 4.7) was obtained as pale yellow crystals with 86% yield, and m.pt. of 189.4-190.4 ^{o}C.

The ^{1}H NMR (400 MHz, MeOD-$d_{6,}$ δ_H ppm) spectrum of SB2B displayed a total of ten signals and sixteen protons. A downfield signal at δ_H (ppm) 9.525 (s, 1H, H-7', CH) was assigned to the azomethine proton. Four signals at δ_H (ppm) 7.614 (q, $J_{2',4',2',6'}$ = 2.4 Hz, 1H, H-2'), 7.586 (m, $J_{5',4'/5',6'}$ = 6.8 Hz, 1H, H-5'), 7.415 (d, $J_{6',5'}$ = 7.6 Hz, $J_{6,4'/6',2'}$ = 1.2 Hz, 1H, H-6') and 7.394 (d, $J_{4',6'/4',2'}$ = 1.2 Hz, 1H, H-4') correspond to aromatic methine protons from the benzaldehyde ring. The signals at δ_H (ppm) 7.559 (dd, $J_{3,2/3,4} = J_{5,4/5,6}$ = 7.6 Hz, $J_{3,5} = J_{5,3}$ = 2.4 Hz, 2H, H-3, H-5), 7.475 (dd, $J_{2,3} = J_{6,5}$ = 8Hz, $J_{2,4/2,6} = J_{6,2/6,4}$ = 2.4 Hz, 2H, H-2, H-6) and 7.152 (dt, $J_{4,3/4,5}$ = 7.6 Hz, $J_{4,2/4,6}$ = 2 Hz, 1H, H-4) were assigned to the aromatic methine protons of the pyrazole moiety. While the signals at δ_H (ppm) 3.259 (s, 3H, H-11, CH_3) and 2.513 (s, 3H, H-10, CH_3) represent the methyl protons.

EI-MS: *m/z* (relative abundance in %), 309 [M^+] (100), 217 (32), 200(18), 188 (41), 121 (49), and 56 (62). The EI-MS spectrum of SB2B showed a molecular ion, M^+ as base peak corresponding to *m/z* 309. Other prominent peaks were observed at *m/z* 217 $[C_{11}H_8FN_3O]^+$, 200 $[C_{11}H_9N_3O]^+$, 188 $[C_{11}H_{11}N_2O]^+$, 121 $[C_6H_7N_3]^{3+}$, and 56 $[C_3H_6N]^{3\bullet}$.

The infrared absorption spectrum of SB2B showed vibrational bands with $\bar{\upsilon}$ (cm^{-1}) for =C-H anti-sym stretch of aromatic (3052), C-H anti-sym. stretch of aliphatic (2956) -C=O stretch of the carbonyl on the pyrazole moiety (1646), C=N stretch of the azomethine bond (1569), C=C stretch of aromatic (1470), C-N stretch (1307) and N-N stretch of pyrazole (1236).

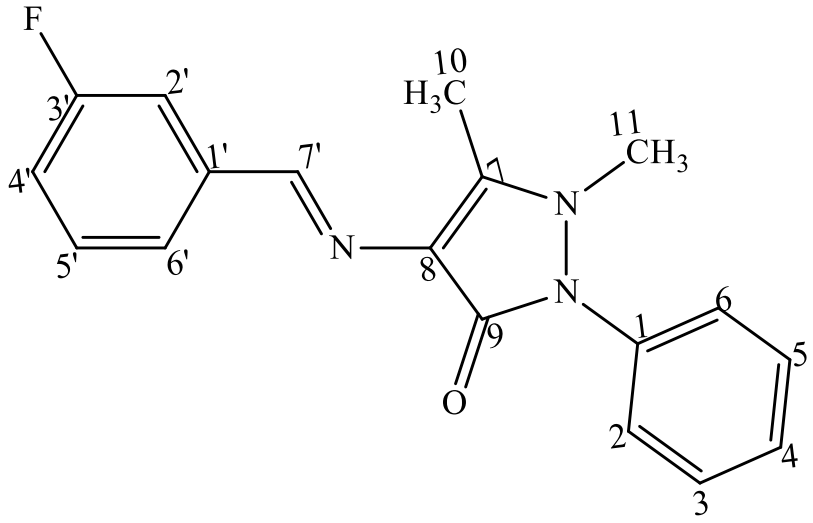

Scheme 4.7: Structure of SB2B

4.2.8 Characterisation of (Z)-4-((4-chlorobenzylidene)amino)-1,5-dimethyl-2-phenyl-1,2-dihydro-3H-pyrazol-3-one (SB3)

The compound of (Z)-4-((4-chlorobenzylidene)amino)-1,5-dimethyl-2-phenyl-1,2-dihydro-3H-pyrazol-3-one (Scheme 4.8) was obtained as pale yellow crystals with 90% yield and and m.pt. of 252.3-253.5 ^{o}C [literature 255 ^{o}C (Murtaza *et al.*, 2017)].

The ^{1}H NMR (500 MHz, DMSO-$d_{6,}$ δ_H ppm) spectrum of SB3 displayed a total of eight signals and sixteen protons. A downfield signal at δ_H (ppm) 9.550 (s, 1H, H-7', CH) was assigned to the azomethine proton. Two signals at δ_H (ppm) 7.827 (d, $J_{2',3'} = J_{6',5'}$ = 8.5 Hz, 2H, H-2', H-6') and 7.539 (d, $J_{3',2'} = J_{5',6'}$ = 8.5 Hz, 2H, H-3', H-5') appeared as doublet corresponding to the chemically equivalent methine protons from the benzaldehyde ring. They appeared downfield due to the presence of chlorine in the ring. The signals at δ_H (ppm) 7.509 (d, $J_{3,2/3,4} = J_{5,4/5,6}$ = 8.5 Hz, 2H, H-3, H-5), 7.387 (dd, $J_{2,3} = J_{6,5}$ = 8 Hz, $J_{2,4/2,6} = J_{6,4/6,2}$ = 1 Hz, 2H, H-2, H-6) and 7.371 (d, $J_{4,3/4,5}$ = 7.5 Hz,1H, H-4) were assigned to the aromatic methine protons of the pyrazole moiety. While the signals at 3.183 (s, 3H, H-11, CH_3) and 2.447 (s, 3H, H-10, CH_3) were assigned to the methyl protons.

EI-MS: *m/z* (relative abundance in %), 325.5 [M^+] (100), 326 (23), 327 (35), 233 (23), 216 (15), 188 (28), 121 (27), and 56 (73). The EI-MS spectrum of SB3 showed a molecular ion, M^+ as the base peak corresponding to *m/z* 325. M^++1 and M^++2 peak at *m/z* 326 and 327, respectively were observed. Other prominent peaks were observed at *m/z* 233 $[C_{11}H_8ClN_3O]^+$, 217 $[C_{11}H_8ClN_3]^{2+}$, 188 $[C_{11}H_{11}N_2O]^+$, 121 $[C_6H_7N_3]^{3+}$, and 56 $[C_3H_6N]^{3\bullet}$.

The infrared absorption spectrum of SB3 showed vibrational bands with $\bar{\upsilon}$ (cm^{-1}) =C-H anti-sym stretch of aromatic (3060), C-H anti-sym. stretch of aliphatic (2936) -C=O stretch of carbonyl (1650), C=N stretch of the azomethine bond (1594), C=C stretch of aromatic (1570), C-N stretch (1302) and N-N stretch (1214) of pyrazole.

The analysis of the UV spectrum of SB3 in chloroform revealed maximum absorption bands (nm) at 249, 260, and 336. The longer wavelength at 336 and 260 showed n-π* transitions. The absorptions at 249 showed π-π* transition.

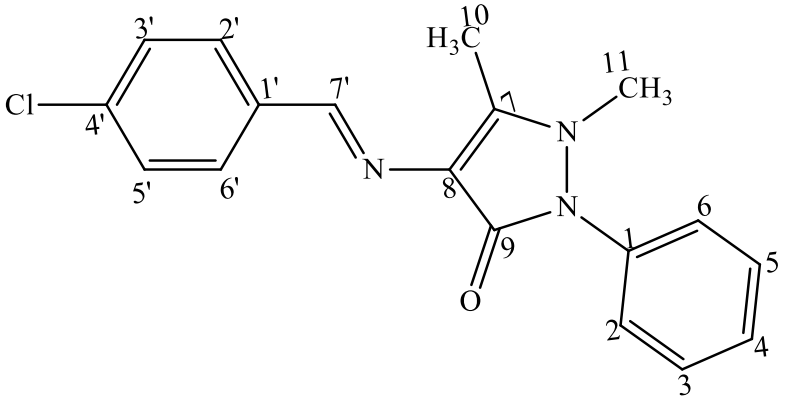

Scheme 4. 8: Structure of SB3

4.2.9 Characterisation of (Z)-4-((2-chlorobenzylidene)amino)-1,5-dimethyl-2-phenyl-1,2di hydro-3H-pyrazol-3-one (SB3A)

The compound (Z)-4-((2-chlorobenzylidene)amino)-1,5-dimethyl-2-phenyl-1,2-dihydro-3H-pyrazol-3-one (Scheme 4.9) was obtained as pale yellow crystals with 92% yield, and m.pt. of 192.1-193. 0^{o}C [literature 210 ^{o}C (Baluja and Chanda, 2016)].

The ^{1}H NMR (400 MHz, MeOD-$d_{6,}$ δ_H ppm) spectrum of SB3A displayed a total of ten signals and sixteen protons. A downfield signal δ_H (ppm) at 9.979 (s, 1H, H-7', CH) was assigned to the azomethine proton. Four signals at 8.210 (dd, $J_{6',5'}$ = 9.6 Hz, $J_{6',4'}$ = 1.2 Hz, 1H, H-6'), 7.473 (t, $J_{4',3'/4',5'}$ = 7.6Hz, $J_{4',6'}$ = 1.2 Hz, 1H, H-4'), 7.368 (dd, $J_{3',5'}$ =2.8 Hz, 1H, H-3') and 7.351 (dd, $J_{5',4'/5',6'}$ = 6.8 Hz, $J_{5',3'}$ = 2.8 Hz, 1H, H-5') were assigned to aromatic methine protons on the benzaldehyde ring. The signals at δ_H (ppm) 7.575 (t, $J_{3,2/3,4} = J_{5,4/5,6}$ = 8 Hz, $J_{3,5} = J_{5,3}$ = 2 Hz, 2H, H-3, H-5), 7.416 (dd, $J_{2,3} = J_{6,5}$ = 7.6 Hz, $J_{2,4} = J_{6,4}$ = 1.6 Hz, 2H, H-2, H-6) and 7.400 (d, $J_{4,2/4,6}$ = 1.2 Hz, 1H, H-4) were assigned to the aromatic methine protons of the pyrazole moiety. While the signals at 3.268 (s, 3H, H-11, CH_3) and 2.525 (s, 3H, H-10, CH_3) correspond to the methyl protons of the pyrazole moiety.

EI-MS: *m/z* (relative abundance in %), 325 [M^+] (89), 290 (100), 233 (36), 188 (58), 121 (54), and 56 (49). The EI-MS spectrum of SB3A showed the molecular ion peak M^+ at *m/z* 325, M^++1 and M^++2 peak at *m/z* 326 and 327, respectively were observed. Other prominent peaks were observed at *m/z* 290 $[C_{18}H1_6N_3]^+$, 233 $[C_{11}H_8ClN_3O]^+$, 188 $[C_{11}H_{11}N_2O]^+$, 121 $[C_6H_7N_3]^{3+}$, and 56 $[C_3H_6N]^{3\bullet}$.

The infrared absorption spectrum of SB3A showed vibrational bands with $\bar{\upsilon}$ (cm^{-1}) =C-H anti-sym stretch of aromatic(3056), C-H anti-sym. stretch of aliphatic (2936) -C=O stretch of carbonyl (1648), C=N stretch of the azomethine bond (1589), C=C stretch of aromatic (1562), C-N stretch (1305) and N-N stretch (1213) of pyrazole moiety.

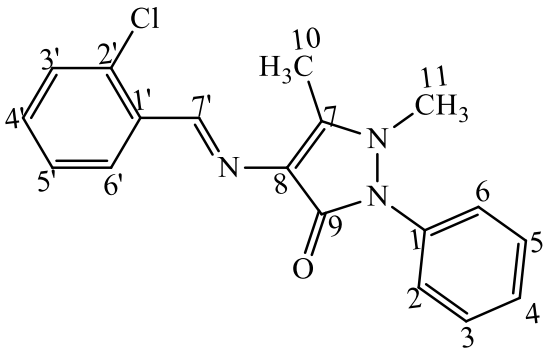

Scheme 4. 9: Structure of SB3A

4.2.10 Characterisation of 4-((4-bromobenzylidene)amino)-1,5-dimethyl-2-phenyl-1,2-dihy dro-3H-pyrazol-3-one (SB4)

The compound 4-((4-bromobenzylidene)amino)-1,5-dimethyl-2-phenyl-1,2-dihydro-3H-pyrazol-3-one (Scheme 4.10) appeared as a pale yellow crystals with 75% yield, and m.pt. of 251.9-252.8 ^{o}C [literature 256-257^{o}C (Bensaber *et al.,* 2014)].

The ^{1}H NMR (500MHz, DMSO-$d_{6,}$ δ_H ppm) spectrum of SB4 displayed a total of eight signals and sixteen protons. A downfield signal at 9.535 (s, 1H, H-7', CH) was assigned to the azomethine proton. Two signals at 7.756 (d, $J_{2',3'/6',5'}$ = 8.5 Hz, 2H, H-2', H-6') and 7.646 (d, $J_{3',2'/5',6'}$ = 8.5 Hz, 2H, H-3', H-5') appeared as doublets corresponding to the chemically equivalent methine protons from the benzaldehyde ring. The presence of bromine in the ring causes these signals to appear more downfield relative to other aromatic protons in the spectrum. The signals at 7.539 (t, $J_{3,2/3,4} = J_{5,4/5,6}$ = 7.5 Hz, 2H, H-3, H-5), 7.387 (d, $J_{2,3} = J_{6,5}$ = 8.5 Hz, 2H, H-2, H-6) and 7.378 (d, $J_{4,3/4,5}$ = 7.5 Hz, 1H, H-4) were assigned to the aromatic methine protons of the pyrazole moiety. While the signals at 3.183 (s, 3H, H-11, CH_3) and 2.445 (s, 3H, H-10, CH_3) correspond to the methyl protons of the pyrazole moiety.

EI-MS: *m/z* (relative abundance in %), 370 [M^+] (66), 56 (100), 371 (21), 372 (62) 277 (28), 260 (25), 188 (50), 121 (55), and 44 (40). The EI-MS spectrum of SB4 showed a molecular ion, M^+ corresponding to a *m/z* 370. Molecular ion peaks at *m/z* of 371 and 372 corresponding to M^++1 and M^++2, respectively was also observed. Other prominent peaks were observed at *m/z* 277 $[C_{11}H_8BrN_3O]^+$, 260 $[C_{11}H_8BrN_3]^{2+}$, 244 $[C_{11}H_8N_4O_3]^+$, 188 $[C_{11}H_{11}N_2O]^+$, 121 $[C_6H_7N_3]^{3+}$, 56 $[C_3H_6N]^{3\bullet}$ and 44 $[CH_3N_2]^{2+}$.

The infrared absorption spectrum of SB4 showed vibrational bands with $\bar{\upsilon}$ (cm^{-1}) for =C-H anti-sym stretch of aromatic (3058), C-H anti-sym. stretch of aliphatic (2935) -C=O stretch of carbonyl (1649), C=N stretch of the azomethine bond (1593), C=C stretch of aromatic (1569), C-N stretch (1302) and N-N stretch (1168) of pyrazole moiety.

The analysis of the UV spectrum of SB4 in chloroform revealed maximum absorptions bands (nm) at 249, 261, and 338. The longer wavelength at 338 and 261 showed n-π* transitions. The absorptions at 249 showed π-π* transitions.

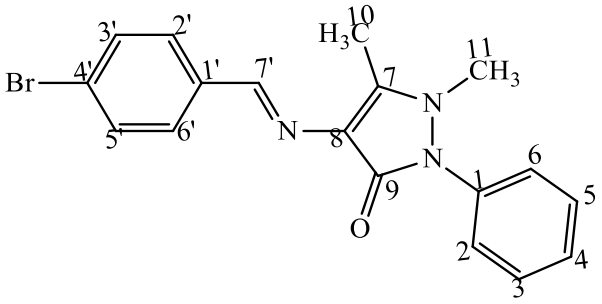

Scheme 4. 10: Structure of SB4

4.2.11 Characterisation of 4-((2-bromobenzylidene)amino)-1,5-dimethyl-2-phenyl-1,2-dihy dro-3H-pyrazol-3-one (SB4A)

The compound 4-((2-bromobenzylidene)amino)-1,5-dimethyl-2-phenyl-1,2-dihydro-3H-pyrazol-3-one (Scheme 4.11) was obtained as yellow crystals with 88% yield, and m.pt. of 177.3-179.9 ^{o}C.

The ^{1}H NMR (400 MHz, MeOD-$d_{6,}$ δ_H ppm) spectrum of SB4A displayed a total of ten signals and sixteen protons. A downfield signal at δ_H (ppm) 9.930 (s, 1H, H-7', CH) was assigned to the azomethine proton. The signals at δ_H (ppm) 8.192 (dd, $J_{6',5'}$ = 8 Hz, $J_{6',4'}$ = 1.6 Hz, 1H, H-6'), 7.614 (d, $J_{3',4'}$ = 8 Hz, 2H, H-3'), 7.472 (tt, $J_{5',4',/5',6'}$ =7.2 Hz, $J_{5',3'}$ =1.6 Hz, 1H, H-5') and 7.303 (dd, $J_{4',3'/4',5'}$ = 8 Hz, $J_{4',6'}$ = 1.2 Hz 1H, H-4') represent the aromatic methine protons of the benzaldehyde ring. The signals at δ_H (ppm) 7.578 (t, $J_{3,2/3,4}$ = $J_{5,4/5,6}$ =8 Hz, 2H, H-3, H-5), 7.420 (d, $J_{4,2/4,6}$ = 1.6 Hz, 1H, H-4) and 7.398 (d, $J_{2,3}$ = $J_{6,5}$ = 7.2 Hz, 2H, H-2, H-6) were assigned to the aromatic methine protons of the pyrazole moiety. While the signals at δ_H (ppm) 3.273 (s, 3H, H-11, CH_3) and 2.527 (s, 3H, H-10, CH_3) correspond to the methyl protons of the pyrazole moiety.

EI-MS: *m/z* (relative abundance in %), 369 [M^+-1] (56), 290 (100), 370 (17), 371 (54), 277 (27), 188 (64), 121 (58), and 56 (51). The EI-MS spectrum of SB4A showed a molecular ion, M^+-1, M^+ and M^++1 corresponding to a *m/z* 369, 370 and 371. The cleavage of the bromine bond produced the fragment $[C_{18}H_{16}N_3O]^+$ at *m/z* 290 corresponding to the base peak. Other prominent peaks were observed at *m/z* 277 $[C_{11}H_8BrN_3O]^+$, 188 $[C_{11}H_{11}N_2O]^+$, 121 $[C_6H_7N_3]^{3+}$, and 56 $[C_3H_6N]^{3\bullet}$.

The infrared absorption spectrum of SB4A showed vibrational bands with $\bar{\upsilon}$ (cm^{-1}) for =C-H anti-sym stretch of aromatic (3061), C-H anti-sym. stretch of aliphatic (2928) -C=O stretch of carbonyl (1651), C=N stretch of azomethine bond (1584), C=C stretch of aromatic (1563), C-N stretch (1305) and N-N stretch (1212) of pyrazole moiety.

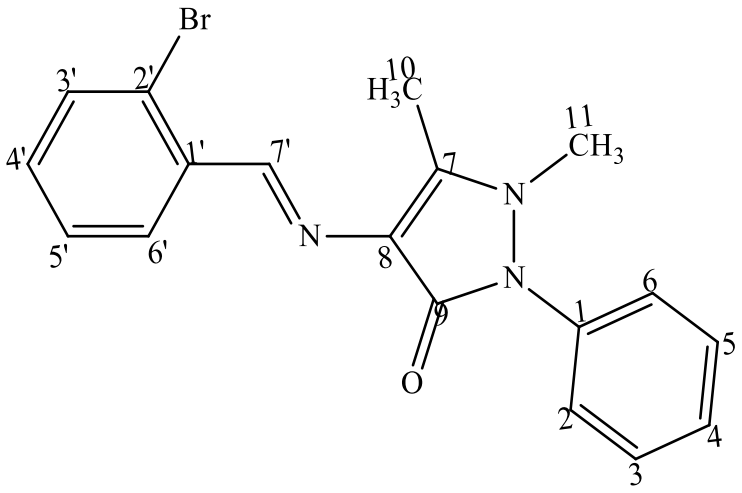

Scheme 4. 11: Structure of SB4A

4.2.12 Characterisation of 4-((3-bromobenzylidene)amino)-1,5-dimethyl-2-phenyl-1,2-dihy dro-3H-pyrazol-3-one (SB4B)

The compound 4-((3-bromobenzylidene)amino)-1,5-dimethyl-2-phenyl-1,2-dihydro-3H-pyrazol-3-one (Scheme 4.12) was obtained as yellow crystals, with a yield of 81%, and m.pt. of 195.1-196.5 ^{o}C [literature 169-170 ^{o}C (Senbagam *et al.,* 2016)].

The ^{1}H-NMR (400 MHz, MeOD-$d_{6,}$ δ_H ppm) spectrum of SB4B displayed a total of ten signals and sixteen protons. A downfield signal at δ_H (ppm) 9.522 (s,1H, H-7', CH) was assigned to the azomethine proton. The signals at δ_H (ppm) 7.996 (st, $J_{2',4'/2',6'}$ =1.6 Hz,1H, H-2'), 7.767 (d, $J_{6',5'}$ =7.6 Hz,1H, H-6'), 7.609 (td, $J_{4',3'/4',5'}$ = 8 Hz, $J_{4',2'/4',6'}$ =1.6 Hz,1H, H-4') and 7.424 (t, $J_{5',4',/5',6'}$ =7.6 Hz, 1H, H-5') were assigned to the aromatic methine protons of the benzaldehyde ring. The signals at δ_H (ppm) 7.546 (t, $J_{3,2/3,4} = J_{5,4/5,6}$ = 8 Hz, 2H, H-3, H-5), 7.396 (d, $J_{2,3} = J_{6,5}$ = 8 Hz, $J_{2,4} = J_{6,4}$ = 1.2 Hz, 2H, H-2, H-6) and 7.373 (d, $J_{4,3/4,5}$ = 7.2 Hz, 1H, H-4) represent the aromatic methine protons of the pyrazole moiety. While the signals at δ_H (ppm) 3.197 (s, 3H, H-11, CH_3) and 2.460 (s, 3H, H-10, CH_3) were assigned to the methyl protons of the pyrazole moiety.

EI-MS: *m/z* (relative abundance in %), 369 [M^++2] (71), 56 (100), 370 (22), 371 (69), 277 (25), 188 (84) and 121 (77). The EI-MS spectrum of SB4B showed a molecular ion, M^+-1, M^+ and M^++1 corresponding to a *m/z* 369, 370 and 371. The fragmentation of $[C_3H_6N]^{3\bullet}$ with *m/z* 56 from the pyrazole moiety corresponds to the base peak. Other prominent peaks were observed at *m/z* 277 $[C_{11}H_8BrN_3O]^+$, 188 $[C_{11}H_{11}N_2O]^+$, and 121 $[C_6H_7N_3]^{3+}$.

The infrared absorption spectrum of SB4B showed vibrational bands with $\bar{\upsilon}$ (cm^{-1}) for =C-H anti-sym stretch of aromatic (3052), C-H anti-sym. stretch of aliphatic (2964) -C=O stretch of carbonyl (1645), C=N stretch of the azomethine bond (1561), C=C stretch of aromatic (1490), C-N stretch (1308) and N-N stretch (1206) of pyrazole.

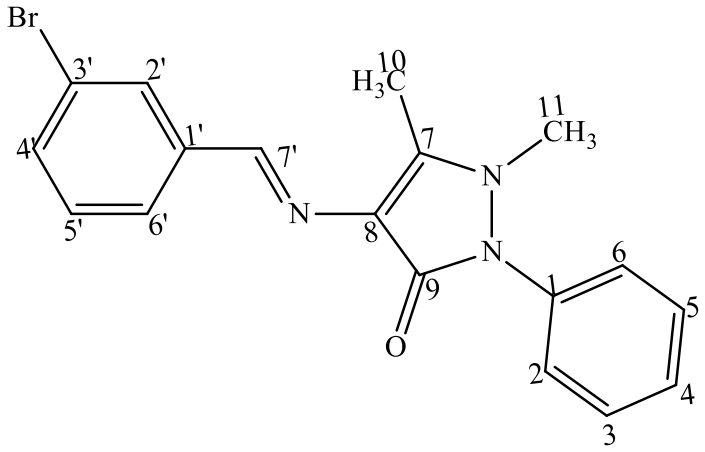

Scheme 4. 12: Structure of SB4B

4.2.13 Characterisation of 4-((4-hydroxy-3-methoxybenzylidene)amino)-1,5-dimethyl-2-phenyl-1,2-dihydro-3H-pyraz- ol-3-one (SB5)

The compound 4-((4-hydroxy-3-methoxybenzylidene)amino)-1,5-dimethyl-2-phenyl-1,2-dihydro-3H-pyraz- ol-3-one (Scheme 4.13) appeared as pale yellow crystals with a yield of 82%, and m.pt. of 207.1-208.3 ^{o}C [literature 207 ^{o}C (Shoaib *et al.,* 2015)].

The ^{1}H NMR (500 MHz, MeOD-$d_{6,}$ δ_H ppm) spectrum of SB5 displayed a total of eleven signals and nineteen protons. The azomethine proton was observed downfield at δ_H (ppm) 9.395 (s, 1H, H-7', CH). Six signals at δ_H (ppm) 7.560 (t, $J_{3,2/3,4}$ = $J_{5,4/5,6}$ = 7.5 Hz, 2H, H-3, H-5), 7.511 (d, $J_{2',6'}$ = 2 Hz, 1H, H-2'), 7.445 (d, $J_{6',5'}$ = 7 Hz, 1H, H-6') 7.412 (d, $J_{2,3,}$ = $J_{6,5}$ = 8 Hz, $J_{2,4}$ = $J_{6,4}$ = 1 Hz, 2H, H-2, H-6), 7.221 (dd, $J_{4,3/4,5}$ = 8 Hz, $J_{4,2/4,6}$ = 1.5 Hz, 1H, H-4), and 6.845 (d, $J_{5',6'}$ = 8 Hz, 1H, H-5') were assigned to the aromatic methine protons. Three upfield signals at δ_H (ppm) 3.913 (s, 3H, H-8', OCH_3) 3.203 (s, 3H, H-11, CH_3) and 2.475 (s, 3H, H-10, CH_3) corresponds to the methoxy and two methyl protons. The hydroxyl proton expected to resonate downfield was not captured in the spectra due to the exchange of proton with the solvent (methanol) used.

EI-MS: *m/z* (relative abundance in %), 337 [M^+] (100), 56 (66), 245 (22), 228 (25), 121 (17), and 188.1 (11). The EI-MS spectrum of SB5 showed the molecular ion, M^+ as the base peak at *m/z* 337. Other prominent peaks were observed at *m/z* 245 $[C_{12}H_{11}N_3O_3]^+$, 228 $[C_{12}H_{11}N_3O_2]^{2+}$, 188 $[C_{11}H_{11}N_2O]^+$, 121 $[C_6H_7N_3]^{3+}$, and 56 $[C_3H_6N]^{3\bullet}$.

The infrared absorption spectrum of SB5 showed vibrational bands with $\bar{\upsilon}$ (cm^{-1}) for O-H stretch of the hydroxyl on the benzylidene (3653), =C-H anti-sym stretch of aromatic (3105), C-H anti-sym. stretch of aliphatic (2942) -C=O stretch of carbonyl (1627), C=N stretch of the azomethine bond (1580), C=C stretch of aromatic (1517), C-O bend of the hydroxyl (1416), C-N stretch of pyrazolone (1345), C-O stretch of the hydroxyl (1285), C-O of the methoxyl (1256 and 1037) and N-N stretch of pyrazole (1214).

The analysis of the UV spectrum of SB5 in chloroform revealed maximum absorption bands (nm) at 259, and 337, these absorption bands indicate n-π* transitions.

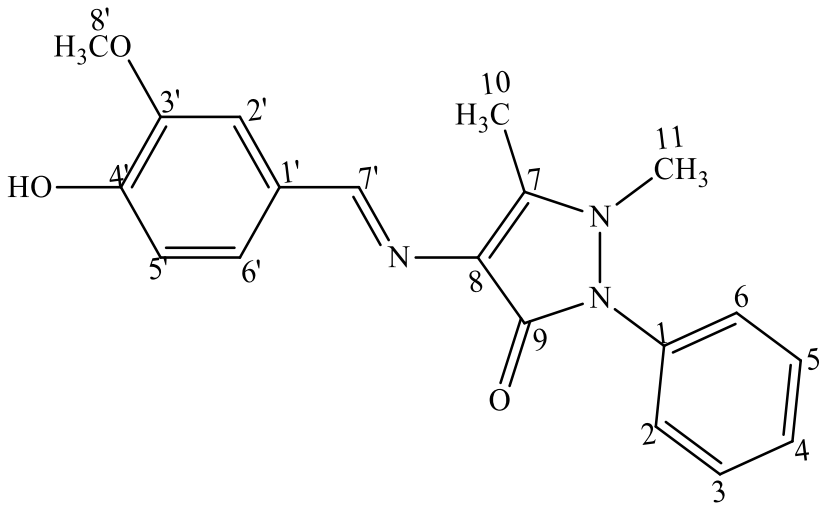

Scheme 4. 13: Structure of SB5

4.2.14 Characterisation of 4-((2-hydroxy-3-methoxybenzylidene)amino)-1,5-dimethyl-2-phenyl-1,2-dihydro-3H-pyrazol-3-one (SB5A)

The compound 4-((2-hydroxy-3-methoxybenzylidene)amino)-1,5-dimethyl-2-phenyl-1,2-dihydro-3H-pyrazol-3-one (Scheme 4.14) appeared as yellow crystals with a yield of 89% (0.1198 g), and m.pt. of 230.1-234.4 ^{o}C.

The ^{1}H NMR (400 MHz, DMSO-$d_{6,}$ δ_H ppm) spectrum of SB5A displayed a total of eleven signals and nineteen protons. A downfield signal at δ_H (ppm)13.011 (s, 1H, H-4', OH) was assigned to the hydroxyl proton on the benzaldehyde ring. A signal at δ_H (ppm) 9.673 (s,1H, CH, H-7') was assigned to the azomethine proton. Three signals at δ_H (ppm)7.553 (dt, t, $J_{3,2/3,4} = J_{5,4/5,6} = 7.6$ Hz, $J_{3,5} = J_{5,3} = 1.6$ Hz, 2H, H-3, H-5), 7.409 (dd, $J_{2,3} = J_{6,5,} = 7.6$ Hz, $J_{2,4/2,6} = J_{6,4/6,2} = 1.2$ Hz, 2H, H-2, H-6) and 7.375 (d, $J_{4,2/4,6} = 1.2$Hz, 1H, H-4) correspond to the aromatic methine protons of the pyrazole moiety. The signals at δ_H (ppm) 7.059 (dd, $J_{6',5'} = 8$ Hz, $J_{6',4'} = 1.2$ Hz, 1H, H-6'), 7.039 ($J_{4',5'} = 6.8$ Hz, 1H, H-4') and 6.860 (t, $J_{5',4'/5',6'} = 8$ Hz,1H, H-5') represent the aromatic methine protons on the benzaldehyde ring. Three upfield signals observed at δ_H (ppm) 3.796 (s, 1H, H-8', OCH_3). 3.202 (s, 3H, H-11, CH_3) and 2.399 (s, 3H, H-10, CH_3) correspond to the methoxy and two methyl protons.

EI-MS: *m/z* (relative abundance %), 337 [M^+] (100), 245 (18), 121 (16), 188 (20), and 56 (28). The EI-MS spectrum of SB5 showed the molecular ion, M^+ as the base peak at *m/z* Other prominent peaks were observed at *m/z* 245 $[C_{12}H_{11}N_3O_3]^+$, 228 $[C_{12}H_{11}N_3O_2]^{2+}$, 188 $[C_{11}H_{11}N_2O]^+$, 121 $[C_6H_7N_3]^{3+}$, and 56 $[C_3H_6N]^{3\bullet}$.

The infrared absorption spectrum of SB5A showed vibrational bands with $\bar{\upsilon}$ (cm^{-1}) for O-H stretch of the hydroxyl (3736), =C-H anti-sym stretch of aromatic (3069),C-H anti-sym. stretch of aliphatic (2924) -C=O stretch of carbonyl (1664), C=N stretch of the azomethine bond (1593), C=C stretch of aromatic (1487), C-O bend of hydroxyl (1419), C-N stretch of pyrazole (1296), C-O of the methoxy (1247 and 1068) and N-N stretch of pyrazole (1170).

The analysis of the UV spectrum of SB5A in chloroform revealed maximum absorption band (nm) at 335. This wavelength indicates n-π^* transitions.

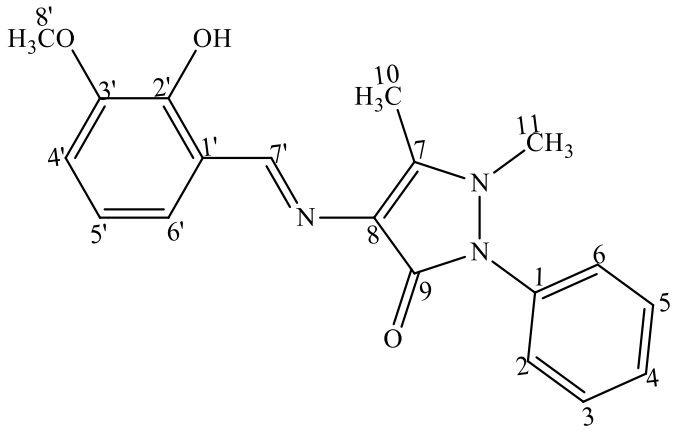

Scheme 4. 14: Structure of SB5A

4.2.15 Characterisation of 4-((3-hydroxy-4-methoxybenzylidene)amino)-1,5-dimethyl-2-phenyl-1,2-dihydro-3H-pyrazol-3-one (SB5B)

The compound 4-((3-hydroxy-4-methoxybenzylidene)amino)-1,5-dimethyl-2-phenyl-1,2-dihydro-3H-pyrazol-3-one (scheme 4.15) was obtained as pale yellow crystals with yield 92%, and m.pt. of 243.8-244.5 ^{o}C [literature 246.8-247.2 ^{o}C (Teran *et al.*, 2019].

The ^{1}H NMR (500 MHz, MeOD-d_6, δ_H ppm) spectrum displayed a total of eleven signals and nineteen protons. A signal at δ_H (ppm) 9.388 (s, 1H, CH, H-7') was assigned to the azomethine proton. Six signals at δ_H (ppm) 7.565 (dt, $J_{3,2/3,4} = J_{5,4/5,6}$ = 7.5 Hz, $J_{3,5} = J_{5,3}$ = 1.5 Hz, 2H, H-3, H-5), 7.454 (dt, $J_{2',6'}$ = 2.5Hz, 1H, H-2'), 7.422 (dd, $J_{4,2/4,6}$ = 2 Hz, 1H, H-4), 7.397 ($J_{2,4/2,6} = J_{6,4,/6,2}$ = 2 Hz, 2H, H-2, H-6), 7.214 (dd, $J_{6',5'}$ = 8.5Hz, $J_{6',2'}$ = 2Hz, 1H, H-6'), and 6.980 (d, $J_{5',6'}$ = 8.5Hz, 1H, H-5') were assigned to the aromatic methine protons. Three upfield signals for the methoxy, and two methyl protons were observed at δ_H (ppm) 3.896 (s, 1H, H-8', OCH_3), 3.218 (s, 3H, H-11, CH_3) and 2.484 (s,3H, H-10, CH_3). The hydroxyl proton expected to resonate downfield was not captured in the spectra due to the exchange of proton with the solvent (methanol) used.

EI-MS: *m/z* (relative abundance in %), 337 [M^+] (70), 56 (100), 245 (30), 228 (33), 188 (28), and 121 (35). The EI-MS spectrum showed the molecular ion, M^+ at *m/z* 336. The fragment $[C_3H_6N]^{3\bullet}$ with *m/z* 56 from the pyrazole moiety corresponds to the base peak. Other prominent fragment peaks are observed at *m/z* 245 $[C_{12}H_{11}N_3O_3]^+$, 228 $[C_{12}H_{11}N_3O_2]^{2+}$, 188 $[C_{11}H_{11}N_2O]^+$, and 121 $[C_6H_7N_3]^{3+}$.

The infrared absorption spectrum showed characteristic absorption bands for O-H stretch of hydroxyl (3740), =C-H anti-sym stretch of aromatic (3069), C-H anti-sym. stretch of aliphatic (2963) -C=O stretch of the carbonyl (1615), C=N stretch of the azomethine bond (1568), C=C stretch of aromatic (1519), C-O bend of hydroxyl (1425), C-O stretch of hydroxyl (1288), C-N stretch of pyrazole (1310) C-O of the methoxy (1255 and 1027) and N-N stretch of pyrazole (1215).

The analysis of the UV spectrum in chloroform revealed maximum absorption bands (nm) at 260 and 337 which indicate n-π* transitions.

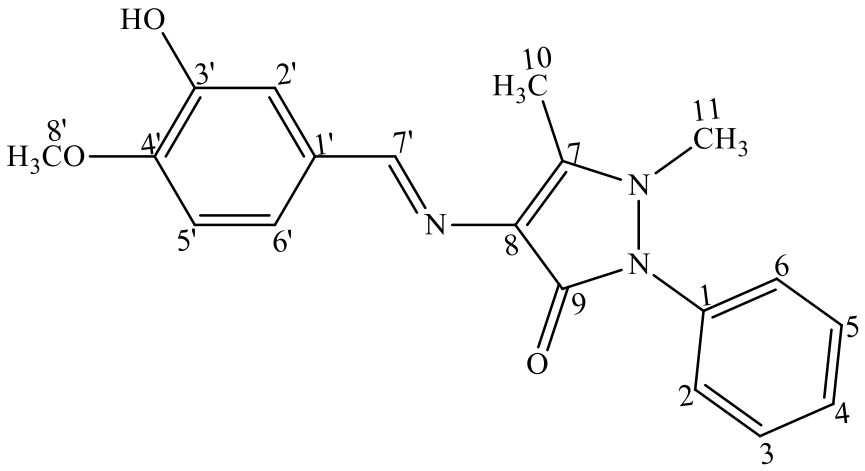

Scheme 4. 15: Structure of SB5B

4.2.16 Characterisation of 4-((4-methoxybenzylidene)amino)-1,5-dimethyl-2-phenyl-1,2-dihydro-3H-pyrazol-3-one (SB6)

The compound 4-((4-methoxybenzylidene)amino)-1,5-dimethyl-2-phenyl-1,2-dihydro-3H-pyrazol-3-one (Scheme 4.16) was obtained as dark cream crystals, with 78% yield, and m.pt. of 171.9-172.5 ^{o}C [literature 169.8-170.3 ^{o}C (Teran *et al.*, 2019)].

The ^{1}H NMR (500 MHz, MeOD-d_6, δ_H ppm) spectrum displayed a total of nine signals and nineteen protons. A downfield signal at δ (ppm)9.455 (s,1H, CH, H-7') was assigned to the azomethine proton. Two signals at δ_H (ppm) 7.781 (dd, $J_{2',3'} = J_{6',5'} = 8.5$ Hz, $J_{2',6'} = J_{6',2'} = 3$ Hz, 2H, H-2', H-6') and 6.991 (d, $J_{3',2'} = J_{5',6'} = 8.5$ Hz, $J_{3',5'} = J_{5',3'} = 1$ Hz, 2H, H-8', H-5') appeared as doublets corresponding to the chemically equivalent methine protons on the benzaldehyde ring. The signals at δ_H (ppm) 7.564 (t, $J_{3,4/3,1} = J_{5,4/5,6} = 8$ Hz, $J_{3,5} = J_{5,3} = 1.5$ Hz, 2H, H-3, H-5), 7.451 (d, $J_{4,3/4,5} = 7.5$ Hz, $J_{4,2/4,6}$,=1 Hz, 1H, H-4) and 7.421 (dd, $J_{2,3} = J_{6,5} = 8.5$ Hz, $J_{2,4/2,6} = J_{6,4,/6,2} = 1$ Hz, 2H, H-2, H-6) were assigned to the aromatic methine protons of the pyrazole moiety. While the signals at δ_H (ppm) 3.838 (s, 3H, H-8', OCH_3), 3.215 (s, 3H, H-11, CH_3) and 2.482 (s, 3H, H-10, CH_3) were assigned to the methoxy and two methyl protons, respectively.

EI-MS: *m/z* (relative abundance in %), 321 [M^+] (100), 229 (22), 212 (20), 188 (14), 121 (20), and 56 (71). The EI-MS spectrum showed the molecular ion (and the base peak) M^+ at *m/z* 321. Other prominent fragment peaks were observed at *m/z* 229 $[C_{12}H_{11}N_3O_2]^+$, 212 $[C_{12}H_{11}N_3O]^{2+}$, 188 $[C_{11}H_{11}N_2O]^+$, 121$[C_6H_7N_3]^{3+}$ and 56 $[C_3H_6N]^{3\bullet}$.

The infrared absorption spectrum showed characteristic vibrational frequencies $\bar{\upsilon}$ (cm^{-1}) for =C-H anti-sym stretch of aromatic (3050), C-H anti-sym. stretch of aliphatic (2934) -C=O stretch of the carbonyl (1646), C=N stretch of the azomethine bond (1592), C=C stretch of aromatic (1506), C-N stretch of pyrazole (1306), C-O of the methoxy (1247 and 1029) and N-N stretch of pyrazole (1163).

The analysis of the UV spectrum in chloroform revealed maximum absorption bands (nm) at 249, 261, 266 and 333. The longer wavelength at 338 261 and 260 indicate n-π* transitions. The absorptions at 249 showed π-π* transitions.

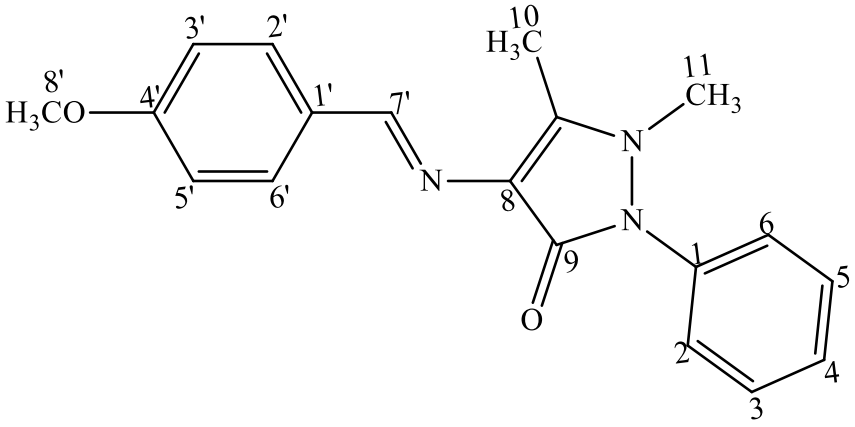

Scheme 4. 16: Structure of SB6

4.2.17 Characterisation of 4-((2-methoxybenzylidene)amino)-1,5-dimethyl-2-phenyl-1,2-dihydro-3H-pyrazol-3-one (SB6A)

The compound 4-((2-methoxybenzylidene)amino)-1,5-dimethyl-2-phenyl-1,2-dihydro-3H-pyrazol-3-one (Scheme 4.17) appeared as yellow crystals, with 87% yield, and m.pt. of 214.5-215.5 ^{o}C [literature 220 ^{o}C (Hokelek *et al.*, 2001)].

The ^{1}H NMR (400 MHz, MeOD-d_6, δ_H ppm) spectrum displayed a total of ten signals and nineteen protons. A downfield signal at δ_H (ppm) 9.891(s,1H, H-7', CH) was assigned to the azomethine proton. Four signals 8.070 (dd, $J_{6',5'}$ = 8 Hz, $J_{6',4'}$ = 1.6 Hz, 1H, H-6'), 7.453 (d, $J_{4',3'/4',5'}$ = 7.6 Hz, 1H, H-4'), 7.035 (d, $J_{5',4'/5',6'}$ = 8.4 Hz, 1H, H-5') and 6.986 (d, $J_{3',4'}$ = 7.2 Hz, 1H, H-3') represent aromatic methine protons on the benzaldehyde ring. The signals at δ_H (ppm) 7.567 (t, $J_{3,4/3,2}$ = $J_{5,4/5,6}$ = 7.6 Hz, 2H, H-3, H-5) 7.414 (dd, $J_{2,3}$ = $J_{6,5}$ = 7.6 Hz, $J_{2,4/2,6}$ = $J_{6,4/6,2}$ = 1.2 Hz, 2H, H-2, H-6) and 7.365 (d, $J_{4,2/4,6}$, = 1.6 Hz, 1H, H-4) were assigned to the aromatic methine protons of the pyrazole moiety. While the signals at δ_H (ppm) 3.863 (s, 3H, H-8', OCH_3), 3.228 (s, 3H, H-11, CH_3) and 2.498 (s, 3H, H-10, CH_3) were assigned to the methoxy proton and the two methyl protons, respectively.

EI-MS: *m/z* (relative abundance in %), 321 [M^+] (100), 322 (37), 229 (75), 188 (35), 121 (40), and 56 (67), The EI-MS spectrum showed the molecular ion (and the base peak) M^+ at *m/z* 321. Molecular ion M^++1 peak at *m/z* 322 was also observed. Other prominent fragment peaks were observed at *m/z* 229 $[C_{12}H_{11}N_3O_2]^+$, 188 $[C_{11}H_{11}N_2O]^+$, 121 $[C_6H_7N_3]^{3+}$ and 56 $[C_3H_6N]^{3\bullet}$.

The infrared absorption spectrum showed characteristic vibrational bands for =C-H anti-sym stretch of aromatic (3066), C-H anti-sym. stretch of aliphatic (2931) -C=O stretch of the carbonyl (1650), C=N stretch of the azomethine bond (1594), C=C stretch of aromatic (1571), C-N stretch of pyrazole (1304), C-O of the methoxy (1245 and 1043) and N-N stretch of pyrazole (1178).

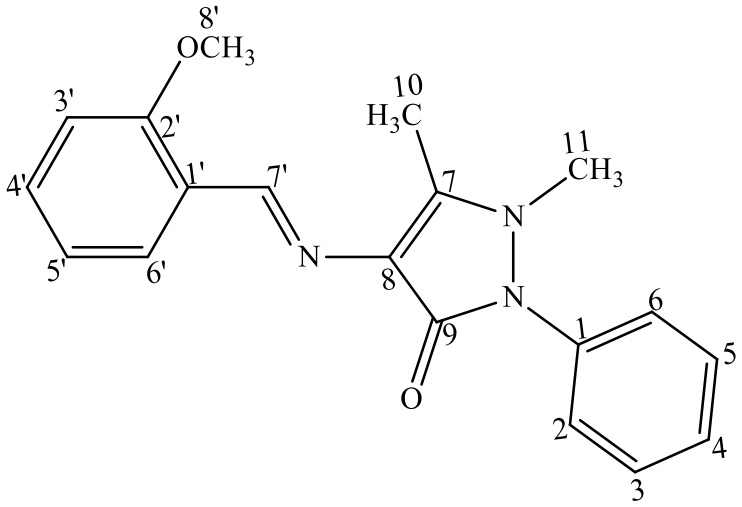

Scheme 4. 17: Structure of SB6A

4.2.18 Characterisation of 4-((3-methoxybenzylidene)amino)-1,5-dimethyl-2-phenyl-1,2-dihydro-3H-pyrazol-3-one (SB6B)

The compound 1,5-dimethyl-4-((4-methylbenzylidene)amino)-2-phenyl-1,2-dihydro-3H-pyrazol-3-one (4.18) appeared as pale yellow crystals, with 90% yield, and m.pt. of 126.8-127.4 ^{o}C.

The ^{1}H NMR (400 MHz, MeOD-d_6, δ_H ppm) spectrum displayed a total of ten signals and nineteen protons. A downfield signal at δ_H (ppm) 9.499 (s, 1H, H-7', CH) was assigned to the azomethine proton. Four signals at δ_H (ppm) 7.466 (d, $J_{6',5'}$ = 7.6 Hz, 1H, H-6'), 7.397 (s, 1H, H-2'), 7.323 (d, $J_{5',4'/5',6'}$ = 7.6 Hz, 1H, H-5') and 6.991 (d, $J_{4',5'}$ = 7.6 Hz, $J_{4',6'/4',2'}$ = 2H, H-4') were assigned to the aromatic methine protons on the benzaldehyde ring. The signals at δ_H (ppm) 7.575 (t, $J_{3,4/3,2} = J_{5,4/5,6}$ = 7.6 Hz, 2H, H-3, H-5) 7.428 (dd, $J_{2,3} = J_{6,5}$ = 7.6 Hz, $J_{2,4/2,6} = J_{6,4/6,2}$ = 1.6 Hz, 2H, H-2, H-6) and 7.365 (d, $J_{4,3/4,5}$ =7.6 Hz, $J_{4,2/4,6}$ = 1.6 Hz, 1H, H-4) were assigned to the aromatic methine protons of the pyrazole moiety. While the signals at δ_H (ppm) 3.840 (s, 3H, H-8', OCH_3), 3.244 (s, 3H, H-11, CH_3) and 2.507 (s, 3H, H-10, CH_3) were assigned to the methoxy protons and two methyl protons, respectively.

EI-MS: *m/z* (relative abundance in %), 321 [M^+] (100), 322 (54), 229 (50), 212 (33), 188 (53), 121 (53), 77(18) and 56 (77). The EI-MS spectrum showed the molecular ion (and the base peak) M^+ at *m/z* 321. Molecular ion M^++1 peak at *m/z* 322 was also observed. Other prominent fragment peaks were observed at *m/z* 229 $[C_{12}H_{11}N_3O_2]^+$, 212 $[C_{12}H_{11}N_3O]^{2+}$, 188 $[C_{11}H_{11}N_2O]^+$, 121 $[C_6H_7N_3]^{3+}$, 77 $[C_6H_5]^+$ and 56 $[C_3H_6N]^{3\bullet}$.

The infrared absorption spectrum showed characteristic vibrational bands for -C=O stretch of the carbonyl (1652), C=N stretch of the azomethine bond (1572), C=C stretch of aromatic (1486), C-N stretch of pyrazole (1264), C-O of the methoxy (1264 and 1045) and N-N stretch of pyrazole (1129).

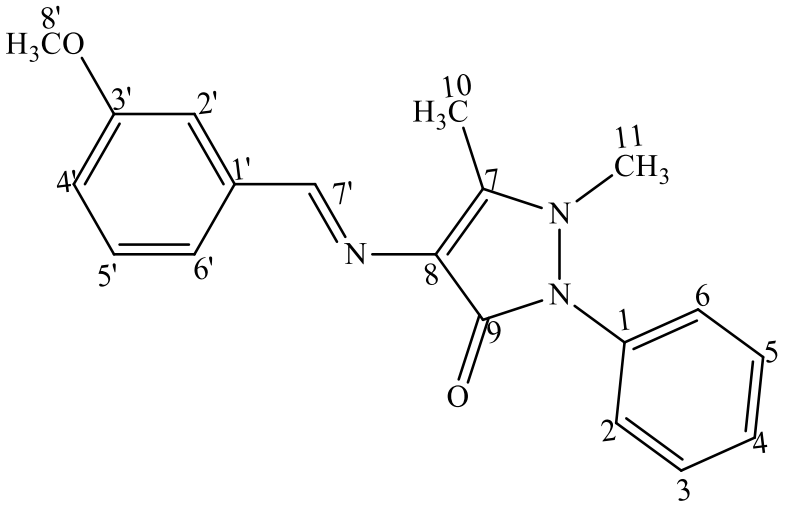

Scheme 4. 18: Structure of SB6B

4.2.19 Characterisation of 1,5-dimethyl-4-((4-methylbenzylidene)amino)-2-phenyl-1,2-dihydro-3H-pyrazol-3-one (SB7)

The compound 1,5-dimethyl-4-((4-methylbenzylidene)amino)-2-phenyl-1,2-dihydro-3H-pyrazol-3-one (Scheme 4.19) was obtained as yellow crystals, with 74% yield, and m.pt. of 184.3-184.8 ^{o}C.

The ^{1}H NMR (500 MHz, MeOD-d_6, δ_H ppm) spectrum displayed a total of nine signals and nineteen protons. A downfield signal at δ_H (ppm) 9.490 (s, 1H, H-7', CH) was assigned to the azomethine proton. Two signals at δ_H (ppm) 7.716 (d, $J_{2',3'} = J_{6',5'} = 8$ Hz, 2H, H-2', H-6') and 7.250 (d, $J_{3',2'} = J_{5',4'} = 8$ Hz, 2H, H-3', H-5') appeared as doublets corresponding to the chemically equivalent methine protons on the benzaldehyde ring. The signals at δ (ppm) 7.568 (t, $J_{3,4/3,2} = J_{5,4/5,4} = 8$ Hz, $J_{3,5} = J_{5,3} = 2$ Hz, 2H, H-3, H-5), 7.457 (t, $J_{4,3/4,5} = 7.5$ Hz, 1H, H-4) and 7.415 (dd, $J_{2,3} = J_{6,5} = 9$ Hz, $J_{2,4/2,6} = J_{6,4/6,2} = 1.5$ Hz, 2H, H-2, H-6) were assigned to the aromatic methine protons of the pyrazole moiety. While the signals at δ_H (ppm) 3.230 (s, 3H, H-11, CH_3) 2.494 (s, 3H, H-10, CH_3) and 2.373 (s, 3H, H-8', CH_3) represent the three methyl protons.

EI-MS: *m/z* (relative abundance in %), 305 [M^+] (100), 213 (25), 188 (20), 121 (26), and 56 (61). The EI-MS spectrum showed the molecular ion (and the base peak) M^+ at *m/z* 305. Other prominent fragment peaks were observed at *m/z* 213 $[C_{12}H_{11}N_3O]^+$, 188 $[C_{11}H_{11}N_2O]^+$, 121 $[C_6H_7N_3]^{3+}$and 56 $[C_3H_6N]^{3\bullet}$.

The infrared absorption spectrum showed vibrational bands with characteristic vibrational frequencies $\bar{\upsilon}$ (cm^{-1}) for =C-H anti-sym stretch of aromatic (3056), C-H anti-sym. stretch of aliphatic (2920) -C=O stretch of the carbonyl (1653), C=N stretch of the azomethine bond (1577), C=C stretch of aromatic (1498), C-N stretch (1302) and N-N stretch (1213) of pyrazole moiety.

The analysis of the UV spectrum in chloroform revealed maximum absorptions bands (nm) at 259, 327 which indicates n-π* transitions.

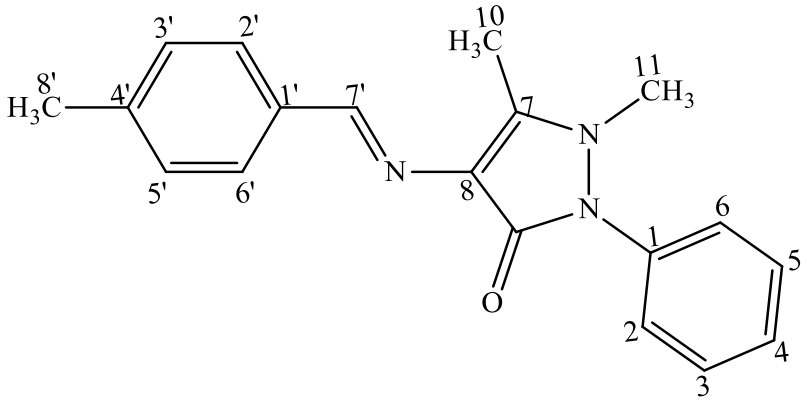

Scheme 4. 19: Structure of SB7

4.2.20 Characterisation of 4-(((1,5-dimethyl-3-oxo-2-phenyl-2,3-dihydro-1H-pyrazol-4-yl)imino)methyl)benzonitrile (SB8)

The compound 4-(((1,5-dimethyl-3-oxo-2-phenyl-2,3-dihydro-1H-pyrazol-4-yl)imino) methyl)benzonitrile (Scheme 4.20) was obtained as a yellow powder with 85% yield, and m.pt. of 300-301.4 ^{o}C.

The ^{1}H NMR (500 MHz, DMSO-d_6, δ_H ppm) spectrum displayed a total of eight signals and sixteen protons. A downfield signal at δ_H (ppm) 9.599 (s,1H, H-7', CH) was assigned to the azomethine proton. Two signals at δ_H (ppm) 7.980 (d, $J_{2',3'} = J_{6',5'} = 8$ Hz, 2H, H-2', H-6') and 7.894 (d, $J_{3',2'} = J_{5',6'} = 8.5$ Hz, 2H, H-3', H-5') appeared as doublets corresponding to the chemically equivalent aromatic methine protons on the benzaldehyde ring. The electron withdrawing effect of the cyano substituent on the benzaldehyde deshielded the methine group on the benzaldehyde and thus caused them to resonate more downfield relative to other aromatic protons in the spectrum. The signals at δ_H (ppm) 7.548 (t, $J_{3,4/3,2} = J_{5,4/5,6} = 8$ Hz, $J_{3,5} = J_{5,3} = 2$Hz, 2H, H-3, H-5), 7.406 (d, $J_{4,3/4,5} = 7.5$ Hz, 1H, H-4) and 7.373 (dd, $J_{2,3} = J_{6,5} = 8.5$ Hz, $J_{2,4/2,6} = J_{6,4/6,2} = 1$ Hz, 2H, H-2, H-6) were assigned to the aromatic methine protons of the pyrazole moiety. While the signals at δ_H (ppm) 3.226 (s, 3H, H-11, CH_3) and 2.475 (s, 3H, H-10, CH_3) correspond to the methyl protons of the pyrazole moiety.

EI-MS: *m/z* (relative abundance in %), 316 [M^+] (100), 224 (20), 188 (30), 121 (36) and 56 (52). The EI-MS spectrum showed the molecular ion (and the base peak) M^+ at *m/z* 316. Other prominent fragment peaks were observed at *m/z* 224 $[C_{12}H_8N_4O]^+$, 188 $[C_{11}H_{11}N_2O]^+$, 121 $[C_6H_7N_3]^{3+}$and 56 $[C_3H_6N]^{3\bullet}$.

The infrared absorption spectrum showed characteristic vibrational bands with $\bar{\upsilon}$ (cm^{-1}) for =C-H anti-sym stretch of aromatic (3062), C-H anti-sym. stretch of aliphatic (2925) -C=O stretch of the carbonyl on the pyrazole moiety (1648), C=N stretch of the azomethine bond (1590), C=C stretch of aromatic (1564), C≡N stretch of the cyano substituent (2222), C-N stretch (1307) and N-N stretch (1171) of pyrazole moiety.

The analysis of the UV spectrum in chloroform revealed maximum absorption bands (nm) at 260, 267, and 360 which indicate the n-π* transitions.

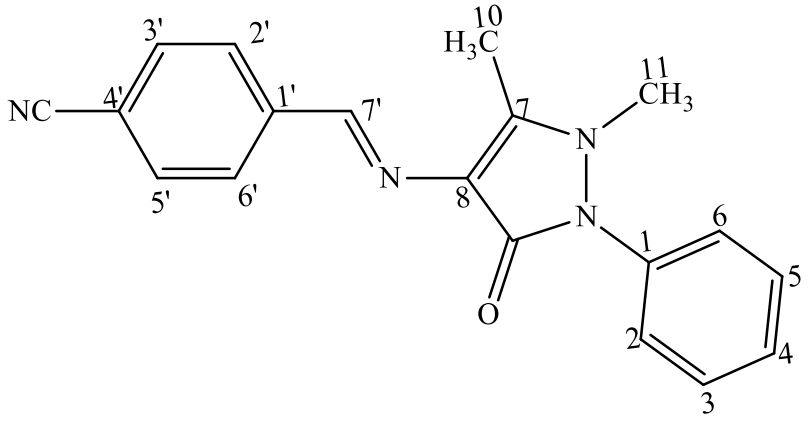

Scheme 4. 20: Structure of SB8

4.2.21 Characterisation of 4-(3-hydroxybenzylideneamino)-1,2-dihydro-2,3-dimethyl-1-phenylpyrazol-5-one (SB9)

The compound 4-(3-hydroxybenzylideneamino)-1,2-dihydro-2,3-dimethyl-1-phenylpyrazol-5-one (Scheme 4.21) was obtained as pale-yellow crystals with 86% yield, and m.pt. of 270.3-271.4 °C [literature 228-230 ^{o}C (Kasyap *et al.*, 2018)].

The ^{1}H NMR (500 MHz, DMSO-d_6, δ_H ppm) spectrum displayed a total of eleven signals and seventeen protons. A downfield signal at δ_H (ppm) 9.547 (s, 1H, H-3', OH) was assigned to the hydroxyl proton on the benzaldehyde ring. The signals at δ_H (ppm) 9.474 (s,1H, H-7', CH) corresponds to the azomethine proton. Four signals at δ_H (ppm) 7.355 (d, $J_{2',6'/2',4'}$ = 2.5 Hz, 1H, H-2'), 7.251 (d, $J_{6',5'}$ = 8 Hz, $J_{6',2'/6',4'}$ = 3 Hz, 1H, H-6'), 7.179 (d, $J_{5',4'}$ = 7.5 Hz, 1H, H-5') and 6.825 (d, $J_{4',5'}$ = 8 Hz, $J_{4',2'/4',6'}$ = 2.5 Hz, 1H, H-4') were assigned to the aromatic methine protons on the benzaldehyde ring. The signals at δ_H (ppm) 7.535 (t, $J_{3,4/3,2} = J_{5,4/5,6}$ = 8 Hz, $J_{3,5} = J_{5,3}$ = 2 Hz, 2H, H-3, H-5), 7.376 (dd, $J_{2,3} = J_{6,5}$ = 9 Hz, $J_{2,4/2,6} = J_{6,4/6,2}$ = 1.5 Hz, 2H, H-2, H-6) and 7.235 (d, $J_{4,3/4,5}$ = 7.5 Hz, 1H, H-4) were assigned to the aromatic methine protons of the pyrazole moiety. While the upfield signals at δ_H (ppm) 3.164 (s, 3H, H-11, CH_3) and 2.434 (s, 3H, H-10, CH_3) correspond to the methyl protons of the pyrazole moiety.

EI-MS: *m/z* (relative abundance in %), 307 [M^+] (100), 215 (23), 188 (29), 121 (34), and 56 (54). The EI-MS spectrum showed the molecular ion (and the base peak) M^+ at *m/z* 307. Other prominent fragment peaks were observed at *m/z* 215 $[C_{12}H_9N_3O_2]^+$, 188 $[C_{11}H_{11}N_2O]^+$, 121 $[C_6H_7N_3]^{3+}$and 56 $[C_3H_6N]^{3\bullet}$.

The infrared absorption spectrum showed diagnostic bands with vibrational frequencies $\bar{\upsilon}$ (cm^{-1}) for O-H stretch of the hydroxyl (3144), C=O stretch of the carbonyl (1619), C=N stretch of the azomethine bond (1591), C=C stretch of aromatic (1558), C-O bend of hydroxyl (1389), C-N stretch of pyrazole (1308), C-O stretch of hydroxyl (1236), and N-N stretch of pyrazole (1171).

The analysis of the UV spectrum of SB9 in chloroform revealed maximum absorption bands (nm) at 260 and 266 which indicate n-π* transitions.

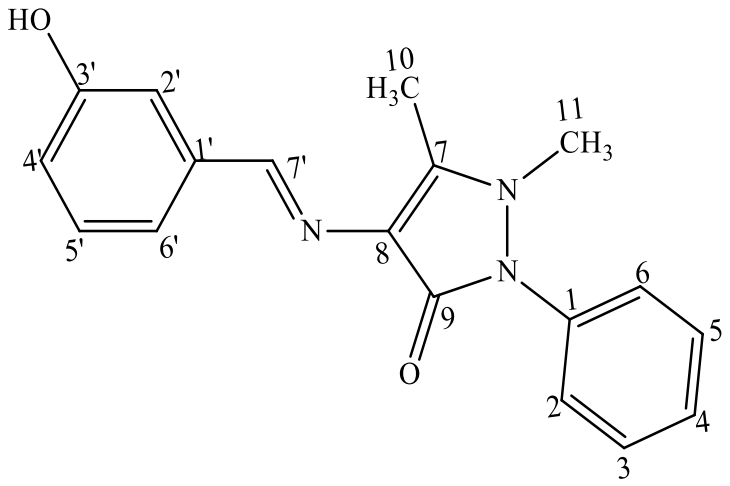

Scheme 4. 21: Structure of SB9

4.2.22 Characterisation of 4-(4-hydroxybenzylideneamino)-1,2-dihydro-2,3-dimethyl-1-phenylpyrazol-5-one (SB9B)

The compound 4-(4-hydroxybenzylideneamino)-1,2-dihydro-2,3-dimethyl-1-phenylpyrazol-5-one (Scheme 4.22) was obtained as cream crystals, with 89% yield, and m.pt. 229.6-230.1 °C [literature 202 ºC (Baluja and Chanda, 2016)].

The ^{1}H NMR (500 MHz, DMSO-$d_{6,}$ δ_H ppm) spectrum displayed a total of nine signals and seventeen protons. A downfield signal at δ (ppm) 9.885 (s, 1H, H-4', OH) was assigned to the hydroxyl proton on the benzaldehyde ring. A downfield signal at δ_H (ppm) 9.454 (s,1H, H-7', CH) was assigned to the azomethine proton. Two signals at δ_H (ppm) 7.642 (d, $J_{2',3'}$ = $J_{6',5'}$ = 8.5 Hz, 2H, H-2', H-6') and 6.833 (d, $J_{3',2'}$ = $J_{5',6'}$ = 8.5 Hz, 2H, H-3', H-5') were observed as doublets corresponding to the chemically equivalent methine protons on the benzaldehyde ring. The signals at δ_H (ppm) 7.524 (t, $J_{3,4/3,2}$ = $J_{5,4/5,6}$ = 8 Hz, 2H, H-3, H-5), 7.370 (d, $J_{2,3}$ = $J_{6,5}$ = 7.5 Hz, 2H, H-2, H-6) and 7.343 (d, $J_{4,3/4,5}$ = 7.5 Hz, 1H, H-4) were assigned to the aromatic methine protons of the pyrazole moiety. While the signals at δ_H (ppm) 3.118 (s, 3H, H-10, CH_3) and 2.407(s, 3H, H-11, CH_3) correspond to the methyl protons of the pyrazole moiety.

EI-MS: *m/z* (relative abundance in %), 321 [M^+] (100), 215 (47), 188 (34), 121 (23), and 56 (62). The EI-MS spectrum showed the molecular ion (and the base peak) M^+ at *m/z* 307. Other prominent fragment peaks were observed at *m/z* 215 $[C_{12}H_9N_3O_2]^+$, 188 $[C_{11}H_{11}N_2O]^+$, 121 $[C_6H_7N_3]^{3+}$and 56 $[C_3H_6N]^{3\bullet}$.

The infrared absorption spectrum showed vibrational bands with characteristic vibrational frequencies $\bar{\upsilon}$ (cm^{-1}) for O-H stretch of the hydroxyl on the benzylidene (3591), =C-H anti-sym stretch of aromatic (3060), -C=O stretch of carbonyl (1605), C=N stretch of the azomethine bond (1578), C=C stretch of aromatic (1511), C-O bend of hydroxy (1389), C-N stretch of pyrazole (1318), C-O stretch of hydroxyl (1239), and N-N stretch of pyrazole (1161).

The analysis of the UV spectrum in chloroform revealed maximum absorption bands (nm) at 267, 333 and 2334 which indicate n-π* transitions.

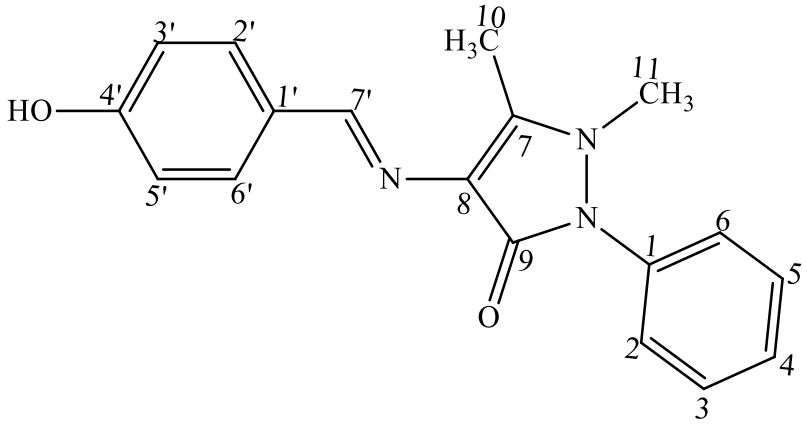

Scheme 4. 22: Structure of SB9B

4.2.23 Characterisation of 4-((3-hydroxy-4-nitrobenzylidene)amino)-1,5-dimethyl-2-phenyl -1,2-dihydro-3H-pyrazol-3-one (SB10)

The compound 4-((3-hydroxy-4-nitrobenzylidene)amino)-1,5-dimethyl-2-phenyl-1,2-dihydro-3H- pyrazol-3-one (Scheme 4.23) appeared as bright orange crystals, with 95% yield, and m.pt. of 232.8-234.5 ^{o}C.

The ^{1}H-NMR (500MHz, DMSO-$d_{6,}$ δ_H ppm) spectrum displayed a total of ten signals and sixteen protons. The downfield signals at δ_H (ppm) 11.098 (s, 1H, H-3' OH) and 9.510 (s, 1H, H-7', CH) were assigned to the hydroxyl proton and azomethine proton, respectively. Three signals at δ_H (ppm) 7.952 (d, $J_{5',6'}$ = 8.5 Hz, 1H, H-5'), 7.410 (dd, $J_{6',5'}$ = 7 Hz, $J_{6',1'}$ = 1.5 Hz, 1H, H-6') 7.354 (s, 1H, H-2') were assigned to the aromatic methine protons on the benzaldehyde ring. The signals at δ_H (ppm) 7.550 (t, $J_{3,2/3,4} = J_{5,4/5,6}$ = 8Hz, 2H, H-3, H-5), 7.504 (d, $J_{4,2/4,6}$ = 1.5Hz, 1H, H-4) and 7.382 (dd, $J_{2,3} = J_{6,5}$ = 6.5 Hz, $J_{2,4/2,6} = J_{6,4/6,}$ = 1 Hz, 2H, H-2, H-6) were assigned to the aromatic methine protons of the pyrazole moiety. While the signals at δ_H (ppm) 3.231 (s, 3H, H-11, CH_3) and 2.471 (s, 3H, H-10, CH_3) correspond to the methyl protons.

EI-MS: *m/z* (relative abundance in %), 352 [M^+] (100), 260 (18), 188 (37), 121 (38), and 56 (67). The EI-MS spectrum showed the molecular ion (and the base peak) M^+ at *m/z* 352. Other prominent fragment peaks were observed at *m/z* 260 $[C_{11}H_8N_4O_4]^+$, 188 $[C_{11}H_{11}N_2O]^+$, 121 $[C_6H_7N_3]^{3+}$and 56 $[C_3H_6N]^{3\bullet}$.

The infrared absorption spectrum showed diagnostic bands with vibrational frequencies $\bar{\upsilon}$ (cm^{-1}) for O-H stretch of the hydroxyl (3633), =C-H anti-sym stretch of aromatic (3057), C-H anti-sym. stretch of aliphatic (2929) -C=O stretch of carbonyl (1612), C=N stretch of the azomethine bond (1586), C=C stretch of aromatic (1550), asymmetric N=O of nitro substituent (1527), C-O bend of hydroxyl (1424), symmetric N=O of nitro substituent (1354), C-N stretch (1292), and N-N stretch (1229) of pyrazole moiety.

The analysis of the UV spectrum in chloroform revealed maximum absorption bands (nm) at 248, 288 and 409. The longer wavelength at 288 and 409 showed n-π* transitions. The absorptions at 249 showed π-π*transitions.

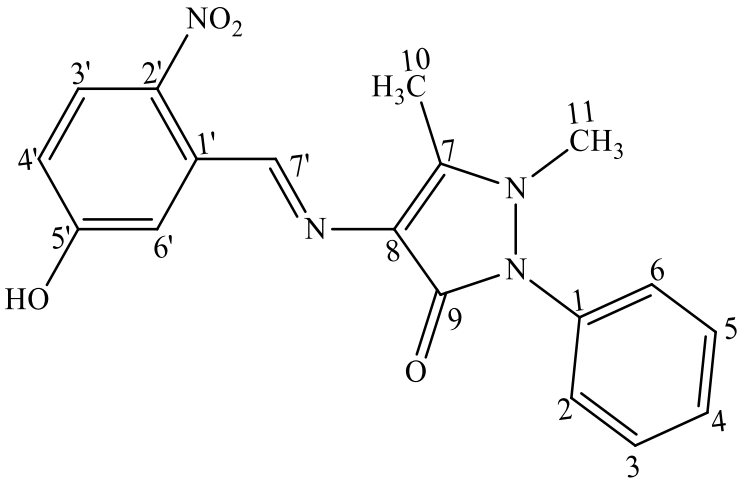

Scheme 4. 23: Structure of SB10

4.2.24 Characterisation of 4-((3,4-dihydroxybenzylidene)amino)-1,5-dimethyl-2-phenyl-1,2-dihydro-3H-pyrazol-3-one (SB11)

The compound 4-((3,4-dihydroxybenzylidene)amino)-1,5-dimethyl-2-phenyl-1,2-dihydro-3H-pyrazol-3-one (Scheme 4.24) appeared as light brown crystals, with 91% yield, and m.pt. of 275.9-276.6 ^{o}C [literature 279.2-280.5 ^{o}C (Teran *et al.*, 2019)].

The ^{1}H NMR (500 MHz, DMSO-d_6, δ_H ppm) spectrum displayed a total of eleven signals and seventeen protons. A downfield signal at δ_H (ppm) 9.370 (s,1H, H-7', CH) was assigned to the azomethine proton. A downfield signal at δ_H (ppm) 9.204 (s, 1H, H-3', OH) and a upfield signal at δ (ppm) 3.451 (q,1H, H-4', OH) correspond to the hydroxyl protons on the benzaldehyde ring. The signals at δ_H (ppm) 7.523 (t, $J_{3,2/3,4} = J_{5,4/5,6} = 8$ Hz,2H, H-3, H-5), 7.367 (s, 1H, H-2'), 7.352 (d, $J_{2,3} = J_{6,5} = 7$ Hz, 2H, H-2, H-6), 7.287 (d, $J_{6',2'} = 2$ Hz, 1H, H-6'), 7.020 (dd, $J_{4,3/4,5} = 8$ Hz $J_{4,2/4,6} = 2$ Hz, 1H, H-4) and 6.784 (d, $J_{5',6'} = 8.5$ Hz, 1H, H-5') were assigned to the aromatic methine protons. While the upfield signals at δ_H (ppm) 3.114 (s, 3H, H-11, CH_3) and 2.400 (s, 3H, H-10, CH_3) were assigned to the methyl protons of the pyrazole moiety.

EI-MS: *m/z* (relative abundance in %), 323 [M^+] (100), 324.3 (40), 231 (46), 188 (15), 121 (16), and 56 (37). The EI-MS spectrum of SB11 showed the molecular ion (and the base peak) M^+ at *m/z* 323. Other prominent fragment peaks were observed at *m/z* 231 $[C_{11}H_9N_3O_3]^+$, 188 $[C_{11}H_{11}N_2O]^+$, 121 $[C_6H_7N_3]^{3+}$and 56 $[C_3H_6N]^{3\bullet}$.

The infrared absorption spectrum showed vibrational bands with characteristic vibrational frequencies $\bar{\upsilon}$ (cm^{-1}) for O-H stretch of hydroxyl (3495), =C-H anti-sym stretch of aromatic (3062), C-H anti-sym. stretch of aliphatic (2943) -C=O stretch of carbonyl (1616), C=N stretch of the azomethine bond (1589), C=C stretch of aromatic (1561), C-O bend of hydroxyl (1377), C-N stretch of pyrazole (1289) C-O of methoxy (1266 and 1071) and N-N stretch of pyrazole (1222).

The analysis of the UV spectrum in chloroform revealed maximum absorption bands (nm) at 249, 261, and 338. The longer wavelength at 338and 261 showed n-π* transitions. The absorptions at 249 showed π-π* transitions.

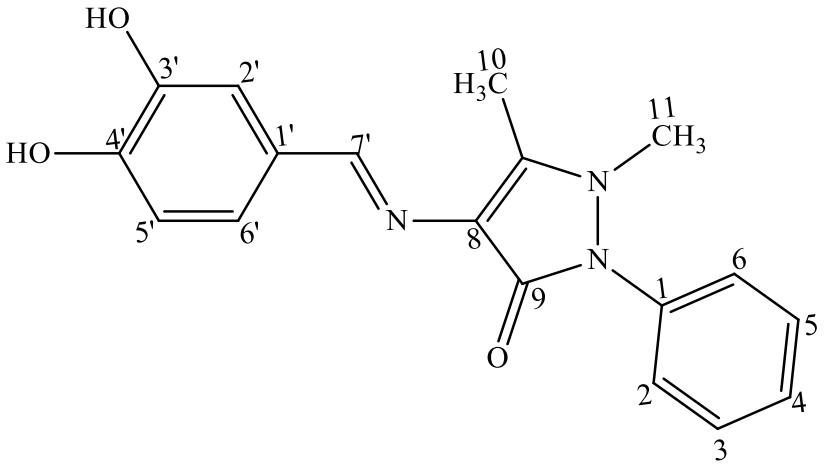

Scheme 4. 24: Structure SB11

4.2.25 Characterisation of 4-((2,4-dihydroxybenzylidene)amino)-1,5-dimethyl-2-phenyl-1,2-dihydro-3H-pyrazol-3-one (SB11A)

The compound 4-((2,4-dihydroxybenzylidene)amino)-1,5-dimethyl-2-phenyl-1,2-dihydro-3H-pyrazol-3-one (Scheme 4.25) was obtained as yellow crystals, with 90% yield, and m.pt. 228.5-230.0 ^{o}C [literature 231.5 ^{o}C (Alam *et al.*, 2012)].

The ^{1}H NMR (500 MHz, DMSO-d_6, δ_H ppm) spectrum of SB11A displayed a total of eleven signals and seventeen protons. Three downfield signals at δ_H (ppm) 13.307 (s, 1H, H-2', O-H), 10.045 (s, 1H, H-4', O-H) and 9.545 (s, 1H, H-7', CH) were assigned to the two hydroxyl protons and to the azomethine proton, respectively. Three signals at δ_H (ppm) 7.538 (t, $J_{3,2/3,4} = J_{5,4/5,6} = 8$ Hz, 2H, H-3, H-5), 7.381 (dd, $J_{2,3} = J_{6,5} = 6.5$ Hz, $J_{2,4/2,6} = J_{6,4/6,2} = 1.5$ Hz, 2H, H-2, H-6),7.370 (d, $J_{4,3/4,5} = 6.5$ Hz, 1H, H-4), 7.245 (d, $J_{6',5'} = 8.5$ Hz, 1H, H-6'), 6.349 (dd, $J_{5',6'} = 8$ Hz $J_{5',3'} = 2$ Hz, 1H, H-5') and 6.253 (d, $J_{3',5'} = 2$ Hz, 1H, H-3') correspond to the aromatic methine protons. While the signals at δ_H (ppm) 3.148 (s, 3H, H-11, CH_3), 2.349 (s, 3H, H-10, CH_3) were assigned to the methyl protons.

EI-MS: *m/z* (relative abundance in %), 323 [M^+] (100), 231 (23), 188 (16), 121.1 (19), and 56 (56). The EI-MS spectrum of SB11A showed the molecular ion (and the base peak) M^+ at *m/z* 323. Molecular ion peak M^++1 at *m/z* 324 was also observed. Other prominent fragment peaks were observed at *m/z* 231 $[C_{11}H_9N_3O_3]^+$, 188 $[C_{11}H_{11}N_2O]^+$, 121 $[C_6H_7N_3]^{3+}$and 56 $[C_3H_6N]^{3\bullet}$.

The infrared absorption spectrum of SB11A showed diagnostic bands with vibrational frequencies $\bar{\upsilon}$ (cm^{-1}) for O-H stretch of hydroxyl (3450), =C-H anti-sym stretch of aromatic (3059), C-H anti-sym. stretch of aliphatic (2921) -C=O stretch of carbonyl (1616), C=N stretch of the azomethine bond (1580), C=C stretch of aromatic (1512), C-O bend of hydroxyl (1366), C-N stretch of pyrazole (1318), C-O stretch of hydroxyl (1225) and N-N stretch of pyrazole (1160).

The analysis of the UV spectrum of SB11A in chloroform revealed maximum absorption bands (nm) at 249, 286 and 347. The longer wavelength at 286 and 347 indicate n-π* transitions. The absorptions at 249 infer π-π* transitions.

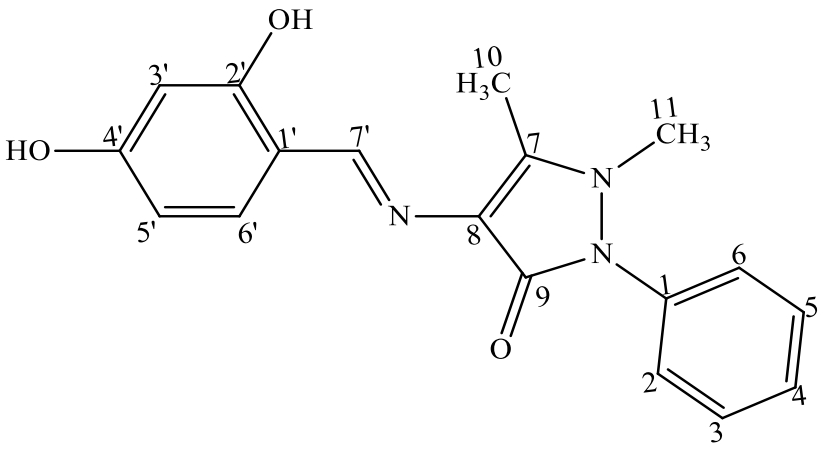

Scheme 4. 25: Structure of SB11A

4.2.26 Characterisation of 4-((2,3-dihydroxybenzylidene)amino)-1,5-dimethyl-2-phenyl-1,2 -dihydro-3H-pyrazol-3-one (SB11B)

The compound 4-((2,3-dihydroxybenzylidene)amino)-1,5-dimethyl-2-phenyl-1,2-dihydro-3H-pyrazol-3-one (Scheme 4.26) appeared as bright orange crystals with 92% yield, and m.pt. of 212.2-214.5 ^{o}C.

The ^{1}H NMR (400 MHz, DMSO-$d_{6,}$ δ_H ppm) spectrum of SB11B displayed a total of eleven signals and seventeen protons. Three downfield signals at δ_H (ppm)13.054 (s, 1H, H-2', OH), 9.073 (s, 1H, H-3', OH) and 9.644 (s, 1H, H-7', CH) were assigned to the two hydroxyl protons and the azomethine proton, respectively, The aromatic methine protons on the benzaldehyde ring are represented by the signals at δ_H (ppm) 6.900 (dd, $J_{6',5'}$ = 7.6 Hz, $J_{6',4'}$ =1.2 Hz, 1H, H-6'), 6.586 (dd, $J_{4',5'}$ = 8 Hz, $J_{4',6'}$ = 1.2 Hz, 1H, H-4') and 6.740 (t, $J_{5',4'/5',6'}$ = 8 Hz, 1H, H-5'). The signals at δ_H (ppm) 7.554 (t, $J_{3,2/3,4}$ = $J_{5,4/5,6}$ = 8 Hz, 2H, H-3, H-5), 7.408 (d, $J_{2,3}$ = $J_{6,5}$ = 8.8 Hz, 2H, H-2, H-6) and 7.386 (d, $J_{4,3/4,5}$ = 8.4 Hz, 1H, H-4) were assigned to the aromatic methine protons of the pyrazole moiety. While the signals at δ_H (ppm) 3.159 (s, 3H, H-11, CH_3) and 2.402 (s, 3H, H-10, CH_3) correspond to the methyl protons of the pyrazole moiety.

EI-MS: *m/z* (relative abundance in %), 323 [M^+] (100), 231 (23), 188 (16), and 56 (56), The EI-MS spectrum of SB11B showed the molecular ion (and the base peak) M^+ at *m/z* 323. Molecular ion peak M^++1 at *m/z* 324 was also observed. Other prominent fragment peaks were observed at *m/z* 231 $[C_{11}H_9N_3O_3]^+$, 188 $[C_{11}H_{11}N_2O]^+$, and 56 $[C_3H_6N]^{3\bullet}$.

The infrared absorption spectrum of SB11B showed vibrational bands with characteristic vibrational frequencies $\bar{\upsilon}$ (cm^{-1}) for O-H stretch of hydroxyl (3453), C-H anti-sym. stretch of aliphatic (2943) -C=O stretch of carbonyl (1659), C=N stretch of azomethine bond (1563), C-O bend of hydroxyl (1367), C-N stretch of pyrazole (1267) and N-N stretch of pyrazole (1200).

The analysis of the UV spectrum of SB11B in chloroform revealed maximum absorption bands (nm) at 260, and 335. These wavelengths correspond to n-π* transitions.

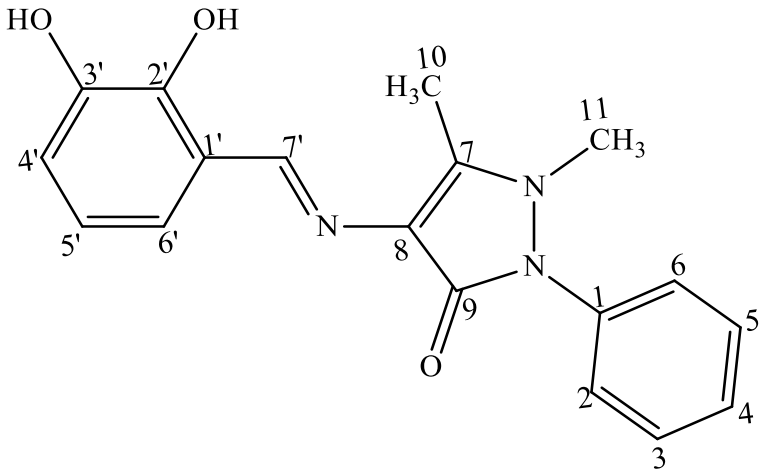

Scheme 4. 26: Structure of SB11B

4.2.27 Characterisation of 4-((2-chloro-4-fluorobenzylidene)amino)-1,5-dimethyl-2-phenyl-1,2-dihydro-3H-pyrazol-3-one (SB12)

The compound 4-((2-chloro-4-fluorobenzylidene)amino)-1,5-dimethyl-2-phenyl-1,2-dihydro-3H-pyrazol-3-one (Scheme 4.27) was obtained as yellow crystals with 94% yield, and m.pt. of 210.0-211.3 ^{o}C .

The ^{1}H NMR (400 MHz, DMSO-$d_{6,}$ δ_H ppm) spectrum of SB12 displayed a total of nine signals and fifteen protons. A downfield signal at δ_H (ppm) 9.909 (s, 1H, H-7', CH) was assigned to the azomethine proton. Three signals at δ_H (ppm) 8.216 (dd, $J_{6',5'}$ = 8.8 Hz, 1H, H-6'), 7.358 (s, IH, H-3') and 7.341 (dd, $J_{5',6'}$ = 8.4 Hz, $J_{5',3'}$ = 2.4 Hz, 1H, H-5') correspond to the aromatic methine protons on the benzaldehyde ring. The signals at δ_H (ppm) 7.546 (d, $J_{3,2/3,4}$ = $J_{5,4/5,6}$ = 8 Hz, 2H, H-3, H-5), 7.494 (d, $J_{4,2/4,6}$ = 2.4 Hz, 1H, H-4) and 7.400 (d, $J_{2,3}$ = $J_{6,5}$ = 8.4 Hz, 2H, H-2, H-6) were assigned to the aromatic methine protons of the pyrazole moiety. While the signals at δ_H (ppm) 3.212 (s, 3H, H-11, CH_3) and 2.466 (s, 3H, H-10, CH_3) represent the methyl protons of the pyrazole moiety.

The signals from ^{13}C NMR (100 M-Hz, DMSO-d_6) broad band spectrum displayed seven characteristic peaks of quaternary carbons observed downfield at δ 163.67 (C-9), 161.67 (C-4'), 159.24 (C-7), 152.32 (C-2'), 134.60 (C-1), 131.3 (C-1') and 116.0 (C-8). Nine methine carbons were observed which were assigned as C-7' (148.60) azomethine carbon and 128.4 (C-6'), 116.9 (C-3') and 115.1 (C-5') on the benzaldehyde ring, 129.1 (C-5), 127.9 (C-4), 129.1 (C-3), 124.9 (C-2) and 124.9 (C-6) on the phenyl ring. DEPT-135 confirmed the absence of methylene carbons while DEPT-90 confirmed the presence of the nine methine carbons. The two methyl carbons present appear upfield at 9.65 (C-10) and 35.07 (C-11).

EI-MS: *m/z* (relative abundance in %), 343 [M^+] (100), 251 (39), 188 (58), 121 (44), and 56 (44). The EI-MS spectrum of SB12 showed the molecular ion (and the base peak) M^+ at *m/z* 343. Other prominent fragment peaks were observed at *m/z* 308 $[C_{18}H_{15}FN_3O]^+$, 251 $[C_{11}H_9ClFN_3O]^+$, 188 $[C_{11}H_{11}N_2O]^+$, 121 $[C_6H_7N_3]^{3+}$and 56 $[C_3H_6N]^{3\bullet}$.

The infrared absorption spectrum of SB12 showed vibrational bands with characteristic vibrational frequencies $\bar{\upsilon}$ (cm^{-1}) for =C-H anti-sym stretch of aromatic (3069), C-H anti-sym. stretch of aliphatic (2920) -C=O stretch of carbonyl (1651), C=N stretch of azomethine bond (1593), C=C stretch of aromatic (1483), C-N stretch (1306) and N-N stretch (1163) of pyrazole moiety.

The analysis of the UV spectrum of SB12 in chloroform revealed maximum absorption bands (nm) at 249, 260, and 338. The longer wavelength at 338 and 260 showed n-π* transitions. The absorptions at 249 showed π-π* transitions.

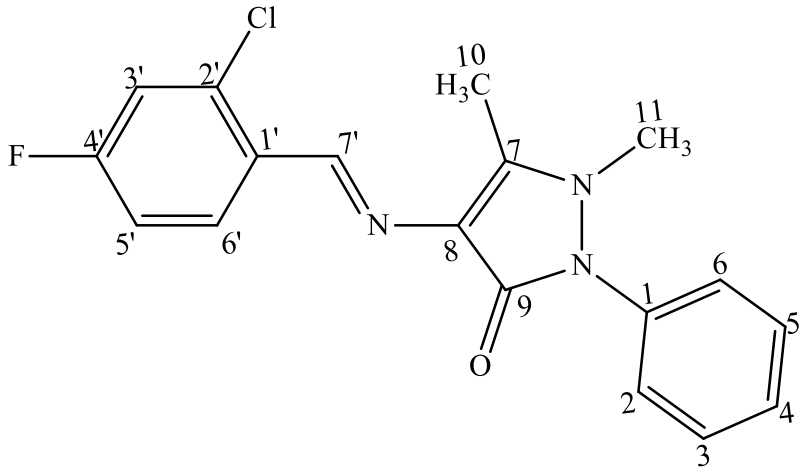

Scheme 4. 27: Structure of SB12

4.2.28 Characterisation of 4-((3,4-dimethylbenzylidene)amino)-1,5-dimethyl-2-phenyl-1,2-dihydro-3H-pyrazol-3-one (SB13)

The compound 4-((3,4-dimethylbenzylidene)amino)-1,5-dimethyl-2-phenyl-1,2-dihydro-3H-pyrazol-3-one (Scheme 4.28) was obtained as pale yellow crystals, with 89% yield, and m.pt. of 179.6-180 ^{o}C.

The ^{1}H NMR (400 MHz, MeOD-$d_{6,}$ δ_H ppm) spectrum of SB13 displayed a total of eleven signals and twenty-one protons. A downfield signal at δ_H (ppm) 9.455 (s,1H, H-7', CH) was assigned to the azomethine proton. Three signals at δ_H (ppm) 7.592 (s, IH, H-2'), 7.456 (d, $J_{6',5'}$ = 7.6 Hz, 1H, H-6') and 7.192 (d, $J_{5',6'}$ = 7.6 Hz, 1H, H-5') were assigned to the aromatic methine protons on the benzaldehyde ring. The signals at δ_H (ppm) 7.569 (d, $J_{4,3/4,5}$ = 7.6 Hz, 1H, H-4), 7.550 (d, $J_{3,4/3,2}$ = $J_{5,4/5,6}$ = 7.6 Hz, 2H, H-3, H-5) and 7.414 (dd, $J_{2,3}$ = $J_{6,5}$ = 8.8 Hz, $J_{2,4}$ = $J_{6,4}$ = 1.2 Hz, 2H, H-2, H-6) were assigned to the aromatic methine protons of the pyrazole moiety. Two upfield signals at δ_H (ppm) 3.223 (s, 3H, H-10, CH_3) and 2.491(s, 3H, H-11, CH_3) were assigned to the methyl protons of the pyrazole moiety. The signal at δ_H (ppm) 2.296 (s, 6H, H-2', H-3', CH_3) represent the six methyl protons on the benzaldehyde ring.

The ^{13}C NMR (100 MHz, DMSO-$d_{6,}$ δ ppm) broad band spectrum of SB13 revealed seventeen resonances corresponding to twenty carbon atoms which were resolved using DEPT experiments into seven quaternaries, nine methine, and four methyl carbons. Seven characteristic peaks observed at 152.32 (C-7), 134.80 (C-4'), 136.50 (C-1), 135.20 (C-3'), 134.6 (C-1') and 116.6 (C-8) represent the quaternaries carbons. Nine methine carbons were observed which were assigned as C-7' (154.70) of azomethine carbon, 129.80 (C-2'), 128.1 (C-5') and 124.9 (C-6') on the benzaldehyde ring, 129.1 (C-5), 126.8 (C-4), 129.1 (C-3), 124.5 (C-2) and 124.5 (C-6) on the phenyl ring. DEPT-135 confirmed the absence of methylene carbons while DEPT-90 confirmed the presence of the nine methine carbons. The four methyl carbons present appear upfield at 19.34 (C-8') 19.42 (C-9'), 9.80 (C-10) and 35.4 (C-11).

EI-MS: *m/z* (relative abundance in %), 319 [M^+] (100), 320 (45), 227 (27), 210 (27), 185 (16), 188 (58), and 121 (34), The EI-MS spectrum of SB13 showed the molecular ion (and the base peak) M^+ at *m/z* 319. Molecular ion peak at M^++1 at *m/z* 320 was also observed.

Other prominent fragment peaks were observed at *m/z* 227 $[C_{13}H_{13}N_3O]^+$, 210 $[C_{13}H_{13}N_3]^{2+}$, 188 $[C_{11}H_{11}N_2O]^+$, 185 $[C_{10}H_8N_3]^+$, and 121 $[C_6H_7N_3]^{3+}$.

The infrared absorption spectrum of SB13 showed vibrational bands with characteristic vibrational frequencies $\bar{\upsilon}$ (cm^{-1}) for =C-H anti-sym stretch of aromatic (3051), C-H anti-sym. stretch of aliphatic (2922) -C=O stretch of carbonyl (1651), C=N stretch of azomethine bond (1587), C=C stretch of aromatic (1496), C-N stretch (1300) and N-N stretch (1136) of pyrazole moiety.

The analysis of the UV spectrum of SB13 in chloroform revealed maximum absorption bands (nm) at 260, and 331. These wavelengths are indicative of n-π^* transitions.

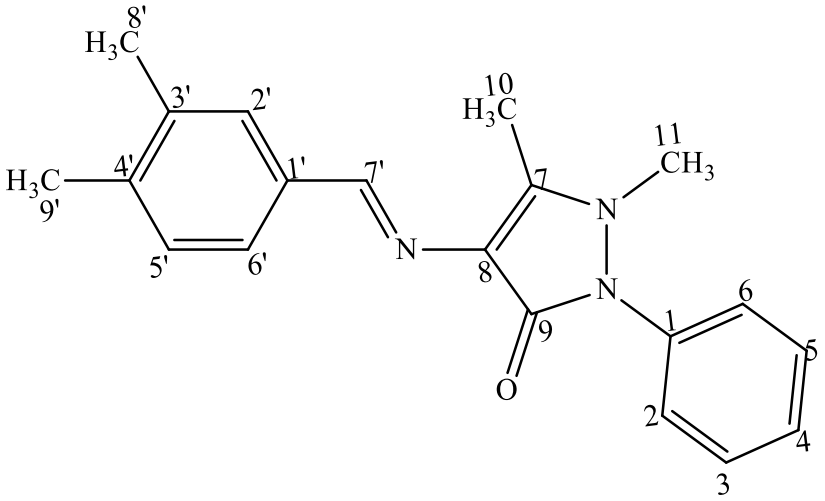

Scheme 4. 28. Structure of SB13

4.2.29 Characterisation of 4-((2,3,4-trihydroxybenzylidene)amino)-1,5-dimethyl-2-phenyl-1,2-dihydro-3H-pyrazol-3-one (SB17)

The compound 4-((2,3,4-trihydroxybenzylidene)amino)-1,5-dimethyl-2-phenyl-1,2-dihydro-3H-pyrazol-3-one (Scheme 4.29) appeared as dark yellow crystals with 90% yield, and m.pt. 257.5-261.2 ^{o}C.

The ^{1}H NMR (500 MHz, DMSO-$d_{6,}$ δ_H ppm) spectrum of SB13 displayed a total of eleven signals and seventeen protons. The downfield signals at δ_H (ppm) 13.411 (s, 1H, OH, H-2'), 9.519 (s, 1H, OH, H-4') and 8.396 (s, 1H, H-3', OH) were assigned to the hydroxyl protons on the benzaldehyde ring. The signal at δ_H (ppm) 13.411 (s, 1H, OH, H-2') was more deshielded due to the conjugation resulting from the Imine bond. A downfield signal at δ_H (ppm) 9.519 (s, 1H, H-7', CH) was assigned to the azomethine proton. Five signals at δ_H (ppm) 7.540 (t, $J_{3,4/3,5} = J_{5,4/5,4} = 7.5$ Hz, 2H, H-3, H-5), 7.384 (dd, $J_{2,3} = J_{6,5} = 7$ Hz, $J_{2,4} = J_{6,4} = 2$ Hz, 2H, H-2, H-6), 7.363 (d, $J_{4,2/4,6} = 2$ Hz, 1H, H-4), 6.753 (d, $J_{6',5'} = 8.5$ Hz, 1H, H-6') and 6.374 (d, $J_{5',6'} = 8$ Hz, 1H, H-5') were assigned to aromatic methine protons. While the signals at δ_H (ppm) 3.156 (s, 3H, H-11, CH_3) and 2.369 (s, 3H, H-10, CH_3) correspond to the methyl protons of the pyrazole moiety.

EI-MS: *m/z* (relative abundance in %), 339 [M^+] (100), 247 (35), 231 (42), 188 (34), 121 (35), and 56 (64). The EI-MS spectrum of SB17 showed the molecular ion (and the base peak) M^+ at *m/z* 339. Other prominent fragment peaks were observed at *m/z* 247 $[C_{11}H_9N_3O_4]^+$, 231 $[C_{11}H_9N_3O_3]^{2+\ +}$, 188 $[C_{11}H_{11}N_2O]^+$, 121 $[C_6H_7N_3]^{3+}$ and 56 $[C_3H_6N]^{3\bullet}$.

The infrared absorption spectrum of SB17 showed vibrational bands with characteristic vibrational frequencies $\bar{\upsilon}$ (cm^{-1}) for O-H stretch of hydroxyl (3438), = C-H anti-sym. stretch of aliphatic (2926) -C=O stretch of carbonyl (1610), C=N stretch of azomethine bond (1508) C-O bend of hydroxyl (1393), C-N stretch pyrazole (1319), C-O stretch of hydroxy (1276) and N-N stretch of pyrazole (1207).

The analysis of the UV spectrum of SB17 in chloroform revealed maximum absorption band (nm) at 245 nm which indicates π-π^* transition.

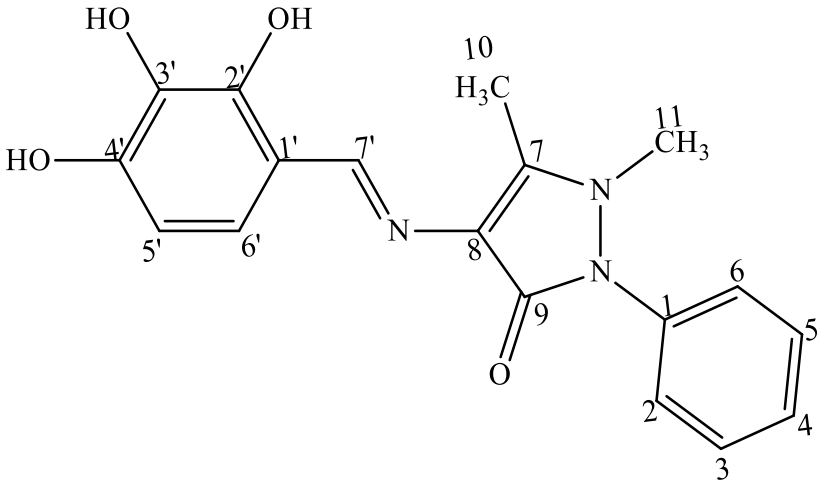

Scheme 4. 29: Structure of SB17

4.2.30 Characterisation of 4-(4-hydroxy-3,5-dimethoxybenzylidene)amino)-1,5-dimethyl-2-phenyl-1,2-dihydro-3H-pyrazol-3-one (SB-19)

The compound 4-((4-hydroxy-3,5-dimethoxybenzylidene)amino)-1,5-dimethyl-2-phenyl-1,2-dihydro-3H-pyrazol-3- one (Scheme 4.30) appeared as off white powder with 95% yield, and m.pt. 255.5-257.0 ^{o}C. [literature 259.2-260.7 ^{o}C (Teran *et al.*, 2019)].

The ^{1}H-NMR (400 MHz, DMSO-d_6 δ_H ppm) spectrum of SB19 showed a total of eleven resonances representing twenty-one protons. The signal at δ_H (ppm) 9.446 (s,1H, CH, H-9) represent the azomethine proton. The signals at δ_H (ppm) 8.846 (S, 1H, H-5', OH) was assigned to the hydroxyl protons on the benzaldehyde ring. The four signals at δ_H (ppm) 7.535 (t, $J_{3,2/3,4}$ = $J_{5,6/5,4}$ = 7.6 Hz, 2H, H-3, H-5), 7.379 (d, $J_{2,3,}$ = $J_{6,5,}$ = 7.2 Hz, 2H, H-2, H-6), 7.360 (d, $J_{4,3/4,5}$ = 7.2 Hz, 1H, H-4) and 7.088 (s, 2H, H-2' H-6') represent the aromatic protons. Three upfield singlets at δ_H (ppm) 3.816 (s, 6H, H-8', H-9', OCH_3), 3.029 (s, 3H, H-11, CH_3) and 2.435 (s, 3H, H-10, CH_3) assigned to the two methoxyl proton and two methyl protons, respectively.

EI-MS: *m/z* (relative abundance in %), 367 [M^+] (100), 368 (33), 275 (27), 258 (29), 233 (7), and 188 (13). The EI-MS spectrum of SB19 showed the molecular ion (and the base peak) M^+ at *m/z* 367. Molecular ion peak at M^++1 at *m/z* 368 was also observed. Other prominent fragment peaks were observed at *m/z* 275 $[C_{13}H_{13}N_3O_4]^+$, 258 $[C_{13}H_{13}N_3O_3]^{2+}$, 188 $[C_{11}H_{11}N_2O]^+$, 121 $[C_6H_7N_3]^{3+}$ and 56 $[C_3H_6N]^{3\bullet}$.

The infrared absorption spectrum of SB19 showed vibrational bands with characteristic vibrational frequencies $\bar{\upsilon}$ (cm^{-1}) for O-H stretch of aromatic (3567), =C-H anti-sym stretch of aromatic (3158), C-H anti-sym. stretch of aliphatic (2968) -C=O stretch of carbonyl (1634.2), C=N stretch of azomethine bond (1588), C=C stretch of aromatic (1513), C-O bend of hydroxyl (1382), C-O stretch of hydroxyl (1296), C-N stretch of pyrazole (1332), C-O of the methoxy (1251 and 1040) and N-N of pyrazole (1210).

The analysis of the UV spectrum of SB19 in chloroform revealed maximum absorption band (nm) at 341 which indicate n-π* transitions.

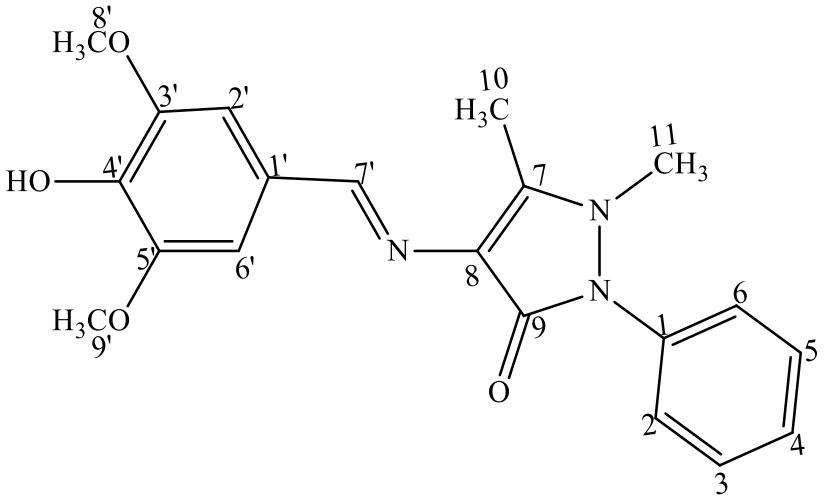

Scheme 4. 30. Structure of SB19

4.2.31. Characterisation of 4-((3-methoxy-2-((4-(methylthio)benzyl)oxy)benzylidene) amino) -1,5-dimethyl-2-phenyl-1H-pyrazol-3(2H)-one (5A-1)

The compound 4-((3-methoxy-2-((4-(methylthio)benzyl)oxy)benzylidene)amino)-1,5-di methyl-2-phenyl-1H-pyrazol-3(2H)-one (Scheme 4.31) was obtained as brown solid, with 84% yield, and melting point 153.4-154.6 ^{o}C.

The ^{1}H NMR spectrum (400 MHz, DMSO-d_6, δ_H (ppm)) showed sixteen signals and total of twenty-seven protons. The azomethine proton was observed downfield at δ_H (ppm) 9.859 (s, 1H, H-7', CH). The signals at δ_H (ppm) 7.377 (d, $J_{3'',2''} = J_{5'',6''} =$ 8.8 Hz, 2H, H-3'', H-5'') and 7.195 (d, $J_{2'',3''} = J_{6'',5''}$ = 8.4 Hz, 2H, H-2'', H-6'') were doublet corresponding to the chemically equivalent methine protons. The three signals at δ_H (ppm) 7.590 (d, $J_{6',5'}$ = 9.2 Hz, 1H, H-6'), 7.355 (d, $J_{4',5'}$ = 8.4 Hz, 1H, H-4') and 7.142 (d, $J_{5',6'/5',4'} =$ 8.4 Hz, 1H, H-5') represent the aromatic protons on the benzaldehyde ring attached to the azomethine bond. The signals at δ_H (ppm) 7.553 (t, $J_{3,2/3,4} = J_{5,4/5,6}$ = 8.4 Hz, 2H, H-3, H-5), 7.394 (dd, $J_{2,3} = J_{6,5}$ = 6.8 Hz, $J_{2,4} = J_{6,4}$ = 2 Hz, 2H, H-2, H-6) and 7.121 (d, $J_{4,3/4,5}$ = 2 Hz, 1H, H-4) correspond to the aromatic protons on the benzyl ring attached to the pyrazole moiety. The five singlets at δ_H (ppm) 4.931 (s, 2H, H-7'', CH_2), 3.853 (s, 3H, H-8', OCH_3), 3.163 (s, 3H, H-11, CH_3), 2.427 (s, 3H, H-10, CH_3), and 2.427 (s, 3H, H-8'', CH_3) are assigned to the methylene, methoxy and the three methyl protons, respectively.

The FAB- spectrum showed the molecular ion peak M^+ at M^++1 at *m/z* 474. Other prominent peaks were observed at *m/z* 461 $[C_{26}H_{24}N_3O_3S]^+$, and 338 $[C_{19}H_{18}N_3O_3]^+$.

The infrared absorption spectrum of 5A-1 showed diagnostic bands with vibrational frequencies $\bar{\upsilon}$ (cm^{-1}) for C-H anti-sym. stretch of methyl (2924), C-H stretch of methylene (2852), C=O stretch of carbonyl (1645), C=N stretch of azomethine bond (1570), C=C stretch of aromatic (1468), and C-N stretch of pyrazole moiety (1297).

The analysis of the UV spectrum of 5B1 in chloroform revealed maximum absorption bands at 328, 260, 231 and 220. The longer wavelength at 260 and 328 showed n-π* transitions. The absorptions at 231 and 220 showed π-π* transitions.

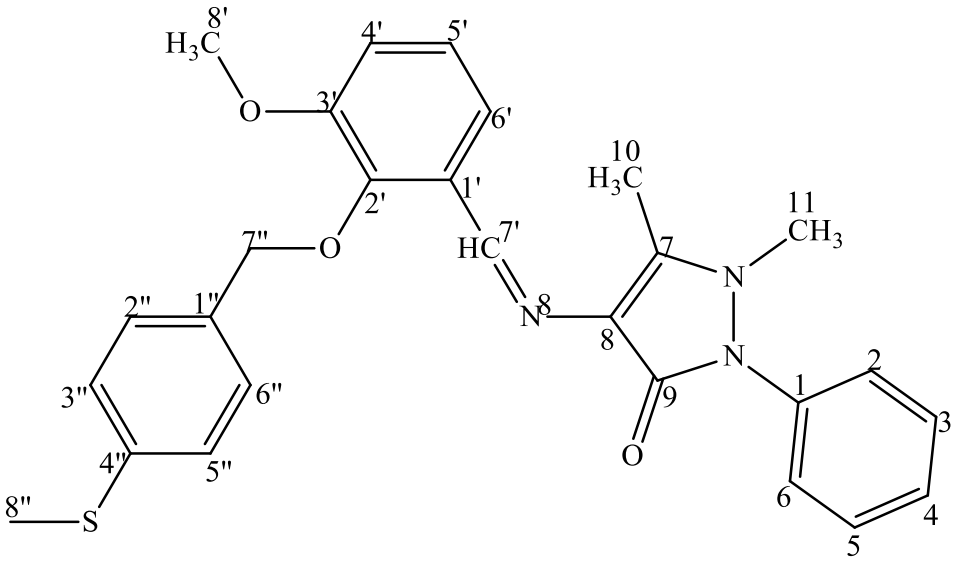

Scheme 4. 31: Structure of 5A-1

4.2.32 Characterisation of 4-((3-methoxy-2-((4-(trifluoromethyl)benzyl)oxy) benzylidene)amino)-1,5-dimethyl-2-phenyl-1H-pyrazol-3(2H)-one (5A-2)

The compound 4-((3-methoxy-2-((4-(trifluoromethyl)benzyl)oxy)benzylidene)amino)-1,5-dimethyl-2-phenyl-1H-pyrazol-3(2H)-one (Scheme 4.32) was obtained as a pale yellow solid, with 78%, yield, and melting point of 199.9-202.0 ^{o}C.

The ^{1}H NMR spectrum (500 MHz, DMSO-d_6, δ_H (ppm)) showed thirteen signals representing a total twenty-four protons. The singlet peak observed downfield at δ_H (ppm) 9.876 (s, 1H, H-7', CH) was assigned to the azomethine proton. The spectrum showed signals at δ_H (ppm) 7.707 (d, $J_{3'',2''} = J_{5'',6''}$ = 9 Hz, 2H, H-3", H-5") and 7.686 (d, $J_{2'',3''} = J_{6'',5''}$ = 9 Hz, 2H, H-2", 6") as doublet corresponding to the chemically equivalent methine protons from the benzaldehyde ring. The presence of triflouromethyl group on the ring causes these protons to move more downfield relative to other protons in the aromatic region in the spectrum. The three signals at δ_H (ppm) 7.608 (d, $J_{6',4'}$ = 2.5 Hz, $J_{6',5'}$ = 9 Hz, 1H, H-6'), 7.169 (d, $J_{5',6'}$ =8 Hz, 1H, H-5') and 7.144 (d, $J_{4',5'}$ = 7 Hz, $J_{4',6'}$ = 2.5 Hz, 1H, H-4') were assigned to aromatic protons on the benzaldehyde ring attached to the azomethine bond. The signals at δ_H (ppm) 7.538 (t, $J_{3,4/3,2} = J_{5,4/5,6}$ = 7.5 Hz, 2H, H-3, H-5), 7.381 (d, $J_{2,4} = J_{6,4}$ = 2.5 Hz, 2H, H-2, H-6) and 7.374 (dd, $J_{4,3/4,5}$ = 8.5 Hz, 1H, H-4) represent the aromatic protons on the benzyl ring attached to the pyrazole moiety. The singlets at δ_H (ppm) 5.067 (s, 2H, H-7", CH_2), 3.847 (s, 3H, H-7', OCH_3), 3.160 (s, 3H, H-11, CH_3), and 2.421 (s, 3H, H-10, CH_3) represent the methylene, methoxy, proton and two methyl protons, respectively.

The FAB+ spectrum of 5A-2 showed the molecular ion peak M^+ at M^++1 at *m/z* 496.

The infrared absorption spectrum of 5A-2 showed vibrational bands with characteristic vibrational frequencies $\bar{\upsilon}$ (cm^{-1}) for C-H anti-sym. stretch of aromatic (3075), C-H anti-sym. stretch of methyl (2925), C-H. stretch of methylene (2865) -C=O stretch of carbonyl (1657), C=N stretch of the azomethine bond (1585), C=C stretch of aromatic (1474), C-H bend of methylene (1415), C-H bend of methyl (1328), C-N stretch of pyrazole moiety (1294), Asymetric C-O-C stretch of ether (1267) N-N stretch of pyrazole moiety (1213) and symetric C-O-C stretch of ether (1065).

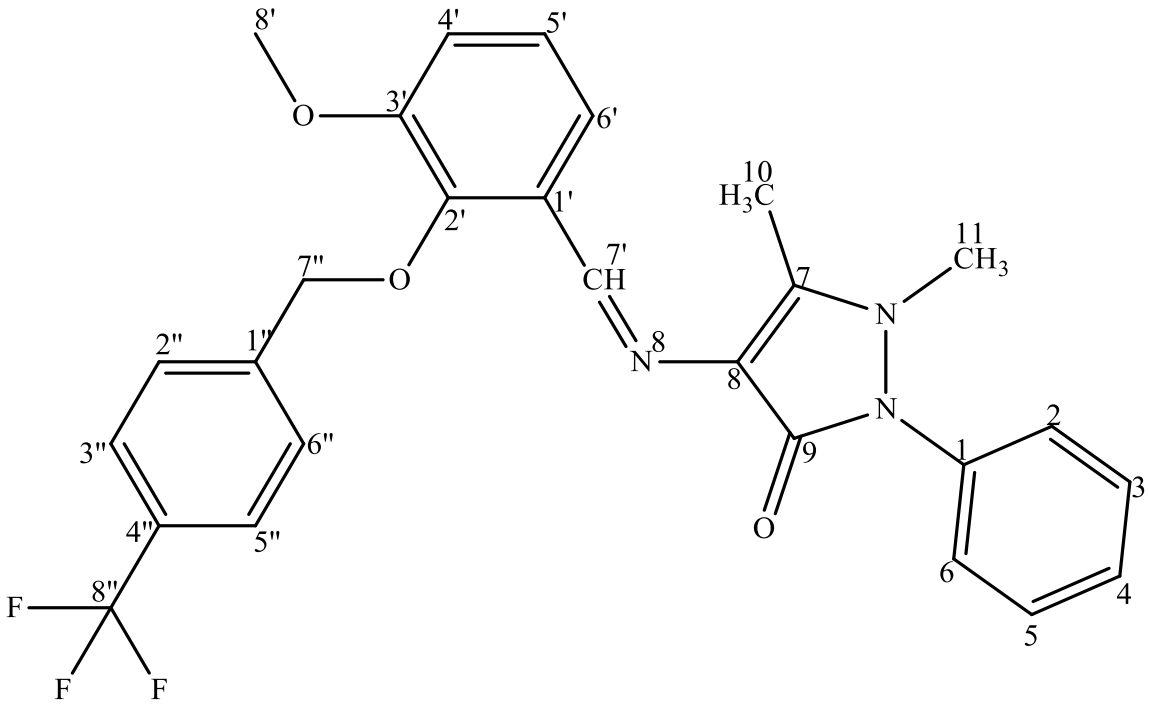

Scheme 4. 32: Structure of 5A-2

4.2.33 Characterisation of 4-((2-((3-chlorobenzyl)oxy)-3-methoxybenzylidene)amino) -1,5-dimethyl-2-phenyl-1H-pyrazol-3(2H)-one (5A-5)

The compound 4-((2-((3-chlorobenzyl)oxy)-3-methoxybenzylidene)amino)-1,5-dimethyl-2-phenyl-1H-pyrazol-3(2H)-one (Scheme 4.33) appeared as brown solid, with 92% yield, and melting point of 157.5-158.4 ^{o}C.

The ^{1}H NMR spectrum (400 MHz, DMSO-d_6, δ_H (ppm)) revealed fourteen signals with a total of twenty-four protons. The signal at δ_H (ppm) 9.913 (s, 1H, CH, H-7') represent the azomethine proton. The signals at δ_H (ppm) 7.563 (s, 1H, H-2") 7.426 (t, $J_{5",6"/5",4"}$ = 7.6 Hz, 1H, H-5"), 7.391 ($J_{4",5"}$ = 8 Hz, 1H, H-4") and 7.372 ($J_{6",5"}$ = 8 Hz, 1H, H-6") were assigned to aromatic protons on the benzaldehyde ring. The signals at δ_H (ppm) 7.599 (q, IH, $J_{6',5'}$ = 6.8 Hz, $J_{6',4'}$ = 2.8 Hz, 1H, H-6'), 7.165 (d, $J_{5',4'/5',6'}$ = 8 Hz, 1H, H-5') and 7.135 (d, $J_{4',5'}$ = 8 Hz, $J_{4',6'}$, = 2.8 Hz, 1H, H-4') represent the aromatic protons on the benzaldehyde ring attached to the azomethine bond. While signals at δ_H (ppm) 7.538 (t, $J_{3,2/3,4} = J_{5,4/5,6}$ = 8 Hz 2H, H-3, H-5), 7.354 (dd, $J_{2,3} = J_{6,5}$ = 7.2 Hz, $J_{2,4/2,6} = J_{6,4/6,2}$ = 3.2 Hz, 2H, H-2 H-6) and 7.341 (d, $J_{4,2/4,6}$ = 2 Hz, 1H, H-4) correspond to the aromatic protons on the benzyl ring attached to the pyrazole moiety. The signals at δ_H (ppm) 4.969 (s, 2H, H-7", CH_2), 3.849 (s, 1H, H-8', OCH_3), 3.165 (s, 3H, H-11, CH_3), 2.427 (s, 3H, H-10, CH_3) represent the methylene, methoxy and two methyl protons, respectively.

The FAB+ spectrum of 5A-5 showed the molecular ion peak M^+ at M^++1 at *m/z* 462. The fragment $[C_{19}H_{18}N_3O_3]^+$ at *m/z* 336 was also a prominent peak.

The infrared absorption spectrum of 5A-5 showed diagnostic bands $\bar{\upsilon}$ (cm^{-1}) for C-H anti-sym. stretch of aromatic (3177), C-H anti-sym. stretch of methyl (3070), C-H. stretch of methoxy (292), C-H. stretch of methylene (2847) -C=O stretch of carbonyl (1647), C=N stretch of azomethine bond (1580), C=C stretch of aromatic (1515), C-H bend of methylene (1456), C-N stretch of pyrazole moiety (1331), Asymetric C-O-C stretch of ether (1263) N-N stretch of pyrazole moiety (1238) and symetric C-O-C stretch of ether (1026).

The analysis of the UV spectrum of 5B5 in chloroform revealed maximum absorption bands at 339.This wavelength showed n-π* transitions.

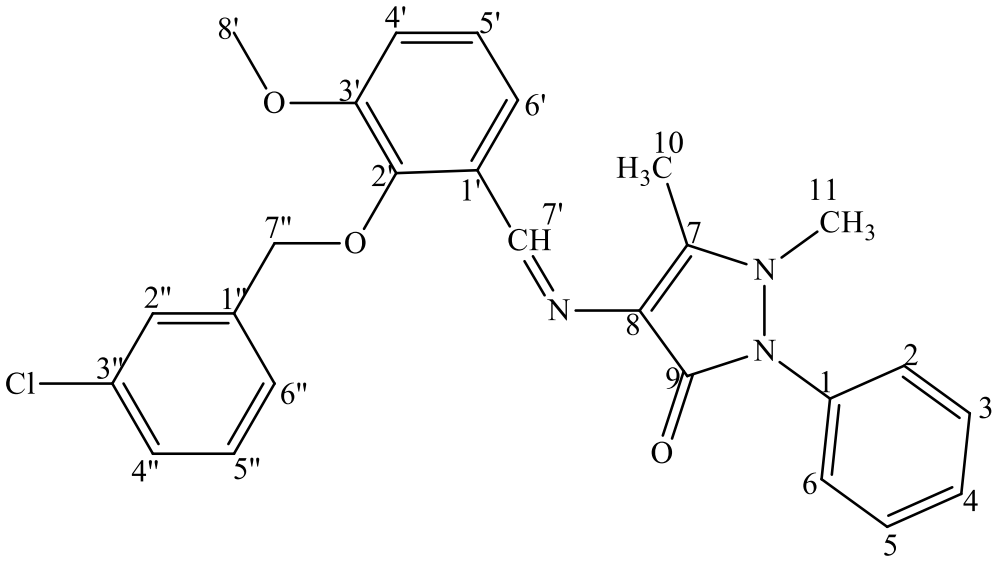

Scheme 4. 33: Structure of 5A-5

4.2.34 Characterisation of 4-((2-((2-bromobenzyl)oxy)-3-methoxybenzylidene)amino) -1,5-dimethyl-2-phenyl-1,2-dihydro-3H-pyrazol-3-one (5A-6)

The compound 4-((2-((2-bromobenzyl)oxy)-3-methoxybenzylidene)amino)-1,5-dimethyl-2-phenyl-1,2-dihydro-3H-pyrazol-3-one (Scheme 4.34) appeared as pale yellow solid with 88% yield, and melting point of 172.5-173.7 ^{o}C.

The ^{1}H NMR spectrum (400 MHz, MeOD-d_6) showed fifteen signals and a total of twenty-four protons. The azomethine proton appeared downfield at δ_H (ppm) 9.882 (s, 1H, H-7', CH). The four signals at δ_H (ppm) 7.752 (dd, $J_{3'',4''}$ = 7.6 Hz, 1H, H-3''), 7.587 (d, $J_{4'',5''}$ = 8Hz, 1H, H-4''), 7.408 (dd, $J_{5'',4''/5'',6''}$ = 8.4 Hz, 1H, H-5'') and 7.277 (d, $J_{6'',4''}$ = 1.6 Hz, $J_{6'',5''}$ = 7.6 Hz, 1H, H-6'') were assigned to aromatic protons on the benzaldehyde. The signals at δ_H (ppm) 7.632 (dd, $J_{6',5'}$ = 7.2 Hz, $J_{6',4'}$ = 2 Hz, 1H, H-6'), 7.182 (d, $J_{5',4'}$ = 8Hz, 1H, H-5') and 7.144 (d, $J_{4',5'}$ = 8 Hz, $J_{4',6'}$ = 2.4 Hz, 1H, H-4') represent the aromatic protons on the benzaldehyde ring attached to the azomethine bond. While signals at δ_H (ppm) 7.535 (t, $J_{3,2/3,4} = J_{5,4/5,6} =$ 8 Hz, 2H, H-3, H-5), 7.374 (dd, $J_{2,3} = J_{6,5} =$ 7.6 Hz, 2H, H-2, H-6) and 7.358 (dd, $J_{4,3/4,5}$ = 8.4 Hz, 1H, H-4) correspond to the aromatic protons on the benzyl ring attached to the pyrazole. The signals at δ_H (ppm) 5.047 (s, 2H, H-7'', CH_2), 3.828 (s, 1H, H-8', OCH_3), 3.156 (s, 3.H, H-11, CH_3) and 2.420 (s, 3H, H-10, CH_3) represent the methylene, methoxyl and two methyl protons, respectively.

The FAB- spectrum of 5A-6 showed the molecular ion peak M^+ at M^+-1 at *m/z* 506. The fragment $[C_{19}H_{18}N_3O_3]^+$ at *m/z* 336 was also prominent peak.

The infrared absorption spectrum of 5A-6 showed vibrational bands $\bar{\upsilon}$ (cm^{-1}) for C-H anti-sym. stretch of aromatic (3065), C-H anti-sym. stretch of methyl (2927), C-H. stretch of methylene (2841) C=O stretch of the carbonyl on the pyrazole (1648), C=N stretch of azomethine bond (1572), C=C stretch of aromatic (1475), C-N stretch of pyrazole (1300), Asymetric C-O-C stretch of ether (1266), and symetric C-O-C stretch of ether (1014).

The analysis of the UV spectrum of 5B8 in chloroform revealed maximum absorption bands at 333, This wavelength showed n-π^* transitions.

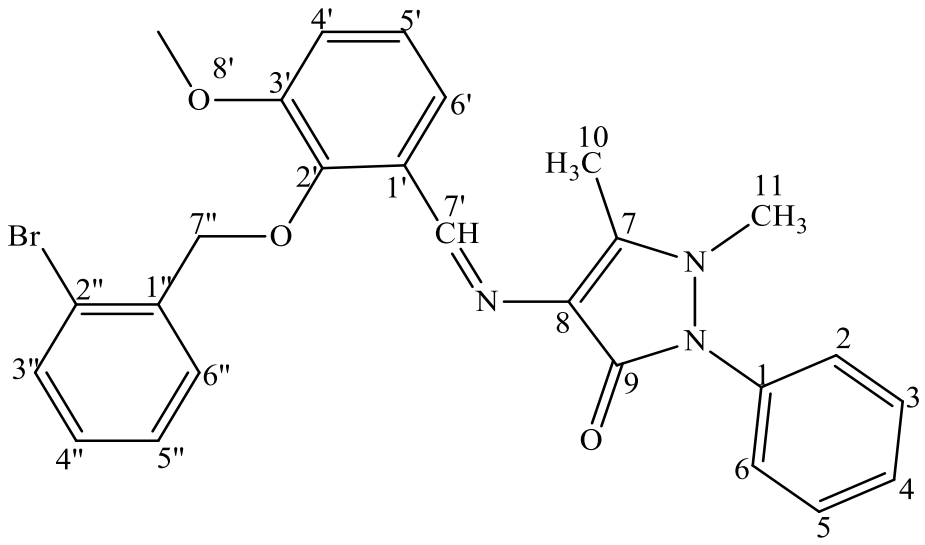

Scheme 4. 34. Structure of 5A-6

4.2.35 Characterisation of 4-((3-methoxy-2-((3-nitrobenzyl)oxy)benzylidene)amino)-1,5-dimethyl-2-phenyl-1H-pyrazol-3(2H)-one (5A-8)

The compound 4-((3-methoxy-2-((3-nitrobenzyl)oxy)benzylidene)amino)-1,5-dimethyl-2-phenyl-1H-pyrazol-3(2H)-one (Scheme 4.34) appeared as golden yellow solid with 78% yield, and melting point of 175.9-176.7 ^{o}C.

The ^{1}H NMR spectrum (400 MHz, MeOD-d_6) showed fifteen signals and a total of twenty-four protons. The most downfield signal at δ_H (ppm) 9.814 (s,1H, H-7', CH) was assigned to the azomethine proton. The four signals at δ_H (ppm) 8.324 (s, IH, H-2''), 8.161 (dd, $J_{4'',5''}$ =8Hz, $J_{4'',6''/4'',2''}$ = 1.6Hz, 1H, H-4''), 7.884 (d, $J_{5'',4''/5'',6''}$ = 8Hz, 1Hz, H-5'') and 7.592 (dd, $J_{6'',5''}$ = 8.4Hz, $J_{6'',4''/6'',2''}$ = 2.4Hz, 1H, H-6''), were assigned to aromatic protons on the benzaldehyde ring. The signals at δ_H (ppm) 7.631 (d, $J_{4',5'}$ = 8Hz, 1H, H-4'), 7.180 (d, $J_{6',5'}$ = 8Hz, 1H, H-6'), 7.154 (d, $J_{5',4'/5',6'}$ = 8Hz, 1H, H-5'), represent the aromatic protons on the benzaldehyde ring attached to the azomethine bond. While signals at δ_H (ppm) 7.532 (t, J $_{3,2/3,4}$ = J $_{5,4/5,6}$ = 7.6Hz, 2H, H-3, H-5), 7.372 (dd, J $_{2,4}$ = J $_{6,4}$ = 3.2 Hz, 2H, H-2, H-6) and 7.362 (d, J $_{4,3/4,5}$ = 8.4 Hz, 1H, H-4) correspond to the aromatic protons on the benzyl ring attached to the pyrazole moiety. The signals at δ_H (ppm) 5.114 (s, 2H, H-7'', CH_2), 3.859 (s, 3H, H-8', OCH_3), 3.157 (s, 3H, H-11, CH_3) and 2.49 (s, 3H, H-10, CH_3) represent the methylene, methoxy and methyl protons, respectively.

The FAB+ spectrum of 5A-8 showed the molecular ion peak M^+ at M^++1 at *m/z* 473. Another prominent peak was observed at *m/z* 336 $[C_{19}H_{18}N_3O_3]^+$.

The infrared absorption spectrum of 5A-8 showed vibrational bands $\bar{\upsilon}$ (cm^{-1}) for C-H anti-sym. stretch of aromatic (3186), C-H anti-sym. stretch of methyl (3067, C-H. stretch of methoxy (2924), C-H. stretch of methylene (2854) -C=O stretch of carbonyl (1646), C=N stretch of azomethine bond (1521), C=C stretch of aromatic (1465), C-H bend of methylene (1426), C-N stretch of pyrazole moiety (1301), Asymetric C-O-C stretch of ether (1269) N-N stretch of pyrazole moiety (1213) and symetric C-O-C stretch of ether (1015).

The analysis of the UV spectrum of 5B8 in chloroform revealed maximum absorption bands at 333 and 260. These wavelengths showed n-π* transitions.

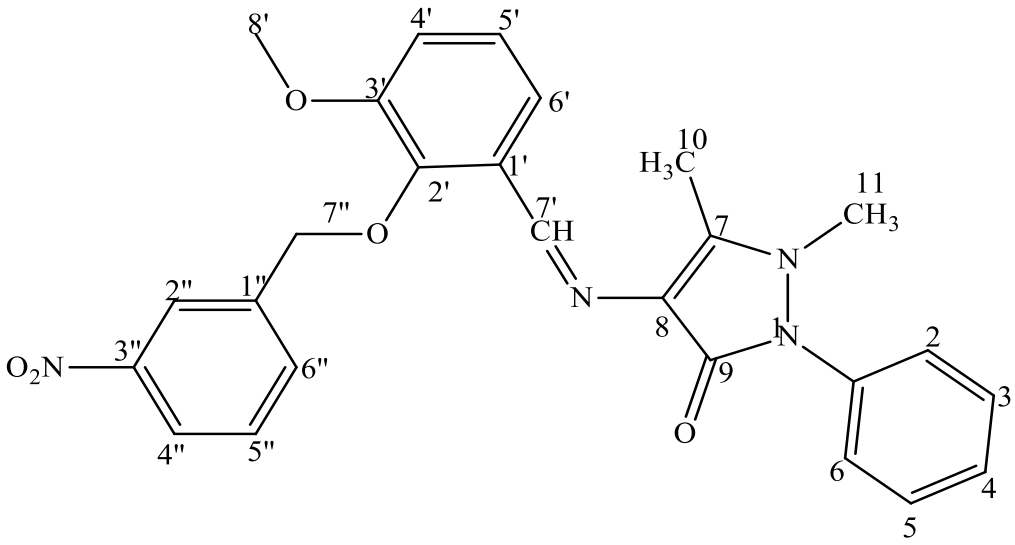

Scheme 4. 35: Structure of 5A-8

4.2.36 Characterisation of 4-((3-methoxy-2-((3-methoxybenzyl)oxy)benzylidene) amino)-1,5-dimethyl-2-phenyl-1H-pyrazol-3(2H)-one (5A-9)

The compound 4-((3-methoxy-2-((3-methoxybenzyl)oxy)benzylidene)amino)-1,5-dimeth yl-2-phenyl-1H-pyrazol-3(2H)-one (Scheme 4.36) appeared as brown solid, with 87% yield, and melting point of 124.6-125.5 ^{o}C.

The ^{1}H NMR spectrum (500 MHz, DMSO-d_6) showed sixteen signals and a total of twenty-seven protons. The most downfield signal at δ_H (ppm) 9.955 (s,1H, CH, H-7') was assigned to the azomethine proton. The four signals at δ_H (ppm) 7.230 (t, $J_{5'',4''/5'',6''}$ = 8Hz, 1Hz, H-5''), 7.121 (s, IH, H-2''), 7.106 ($J_{6'',4''/6'',2''}$ = 1.5Hz, 1H, H-6'') and 6.846 (d, $J_{4'',5''}$ =8Hz, $J_{4'',6''/4'',2''}$ = 2Hz, 1H, H-4'') were assigned to aromatic protons on the benzaldehyde ring. The signals at δ_H (ppm) 7.606 (q, $J_{4',5'}$ = 9Hz, $J_{4',6'}$ = 3Hz, 1H, H-4'), 7.133 (d, $J_{6',2'}$ = 2.5Hz, 1H, H-6') and 6.992(d, $J_{3',2'/3',4'}$ = 7.5Hz, 1H, H-3') represent the aromatic protons on the benzaldehyde ring attached to the azomethine bond. While signals at δ_H (ppm) 7.544 (t, $J_{3,2/3,4} = J_{5,4/5,6}$ = 7.5Hz, 2H, H-3, H-5), 7.382 (dd, $J_{2,3} = J_{6,5}$ = 7.5 Hz, $J_{2,4} = J_{6,4}$ = 3 Hz, 2H, H-2, H-6) and 7.367 (d, $J_{4,3/4,5}$ = 8.5 Hz, 1H, H-4) correspond to the aromatic protons on the benzyl ring attached to the pyrazole moiety. The signals at δ_H (ppm) 4.930 (s, 2H, H-7'', CH_2), 3.861 (s, 3H, H-8'', OCH_3), 3.713 (s, 3H, H-8', OCH_3), 3.168 (s, 3H, H-11, CH_3) and 2.432 (s, 3H, H-10, CH_3) represent the methylene, the two methoxy and two methyl protons, respectively.

The signals from ^{13}C NMR (100 M-Hz, DMSO-d_6) broad band spectrum displayed nine characteristic peaks of quaternary carbons observed at δ 159.67 (C-9), 159.23 (C-7), 152.84 (C-3''), 152.26 (C-3'), 146.98 (C-2'), 138.38 (C-2''), 134.61 (C-1''), 131.36 (C-1') and 116.92 (C-8). Thirteen methine carbons were observed which were observed at δ 150.50 (C-7') 129.15 (C-3), 129.15 (C-3), 129.08 (C-4), 126.80 (C-5''), 124.48 (C-2), 124.20 (C-6), 120.66 (C-6'), 116.92 (C-2''), 116.89 (C-4''), 114.42 (C-4'), 114.24 (C-5'), and 113.24 (C-6''). DEPT-135 confirmed the presence of two methylene carbons at δ 56.02 (C-1'' and C-1'''). The four methyl carbons present appear upfield at 9.72 (C-10), 35.35 (C-11), 54.93 (C-8'') and 55.87 (C-8')

The FAB- spectrum of 5A-9 showed the molecular ion peak M^+ at M^+-1 at *m/z* 456. The fragment $[C_{19}H_{18}N_3O_3]^+$ at *m/z* 336 was also observed.

The infrared absorption spectrum of 5A-9 showed vibrational bands $\bar{\upsilon}$ (cm^{-1}) for C-H anti-sym. stretch of aromatic (3059), C-H anti-sym. stretch of methyl (2952), -C=O stretch of the carbonyl (1655), C=N stretch of the azomethine bond (1595), C=C stretch of aromatic (1464), C-H bend of methylene (1411), C-N stretch of pyrazole moiety (1297), Asymetric C-O-C stretch of ether, (1266) N-N stretch of pyrazole moiety (1206) and symetric C-O-C stretch of ether (1036).

The analysis of the UV spectrum of 5A-9 in chloroform revealed maximum absorption bands at 333. This wavelength showed n-π* transitions.

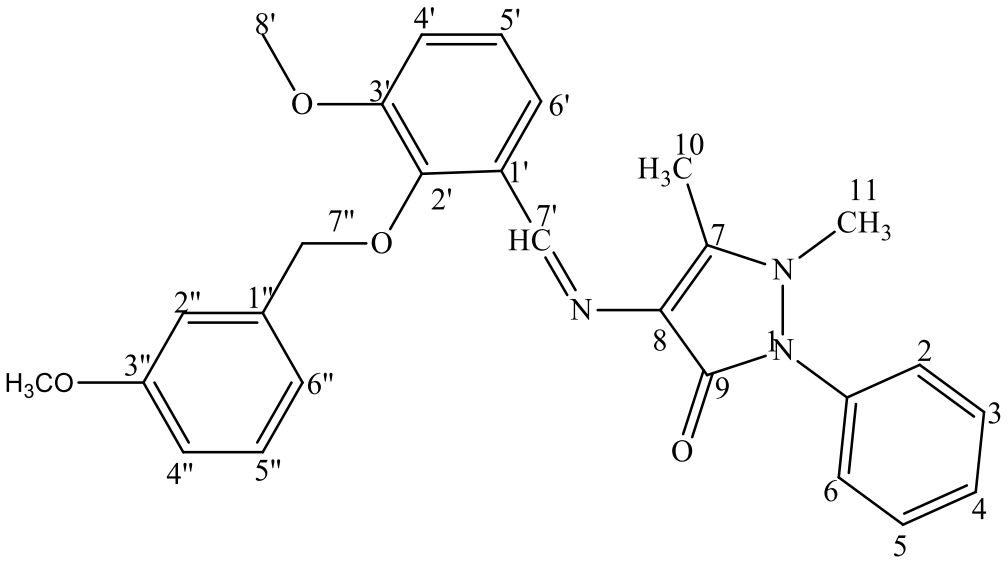

Scheme 4.36. Structure of 5A-9

4.2.37 Characterisation of 1,5-dimethyl-4-((4-((4-(methylthio)benzyl)oxy)benzylidene)amino)-2-phenyl-1,2-dihydro-3H-pyrazol-3-one (9B-1)

The compound 1,5-dimethyl-4-((4-((4-(methylthio)benzyl)oxy)benzylidene)amino)-2-phenyl-1,2-dihydro-3H-pyrazol-3-one (Scheme 4.37) was obtained as brown solid, with 81% yield, and melting point of 229.6-230.1 ^{o}C.

The ^{1}H NMR spectrum (400 MHz, DMSO -d_6) showed twelve signals representing a total of twenty-five protons. The singlet peak observed downfield at δ_H (ppm) 9.495 (s, 1H, H-7', CH) was assigned to the azomethine proton. The spectrum showed signals at δ_H (ppm) 7.747 (d, $J_{2',3'} = J_{6',5'}$ = 6.4 Hz, 2H, H-2', H-6') and 7.078 (d, $J_{3',2'} = J_{5',6'}$ = 8.8 Hz, 2H, H-3', H-5') as doublets corresponding to the chemically equivalent methine protons from the benzaldehyde ring. The signals at δ_H (ppm) 7.407 (d, $J_{3'',2''} = J_{5'',6''}$ = 8.4 Hz, 2H, H-3'', H-5''), 7.285(d, $J_{2'',3''} = J_{6'',5''}$ = 8.4 Hz, 2H, H-2'', 6''), represent the aromatic protons on the benzaldehyde ring attached to the azomethine bond. The three signals at δ_H (ppm) 7.532 (t, $J_{3,2/3,4} = J_{5,4/5,6}$ = 8.4 Hz, $J_{3,5} = J_{5,3}$ = 2.4 Hz, 2H, H-3, H-5), 7.370 (d, $J_{2,3} = J_{6,5}$ = 7.6 Hz, 2H, H-2, H-6) and 7.351 (d, $J_{4,3/4,5}$ = 7.6 Hz, 1H, H-4), correspond to the aromatic protons on the benzyl ring attached to the pyrazole moiety. The methylene protons α to the ether bond are deshielded due to the electronegativity of the oxygen, they are observed as singlets at δ_H (ppm) 5.111 (s, 2H, H-7'', CH_2). The signals at δ_H (ppm) 3.136 (s, 3H, H-11, CH_3) 2.420 (s, 3H, H-10, CH_3) and 2.465 (s, 3H, H-7'', CH_3) represent methyl protons.

The FAB+ spectrum of 9B1showed the molecular ion peak M^+ at M^++1 at *m/z* 444. The fragment $[C_{18}H_{16}N_3O_2]^+$ at *m/z* 306 was also observed

The infrared absorption spectrum of 9B1 showed vibrational bands $\bar{\upsilon}$ (cm^{-1}) for C-H anti-sym. C-H anti-sym. stretch of aliphatic (2920), -C=O stretch of carbonyl (1647), C=N stretch of azomethine bond (1500), C-N stretch of pyrazole moiety (1296), Asymetric C-O-C stretch of ether (1239) and N-N stretch of pyrazole moiety (1136).

The analysis of the UV spectrum of 9B1 in chloroform revealed maximum absorption bands at 332, 261, 219. The wavelengths at 332 and 261 indicate n-π* transitions. The wavelength at 219 showed π-π* transition.

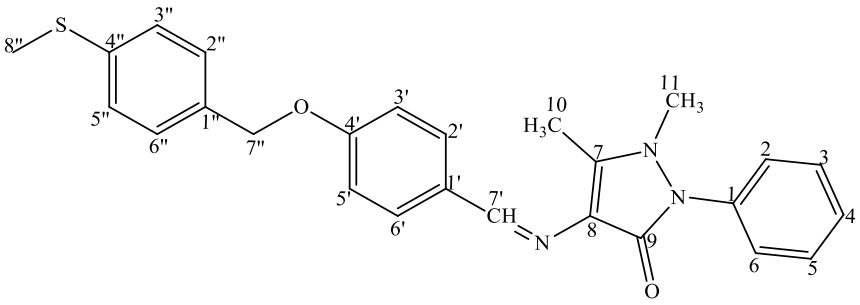

Scheme 4. 37: Structure 9B-1

4.2.38 Characterisation of 1,5-dimethyl-2-phenyl-4-((4-((4-(trifluoromethyl)benzyl) oxy)benzylidene)amino)-1,2-dihydro-3H-pyrazol-3-one (9B-2)

The compound 1,5-dimethyl-2-phenyl-4-((4-((4-(trifluoromethyl)benzyl)oxy) benzylidene)amino)-1,2-dihydro-3H-pyrazol-3-one (Scheme 4.38) appeared as Brown solid, with 86% yield, and melting point of 183.0-185.0 ^{o}C.

The ^{1}H NMR spectrum (400 MHz, DMSO-d_6, δ_H (ppm)) displayed eleven signals and a total of twenty-two protons. The azomethine proton was observed downfield at δ_H (ppm) 9.503 (s, 1H, CH, H-7'). The spectrum showed signals at δ_H (ppm) 7.774 (d, $J_{2',6'} = J_{6',2'}$ = 2.4Hz, 2H, H-2', H-6'), 7.753 (d, $J_{3'',5''} = J_{5'',3''}$ = 2.4Hz, 2H, H-3'', H-5''), 7.691(d, $J_{3',2'} = J_{5',6'}$ = 8Hz, 2H, H-3', H-5'), and 7.108 (d, $J_{2'',3''} = J_{6'',5''}$ = 8.8Hz, 2H, H-2'', H-6''), as doublets corresponding to the chemically equivalent methine protons on the rings. The three signals at δ_H (ppm) 7.514 (t, $J_{3,2/3,4} = J_{5,4/5,6}$ = 8.Hz, 2H, H-3, H-5), 7.371 (d, $J_{4,3/4,5}$ = 7.6 Hz, 1H, H-4), and 7.352 (d, $J_{2,3} = J_{6,5}$ = 7.6 Hz, 2H, H-2, H-6) were assigned to the aromatic methine protons on the benzyl ring attached to the pyrazole moiety. The methylene protons α to the ether bond were observed as singlets at δ_H (ppm) 5.285 (s, 2H, H-7'', CH_2), Two upfield singlets at δ_H (ppm) 3.139 (s, 3H, H-11, CH_3), and 2.423 (s, 3H, H-10, CH_3) represent methyl protons of the pyrazole moiety.

The FAB+ spectrum of showed the molecular ion peak at M^++1 at *m/z* 466. The fragment $[C_{18}H_{16}N_3O_2]^+$ at *m/z* 306 was also observed.

The infrared absorption spectrum of 9B2 showed vibrational bands with $\bar{\upsilon}$ (cm^{-1}) for C-H anti-sym. stretch of aromatic (3062), C-H anti-sym. stretch of aliphatic (2926), -C=O stretch of carbonyl (1631), C=N stretch of azomethine bond (1559), C=C stretch of aromatic (1508), C-H bend of methylene (1419), C-N stretch of pyrazole moiety (1328), Asymetric C-O-C stretch of ether (1244) N-N stretch of pyrazole moiety (1166) and symetric C-O-C stretch of ether (1065).

The analysis of the UV spectrum of 9B2 in chloroform revealed maximum absorption bands at 335, 266, 261, 253. These wavelengths showed n-π* transitions.

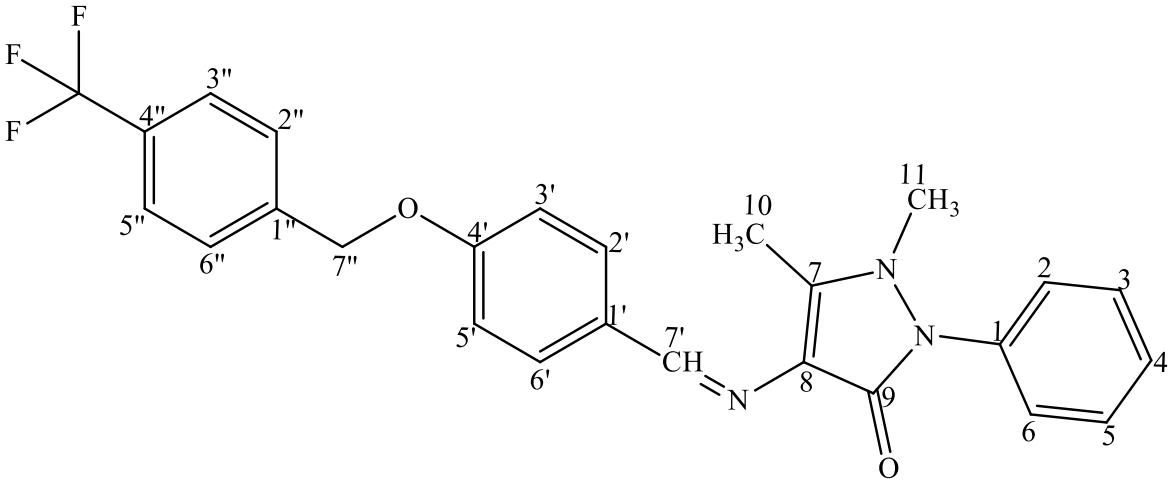

Scheme 4. 38: Structure 9B-2

4.2.39 Characterisation of 4-((4-((3-chlorobenzyl)oxy)benzylidene)amino)-1,5-dimethyl-2-phenyl-1H-pyrazol-3(2H)-one (9B-5)

The compound 4-((4-((3-chlorobenzyl)oxy)benzylidene)amino)-1,5-dimethyl-2-phenyl-1H -pyrazol-3(2H)-one (Scheme 4.39) appeared as brown solid, with 85 % yield, and melting point of 147.0-147.9 ^{o}C.

The ^{1}H NMR spectrum (400 MHz, DMSO-d_6, δ_H (ppm)) displayed twelve signals representing a total of twenty-two protons. The azomethine proton was observed downfield at δ_H (ppm) 9.509 (s,1H, CH, H-7'), The four signals at δ_H (ppm) 8.329 (s,1H, H-2''), 8.212 (dd, $J_{4'',5''}$ = 8.4 Hz, $J_{4'',6''/4'',2''}$ = 1.6 Hz, 1H, H-4'') 7.939 (d, $J_{6'',5''}$ = 8 Hz, 1H, H-6'') and 7.727 (d, $J_{5'',4''/5'',6''}$ = 8 Hz, 1H, H-5'') represent the aromatic methine protons on the benzyl ring attached to the azomethine bond. These protons move more downfield compared to other aromatic protons in the spectrum due to the presence of nitro group in the ring. The spectrum showed signals at δ_H (ppm) 7.778 (d, $J_{2',3'} = J_{6',5'}$ = 8.4 Hz, 2H, H-2', H-6') and 7.133 (d, $J_{3',2'} = J_{5',6'}$ = 8.8 Hz, 2H, H-3', H-5'), as doublets corresponding to the chemically equivalent methine protons on the benzyl ring attached to the ether bond. The three signals at δ_H (ppm) 7.535 (t, $J_{3,2/3,4} = J_{5,4/5,6}$ = 8.4 Hz, 2H, H-3, H-5), 7.373 (d, $J_{4,3/4,5}$ = 7.6 Hz, 1H, H-4) and 7.354 (d, $J_{2,3} = J_{6,5}$ = 7.6 Hz, 2H, H-4, H-6) were assigned to the aromatic methine protons on the benzyl ring attached to the pyrazole moiety. Three singlets at δ_H (ppm) 5.330 (s, 2H, H-7'', CH_2), 3.142 (s, 3H, H-11, CH_3) and 2.426 (s, 3H, H-10, CH_3) correspond to the methylene and two methyl protons, respectively.

The FAB+ spectrum of 9B-5 showed the molecular ion peak at M^++1 at *m/z* 432. The fragment $[C_{18}H_{16}N_3O_2]^+$ at *m/z* 306 was also observed. The infrared absorption spectrum of 9B-5 showed vibrational band with $\bar{\upsilon}$ (cm^{-1}) for C-H anti-sym. stretch of aromatic (3094), C-H anti-sym. stretch of methyl (2925), -C=O stretch of carbonyl (1645), C=N stretch of azomethine bond (1577), C=C stretch of aromatic (1527), N=O asymmetric stretch of nitro substituent (1488), C-H bend of methylene (1455), C-H bend of methyl (1378), N=O symmetric stretch of nitro substituent (1349), C-N stretch of pyrazole moiety (1300), Asymetric C-O-C stretch of ether (1258) N-N stretch of pyrazole moiety (1176) and symetric C-O-C stretch of ether (1027).

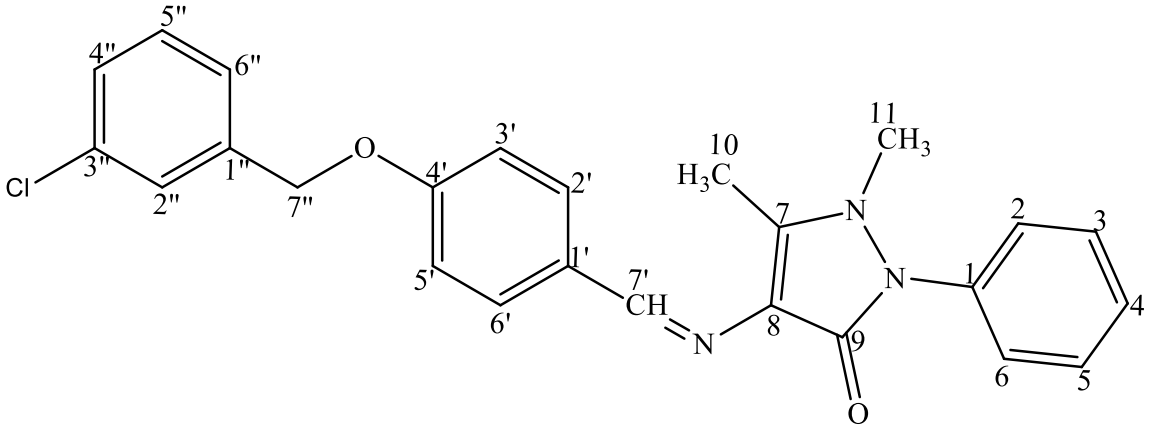

Scheme 4. 39: Structure 9B-5

4.2.40 Characterisation of 4-((4-((2-bromobenzyl)oxy)benzylidene)amino)-1,5-dimeth yl-2-phenyl-1H-pyrazol-3(2H)-one (9B-6)

The compound 4-((4-((2-bromobenzyl)oxy)benzylidene)amino)-1,5-dimethyl-2-phenyl-1H-pyrazol-3(2H)-one (Scheme 4.40) appeared as pale yellow solid, with 98 % yield, and melting point of . 205.8-206.9 ^{o}C.

The ^{1}H NMR spectrum (400 MHz, DMSO-$d_{6,}$ δ_H (ppm)) displayed twelve signals representing a total of twenty-two protons. The azomethine proton was observed downfield at δ_H (ppm) 9.515 (s,1H, CH, H-7'), The four signals at δ_H (ppm) 7.697 (dd, $J_{3",4"}$ = 8 Hz, 1H, H-3"), 7.610 (dd, $J_{6",5"}$ = 8 Hz, $J_{6",4"}$ = 1.6 Hz, 1H, H-6") 7.452 (t, $J_{5",4"/5",4"}$ = 8 Hz, 1H, H-5") and 7.339 (dt, $J_{4",3"/4",5"}$ = 7.6 Hz, $J_{4",6"}$ = 1.6 Hz,1H, H-4") represent the aromatic methine protons on the benzaldehyde ring. The spectrum showed signals at δ_H (ppm) 7.779 (d, $J_{2',3'}$ = $J_{6',5'}$ = 8.4 Hz, 2H, H-2', H-6') and 7.112 (d, $J_{3',2'}$ = $J_{5',6'}$ = 8.8 Hz, 2H, H-3', H-5') as doublets corresponding to the chemically equivalent methine protons on the benzaldehyde ring attached to the azomethine bond. The three signals at δ_H (ppm) 7.536 (t, $J_{3,2/3,4}$ = $J_{5,4/5,6}$ = 8 Hz, 2H, H-3, H-5), 7.376 (d, $J_{2,3}$ = $J_{6,5}$ = 8 Hz, 2H, H-2, H-6) and 7.356 (d, $J_{4,3/4,5}$ = 8 Hz, 1H, H-4) were assigned to the aromatic methine protons on the benzyl ring attached to the pyrazole moiety. The methylene protons α to the ether bond were observed as singlets at δ_H (ppm) 5.180 (s, 2H, H-7", CH_2), Two up field singlets at δ_H (ppm) 3.143 (s, 3H, H-11, CH_3) and 2.429 (s, 3H, H-10, CH_3) correspond to the methyl protons of the pyrazole moiety.

The FAB+ spectrum of 9B-6 showed the molecular ion peak at M^{+}+1 at *m/z* 476. The fragment $[C_{18}H_{16}N_3O_2]^{+}$ was also observed at *m/z* 306.

The infrared absorption spectrum of 9B-6 showed vibrational bands with $\bar{\upsilon}$ (cm^{-1}) for C-H anti-sym. stretch of aromatic (3094), C-H anti-sym. stretch of methyl (2925), -C=O stretch of carbonyl (1645), C=N stretch of azomethine bond (1577), C=C stretch of aromatic (1527), N=O asymmetric stretch of nitro substituent (1488), C-H bend of methylene (1455), C-H bend of methyl (1378), N=O symmetric stretch of nitro substituent (1349), C-N stretch of pyrazole moiety (1300), Asymetric C-O-C stretch of ether (1258) N-N stretch of pyrazole moiety (1176) and symetric C-O-C stretch of ether (1027).

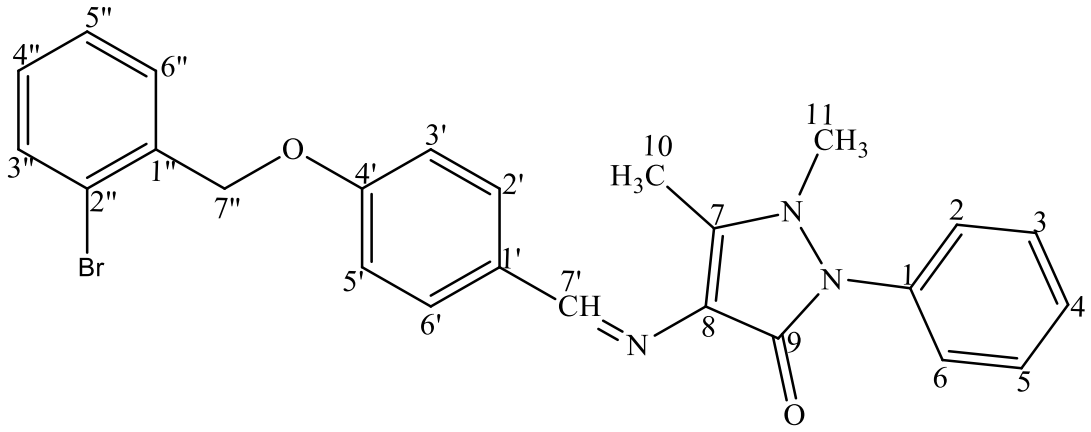

Scheme 4. 40: Structure 9B-6

4.2.41 Characterisation of 1,5-dimethyl-4-((4-((3-nitrobenzyl)oxy)benzylidene)amino)-2-phenyl-1,2-dihydro-3H-pyrazol-3-one (9B-8)

The compound 1,5-dimethyl-4-((4-((3-nitrobenzyl)oxy)benzylidene)amino)-2-phenyl-1,2-dihy dro-3H-pyrazol-3-one (Scheme 4.41) appeared as yellow solid, with 93 % yield, and melting point of 162.0-163.9 ^{o}C.

The ^{1}H NMR spectrum (400 MHz, DMSO-d_6, δ_H (ppm)) displayed twelve signals representing a total of twenty-two protons. The azomethine proton was observed downfield at δ_H (ppm) 9.509 (s,1H, CH, H-7'), The four signals at δ_H (ppm) 8.329 (s,1H, H-2''), 8.212 (dd, $J_{4'',5''}$ = 8.4 Hz, $J_{4'',6''/4'',2''}$ = 1.6 Hz, 1H, H-4'') 7.939 (d, $J_{6'',5''}$ = 8 Hz, 1H, H-6'') and 7.727 (d, $J_{5'',4''/5'',6''}$ = 8 Hz, 1H, H-5'') are the aromatic methine protons on the benzyl ring attached to the azometine bond. These protons move more downfield due to the presence of nitro group in the ring. The signals at δ_H (ppm) 7.778 (d, $J_{2',3'} = J_{6',5'}$ = 8.4 Hz, 2H, H-2', H-6') and 7.133 (d, $J_{3',2'} = J_{5',6'}$ = 8.8 Hz, 2H, H-3', H-5'), are doublets corresponding to the chemically equivalent methine protons on the benzyl ring attached to the ether bond. The three signals at δ_H (ppm) 7.535 (t, $J_{3,2/3,4} = J_{5,4/5,6}$ = 8.4 Hz, 2H, H-3, H-5), 7.373 (d, $J_{4,3/4,5}$ 7.6 Hz, 1H, H-4) and 7.354 (d, $J_{2,3} = J_{6,5}$ = 7.6 Hz, 2H, H-2, H-6) were assigned to the aromatic methine protons attached to the pyrazole. Three singlets at δ_H (ppm) 5.330 (s, 2H, H-7'', CH_2), 3.142 (s, 3H, H-11, CH_3) and 2.426 (s, 3H, H-10, CH_3) correspond to the methylene and two methyl protons, respectively.

The FAB+ spectrum of 9B8 showed the molecular ion peak at M^+-1 at *m/z* 441. The fragment $[C_{18}H_{16}N_3O_2]^+$ at *m/z* 306 was also observed.

The infrared absorption spectrum of 9B8 showed vibrational bands with $\bar{\upsilon}$ (cm^{-1}) for C-H anti-sym. stretch of aromatic (3094), C-H anti-sym. stretch of methyl (2925), C=O stretch of carbonyl (1645), C=N stretch of azomethine bond (1577), C=C stretch of aromatic (1527), N=O asymmetric stretch of nitro substituent (1488), N=O symmetric stretch of nitro substituent (1349), C-N stretch of pyrazole (1300).

The analysis of the UV spectrum of 9B2 in chloroform revealed maximum absorption bands at 335, 266 and 262. These wavelengths showed n-π* transitions.

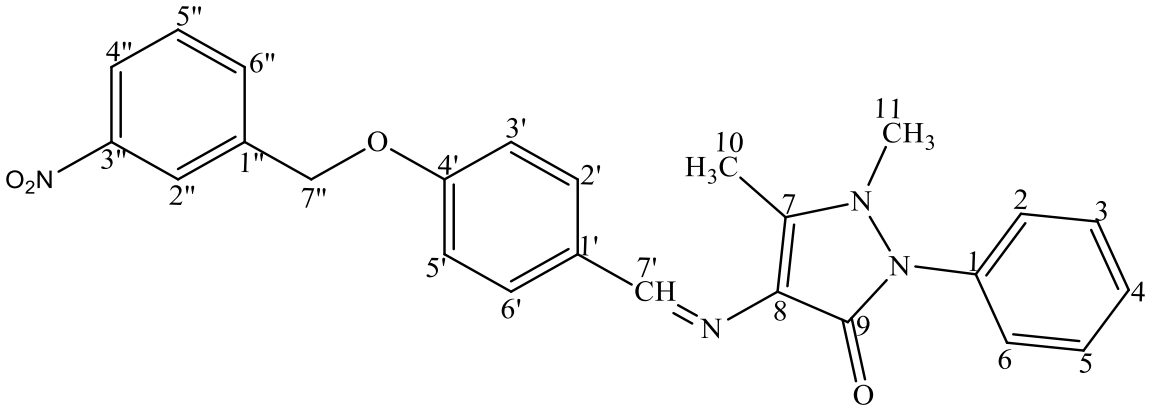

Scheme 4. 41: Structure 9B-8

4.2.42 Characterisation of 4-((4-((3-methoxybenzyl)oxy)benzylidene)amino)-1,5-dimethyl-2-phenyl-1,2-dihydro-3H-pyrazol-3-one (9B-9)

The compound 4-((4-((3-methoxybenzyl)oxy)benzylidene)amino)-1,5-dimethyl-2-phenyl-1,2-dihydro-3H-pyrazol-3-one (Scheme 4.42) was obtained as pale yellow solid, with 56% yield, and melting point of 128.7-129.9 ^{o}C.

The ^{1}H NMR spectrum (500 MHz, DMSO-d_6, δ_H (ppm)) displayed thirteen signals representing a total of twenty-five protons. The azomethine proton was observed downfield at δ_H (ppm) 9.500 (s,1H, CH, H-7'). The spectrum showed signals at δ_H (ppm) 7.752 (d, $J_{2',3'} = J_{6',5'}$ = 9 Hz, 2H, H-2', H-6') and 7.086 (d, $J_{3',2'} = J_{5',6'}$ = 8.5 Hz, 2H, H-3', H-5') as doublets corresponding to the chemically equivalent methine protons on the benzyl ring attached to the ether and azomethine bond. The signals at δ_H (ppm) 7.318 (t, $J_{5'',4''/5'',6''}$ = 8 Hz, 1H, H-5''), 7.024 (d, $J_{2'',4''/2'',6''} = J_{4'',6''/4'',2''}$ = 2.5 Hz, 2H, H-2'', H-4'') and 6.901 (d, $J_{6'',5''}$ = 8Hz, $J_{6'',4''/6'',2''}$ = 1.5Hz,1H, H-6'' were assigned to the aromatic methine protons on the benzyl ring α to the ether bond. There was an overlap observed between protons H-2'' and H-4'' in the spectrum. The three signals at δ_H (ppm) 7.529 (dt, $J_{3,2/3,4} = J_{5,4/5,6}$ = 8 Hz, $J_{3,5} = J_{5,3}$ = 1.5 Hz, 2H, H-3, H-5),7.371 (dt, $J_{4,3/4,5}$ = 8.5 Hz, 1H, H-4) and 7.354 (dt, $J_{2,3} = J_{6,5}$ = 8.5 Hz, 2H, H-2, H-6) were assigned to the aromatic methine protons on the benzyl ring attached to the pyrazole moiety. Four singlets at δ_H (ppm) 5.131 (s, 2H, H-7'', CH_2), 3.752 (s, 3H, H-8'', OCH_3), 3.137 (s, 3H, H-11, CH_3) and 2.422 (s, 3H, H-10, CH_3) represent the methylene, methoxy and the methyl protons, respectively.

The FAB- spectrum of 9B-9 showed the molecular ion peak at M^+-1 at *m/z* 426. Other prominent peak were observed at *m/z* 306 $[C_{18}H_{16}N_3O_2]^+$ and 412 $[C_{25}H_{22}N_3O_3]$+.

The infrared absorption spectrum of 9B9 showed vibrational bands $\bar{\upsilon}$ (cm^{-1}) for C-H anti-sym. stretch of aromatic (3062), C-H anti-sym. stretch of aliphatic (2926), -C=O stretch of carbonyl (1631), C=N stretch of azomethine (1559), C=C stretch of aromatic (1508). Asymetric C-O-C stretch of ether (1244), and symetric C-O-C stretch of ether (1065).

The analysis of the UV spectrum of 9B-9 in chloroform revealed maximum absorption bands at 335, 285, and 254. These wavelengths showed n-π* transitions.

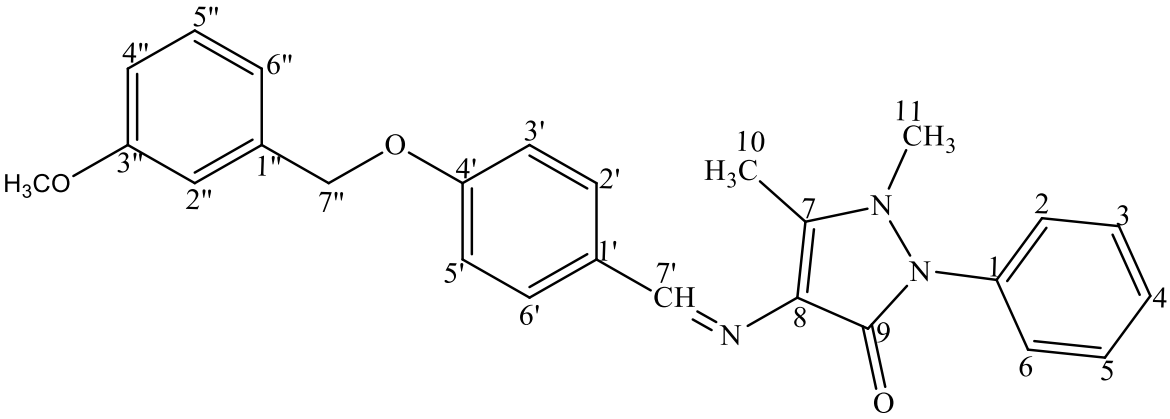

4. 42. Structure 9B-9

4.2.43 Characterisation of 1,5-dimethyl-4-((5-((4-(methylthio)benzyl)oxy)-2-nitrobenzylidene) amino)-2-phenyl-1,2-dihydro-3H-pyrazol-3-one (10-1)

The compound1,5-dimethyl-4-((5-((4-(methylthio)benzyl)oxy)-2-nitrobenzylidene) amino)-2-phenyl-1,2-dihydro-3H-pyrazol-3-one (Scheme 4.43) appeared as Orange solid, with 86% yield, and melting point of 185.0-186.7 ^{o}C.

The ^{1}H NMR spectrum (400 MHz, DMSO-d_6, δ_H (ppm)) displayed thirteen signals representing a total of twenty-four protons. The azomethine proton was observed downfield at δ_H (ppm) 9.927 (s, 1H, CH, H-7'). The signals at δ_H (ppm) 8.049 (d, $J_{3',4'}$ = 8.8 Hz, 1H, H-3'), 7.708 (d, $J_{6',4'}$ = 2.8 Hz, 1H, H-6') and 7.229 (d, $J_{4',3'}$ = 6.4 Hz, $J_{4',6'}$ = 2.8 Hz,1H, H-4') represent the aromatic methine protons on the benzyl ring attached to the azomethine bond. The signals at δ_H (ppm) 7.448 (d, $J_{3'',2''} = J_{5'',6''}$ = 8.4 Hz, 2H, H-3'', H-5'') and 7.303(d, $J_{2'',3''} = J_{6'',5''}$ = 8.4 Hz, 2H, H-2'', 6'') correspond to the chemically equivalent methine protons on the benzyl ring attached to the ether bond. The signals at δ_H (ppm) 7.550 (t, $J_{3,2/3,4} = J_{5,4/5,6}$ = 8 Hz, 2H, H-3, H-5), and 7.411(d, $J_{4,3/4,5}$ = 7.6 Hz, 1H, H-4), 7.374 (d, $J_{2,3} = J_{6,5}$ = 8.8 Hz, $J_{2,4} = J_{6,4}$ = 1.2 Hz, 2H, H-2, H-6) were assigned to the methine protons on the benzyl ring attached to the pyrazole moiety. Four singlets at δ_H (ppm) 5.268 (s, 2H, H-7", CH_2), 3.275 (s, 3H, H-11, CH_3) 3.236 (s, 3H, H-8", CH_3) and 2.466 (s,3H, H-10, CH_3) represent a methylene and three methyl protons, respectively.

The signals from ^{13}C NMR (100 M-Hz, DMSO-d_6) broad band spectrum displayed eight characteristic peaks of quaternary carbons observed downfield at δ 161.60 (C-5'), 159.01 (C-9), 152.55 (C-7), 141.50 (C-4"), 138.26 (C-2'), 134.21 (C-1), 132.59 (C-1") and 116.0 (C-8). Fourteen methine carbons were observed which were assigned as 148.40 (C-7') azomethine carbon and 128.63 (C-2" and C-6"), 127.29 (C-6'), 125.91 (C-3" and C-5"), 116.42 (C-3'), 112.40 (C-4' and C-6') on the benzaldehyde rings, 129.17 (C-5 and C-3), 127.22 (C-4), and 125.15 (C-2 and C-6) on the phenyl ring. DEPT-135 confirmed the presence of a methylene carbon assigned as δ 69.71 (C-7") while DEPT-90 confirmed the presence of the fourteen methine carbons. The three methyl carbons present appear upfield at 9.66 (C-10), 14.58 (C-8") and 34.93 (C-11).

The FAB+ spectrum of 10-1 showed the molecular ion peak at M^{+}+1 at *m/z* 489. The fragment $[C_{18}H_{15}N_4O_4]^{+}$ at *m/z* 351 was also observed.

The infrared absorption spectrum of 10-1 showed vibrational bands with $\bar{\upsilon}$ (cm^{-1}) for C-H anti-sym. stretch of aromatic (3093), C-H anti-sym. stretch of methoxy (2943), C=O stretch of carbonyl (1640), C=N stretch of azomethine (1593), C=C stretch of aromatic (1506), N=O asymmetric stretch of nitro substituent (1421), C-H bend of methyl (1382), C-N stretch of pyrazole moiety (1321), and N=O asymmetric stretch of nitro substituent (1421).

The analysis of the UV spectrum of 10-1 in chloroform revealed maximum absorption bands at 260 and 220. The wavelengths at 260 showed n-π* transitions, while the wavelength at 220 is indicative of π-π* transition.

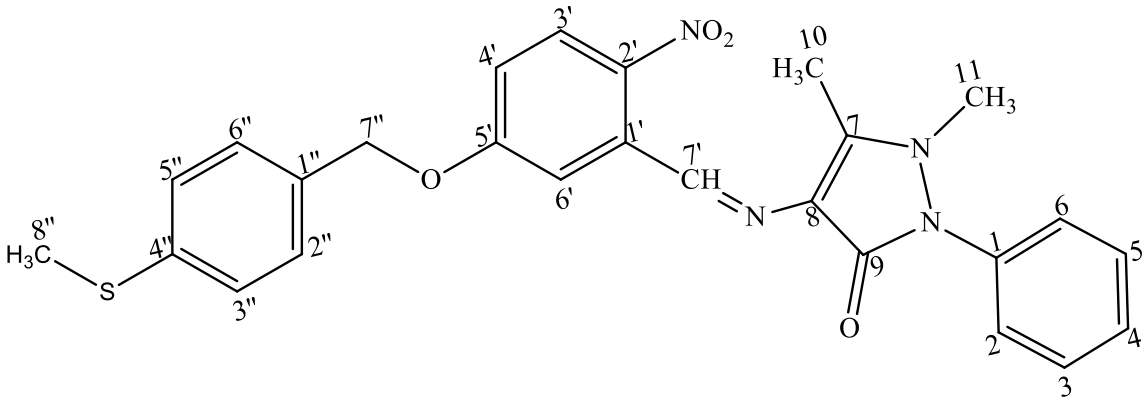

Scheme 4. 43:. Structure 10-1

4.2.44 Characterisation of 1,5-dimethyl-4-((2-nitro-5-((4-(trifluoromethyl)benzyl) oxy)benzyli dene)amino)-2-phenyl-1,2-dihydro-3H-pyrazol-3-one (10-2)

The compound 1,5-dimethyl-4-((2-nitro-5-((4-(trifluoromethyl)benzyl)oxy)benzylidene) amino)-2-phenyl-1,2-dihydro-3H-pyrazol-3-one (Scheme 4.44) appeared as golden yellow solid, with 88% yield, and melting point of 213.0-214.0 ^{o}C.

The ^{1}H NMR spectrum (400 MHz, DMSO-d_6, δ_H (ppm)) displayed twelve signals and a total of twenty-one protons. The azomethine proton was observed downfield at δ_H (ppm) 9.925 (s,1H, CH, H-7'), The signals at δ_H (ppm) 7.801 (d, $J_{3'',2''} = J_{5'',6''}$ = 8.4Hz, 2H, H-3'', H-5'') and 7.721(d, $J_{2'',3''} = J_{6'',5''}$ = 7.6Hz, $J_{2'',6''} = J_{6'',2''}$ = 2.8Hz, 2H, H-2'', 6'') correspond to the chemically equivalent methine protons on the benzyl ring α to the ether bond. The three signals at δ_H (ppm) 8.069 (d, $J_{3',4'}$ = 9.2Hz, 1H, H-3'), 7.733(s, 1H, H-6') and 7.260 (d, $J_{4',3'}$ = 8.8Hz, $J_{4',6'}$ = 2.8Hz,1H, H-4') represent the aromatic methine protons on the benzyl ring attached to the azomethine bond. The signals at δ_H (ppm) 7 .551 (t, $J_{3,2/3,4} = J_{5,4/5,6}$ = 8Hz, 2H, H-3, H-5), 7.412 (d, $J_{4,3/4,5}$ = 7.6 Hz, 1H, H-4) and 7.373 (d, $J_{2,3} = J_{6,5}$ = 8.4Hz, $J_{2,4} = J_{6,4}$ = 1.2Hz, 2H, H-2, H-6) were assigned to the aromatic methine protons on the benzyl ring attached to the pyrazole moiety. Three singlets at δ_H (ppm) 5.440 (s, 2H, H-7'', CH_2), 3.236 (s, 3H, H-11, CH_3) and 2.446 (s, 3H, H-10, CH_3) represent the methylene and methyl protons, respectively.

The FAB+ spectrum of 10-2 showed the molecular ion peak at M^{+}+1 at *m/z* 511. The fragment $[C_{18}H_{16}N_3O_2]^{+}$ at *m/z* 351 was also observed.

The infrared absorption spectrum of 10-2 showed vibrational bands $\bar{\upsilon}$ (cm^{-1}) for C-H anti-sym. stretch of aromatic (3268), C-H anti-sym. stretch of aliphatic (2882), -C=O stretch of carbonyl (1650), C=N stretch of azomethine bond (1579), C=C stretch of aromatic (1512), C-H bend of methylene (1419), N=O asymmetric stretch of nitro substituent (1481), N=O symmetric stretch of nitro substituent (1385), and C-N stretch of pyrazole moiety (1322).

The analysis of the UV spectrum of 10-2 in chloroform revealed maximum absorption bands at 277, 273, 229 and 211. The wavelengths at 277 and 273 showed n-π* transitions. The wavelength at 2229 and 211 are suggestive of π-π* transition.

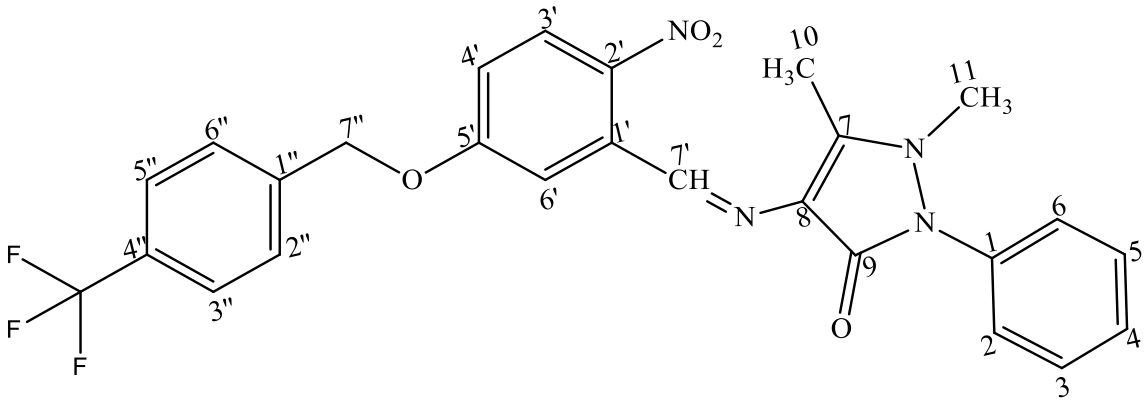

Scheme 4. 44: Structure 10-2

4.2.45 Characterisation of 4-((5-((3-chlorobenzyl)oxy)-2-nitrobenzylidene)amino)-1,5-dimethyl -2-phenyl-1,2-dihydro-3H-pyrazol-3-one (10-5)

The compound 4-((5-((3-chlorobenzyl)oxy)-2-nitrobenzylidene)amino)-1,5-dimethyl -2-phenyl-1,2-dihydro-3H-pyrazol-3-one (Scheme 4.45) was obtained as, orange solid with 96 % yield, and melting point of 164.6-166.0 ^{o}C.

The ^{1}H NMR spectrum (400 MHz, DMSO-d_6, δH (ppm)) displayed twelve signals representing a total of twenty-one protons. The azomethine proton was observed downfield at δ_H (ppm) 9.929 (s, 1H, CH, H-7'). The four signals observed at δ_H (ppm) 7.584 (s, 1H, H-2''), 7.463 (d, $J_{4'',6''/4'',2''}$ = 2.4 Hz, 1H, H-4''), 7.434 (d, $J_{6'',4''/6'',2''}$ = 2 Hz, 1H, H-6'') and 7.422 (d, $J_{5'',4''/5'',6''}$ = 6.4 Hz, 1H, H-5'') represent the aromatic methine protons on the benzyl ring α to the ether bond. The three protons on the benzyl ring attached to the azomethine bond were observed at δ_H (ppm) 8.061 (d, $J_{3',4'}$ = 8.8 Hz, 1H, H-3'), 7.723 (d, $J_{6',4'}$ = 2.8 Hz, 1H, H-6') and 7.248 (d, $J_{4',3'}$ = 8.8 Hz, $J_{4',6'}$ = 2.8 Hz,1H, H-4'). The signals at δ_H (ppm) 7.551 (t, $J_{3,2/3,4} = J_{5,4/5,6}$ = 8 Hz, 2H, H-3, H-5), 7.392 (d, $J_{2,3} = J_{6,5}$= 7.2 Hz, $J_{2,4} = J_{6,4}$= 1.2 Hz, 2H, H-2, H-6) and 7.371 (d, $J_{4,3/4,5}$ = 7.2 Hz, 1H, H-4) were assigned to the aromatic methine protons on the benzyl ring attached to the pyrazole moiety. The methylene protons and two methyl protons were observed as singlets at δ_H (ppm) 5.336 (s, 2H, H-7'', CH_2), 3.236 (s,3H, H-11, CH_3) and 2.469 (s, 3H, H-10, CH_3), respectively.

The FAB- spectrum of 10-5 showed the molecular ion peak at M^+-1 at *m/z* 475. The fragment $[C_{18}H_{16}N_3O_2]^+$ at *m/z* 351 was also observed.

The infrared absorption spectrum of 10-5 showed vibrational bands with $\bar{\upsilon}$ (cm^{-1}) for C-H anti-sym. stretch of aromatic (3052), C-H anti-sym. stretch of aliphatic (2927), -C=O stretch of carbonyl (1645), C=N stretch of azomethine bond (1595), C=C stretch of aromatic (1559), N=O asymmetric stretch of nitro substituent (1502), C-H bend of methylene (1423), N=O symmetric stretch of nitro substituent (1362), and C-N stretch of pyrazole moiety (1319)

The analysis of the UV spectrum of 9B2 in chloroform revealed maximum absorption band at 286 which is indicative of n-π* transitions.

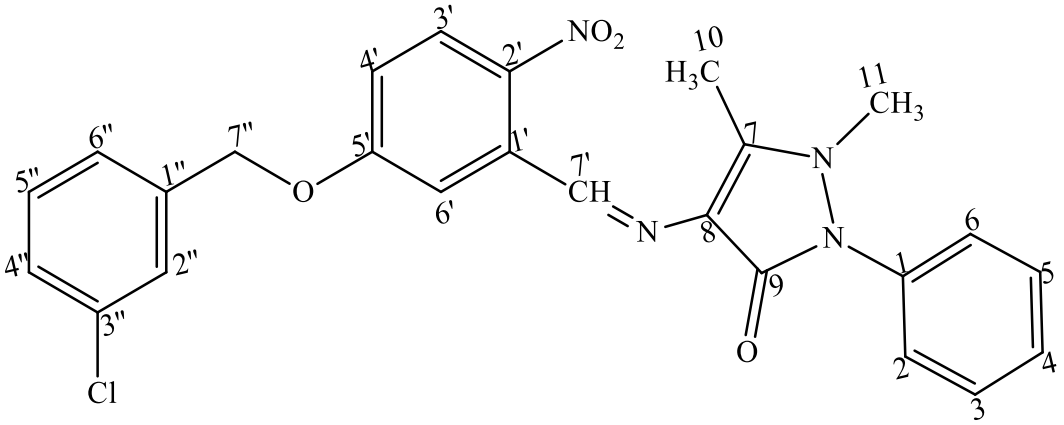

Scheme 4. 45: Structure 10-5

4.2.46 Characterisation of 4-((5-((2-bromobenzyl)oxy)-2-nitrobenzylidene)amino)-1,5-dimethyl-2-phenyl-1H-pyrazol-3(2H)-one (10-6)

The compound 4-((5-((2-bromobenzyl)oxy)-2-nitrobenzylidene)amino)-1,5-dimethyl-2-phenyl-1H-pyrazol-3(2H)-one (Scheme 4.46) appeared as orange solid, with 89 % yield, and melting point of 154.2-156.8 ^{o}C.

The ^{1}H NMR spectrum (400 MHz, DMSO-d_6) displayed twelve signals representing a total of twenty-one protons. The azomethine proton was observed downfield at δ_H (ppm) 9.935 (s,1H, CH, H-7'). The four signals at δ_H (ppm) 7.629 (dd, $J_{3'',4''}$ = 7.6Hz, $J_{3'',5''}$ = 1.6Hz, 1H, H-3''), 7.467 (dt, $J_{5'',4''/5'',6''}$ = 7.6Hz, $J_{5'',3''}$ = 1.2Hz, 1H, H-5''), 7.344 (dd, $J_{6'',5''}$ = 8Hz, $J_{6'',4''}$ = 1.6Hz, 1H, H-6'') and 7.277 (dd, $J_{4'',3''/4'',5''}$ = 9.2Hz, $J_{4'',6''}$ = 2.8Hz, 1H, H-4'') represent the aromatic methine protons on the benzyl ring α to the ether bond. The signals observed at δ_H (ppm) 8.077 (d, $J_{3',4'}$ = 8.8Hz, 1H, H-3') and 7.720 (dd, $J_{4',3'}$ = 7.8Hz, $J_{4',6'}$ = $J_{6',4'}$ = 2.8Hz, 2H, H-4', H-6') were assigned to the aromatic methine protons on the benzyl ring attached to the azomethine bond. The three signals at δ_H (ppm) 7.550 (t, $J_{3,2/3,4}$ = $J_{5,4/5,6}$ = 8Hz, 2H, H-3, H-5), 7.411 (d, $J_{4,3/4,5}$ = 7.6Hz, 1H, H-4) and 7.373 (d, $J_{2,3}$ = $J_{6,5}$ = 8.4 Hz, $J_{2,4}$ = $J_{6,4}$= 1.2 Hz, 2H, H-2, H-6) were assigned to the aromatic methine protons on the benzyl ring attached to the pyrazole moiety. Three upfield singlets at δ_H (ppm) 5.336 (s, 2H, H-7'', CH_2), 3.233 (s, 3H, H-11, CH_3) and 2.457 (s, 3H, H-10, CH_3) correspond to the methylene and two methyl protons, respectively.

The FAB- spectrum of compound 10-6showed the molecular ion peak at M^{+}-1 at *m/z* 520.

The infrared absorption spectrum of 10-6 showed vibrational bands with $\bar{\upsilon}$ (cm^{-1}) for C-H anti-sym. stretch of aromatic (3056), C-H anti-sym. stretch of aliphatic (2927), -C=O stretch of carbonyl (1646), C=N stretch of azomethine bond (1589), C=C stretch of aromatic (1551), N=O asymmetric stretch of nitro substituent (1505), C-H bend of methylene (1459), N=O symmetric stretch of nitro substituent (1362), C-N stretch of pyrazole moiety (1325), Asymetric C-O-C stretch of ether (1274) N-N stretch of pyrazole moiety (1233) and symetric C-O-C stretch of ether (1047).

The analysis of the UV spectrum of 10-8 in chloroform revealed maximum absorption bands at 288. This wavelengths at 2888 showed n-π* transitions.

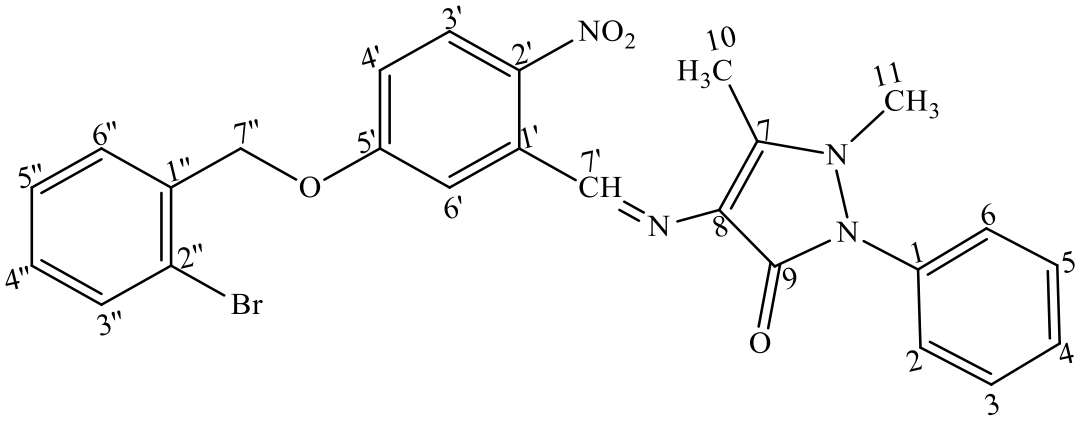

Scheme 4. 46: Structure 10-6

4.2.47 Characterisation of 1,5-dimethyl-4-((2-nitro-5-((3-nitrobenzyl)oxy)benzylidene)amino)-2-phenyl-1,2-dihydro-3H-pyrazol-3-one (10-8)

The compound 1,5-dimethyl-4-((2-nitro-5-((3-nitrobenzyl)oxy)benzylidene)amino)-2-phenyl-1,2-dihydro-3H-pyrazol-3-one (Scheme 4.47) appeared as orange solid, with 96 % yield, and melting point of 167.9-169.^{o}C.

The ^{1}H NMR spectrum (400 MHz, DMSO-d_6, δ_H (ppm)) displayed twelve signals representing a total of twenty-one protons. The azomethine proton was observed downfield at δ_H (ppm) 9.936 (s, 1H, CH, H-7'). The four signals at δ_H (ppm) 8.384 (s,1H, H-2''), 8.237(dd, $J_{4'',5''}$ = 8 Hz, $J_{4'',6''/4'',2''}$ = 1.6 Hz, 1H, H-4''), 7.9827 (d, $J_{6'',5''}$ = 7.6 Hz, 1H, H-6'') and 7.730 (d, $J_{5'',4''/5'',6''}$ = 8 Hz, 1H, H-5'') represent the aromatic protons on the benzyl ring α to the ether bond. The signals observed at δ_H (ppm) 8.073 (d, $J_{3',4'}$ = 9.2Hz, 1H, H-3'), 7.747(d, $J_{6',4'}$ = 2.8 Hz, 1H, H-6') and 7.282 (d, $J_{4',3'}$ = 9.2 Hz, $J_{4',6'}$ = 2.8Hz, 1H, H-4') were assigned to the aromatic protons on the benzyl ring attached to the azomethine bond. Three signals at δ_H (ppm) 7.550 (t, $J_{3,2/3,4} = J_{5,4/5,6}$ = 8 Hz, 2H, H-3, H-5), 7.411 (d, $J_{4,3/4,5}$ = 7.6 Hz, 1H, H-4) and 7.373 (d, $J_{2,3} = J_{6,5}$= 8.4 Hz, $J_{2,4} = J_{6,4}$= 1.2 Hz, 2H, H-2, H-6) were assigned to aromatic protons on the benzyl ring attached to the pyrazole. Three upfield singlets at δ_H (ppm) 5.478 (s, 2H, H-7'', CH_2), 3.235 (s, 3H, H-11, CH_3) and 2.454 (s, 3H, H-10, CH_3) correspond to the methylene and two methyl protons, respectively.

The FAB+ spectrum of compound 10-8 showed the molecular ion peak at M^{+}+1 at *m/z* 488.

The infrared absorption spectrum of 10-8 showed vibrational bands $\bar{\upsilon}$ (cm^{-1}) for C-H anti-sym. stretch of aromatic (3072), C-H anti-sym. stretch of aliphatic (2926), C=O stretch of carbonyl (1647), C=N stretch of azomethine bond (1566), C=C stretch of aromatic (1523), C-N stretch of pyrazole (1347), Asymetric C-O-C stretch of ether (1296) N-N stretch of pyrazole (1237) and symetric C-O-C stretch of ether (1086).

The analysis of the UV spectrum of 10-8 in chloroform revealed maximum absorption bands at 267, 261, 254 and 221. The wavelengths at 267, 261 and 254 showed n-π* transitions. The wavelength at 221 is indicative of π-π* transition.

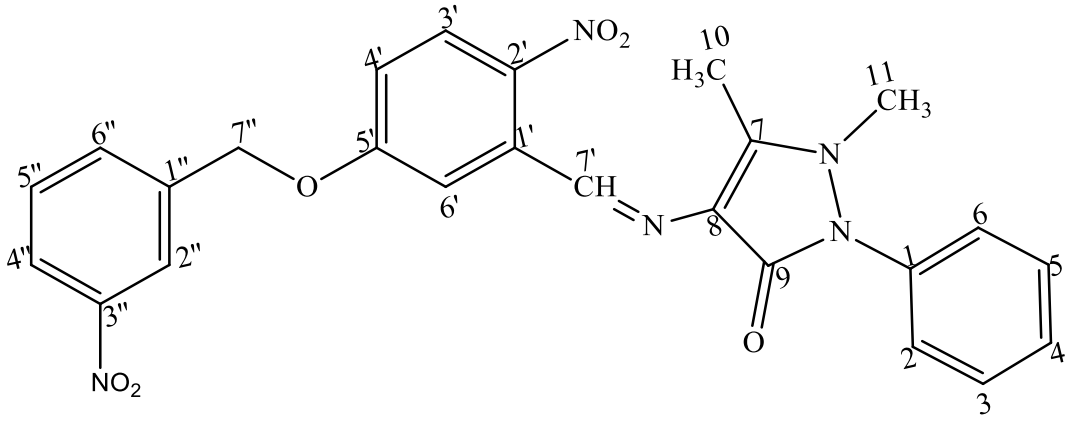

Scheme 4. 47: Structure 10-8

4.2.48 Characterisation of 4-((5-((3-methoxybenzyl)oxy)-2-nitrobenzylidene)amino)-1,5-di methyl-2-phenyl-1,2-dihydro-3H-pyrazol-3-one (10-9)

The compound 4-((5-((3-methoxybenzyl)oxy)-2-nitrobenzylidene)amino)-1,5-di methyl-2-phenyl-1,2-dihydro-3H-pyrazol-3-one (Scheme 4.48) appeared as deep yellow solid, with 80 % yield, and melting point of 167.3-168.3 ^{o}C.

The ^{1}H NMR spectrum (500 MHz, DMSO-d_6) displayed thirteen signals representing a total of twenty-four protons. The azomethine proton was observed downfield at δ_H (ppm) δ_H 9.927(s,1H, CH, H-7'). The three signals observed at δ_H (ppm) 8.051 (d, $J_{3',4'}$ = 9 Hz, 1H, H-3'), 7.718 (d, $J_{6',4'}$ = 3 Hz, 1H, H-6'), 7.409 (dd, $J_{4',3'}$ = 7.5 Hz, $J_{4',6'}$ = 2 Hz,1H, H-4') correspond to the methine protons on the benzyl ring attached to the azomethine bond. The signals at at δ_H (ppm) 7.235 (d, $J_{6'',5''}$ = 9 Hz, $J_{6'',4''/6'',2''}$ = 3 Hz, 1H, H-6''), 7.064 (d, $J_{4'',5''}$ = 7 Hz, $J_{4'',6''}$ = $J_{2'',4''/2'',6''}$ = 3 Hz, 2H, H-2'' H-4''), 6.929 (d, $J_{5'',4''/5'',6''}$ = 8 Hz, 1H, H-5'') represent the aromatic methine protons on the benzyl ring α to the ether bond. The three signals at δ_H (ppm) 7.546 (t, $J_{3,2/3,4} = J_{5,4/5,6}$ = 8 Hz, t, $J_{3,5} = J_{5,3}$ = 1.5 Hz, 2H, H-3, H-5), 7.372 (dd, $J_{2,3} = J_{6,5}$= 8 Hz, $J_{2,4} = J_{6,4}$ = 1.5 Hz, 2H, H-2, H-6) and 7.340 (t, $J_{4,3/4,5}$ = 8 Hz, $J_{4,2/4,6}$ = 1.5 Hz, 1H, H-4) were assigned to the aromatic methine protons on the benzyl ring attached to the pyrazole moiety. The four upfield singlets at δ_H (ppm) 5.284 (s, 2H, H-7'', CH_2), 3.761 (s, 3H, H-8'', OCH_3), 3.235 (s, 3H, H-11, CH_3), 2.460 (s, 3H, H-10, CH_3) represent a methylene, methoxy and two methyl protons, respectively.

The FAB- spectrum of compound 10-9 showed the molecular ion peak at M^+-1 at *m/z* 472. The fragment $[C_{18}H_{16}N_3O_2]^+$ at *m/z* 351 was also observed.

The infrared absorption spectrum of 10-9 showed vibrational bands $\bar{\upsilon}$ (cm^{-1}) for C-H anti-sym. stretch of aromatic (3076), C-H anti-sym. stretch of aliphatic (2912), -C=O stretch of carbonyl (1648), C=N stretch of azomethine bond (1587), C=C stretch of aromatic (1510), C-H bend of methylene (1456) and C-N stretch of pyrazole moiety (1326),

The analysis of the UV spectrum of 10-9 in chloroform revealed maximum absorption bands at 283 and 249. The wavelengths showed n-π* transitions and π-π* transition, respectively.

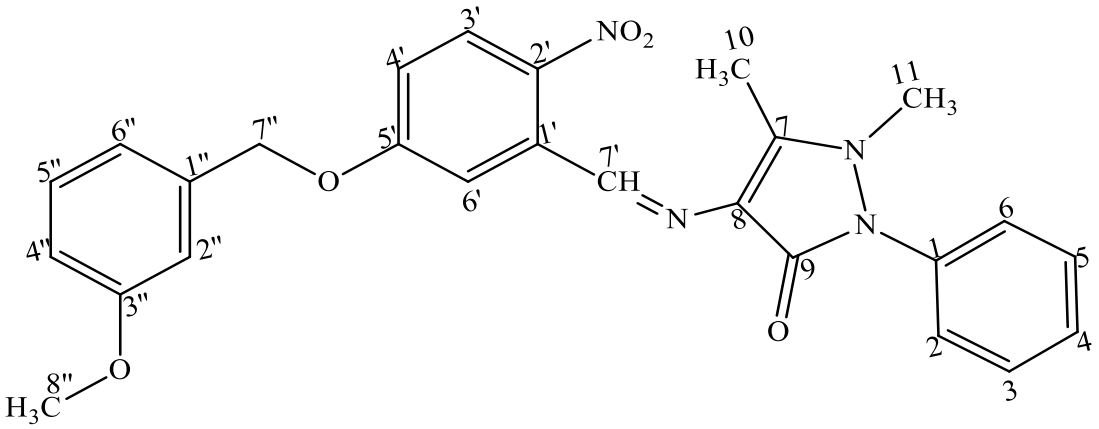

Scheme 4. 48: Structure 10-9

4.2.49 Characterisation of 4-((3-methoxy-4-(prop-2-yn-1-yloxy)benzylidene)amino)-1,5-di methyl-2-phenyl-1,2-dihydro-3H-pyrazol-3-one (SB-A)

The compound 4-((3-methoxy-4-(prop-2-yn-1-yloxy)benzylidene)amino)-1,5-dimethyl-2-phenyl-1,2-dihydro-3H-pyrazol-3-one (Scheme 4.49) appeared as brown solid, with 91% yield, and melting point of 141.9-142.8 ^{o}C.

The ^{1}H NMR spectrum (500 MHz, DMSO-$d_{6,}$ δ_H (ppm)) displayed twelve signals and a total of twenty-one protons. The azomethine proton was observed downfield at δ_H (ppm) 9.490 (s, 1H, CH, H-7'). The signals at δ_H (ppm) 7.479 (d, $J_{2',6'}$ = 1.5 Hz, 1H, H-2'), 7.287 (dd, $J_{6',5'}$ = 8 Hz, $J_{6',2'}$ = 2 Hz, 1H, H-6'), and 7.091(d, $J_{5',6'}$ = 8.4 Hz, 1H, H-5') represent the aromatic protons on the benzyl ring. The three signals at δ_H (ppm) 7.532 (dt, $J_{3,2/3,4} = J_{5,4/5,6}$ = 8.5 Hz, 2H, H-3, H-5), 7.372 (d, $J_{4,3/4,5}$ = 7.5 Hz, 1H, H-4) and 7.357 (dd, $J_{2,3} = J_{6,5}$ = 8 Hz, 2H, H-2, H-6) were assigned to the aromatic protons on the benzyl ring attached to the pyrazole moiety. The methylene protons were deshielded due to the electronegativity of the oxygen attached to it and were observed at δ_H (ppm) 4.839 (d, $J_{1'',3''}$ = 2.5 Hz, 2H, H-1''). The alkynyl proton was observed at δ_H (ppm) 3.593 (t, $J_{3'',1''}$ = 2.5 Hz, 1H, H-3''). Three upfield singlets at δ_H (ppm) 3.830 (s, 3H, H-8', OCH_3), 3.145 (s, 3H, H-11, CH_3) and 2.442 (s, 3H, H-10, CH_3) represent the methoxy and methyl protons, respectively.

EI-MS: *m/z* (relative abundance in %), 375 [M^+] (100), 336 (67), 337 (27), 266 (17), 121 (17) and 56 (57). The EI-MS spectrum of SB-A showed a molecular ion, M^+ as the base peak corresponding to *m/z* 375. Other prominent peak were observed at *m/z* 336 $[C_{19}H_{18}N_3O_3]^+$, 226 $[C_{15}H_{13}N_3O_2]^+$, 121 $[C_5H_4N_3O]^+$, and 56 $[C_3H_6N]^{3+}$.

The infrared absorption spectrum of SBA showed vibrational bands with $\bar{\upsilon}$ (cm^{-1}) for C-H of alkyne (-C≡C-H) (3287), C-H anti-sym. stretch of aromatic (3079), C-H anti-sym. stretch of methyl (2983), C-H. stretch of methoxy (2938), C-H stretch of methylene (2865), C≡C stretch of alkyne (2129), C=O stretch of carbonyl (1652), C=N stretch of the azomethine (1599), C=C stretch of aromatic (1577), and C-H bend of methylene (1454).

The analysis of the UV spectrum of SBA in chloroform revealed maximum absorption bands at 260 and 338. This is suggestive of and n-π* transition.

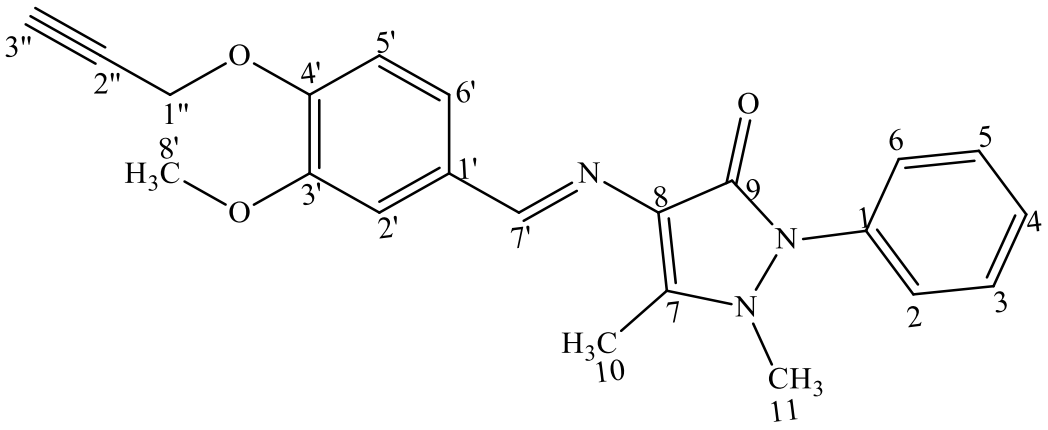

Scheme 4. 49: Structure of SB-A

4.2.50 Characterisation of 4-((3-methoxy-2-(prop-2-yn-1-yloxy)benzylidene)amino)-1,5-dimethyl-2-phenyl-1,2-dihydro-3H-pyrazol-3-one (SB-B)

The compound 4-((3-methoxy-2-(prop-2-yn-1-yloxy)benzylidene)amino)-1,5-dimethyl-2-phenyl -1,2-dihydro-3H-pyrazol-3-one (Scheme 4.50) appeared as cream solid, with 93% yield, and melting point of 215.1-216.4 ^{o}C.

The ^{1}H NMR spectrum (500 MHz, DMSO-d_6, δ_H (ppm)) displayed twelve signals and a total of twenty-one protons. The azomethine proton was observed downfield at δ_H (ppm) 9.856 (s, 1H, CH, H-7'). The signals at δ_H (ppm) 7.639 (d, $J_{6',5'}$ = 7.5Hz, $J_{6',4'}$ = 1.5 Hz, 1H, H-6'), 7.163 (t, $J_{5',4'/5',6'}$ = 8 Hz, 1H, H-5') and 7.115 (dd, $J_{4',5'}$ = 8 Hz, $J_{4',6'}$ = 1.5Hz, 1H, H-4' corresponding to the aromatic methine protons on the benzyl ring. The three signals at δ_H (ppm) 7.532 (dt, $J_{3,2/3,4} = J_{5,4/5,6}$ = 8.5 Hz, $J_{3,5} = J_{5,3}$ = 2 Hz, 2H, H-3, H-5), 7.3737 (d, $J_{4,3/4,5}$ = 7.5 Hz, 1H, H-4) and 7.363 (dd, $J_{2,3} = J_{6,5}$ = 8.5 Hz, 2H, H-2, H-6), were assigned to the aromatic methine protons on the benzyl ring attached to the pyrazole moiety. The signals at δ_H (ppm) 4.739 (d, $J_{1'',3''}$ = 2.5 Hz, 2H, H-1'') and 3.418 (t, $J_{3'',1''}$ = 2.5 Hz, 1H, H-3'') represent the methylene and the alkynyl protons, respectively. Three upfield singlet observed at δ_H (ppm) 3.828 (s, 3H, H-8', OCH_3), 3.169 (s, 3H, H-11, CH_3) and 2.442 (s, 3H, H-10, CH_3) represent the methoxy and two methyl protons, respectively.

EI-MS: *m/z* (relative abundance in %), [M^+] (100), 336 (67), 337 (27), 266 (17), 121 (17) and 56 (57). The EI-MS spectrum of SBB showed a molecular ion, M^+ as the base peak corresponding to *m/z* 375. Other prominent peak were observed at *m/z* 336 $[C_{19}H_{18}N_3O_3]^+$, 226 $[C_{15}H_{13}N_3O_2]^+$, 121 $[C_5H_4N_3O]^+$, and 56 $[C_3H_6N]^{3+}$.

The infrared absorption spectrum of SB-B showed vibrational bands $\bar{\upsilon}$ (cm^{-1}) for acetylenic C-H of alkyne (-C≡C-H) (3284), C-H anti-sym. stretch of aromatic (3074), C-H. stretch of methoxy (2938), C-H stretch of methylene (2835), C≡C stretch of alkyne (2119), -C=O stretch of carbonyl (1651), C=N stretch of the azomethine bond (1572), C=C stretch of aromatic (1466), C-H bend of methylene (1419), and C-N stretch of pyrazole moiety (1300).

The analysis of the UV spectrum of SB-B in chloroform revealed maximum absorption bands at 333. This is indicative of n-π* transitions.

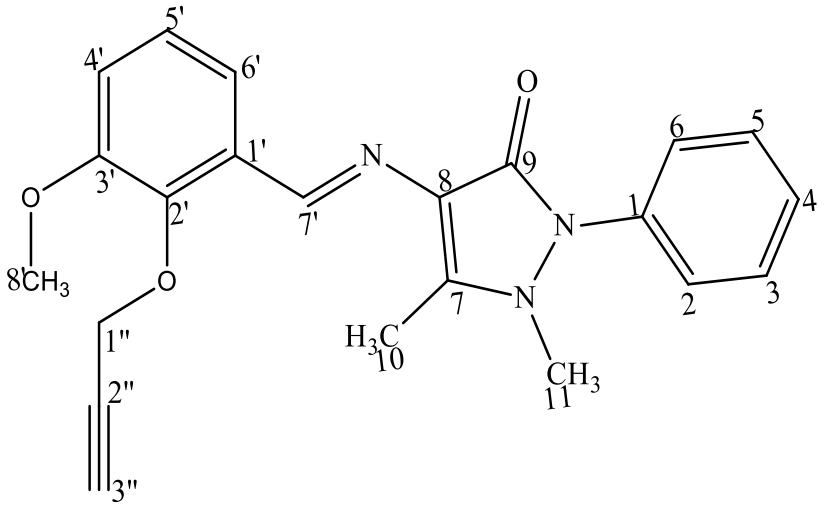

Scheme 4. 50: Structure of SB-B

4.2.51 Characterisation of 4-((4-methoxy-3-(prop-2-yn-1-yloxy)benzylidene)amino) 1,5-dimethyl-2-phenyl-1,2-dihydro-3H-pyrazol-3-one (SB-C)

The compound 4-((4-methoxy-3-(prop-2-yn-1-yloxy)benzylidene)amino)-1,5-dimethyl-2-phenyl -1,2-dihydro-3H-pyrazol-3-one (Scheme 4.51) appeared as brownish yellow solid, with 81% yield, adn melting point of 140.6-141.9 ^{o}C.

The ^{1}H NMR spectrum (500 MHz, DMSO-d_6) displayed twelve signals and a total of twenty-one protons. The azomethine proton was observed downfield at δ_H (ppm) 9.477 (s,1H, CH, H-7'). The six signals at δ_H (ppm) 7.566 (d, $J_{2',6'}$ = 1.5 Hz, 1H, H-2'), 7.533 (dt, $J_{3,2/3,4} = J_{5,4/5,6}$ = 8 Hz, $J_{3,5} = J_{5,3}$ = 2 Hz, 2H, H-3, H-5), 7.374 (d, $J_{4,2/4,6}$ = 1.5 Hz, 1H, H-4), 7.357 (d, $J_{2,3} = J_{6,5}$ = 8 Hz, 2H, H-2, H-6), 7.346 (dd, $J_{6',5'}$ = 8Hz, $J_{6',2'}$ = 2 Hz, 1H, H-6') and 7.061(d, $J_{5',6'}$ = 8.5 Hz, 1H, H-5') corresponding to the aromatic methine protons. The signals at δ_H (ppm) 4.846 (d, $J_{1'',3''}$ = 2.5Hz, 2H, H-1'') and 3.582 (t, $J_{3'',1''}$ = 2.5 Hz, 1H, H-3'') represent the methylene and the alkynyl protons, respectively. Three upfield singlets at δ_H (ppm) 3.813 (s, 3H, H-8', OCH_3). 3.142 (s, 3H, H-11, CH_3) and 2.439 (s, 3H, H-10, CH_3) were assigned to the methoxy and two methyl protons, respectively.

EI-MS: *m/z* (relative abundance in %), 375 [M^+] (100), 376 (71), 283 (67), 266 (47), 188 (30), 121 (33) and 56 (87). The EI-MS spectrum of SB-C showed a molecular ion, M^+ as the base peak corresponding to *m/z* 375. Molecular ion M^++1 peak at *m/z* 376 was also observed. Other prominent peaks were observed at *m/z* 283 $[C_{15}H_{13}N_3O_3]^+$, 226 $[C_{15}H_{13}N_3O_2]^+$,188 $[C_{11}H_{11}N_2O]^+$, 121 $[C_5H_4N_3O]^+$, and 56 $[C_3H_6N]^{3+}$.

The infrared absorption spectrum of SB-C showed vibrational bands with $\bar{\upsilon}$ (cm^{-1}) for acetylenic C-H of alkyne (-C≡C-H) (3287), C-H anti-sym. stretch of aromatic (3079), C-H anti-sym. stretch of methyl (2983), C-H. stretch of methoxy (2938), C-H stretch of methylene (2865), C≡C stretch of alkyne (2129), C=O stretch of carbonyl (1652), C=N stretch of azomethine (1599), C=C stretch of aromatic (1577), C-H bend of methylene (1454), C-N stretch of pyrazole (1338 (1260) and N-N stretch of pyrazole (1223).

The analysis of the UV spectrum of SB-C in chloroform revealed maximum absorption bands at 337. This is indicative of n-π* transitions.

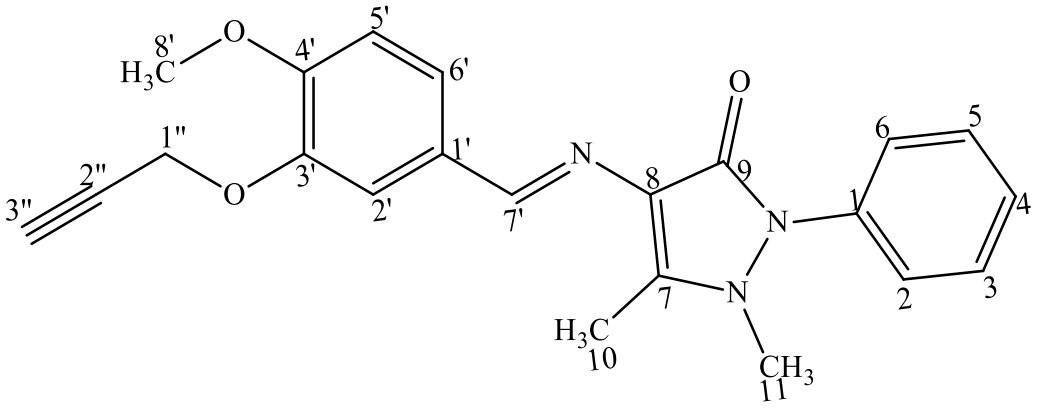

Scheme 4. 51: Structure of SB-C

4.2.52 Characterisation of 1,5-dimethyl-2-phenyl-4-((3-(prop-2-yn-1-yloxy)-benzylidene)amino)-1,2-dihydro-3H-pyrazol-3-one (SB-D)

The compound 1,5-dimethyl-2-phenyl-4-((3-(prop-2-yn-1-yloxy)benzylidene)amino)-1,2-di hydro-3H-pyrazol-3-one (Scheme 4.52) appeared as pale yellow solid, with 83 % yield, and melting point of 143.9-144.3 ^{o}C.

The ^{1}H NMR spectrum (500 MHz, DMSO-d_6, δ_H (ppm)) displayed twelve signals and a total of nineteen protons. The azomethine proton was observed downfield at δ_H (ppm) 9.535 (s, 1H, CH, H-7'). The seven signals at δ_H (ppm) 7.540 (dt, $J_{3,2/3,4} = J_{5,4/5,6}$ = 8 Hz, $J_{3,5} = J_{5,3}$ = 1.5 Hz, 2H, H-3, H-5), 7.442 (d, $J_{6',2'/6',4'}$ = 2.5 Hz, 1H, H-6') 7.395 (d, $J_{2',6'/2',4'}$ = 1.5 Hz, 1H, H-2'), 7.388 (d, $J_{4',6'/4',2'}$ = 2.5 Hz, 1H, H-4'), 7.377 (dd, $J_{2,4} = J_{6,4}$ = 2 Hz, 2H, H-2, H-6), 7.361 (d, $J_{4,2/4,6}$ = 2.5 Hz, 1H, H-4) and 7.050 (ddd, $J_{5',4'/5',6'}$ = 7.5 Hz, 1H, H-5') were assigned to the aromatic methine protons. The signals at δ_H (ppm) 4.854 (d, $J_{1'',3''}$ = 2.5 Hz, 2H, H-1'') and 3.583 (t, $J_{3'',1''}$ = 2.5 Hz, 1H, H-3''), represent the methylene protons and the alkynyl proton, respectively. Two upfield singlets at δ_H (ppm) 3.178 (s, 3H, H-11, CH_3) and 2.455 (s, 3H, H-10, CH_3) represent the methyl protons.

EI-MS: *m/z* (relative abundance in %), 345 [M^+] (100), 346 (99), 306 (22), 253 (51), 236 (41), 214 (16), 188 (74), 121 (61) and 56 (73). The EI-MS spectrum of SB-D showed a molecular ion, M^+ as the base peak corresponding to *m/z* 345. Molecular ion M^++1 peak at *m/z* 346 was also observed. Other prominent peaks were observed at *m/z* 306 $[C_{18}H_{15}N_3O_2]^+$, 253 $[C_{14}H_{11}N_3O_2]^+$, 236 $[C_{14}H_{11}N_3O]^{2+}$, 214 $[C_{12}H_{12}N_3O]^+$, 188 $[C_{11}H_{11}N_2O]^+$, 121 $[C_5H_4N_3O]^+$, and 56 $[C_3H_6N]^{3+}$.

The infrared absorption spectrum of SB-D showed vibrational bands with $\bar{\upsilon}$ (cm^{-1}) for acetylenic C-H of alkyne (-C≡C-H) (3265), C-H anti-sym. stretch of aromatic (3053), C-H anti-sym. stretch of methyl (2984), C-H. stretch of methoxy (2926), C≡C stretch of alkyne (2110), -C=O stretch of carbonyl (1641), C=N stretch of azomethine bond (1572), C=C stretch of aromatic (1484), C-H bend of methyl (1418), and C-N stretch of pyrazole (1377).

The analysis of the UV spectrum in chloroform revealed maximum absorption bands at 221 and 230 indicting π-π* transitions, and at 329 which is suggestive of n-π* transition.

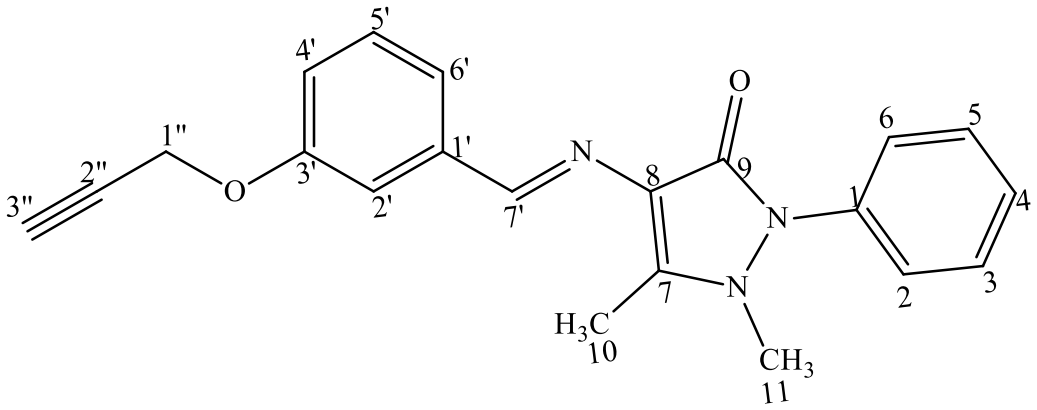

Scheme 4. 52: Structure of SB-D

4.2.53 Characterisation of 1,5-dimethyl-2-phenyl-4-((4-(prop-2-yn-1-yloxy)benzylidene)amino-1,2-dihydro-3H-pyrazol-3-one (SB-E)

The compound 1,5-dimethyl-2-phenyl-4-((4-(prop-2-yn-1-yloxy)benzylidene)amino)-1,2-dihydro-3H-pyrazol-3-one (Scheme 4.53) appeared as pale yellow solid, with % 68 yield, and melting point of 155.9-157.0 ^{o}C.

The ^{1}H NMR spectrum (500MHz, DMSO-d_6, δ_H (ppm)) displayed ten signals and a total of nineteen protons. The azomethine proton was observed downfield at δ_H (ppm) 9.513 (s, 1H, CH, H-7'). The spectrum showed five signals at δ_H (ppm) 770 (d, $J_{2',3'} = J_{6',5'}$ = 9Hz, 2H, H-2', H-6'), 7.531 (t, $J_{3,2/3,4} = J_{5,4/5,6}$ = 8 Hz, 2H, H-3, H-5), 7.374 (d, $J_{4,3/4,5}$ = 8.5 Hz, 1H, H-4), 7.357 (d, $J_{2,3} = J_{6,5}$ = 8.5 Hz, 2H, H-2, H-6) and 7.063 (d, $J_{3',2'} = J_{5',6'}$ = 9 Hz, 2H, H-3',H-5') corresponding to the aromatic methine protons. The signals at δ_H (ppm) 4.854 (d, $J_{1'',3''}$ = 2.5 Hz, 2H, H-1'') and 3.595 (t, $J_{3'',2''}$ = 2.5 Hz, 1H, H-3'') represent the methylene and the alkynyl protons, respectively. Two up field singlets at δ_H (ppm) 3.143 (s, 3H, H-11, CH_3), 2.429 (s, 3H, H-10, CH_3) represent the methyl protons of the pyrazole moiety.

EI-MS: *m/z* (relative abundance in %), 345 [M^+] (100), 346 (62), 306 (27), 253 (45), 236 (47), 188 (38), 121 (57) and 56 (84). The EI-MS spectrum of SB-E showed a molecular ion, M^+ as the base peak corresponding to *m/z* 345. Molecular ion M^++1 peak at *m/z* 346 was also observed. Other prominent peaks were observed at *m/z* 306 $[C_{18}H_{15}N_3O_2]^+$, 253 $[C_{14}H_{11}N_3O_2]^+$, 236 $[C_{14}H_{11}N_3O]^{2+}$, 214 $[C_{12}H_{12}N_3O]^+$, 188 $[C_{11}H_{11}N_2O]^+$, 121 $[C_5H_4N_3O]^+$, and 56 $[C_3H_6N]^{3+}$.

The infrared absorption spectrum of SB-E showed vibrational bands with $\bar{\upsilon}$ (cm^{-1}) for acetylenic C-H of alkyne (-C≡C-H) (3265), C-H anti-sym. stretch of aromatic (3053), C-H anti-sym. stretch of methyl (2984), C-H. stretch of methoxy (2926), C≡C stretch of alkyne (2110), -C=O stretch of carbonyl (1641), C=N stretch of azomethine bond (1572), C=C stretch of aromatic (1484), C-H bend of methyl (1418), and C-N stretch of pyrazole (1377).

The analysis of the UV spectrum of SB-E in chloroform revealed maximum absorption bands at 266 and 334.This is suggestive of n-π* transition.

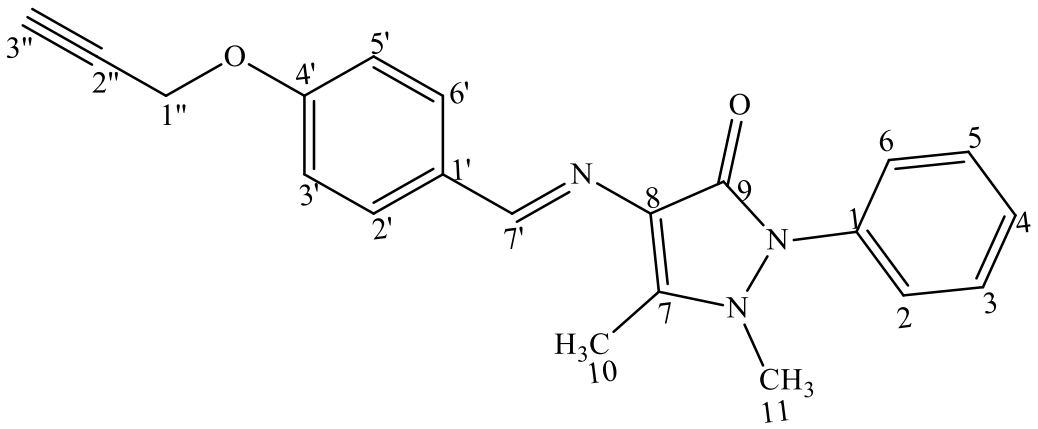

Scheme 4. 53: Structure of SB-E

4.2.54 Characterisation of 4-((3-bromo-5-chloro-2-(prop-2-yn-1-yloxy)benzylidene) amino)-1,5-dimethyl-2-phenyl-1,2-dihydro-3H-pyrazol-3-one (SB-F)

The compound 4-((3-bromo-5-chloro-2-(prop-2-yn-1-yloxy)benzylidene)amino)-1,5-dimethyl-2-phenyl-1,2-dihydro-3H-pyrazol-3-one (Scheme 4.54) was obtained as appeared as yellow solid, with 77% yield, and melting point of 148.5-1449.9 ^{o}C.

The ^{1}H NMR spectrum (500 MHz, DMSO-d_6, δ_H (ppm)) displayed ten signals representing a total of seventeen protons. The azomethine proton was observed downfield at δ_H (ppm) 9.777 (s,1H, CH, H-7'). The two signals at δ_H (ppm) 8.015 (d, $J_{6',4'}$ = 2.5 Hz, 1H, H-6') and 7.833 (d, $J_{4',6'}$ = 2.5 Hz, 1H, H-4') were assigned to the aromatic methine protons on the benzyl ring linked to the ether bond and to the azomethine bond. These protons appeared more downfield compared to other aromatic protons in the compound. The signals at δ_H (ppm) 7.546 (t, $J_{3,2/3,4} = J_{5,4/5,6}$ = 8 Hz, 2H, H-3, H-5), 7.403 (d, $J_{2,3} = J_{6,5}$ = 7.5 Hz, 2H, H-2, H-6) and 7.379 (d, $J_{4,3/4,5}$ = 8 Hz, 1H, H-4). Represent the aromatic methine protons on the benzyl ring attached to the pyrazole moiety. The signals at δ_H (ppm) 4.755 (d, $J_{1'',3''}$ = 2.5 Hz, 2H, H-1'') and 3.582 (t, $J_{3'',1''}$ = 2.5 Hz, 1H, H-3'') represent the methylene and the alkynyl protons, respectively. The signals at δ_H (ppm) 3.224 (s, 3H, H-11, CH_3) and 2.476 (s, 3H, H-11, CH_3) corresponding to the methyl protons.

EI-MS: *m/z* (relative abundance in %), [M^+] (100), 336 (67), 337 (27), 266 (17), 151 (22), 121 (17) and 56 (57). The EI-MS spectrum of SB-F showed a molecular ion, M^+ as the base peak corresponding to *m/z* 458. Other prominent peak were observed at *m/z* 336 $[C_{19}H_{18}N_3O_3]^+$, 226 $[C_{15}H_{13}N_3O_2]^+$, 121 $[C_5H_4N_3O]^+$, and 56 $[C_3H_6N]^{3+}$.

The infrared absorption spectrum of SB-F showed vibrational bands $\bar{\upsilon}$ (cm^{-1}) for acetylenic C-H of alkyne (-C≡C-H) (3293), C-H anti-sym. stretch of aromatic (3210), C-H anti-sym. stretch of methyl (3068), C-H. stretch of methoxy (2926), C≡C stretch of alkyne (2124), -C=O stretch of carbonyl (1660), C=N stretch of the azomethine bond (1586), C=C stretch of aromatic (1553), C-H bend of methyl (1370), and C-N stretch of pyrazole moiety (1301)

The analysis of the UV spectrum of SB-F in chloroform revealed maximum absorption bands at 349. This is suggestive of n-π* transition.

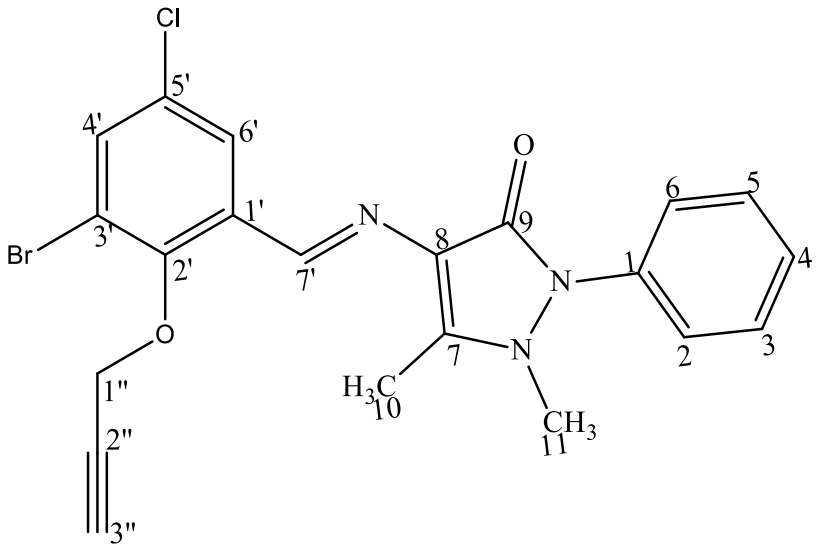

Scheme 4. 54. Structure of SB-F

4.2.55 Characterisation of 1,5-dimethyl-4-((2-nitro-5-(prop-2-yn-1-yloxy)benzylidene)amino-2-phenyl-1,2-dihydro-3H-pyrazol-3-one (SB-G).

The compound 1,5-dimethyl-4-((2-nitro-5-(prop-2-yn-1-yloxy)benzylidene)amino)-2-phenyl-1,2-dihydro-3H-pyrazol-3-one (Scheme 4.55) was obtained as yellow solid, with 91% yield, and melting point of 150.8 -152.3ºC.

The ^{1}H NMR spectrum (500 MHz, DMSO-d_6, δ_H (ppm)) displayed eleven signals representing a total of eighteen protons. The most downfield signal observed at δ_H (ppm) 9.926 (s, 1H, CH, H-7') correspond to the azomethine protein. The six signals observed at δ_H (ppm) 8.069 (d, $J_{3',4'}$ = 9 Hz,1H, H-3'), 7.756 (d, $J_{6',4'}$ = 2.5 Hz,1H, H-6'), 7.550 (t, $J_{3,2/3,4}$ = $J_{5,4/5,6}$ = 8 Hz, 2H, H-3, H-5), 7.411 (d, $J_{4,3/4,5}$ = 7.5 Hz, 1H, H-4), 7.375 (d, $J_{2,3}$ = $J_{6,5}$ = 7.5 Hz, 2H, H-2, H-6) and 7.210 (dd, $J_{4',3'}$ = 9 Hz, $J_{4',6'}$ = 3 Hz, 1H, H-4') were assigned to the aromatic methine protons. The signals at δ_H (ppm) 5.015 (d, $J_{1'',3''}$ = 2.5 Hz, 2H, H-1'') and 3.702 (t, $J_{3'',1''}$ = 2.5 Hz, 1H, H-3'') represent the methylene and the alkynyl protons, respectively. The two upfield signals at δ_H (ppm) 3.240 (s, 3H, H-11, CH_3) and 2.477 (s,3H, H-10, CH_3) were assigned to the methyl protons.

EI-MS: *m/z* (relative abundance in %), 390 [M^+] (16), 56 (100), 306 (11), 202 (65), 83 (12), 121 (17) and 56 (57). The EI-MS spectrum of SB-G showed a molecular ion, M^+ peak corresponding to *m/z* 390. The fragmentation of $[C_3H_6N]^{3\bullet}$ with *m/z* 56 from the pyrazole moiety corresponds to the base peak. Other prominent peak were observed at *m/z* 306 $[C_{18}H_{15}N_3O_2]^+$, and 202 $[C_{11}H_{11}N_3O]^+$.

The infrared absorption spectrum of SB-G showed vibrational bands $\bar{\upsilon}$ (cm^{-1}) for acetylenic C-H of alkyne (-C≡C-H) (3289), C-H anti-sym. stretch of aromatic (3252), C-H anti-sym. stretch of methyl (3061), C-H. stretch of methoxy (2924), C≡C stretch of alkyne (2123), -C=O stretch of carbonyl (1655), C=N stretch of the azomethine bond (1575), C=C stretch of aromatic (1508), N=O asymmetric stretch of nitro substituent (1484), N=O symmetric stretch of nitro substituent (1379), and C-N stretch of pyrazole moiety (1337).

The analysis of the UV spectrum of SB-G in chloroform revealed maximum absorption bands at 249 indicting π-π* transitions, and 290 which is suggestive of n-π* transition.

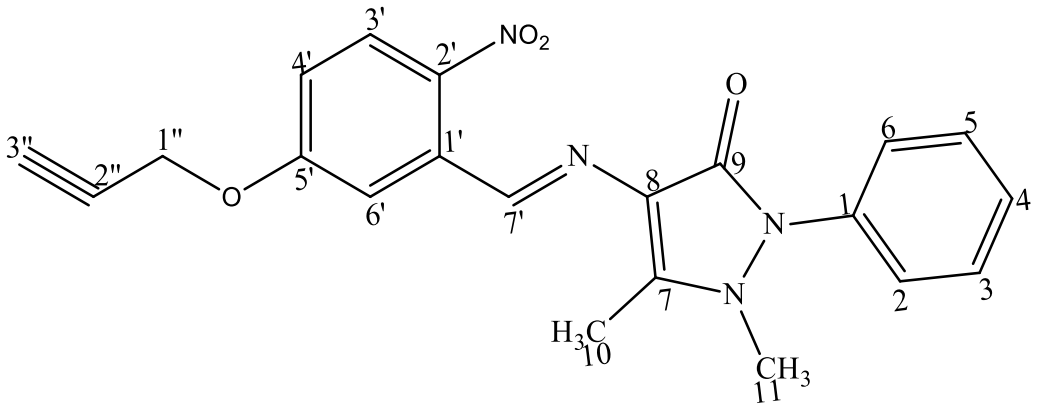

Scheme 4. 55: Structure of SB-G

4.2.56 Characterisation of 4-((2,4-bis(prop-2-yn-1-yloxy)benzylidene)amino)-1,5-dimethyl-2-phenyl-1,2-dihydro-3H-pyrazol-3-one (SB-H)

The compound 4-((2,4-bis(prop-2-yn-1-yloxy)benzylidene)amino)-1,5-dimethyl-2-phenyl-1,2-dihydro-3H-pyrazol-3-one (Scheme 4.56) appeared as yellow solid, with 75 % yield, and melting point of 169.5-170.0 ^{o}C.

The ^{1}H NMR spectrum (500 MHz, DMSO-d_6, δ_H (ppm)) displayed thirteen signals representing a total of twenty-one protons. The azomethine proton was observed downfield at δ_H (ppm) 9.766 (s, 1H, CH, H-7'). Six signals at δ_H (ppm) 7.983 (d, $J_{6',5'}$ = 8.5 Hz, 1H, H-6'), 7.527 (t, $J_{3,2/3,4} = J_{5,4/5,6}$ = 8 Hz, 2H, H-3, H-5), 7.373 (d, $J_{2,3} = J_{6,5}$ = 7.5 Hz, 2H, H-2, H-6), 7.348 (d, $J_{4,3/4,5}$ = 7 Hz, 1H, H-4), 6.756 (d, $J_{3',5'}$ = 2 Hz,1H, H-3') and 6.725 (dd, $J_{5',6'}$ = 9 Hz, $J_{5',3'}$ = 2 Hz, 1H, H-5') corresponding to the aromatic methine protons. The two signals at δ_H (ppm) 4.890 (d, $J_{1'',3''}$ = 2.5 Hz, 2H, H-1'') and 4.853 (d, $J_{1''',3'''}$ = 2.5 Hz, 1H, H-1''') represent the methylene protons. The alkynyl protons were observed upfield at δ_H (ppm) 3.598 (t, $J_{3'',1''}$ = 2.5 Hz, 2H, H-3'') and 3.581(t, $J_{3''',1'''}$ = 2.5 Hz, 1H, H-3'''). Two upfield singlets at δ_H (ppm) 3.134 (s, 3H, H-11, CH_3) and 2.422 (s, 3H, H-10, CH_3) represent the methyl protons.

The signals from ^{13}C NMR (100 M-Hz, DMSO-d_6) broad band spectrum displayed nine characteristic peaks of quaternary carbons observed downfield at δ 159.72 (C-9), 151.98 (C-7), 148.75 (C-4'), 147.10 (C-3'), 134.64 (C-1), 131.27 (C-1'), 116.50 (C-8), 79.12 (C-2') and 78.96 (C-2''). Eleven methine carbons were observed which were assigned as 153.89 (C-7') azomethine carbon and 122.08 (C-6'), 113.71 (C-3'), 115.1 (C-5'), 78.62 (C-3'') and 78.54 (C-3''') on the benzaldehyde ring, 129.12 (C-5 and C-3), 126.78 (C-4), 124.43 (C-2 and C-6), on the phenyl ring. DEPT-135 confirmed the presence of two methylene carbons 56.02 (C-1'' and C-1''') while DEPT-90 confirmed the presence of the eleven methine carbons. The two methyl carbons present appear upfield at 9.78 (C-10) and 35.47 (C-11).

EI-MS: *m/z* (relative abundance in %), 399 [M^+] (100), 400 (67), 360 (72), 290 (35), 188 (21), 121 (24) and 56 (84). The EI-MS spectrum of SB-I showed a molecular ion, M^+ as the base peak corresponding to *m/z* 399. Molecular ion M^++1 peak at *m/z* 400 was also observed. Other prominent peak were observed at *m/z* 360 $[C_{21}H_{17}N_3O_3]^+$, 290 $[C_{17}H_{13}N_3O_2]^+$, 121 $[C_5H_4N_3O]^+$, and 56 $[C_3H_6N]^{3+}$.

The infrared absorption spectrum of SB-H showed vibrational bands $\bar{\upsilon}$ (cm^{-1}) for acetylenic C-H of alkyne (-C≡C-H) (3297), C-H anti-sym. stretch of aromatic (3267), C-H anti-sym. stretch of methyl (3044), C-H. stretch of methoxy (2925), C≡C stretch of alkyne (2117), -C=O stretch of carbonyl (1631), C=N stretch of the azomethine (1598), C=C stretch of aromatic (1499), C-H bend of methylene (1455), and C-N stretch of pyrazole moiety (1338),

The analysis of the UV spectrum of SB-H in chloroform revealed maximum absorption bands at 337 indicting n-π* transitions.

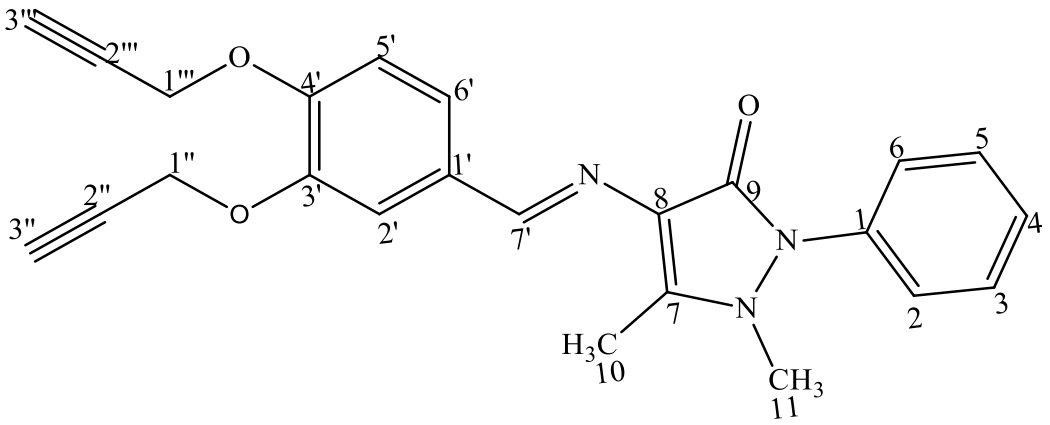

Scheme 4. 56: Structure of SB-H

4.2.57 Characterisation of 4-((2,4-bis(prop-2-yn-1-yloxy)benzylidene)amino)-1,5-dimethyl-2-phenyl-1,2-dihydro-3H-pyrazol-3-one (SB-I)

The compound 4-((2,4-bis(prop-2-yn-1-yloxy)benzylidene)amino)-1,5-dimethyl-2-phenyl-1,2-dihydro-3H-pyrazol-3-one (Scheme 4.57) appeared as yellow solid, with 75 % yield, and melting point of 169.5-170.0 ^{o}C.

The ^{1}H NMR spectrum (500 MHz, DMSO-d_6, δ_H (ppm)) displayed thirteen signals representing a total of twenty-one protons. The azomethine proton was observed downfield at δ_H (ppm) 9.766 (s, 1H, CH, H-7'). Six signals at δ_H (ppm) 7.983 (d, $J_{6',5'}$ = 8.5 Hz, 1H, H-6'), 7.527 (t, $J_{3,2/3,4} = J_{5,4/5,6}$ = 8 Hz, 2H, H-3, H-5), 7.373 (d, $J_{2,3} = J_{6,5}$ = 7.5 Hz, 2H, H-2, H-6), 7.348 (d, $J_{4,3/4,5}$ = 7 Hz, 1H, H-4), 6.756 (d, $J_{3',5'}$ = 2 Hz,1H, H-3') and 6.725 (dd, $J_{5',6'}$ = 9 Hz, $J_{5',3'}$ = 2 Hz, 1H, H-5') corresponding to the aromatic methine protons. The two signals at δ_H (ppm) 4.890 (d, $J_{1'',3''}$ = 2.5 Hz, 2H, H-1'') and 4.853 (d, $J_{1''',3'''}$ = 2.5 Hz, 1H, H-1''') represent the methylene protons. The alkynyl protons were observed upfield at δ_H (ppm) 3.598 (t, $J_{3'',1''}$ = 2.5 Hz, 2H, H-3'') and 3.581(t, $J_{3''',1'''}$ = 2.5 Hz, 1H, H-3'''). Two upfield singlets at δ_H (ppm) 3.134 (s, 3H, H-11, CH_3) and 2.422 (s, 3H, H-10, CH_3) represent the methyl protons.

EI-MS: *m/z* (relative abundance in %), 399 [M^+] (100), 400 (67), 360 (72), 290 (35), 188 (21), 121 (24) and 56 (84). The EI-MS spectrum of SB-I showed a molecular ion, M^+ as the base peak corresponding to *m/z* 399. Molecular ion M^++1 peak at *m/z* 400 was also observed. Other prominent peak were observed at *m/z* 360 $[C_{21}H_{17}N_3O_3]^+$, 290 $[C_{17}H_{13}N_3O_2]^+$, 121 $[C_5H_4N_3O]^+$, and 56 $[C_3H_6N]^{3+}$.

The infrared absorption spectrum of SB-I showed vibrational bands $\bar{\upsilon}$ (cm^{-1}) for acetylenic C-H of alkyne (-C≡C-H) (3297), C-H anti-sym. stretch of aromatic (3267), C-H anti-sym. stretch of methyl (3044), C-H. stretch of methoxy (2925), C≡C stretch of alkyne (2117), -C=O stretch of carbonyl (1631), C=N stretch of the azomethine (1598), C=C stretch of aromatic (1499), C-H bend of methylene (1455), and C-N stretch of pyrazole moiety (1338).

The analysis of the UV spectrum of SB-I in chloroform revealed maximum absorption bands at 337 indicting n-π* transitions.

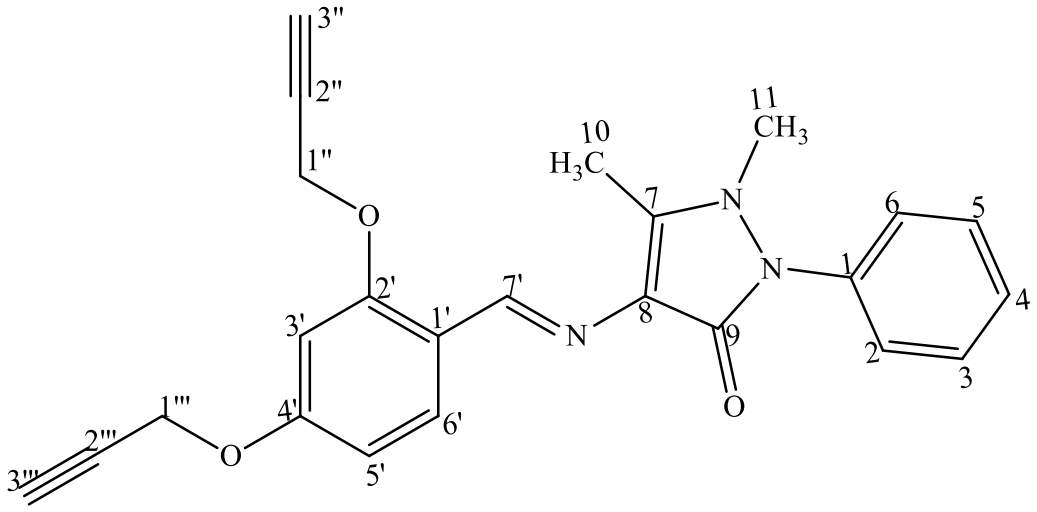

Scheme 4. 57: Structure of SB-I

4.2.58 Characterisation of 4-((3,5-dimethoxy-4-(prop-2-yn-1-yloxy)benzylidene) amino)-1,5-dimethyl-2-phenyl-1,2-dihydro-3H-pyrazol-3-one (SB-J)

The compound 4-((3,5-dimethoxy-4-(prop-2-yn-1-yloxy)benzylidene)amino)-1,5-dimethy -l-2-phenyl-1,2-dihydro-3H-pyrazol-3-one (SB-J) appeared as brown solid, with 93% yield, and melting point of 185.9-187.3 ^{o}C.

The ^{1}H NMR spectrum (400 MHz, DMSO-d_6, δ_H (ppm)) displayed eleven signals representing a total of twenty-one protons. The azomethine proton was observed downfield at δ_H (ppm) 9.497 (s,1H, CH, H-9'). Two chemically equivalent protons observed as singlet at δ_H (ppm) 7.131 (s, 2H, H-2', H-6') correspond to the aromatic protons on the benzyl ring. The three signals at δ_H (ppm) 7.543 (t, $J_{3,2/3,4} = J_{5,4/5,6}$ = 8 Hz, 2H, H-3, H-5), 7.381(d, $J_{4,3/4,5}$ = 7.2 Hz, 1H, H-4), 7.363 (d, $J_{2,3} = J_{6,5}$ = 7.2 Hz, 2H, H-2, H-6), were assigned to the aromatic protons on the benzyl ring attached to the pyrazole moiety. The signals at δ_H (ppm) 4.642 (d, $J_{1'',3''}$ = 2.5 Hz, 2H, H-1'') and 3.436 (t, $J_{3'',1''}$ = 2.5 Hz, 1H, H-3'') represent the methylene and alkynyl protons respectively. The six methoxy protons appeared as singlet at δ_H (ppm) 3.836 (s, 6H, H-8', H-9' OCH_3). The two upfield singlets at δ_H (ppm) 3.165 (s, 3H, H-11, CH_3) and 2.459 (s, 3H, H-10, CH_3) represent the methyl protons.

The signals from ^{13}C NMR (100 M-Hz, DMSO-d_6) broad band spectrum displayed seven characteristic peaks of quaternary carbons observed downfield at δ 163.67 (C-9), 161.7 (C-4'), 159.2 (C-7), 152.32 (C-2'), 134.60 (C-1), 131.3 (C-1') and 116.0 (C-8). Nine methine carbons were observed which were assigned as C-7' (148.60) azomethine carbon and 128.4 (C-6'), 116.9 (C-3') and 115.1 (C-5') on the benzaldehyde ring, 129.1 (C-5), 127.9 (C-4), 129.1 (C-3), 124.9 (C-2) and 124.9 (C-6) on the phenyl ring. DEPT-135 confirmed the absence of methylene carbons while DEPT-90 confirmed the presence of the nine methine carbons. The two methyl carbons present appear upfield at 9.65 (C-10) and 35.07 (C-11).

EI-MS: *m/z* (relative abundance in %), 399 [M^+] (100), 400 (67), 360 (72), 290 (35), 188 (21), 121 (24) and 56 (84). The EI-MS spectrum of SB-J showed a molecular ion, M^+ peak was observed at *m/z* 405. Other prominent peak were observed at *m/z* 366[$C_{20}H_{20}N_3O_4$]$^+$, 121 [$C_5H_4N_3O$] $^+$, and 56 [C_3H_6N]$^{3+}$.

The infrared absorption spectrum of SB-J showed vibrational bands $\bar{\upsilon}$ (cm^{-1}) acetylenic C-H of alkyne (-C≡C-H) (3226), C-H anti-sym. stretch of aromatic (3088), C-H anti-sym. stretch of methyl (3011), C-H. stretch of methoxy (2934), C-H. stretch of methylene (2846) C≡C stretch of alkyne (2111), -C=O stretch of carbonyl (1640), C=N stretch of azomethine bond (1575), C=C stretch of aromatic (1494), C-H bend of methylene (1457), C-H bend of methyl (1377) and C-N stretch of pyrazole moiety (1322).

The analysis of the UV spectrum of 9B2 in chloroform revealed maximum absorption bands at 337 indicting n-π* transitions.

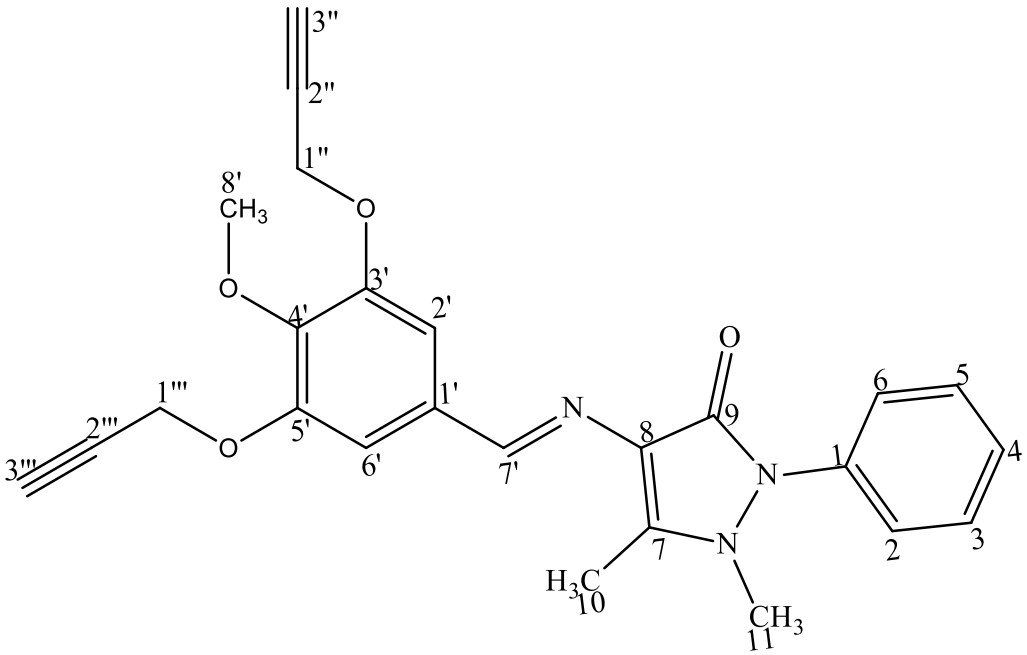

Scheme 4. 58: Structure of SB-J

4.3 Computed and Experimental Spectral Analysis

4.3.1 Vibrational frequency

The functional groups of organic compounds can be identified with the help of Vibrational spectroscopy. FTIR spectra for the synthesised compounds showed vibrational signals at the expected frequencies for relevant functional moiety. The stretching frequencies at 1659-1705 cm^{-1} are due to the imine linkage (C=N) of the compounds indicating the formation of the Schiff bases, these values are within the range reported in the literature (Alam *et al.,* 2012 and Tok *et al.,* 2019). The formation of the Schiff bases was further established by the absence of the NH_2 peak of primary amines in the region of 3350−3310 cm^{-1}. The vibrational frequencies of some prominent bands obtained from the experimental and theoretical calculations are shown on Table 4.2. It was observed that the computed vibrational frequencies agree with the experimental data. The calculated frequencies, however, were slightly higher than the corresponding experimental data due to assumptions inherent in computational chemistry and because computed vibrational frequencies were obtained in vacuum while experimental data were obtained in solvent. Other environmental factors during the experiment could contribute to the lower values obtained in experimental studies.

Table 4. 2: Experimental and Theoretical Vibrational Frequencies υ (cm^{-1}) of the Synthesised Compounds

S/N	Code	Experimental υ (cm^{-1})					B3LYP/6-31+G* (d) υ (cm^{-1})				
		υ_{AR-H}	υ_{Al-H}	$\upsilon_{C=O}$	$\upsilon_{C=N}$	$\upsilon_{C=C}$	υ_{AR-H}	υ_{Al-H}	$\upsilon_{C=O}$	$\upsilon_{C=N}$	$\upsilon_{C=C}$
1	SB0	3043	2936	1643	1594	1563	3197	3042	1765	1675	1645
2	SB1	3102	2928	1643	1596	1572	3189	3046	1766	1672	1652
3	SB1A	3069	2926	1648	1563	1518	3188	3048	1769	1681	1659
4	SB1B	3067	2944	1648	1592	1566	3188	3048	1767	1671	1643
5	SB2	3069	2937	1651	1598	1567	3197	3046	1764	1677	1647
6	SB2A	3057	2938	1649	1570	1487	3187	3042	1767	1664	1645
7	SB2B	3052	2956	1646	1569	1490	3196	3044	1766	1677	1644
8	SB3	3060	2936	1650	1594	1570	3198	3047	1764	1671	1657
9	SB3A	3056	2936	1648	1589	1562	3187	3043	1770	1664	1655
10	SB4	3058	2935	1649	1593	1569	3198	3043	1765	1670	1661
11	SB4A	3061	2928	1651	1585	1563	3198	3047	1770	1662	1654
12	SB4B	3052	2964	1646	1561	1490	3197	3046	1766	1671	1657
13	SB5	3105	2942	1627	1580	1517	3195	3044	1771	1705	1653
14	SB5A	3069	2924	1664	1593	1487	3196	3044	1769	1666	1649
15	SB5B	3089	2963	1615	1568	1519	3195	3040	1764	1684	1651
16	SB6	3050	2934	1646	1592	1506	3196	3040	1763	1680	1658
17	SB6A	3066	2931	1650	1594	1571	3186	3040	1767	1671	1639
18	SB6B	3068	2651	1572	1486	1370	3186	3043	1767	1674	1658
19	SB7	3056	2920	1653	1577	1489	3179	3045	1763	1679	1647
20	SB8	3062	2925	1648	1590	1564	3199	3045	1766	1675	1658
21	SB9	3144	2619	1591	1558	1389	3189	3043	1766	1676	1648
22	SB9B	3060	2621	1605	1578	1511	3187	3040	1763	1681	1659
23	SB10	3057	2929	1612	1586	1550	3189	3049	1769	1660	1639
24	SB11	3076	2943	1616	1589	1560	3194	3046	1777	1704	1657
25	SB11A	3059	2921	1616	1580	1512	3197	3041	1762	1659	1656
26	SB11B	3042	2943	1659	1563	1492	3187	3045	1765	1666	1652
27	SB12	3069	2920	6551	1593	1480	3197	3046	1769	1668	1655
28	SB13	3051	2922	1651	1587	1496	388	3045	1764	1667	1650
29	SB17	3053	2926	1610	1508	1423	3197	3042	1763	1637	1656
30	SB19	3158	2932	1634	1588	1512	3196	3098	1764	1669	1665

Table 4.2: Experimental and Theoretical Vibrational Frequencies υ (cm^{-1}) of Synthesised Compounds

S/N	Code	Experimental υ (cm^{-1})					B3LYP/6-31+G* (d) υ (cm^{-1})				
		υAR-H	υAl-H	υC=O	υC=N	υC=C	υAR-H	υAl-H	υC=O	υC=N	υC=C
31	5A1	3074	2925	1645	1570	1468	3265	3016	1756	1620	1598
32	5A2	3075	2925	1657	1588	1474	3210	3042	1759	1630	1564
33	5A5	3062	2926	1650	1563	1509	3211	3053	1754	1667	1634
34	5A6	3065	2927	1648	1572	1475	3118	3010	1764	1609	1530
35	5A8	3060	2924	1646	1521	1465	3260	3080	1770	1624	1548
36	5A9	3059	2952	1655	1595	1464	3220	3039	1752	1668	1630
37	9B1	3054	2920	1647	1501	1413	3209	3050	1765	1647	1622
38	9B2	3062	2926	1681	1599	1559	3210	3042	1764	1680	1547
39	9B5	3009	2952	1623	1520	1462	3355	3212	1874	1821	1694
40	9B6	3032	2921	1652	1534	1498	3112	3021	1762	1610	1567
41	9B8	3011	2920	1604	1501	1457	3188	3100	1764	1658	1646
42	9B9	3026	2910	1643	1556	1507	3186	3099	1764	1663	1647
43	10-1	3052	2924	1640	1593	1506	3210	3101	1775	1652	1635
44	10-2	3268	2937	1650	1579	1512	3211	3102	1775	1652	1640
15	10-5	3056	2926	1645	1595	1559	3220	3103	1772	1654	1634
46	10-6	3058	2926	1646	1588	1551	3216	3044	1773	1654	1638
47	10-8	3072	2926	1647	1567	1523	3220	3104	1775	1665	1639
48	10-9	3076	2912	1648	1587	1510	3218	3103	1775	1664	1644
49	SBA	3079	2983	1652	1599	1577	3210	3041	1765	1672	1661
50	SBB	3074	2938	1652	1572	1466	3211	3141	1768	1665	1632
51	SBC	3040	2914	1670	1536	1494	3210	3142	1767	1674	1645
52	SBD	3053	2926	1641	1572	1484	3211	3143	1760	1672	1641
53	SBE	3014	2922	1658	1529	1470	3197	3140	1763	1680	1646
54	SBF	3068	2928	1660	1586	1553	3210	3143	1769	1661	1648
55	SBG	3061	2924	1655	1575	1508	3212	3044	1773	1664	1639
56	SBH	3064	2926	1648	1581	1506	3042	3219	1765	1675	1657
57	SBI	3044	2925	1613	1598	1499	3220	3042	1767	1675	1642
58	SBJ	3088	2934	1640	1575	1494	3221	3043	1766	1671	1657

4.3.2 Computed and Experimental Mass Spectral of Synthesised Compounds

The EI-MS spectra of the Schiff bases and acetylenic ether compounds showed abundant molecular ions at various m/z values and most importantly the molecular ion peak M^+ of the compounds. The fast atomic bombardment (FAB) Spectroscopy was employed to know the molecular ions and deduced prominent ions in the ether compounds. The Fab- spectrum of the compounds, showed the molecular ion peak at M^+-1. While the Fab+ spectrum of the compounds showed the molecular ion peak at M^++1. Other prominent peaks were also deduced from the spectra and discussed in section 4.2 for each compound. The molecular ion peak M^+ of the compounds corresponds to the proposed formulae of the synthesised compounds.

4.3.3 Computed and Experimental Electronic Absorption of Synthesised Compound

The UV-visible absorption spectra of the compounds were obtained in chloroform and methanol. The UV spectra of the compounds show similarities, indicating similarity in their structures. The extinction coefficient or molar absorptivity, ε were calculated for each λmax. The $\lambda_{max,}$ absorbance and ε for the experimental and calculated UV-visible spectra are shown in Table 4.3. The experimental UV data agree with the calculated. Molar absorptivity is a measure of the intensity of an electronic transition or how well a molecule absorbs a given wavelength of light. The larger the molar absorptivity, the more probable the electronic transition. All the compounds exhibit characteristic broad absorption peaks in the UV–visible region between 201-422 nm. It was observed that compounds with nitro substituent (SB1, SB10, 10-1, 10-2, 10-5, 10-6, 10-9, and SBG), had higher λmax with compound SB10 having the highest value of λmax of 422 nm. While compound SB0 has the least value of λ_{max} of 201 nm. The bands observed below 250 nm are assigned to the π-π* transitions of conjugation between the lone pair of electrons of p orbital of N atom in azomethine group and conjugated π bond of the benzene ring. The band appearing at higher energy (above 250 nm) are typical n-π* transitions of azomethine (C=N) and n-π* transitions of benzene ring (Radha *et al.*, 2020).

Table 4. 3: Wavelength of Maximum Absorption (λmax) and Molar Absorptivity (ε) of the Studied Compounds

Code	Theoretical			Experimental		
	λmax(nm)	absorbance	ε ($Lmol^{-1}cm^{-1}$)	λmax (nm)	Absorbance	ε ($Lmol^{-1}cm^{-1}$)
SB0	265.76	0.056	1922.086	201.00	0.751	25776.55
	280.66	0.557	19117.89	235.00	1.233	42320.23
	325.58	0.102	3500.94	326.00	1.454	49905.61
SB1	293.52	0.915	27203.81	249.00	1.369	40701.65
	344.72	0.291	8651.702	267.00	1.311	38977.25
	403.84	0.433	12873.49	390.00	1.616	48045.19
SB2	265.39	0.331	10700.20	249.00	0.808	26120.13
	324.32	0.157	5075.321	327.00	1.016	32844.12
SB3	264.14	0.587	18017.19	249.00	0.930	28545.99
	274.40	0.651	19981.58	260.00	0.926	28423.22
	332.43	0.282	8655.617	336.00	1.179	36188.95
SB4	265.17	0.555	14989.87	249.00	0.839	22660.98
	333.57	0.344	9291.019	338.00	1.149	31033.93
SB5	276.18	0.180	5335.388	259.00	1.049	31093.46
	362.52	0.872	25846.99	337.00	1.820	53946.71
SB5A	326.52	0.224	6639.595	335.00	1.503	44550.49
SB5B	264.64	0.080	2371.283	260.00	0.663	19652.01
	336.44	0.221	6550.67	337.00	1.274	37762.69
SB6	268.04	0.901	28036.22	249.00	0.881	27413.88
	284.39	0.077	2395.992	266.00	0.899	27973.99
	318.85	0.924	28751.91	333.00	1.671	51996.14
SB7	267.06	0.031	1015.161	259.00	1.254	41064.94
	323.79	1.117	36578.58	327.00	1.715	56161.38
SB8	272.43	0.055	1738.526	267.00	0.867	27405.49
	360.68	1.386	43810.84	360.00	1.202	37994.69
SB9	266.23	0.546	17764.76	260.00	0.444	14446.07
	326.57	0.214	6962.746	266.00	0.422	13730.27
SB9B	269.88	0.661	21506.43	267.00	0.633	20595.42
SB10	304.28	0.390	11071.99	288.00	0.901	25579.15
	422.07	0.402	11412.67	409.00	1.236	35089.71

Table 4. 3: Wavelength of Maximum Absorption (λmax) and Molar Absorptivity (ε) of the Studied Compounds

Code	Theoretical			Experimental		
	λmax(nm)	Absorbance		λmax(nm)	Absorbance	ε($Lmol^{-1}cm^{-1}$)
Sb11	265.13	0.511	15810.64	261.00	0.392	12128.71
	366.82	0.642	19863.86	337.00	0.571	17667.08
Sb11A	287.72	0.521	16120.05	286.00	0.656	20297.03
	325.56	0.906	28031.18	347.00	1.679	51949.57
Sb11B	273.33	0.900	27846.53	260.00	0.937	28991.34
	321.71	0.589	18224.00	335.00	1.684	52103.96
Sb12	264.64	0.804	23387.05	260.00	0.824	23968.82
	336.44	0.221	6428.529	338.00	0.923	26848.57
Sb13	265.25	0.910	28490.92	260.00	0.741	23199.75
	318.65	0.748	23418.91	331.00	0.111	34783.97
Sb17	322.50	0.959	28264.07	345.00	1.605	47303.27
Sb19	321.11	0.878	23897.66	341.00	1.212	32988.57
5A-1	245.23	1.114	23522.46	220.00	1.192	25169.45
	284.65	0.780	16469.94	260.00	1.280	27027.59
	323.00	0.834	22700.05	328.00	0.913	19278.27
5A-5	322.00	0.925	20023.81	334.00	0.885	19157.91
5A-6	332.00	0.899	17753.12	333.00	0.885	17476.65
5A-8	267.84	1.096	23211.98	260.00	0.812	17197.19
	331.00	0.234	4955.842	333.00	0.704	14909.88
5A-9	331.27	0.825	18031.60	333.00	0.872	19058.86
9B-1	272.65	1.066	24032.28	219.00	1.110	25024.23
	321.74	0.620	13977.50	261.00	1.352	29871.27
9B2	284.09	0.572	12288.39	266.00	0.735	15790.15
	321.78	0.771	16563.55	335.00	1.247	26789.55
9B8	319.84	0.517	11684.14	262.00	0.573	12949.74
	326.02	0.578	13062.74	335.00	0.660	14915.93
9B9	283.59	0.905	21169.59	285.00	0.619	14479.53
	320.61	0.879	20561.40	335.00	0.972	22736.84
10-1	314.89	0.868	17766.49	220.00	0.709	14512.04
	399.90	0.214	4380.21	260.00	0.899	18401.01

Table 4. 3: Wavelength of Maximum Absorption (λmax) and Molar Absorptivity (ε) of the Studied Compounds

Code	Theoretical			Experimental		
	λmax(nm)	Absorbance		λmax(nm)	Absorbance	ε($Lmol^{-1}cm^{-1}$)
10-2	308.55	0.662	12968.44	201.00	0.696	13634.49
	404.00	0.708	13869.57	277.00	0.531	10402.18
10-5	399.92	1.149	24093.10	286.00	1.002	21010.69
10-6	301.75	1.057	20323.01	288.00	1.258	24187.65
10-8	377.62	1.014	20801.28	221.00	1.215	24924.61
	405.82	1.243	25499.00	267.00	1.367	28042.75
10-9	311.57	0.975	20634.92	249.00	1.210	25608.47
	396.99	1.259	26645.50	283.00	1.336	28275.13
SBA	267.37	1.014	27009.03	260.00	1.021	27195.48
	325.37	0.620	16514.39	338.00	1.808	48158.11
SBB	328.10	0.338	9003.009	333.00	0.860	22907.06
SBC	346.32	1.546	41179.45	337.00	1.888	50289.00
SBD	274.92	0.916	26519.97	221.00	1.164	33700.06
	326.45	1.199	34713.38	329.00	1.287	37261.15
SBE	284.72	0.532	15402.43	266.00	0.682	19745.22
	345.68	0.957	27707.00	334.00	1.205	34887.09
SBF	345.68	0.856	18659.80	349.00	1.188	25897.02
SBG	301.90	0.927	23744.88	249.00	0.745	19082.99
	401.18	0.848	21721.31	290.00	0.758	19415.98
SBH	328.73	0.949	23757.67	336.00	1.782	44010.51
SBJ	328.81	1.310	32309.78	337.00	1.573	38796.39

4.3.4 Computed and Experimental ^{1}H NMR and ^{13}C NMR Spectral of the Synthesised Compound

The nuclear magnetic resonance (^{1}H NMR) spectra of the compounds were recorded in methanol and DMSO and the structure elucidation were outlined in section 4.2. The ^{1}H NMR spectra of the compounds showed peaks of aromatic, methyl, and olefinic protons. The sharp singlet at δ_H 9.25-10.18 ppm indicates the presence of azomethine (–CH=N–) proton. The appearance of different pecks at δ_H 7.26-8.21 ppm showed the presence of aromatic protons. Aromatic protons resonate at chemical shift δ_H 6-7 ppm (Pavia *et al.*, 2001). However, the aromatic protons seen around δ_H 8 ppm for some of these compounds are due to the electron rich species on the substituents on the benzaldehyde ring which causes an increase in chemical shift of the protons due to deshielding effect. The sharp singlet at about δ_H 3-2 ppm indicate the presence of -CH_3 groups in the compounds. Methylene protons were observed for the ether compounds. The oxygen of the ether bond deshielded the methylene protons close to it and hence result to higher chemical shift of these protons. The acetylenic proton was observed for all the alkyne-ether compounds at 3.416-3.702 ppm further confirming the formation of the acetylenic ether compounds.

The ^{13}C NMR was done for only some of the new compounds (SB12, SB13, 5A-9, 10-1, SB-H and SB-J) and the spectra gave satisfactory results. ^{13}C NMR spectral showed characteristic peaks of quaternary carbons observed downfield at δ 116.85-163.67. Methine carbons for azomethine were observed around 148.40-154.7 ppm. DEPT-135 confirmed the absence of methylene carbons for the Schiff bases and confirmed the presence of methylene carbons for the ether compounds. This was observed upfield at 56.02-74.80 ppm. DEPT-90 confirmed the presence of methine carbons for the compounds. The methyl carbons present appeared upfield at 9.65-35.07. 4.4, 4.5 and 4.6 summarises the computed (DFT/B3LYP) chemical shifts and experimental chemical shifts of the compounds for comparisons. These data indicate a good correlation between the calculated and the experimental findings.

Table 4. 4: Experimental and Calculated ^{13}C NMR Chemical Shifts of SB12 and SB13

S/N	SB12			SB13		
	Nucleus	Chemical Shift (ppm)		Nucleus	Chemical Shift (ppm)	
		Experimental	Calculated		Experimental	Calculated
1	C-10	9.65	10.0	C-10	9.8	9.9
2	C-11	35.07	36.6	C-8'	19.34	21.1
3	C-5'	115.1	114.0	C-9'	19.42	21.4
4	C-3'	116.9	117.8	C-11	35.4	37.1
5	C-8	116.0	123.3	C-8	116.6	123.5
6	C-2	124.9	121.7	C-2	124.5	121.4
7	C-6	124.9	121.7	C-6	124.5	121.4
8	C-4	127.9	124.3	C-6'	124.9	122.7
9	C-6'	128.4	128.4	C-4	126.8	123.9
10	C-3	129.1	128.8	C-5'	128.1	129.9
11	C-5	129.1	128.8	C-3	129.1	128.6
12	C-1'	131.3	131.9	C-5	129.1	128.6
13	C-1	134.6	136.6	C-2'	129.8	135.3
14	C-2'	148.6	138.2	C-1'	134.6	135.6
15	C-7	152.3	154.6	C-3'	135.2	136.0
16	C-7'	159.2	156.0	C-1	136.5	136.9
17	C-4'	161.7	161.5	C-4'	138.8	139.2
18	C-9	163.7	163.2	C-7	152.0	154.3
19	-	-		C-7'	154.7	161.4
20	-	-		C-9	159.7	163.7

Table 4. 5: Experimental and Calculated ^{13}C NMR Chemical Shifts of 5A-9 and10-1

S/N	5A-9			10-1		
	Nucleus	Chemical Shift (ppm)		Nucleus	Chemical Shift (ppm)	
		Experimental	Calculated		Experimental	Calculated
1	C-10	9.7	9.9	C-10	9.7	9.8
2	C-11	35.4	36.5	C-8"	14.6	13.5
3	C-8"	54.9	57.2	C-11	34.9	36.4
4	C-8'	55.9	59.1	C-7"	69.7	71.5
5	C-7"	70.8	76.9	C-6'	112.4	114.6
6	C-2"	113.2	113.1	C-8	115.6	115.9
7	C-4"	114.2	117.7	C-4'	116.4	120.4
8	C-6"	114.4	120.2	C-2	125.2	121.6
9	C-6'	116.8	121.6	C-6	125.2	121.6
10	C-2	116.9	122.9	C-3	125.9	123.7
11	C-6	116.9	122.9	C-5	125.9	123.7
12	C-8	120.7	123.4	C-3'	127.2	124.4
13	C-5'	124.2	123.8	C-4	127.3	129.4
14	C-4	124.5	125 .0	C-2"	128.6	128.8
15	C-4'	126.8	126.6	C-6"	128.6	128.8
16	C-5"	129.1	127.3	C-3"	129.2	130.7
17	C-5	129.2	128.7	C-5"	129.2	130.7
18	C-3	129.2	128.7	C-1"	132.6	130.0
19	C-1'	131.4	133.8	C-1	132.2	136.8
20	C-1	134.6	136.7	C-1'	134.3	137.9
21	C-1"	138.4	138.5	C-4"	138.3	141.0
22	C-2'	146.9	150.9	C-2'	141.8	144.7
23	C-7'	150.5	152.3	C-7'	148.4	150.2
24	C-3'	152.3	153.5	C-7	152.6	153.7
25	C-3"	152.8	156.3	C-9	159.01	160.7
26	C-7	159.2	160.9	C-5'	161.60	163.4
27	C-9	159.7	163.7	-	-	-

Table 4. 6: Experimental and Calculated ^{13}C NMR Chemical Shifts of SBH and SBJ

S/N	SBH			SBJ		
	Nucleus	Chemical Shift (ppm)		Nucleus	Chemical Shift (ppm)	
		Experimental	Calculated		Experimental	Calculated
1	C-10	9.8	9.9	C-10	9.8	10.0
2	C-11	35.5	36.9	C-11	35.3	36.9
3	C-1"	56.0	59.8	C-3"	55.9	60.1
4	C-1"'	56.0	60.1	C-3"'	55.9	60.1
5	C-3"	78.5	75.3	C-1"	59.2	60.8
6	C-3"'	78.6	75.5	C-1"'	59.2	60.8
7	C-2"	78.9	79.0	C-2"	77.8	75.3
8	C-2"'	79.1	79.2	C-2"'	77.8	75.3
9	C-2'	111.3	116.4	C-8'	79.6	79.5
10	C-6'	113.7	120.6	C-2'	104.2	120.4
11	C-8	116.5	123.2	C-6'	104.2	120.4
12	C-5'	122.1	124.1	C-8	116.3	123.2
13	C-2	124.4	121.5	C-2	124.5	121.3
14	C-6	124.4	121.5	C-6	124.5	121.3
15	C-4	126.8	124.1	C-4	126.8	124.0
16	C-3	129.1	128.7	C-5	129.1	128.7
17	C-5	129.1	128.7	C-3	129.1	128.7
18	C-1"	131.3	136.2	C-1'	133.7	136.1
19	C-1	134.6	136.7	C-1	134.6	136.9
20	C-3'	147.1	149.2	C-4'	136.0	138.2
21	C-4'	148.8	151.2	C-3'	152.1	152.9
22	C-7	151.9	152.7	C-5'	152.1	152.9
23	C-7'	153.9	156.1	C-7	153.4	154.7
24	C-9	159.7	161.9	C-7'	154.4	156.2
25	-	-	-	C-9	159.6	161.2

4.4 Computed and Experimental X-ray Crystallographic Parameters of the Synthesised Compound

A yellow block-like specimen each of $C_{18}H_{15}ClFN_3O$ (SB12) and $C_{20}H_{21}N_3O$ (SB13), a colorless plate-like specimen of $C_{27}H_{27}N_3O_4$ (5A-9) and a gold block-like specimen of $C_{25}H_{21}BrN_4O_4$ (10-6) were used for the X-ray crystallographic analysis. The X-ray intensity data were measured at $\lambda = 1.54178$ Å. Data collection and structure refinement details are summarised in Table 4.7. and 4.8. The crystals of each compound exist as monoclinic structure except compound 10-6 which exit as triclinic. The experimental and computed Selected bond lengths, bond angles and Torsion angles for the compounds are given in Table 4.9, 4.10, 4.11 and 4.12. The calculated and experimentally determined parameters are very close in values. This validates the computational methods used in this work. The ORTEP diagrams of the crystal structure for SB12, SB13, 5A-9 and 10-6 are shown in Figure 4.1, 4.2, 4.3 and 4.4, respectively. The structure determination of the compounds was of good quality and further confirms the structure of the newly synthesised compounds.

Table 4. 7: Selected Crystal and Data Collection for Compound SB12 and SB13

Parameter	SB12	SB13
Formula	$C_{18}H_{15}ClFN_3O$	$C_{20}H_{21}N_3O$
Formula weight	343.78 g/mol	319.40 g/mol
Temperature	300 K	300 K
Wavelength	1.54178 Å	1.54178 Å
Crystal size	0.100 x 0.130 x 0.170 mm	0.100 x 0.140 x 00.220 mm
Crystal habit	Yellow Block	Yellow Block
Crystal system	Monoclinic	Monoclinic
Space group	P 1 21/c 1	P 1 21/n 1
Volume	1638.12(7) $Å^3$	1729.50(12) $Å^3$
Density (calculated)	1.394 g/cm^3	1.227 g/cm^3
Absorption coefficient	2.244 mm^{-1}	0.609 mm^{-1}
F(000)	712	680
Reflections Collected	19428	20543
Maximum θ angle	66.66° (0.84 Å)	68.24° (0.83 Å)
Absorption correction	Multi-Scan	Multi-Scan
Refinement method	Full-matrix least-squares on F^2	Full-matrix least-squares on F^2
Data / restraints /	2888 / 0 / 219	3152 / 0 / 222
Goodness-of-fit on F^2	1.065	1.057
Final R indices	R1 = 0.0407, wR2 = 0.1056	R1 = 0.0792, wR2 = 0.2185
R indices (all data)	R1=0.0470, wR2 = 0.1106	R1 = 0.1030, wR2= 0.2461
R.M.S. deviation	0.053 $eÅ^{-3}$	0.071 $eÅ^{-3}$

Table 4. 8: Selected Crystal and Data Collection for Compound 5A-9 and 10-1

Parameter	5A-9	10-6
Formula	$C_{27}H_{27}N_3O_4$	$C_{25}H_{21}BrN_4O_4$
Formula weight	457.51 g/mol	521.37 g/mol
Temperature	300 K	300 K
Wavelength	1.54178 Å	1.54178 Å
Crystal size	0.060 x 0.300 x 0.600 mm	0.100 x 0.230 x 0.310 mm
Crystal habit	Colorless Plate	Gold Block
Crystal system	Monoclinic	Triclinic
Space group	P 1 21/c 1	P-1
Volume	2424.88(10) $Å^3$	1135.62(5) $Å^3$
Density (calculated)	1.253 g/cm^3	1.525 g/cm^3
Absorption coefficient	0.690 mm^{-1}	2.812 mm^{-1}
F(000)	968	532
Reflections collected	32358	12607
Maximum θ angle	68.25° (0.83 Å)	68.23° (0.83 Å)
Absorption correction	Multi-Scan	Multi-Scan
Refinement method	Full-matrix least-squares on F^2	Full-matrix least-squares on F^2
Data / restraints /	4443 / 0 / 312	4100 / 0 / 310
Goodness-of-fit on F^2	1.034	1.041
Final R indices	R1 = 0.0386, wR2 = 0.0968	R1 = 0.0511, wR2 = 0.1432
R indices (all data)	R1 = 0.0523, wR2 = 0.1083	R1 = 0.0533, wR2 = 0.1463
R.M.S. deviation	0.032 $eÅ^{-3}$	0.098 $eÅ^{-3}$

Table 4. 9: Experimental and Theoretical Bond Lengths (Å), and Angles (º) for SB12

	EXPERIMENTAL	B3LYP/6-31+G*(d)
BOND LENGTH (Å)		
N3-C12	1.278	1.291
N1-N2	1.414	1.414
N1-C7	1.401	1.417
F1-C16	1.355	1.347
C8-C9	1.372	1.372
C12-C13	1.466	1.468
BOND ANGLE (^{o})		
C12-N3-C8	120.22	120.56
N3-C8-C7	129.79	128.99
C14-C13-C12	120.70	120.40
C9-C8-N3	122.06	123.26
C13-C12-N3	119.85	120.25
TORSION ANGLE (^{o})		
O1-C7-C8-N3	2.7000	0.9200
C12-N3-C8-C9	180.00	178.99
C12-C13-C14-C15	-179.15	-179.92
N3-C12-C13-C18	174.48	179.43
C8-N3-C12-C13	179.51	179.99
N3-C12-C13-C18	174.48	179.43

Table 4. 10: Experimental and Theoretical Bond Lengths (Å), and Angles (º) for SB13

	EXPERIMENTAL	B3LYP/6-31+G*(d)
BOND LENGTH (Å)		
C1-C2	1.461	1.464
N1-C11	1.392	1.384
C2-C7	1.397	1.404
N2-N3	1.410	1.414
O1-C10	1.232	1.227
C11-12	1.369	1.371
BOND ANGLE (º)		
C1-N1-C11	121.4	120.61
C7-C2-C1	122.3	122.52
N1-C1-C2	121.4	121.75
N1-C11-10	129.8	129.17
C3-C4-C8	120.5	120.14
N3-C12-C13	122.0	121.75
TORSION ANGLE (º)		
NI-C1-C2-C3	176.80	178.52
C1-N1-C11-C10	3.30	1.57
N1-C11-C12-N3	-170.00	-175.88
N1-C1-C2-C7	-3.20	-1.63
C15-N2-N3-C12	157.40	158.39
N3-N2-C10-O1	171.00	1.73.96
N1-C11-C10-N2	174.30	179.85

Table 4. 11: Experimental and Theoretical Bond (Å) Lengths and Angles (º) For 5A-9

	EXPERIMENTAL	(B3LYP/6-31+G*(d)
BOND LENGTH (Å)		
N1-C15	1.392	1.384
N1-C14	1.276	1.291
C13-C14	1.465	1.465
N2-N3	1.412	1.414
O2-C7	1.434	1.451
O2-C8	1.380	1.376
C6-C7	1.501	1.506
BOND ANGLE (°)		
C14-N1-C15	120.42	120.19
N1-C14-C13	120.29	121.32
C17-N2-N3	106.19	106.46
C8-C13-C14	119.82	119.20
O2-C7-C6	108.66	108.63
O2-C8-C13	119.81	119.74
C5-C6-C7	120.62	120.27
C1-C6-C7	119.56	119.63
TORSION ANGLES (°)		
C14-N1-C15-C17	169.62	-176.76
C15-N1-C14-C13	177.24	-178.68
N1-C15-C17-N2	175.21	175.95
C9-C8-C13-C14	-179.98	-179.56
aO2-C8-C13-C14	-2.02	2.74
C8-O2-C7-C6	-179.11	-177.17

4. 12: Experimental and Theoretical Bond (Å) Lengths and Angles (º) For 10-6

	EXPERIMENTAL	B3LP/6-31G*(d)
BOND LENGTH (Å)		
Br1-C13	1.908	1.923
C5-C14	1.480	1.477
N1-C4	1.460	1.464
O3-C1	1.352	1.358
N2-C14	1.280	1.291
O4-C16	1.230	1.224
BOND ANGLE (º)		
O2-N1-C4	118.7	118.39
C14-N2-C15	121.3	120.56
N2-C14-C5	118.8	119.05
C1-O3-C7	117.31	118.64
C4-C5-C14	125.5	122.47
C5-C4-N1	121.3	122.43
O3-C7-C8	108.32	107.93
TORSION ANGLE (º)		
C15-N2-C14-C5	178.0	176.47
N1-C4-C5-C14	-5.4	-7.66
C1-O3-C7-C8	-168.1	-176.09
N1-C4-C5-C6	178.4	176.70
C7-O3-C1-C2	169.9	178.85
N2-C15-C16-04	3.3	1.26
C16-C15-C17-C24	179.7	176.29
C9-C8-C13-Br1	-179.37	-179.97

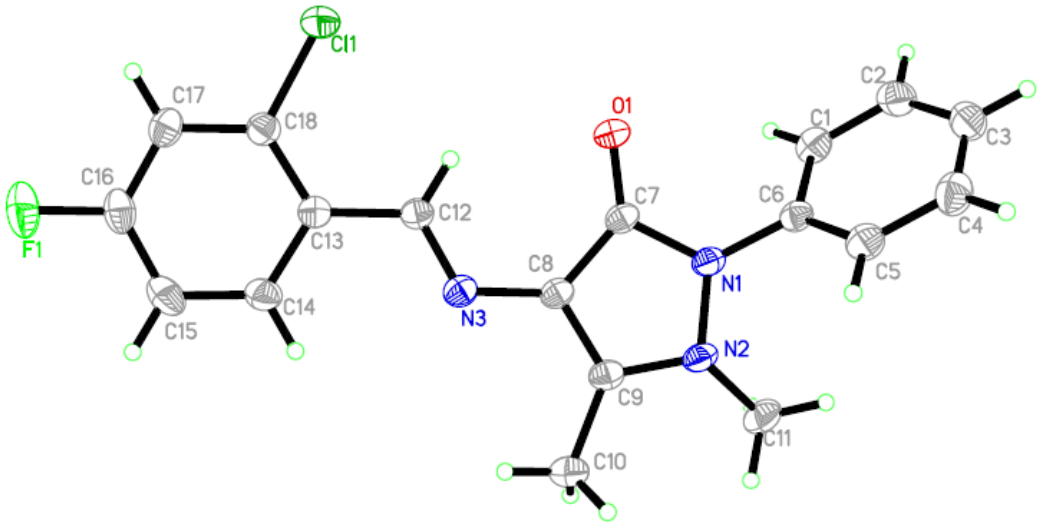

Figure 4. 1: ORTEP Drawing of SB12 with Atomic Numbering Scheme

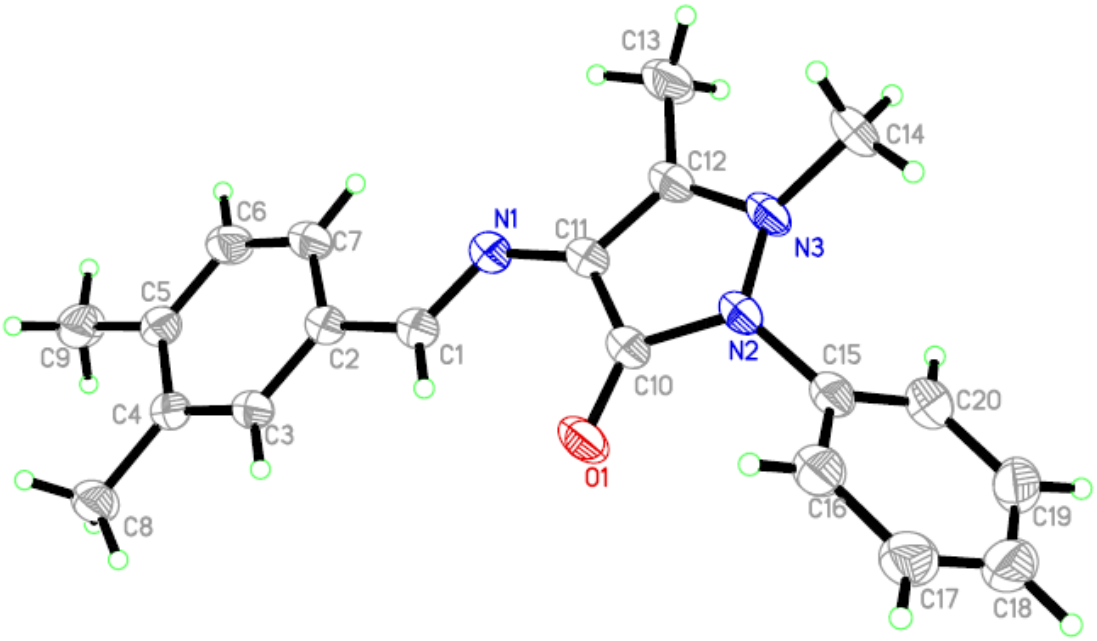

Figure 4. 2: ORTEP Drawing of SB13 with Atomic Numbering Scheme

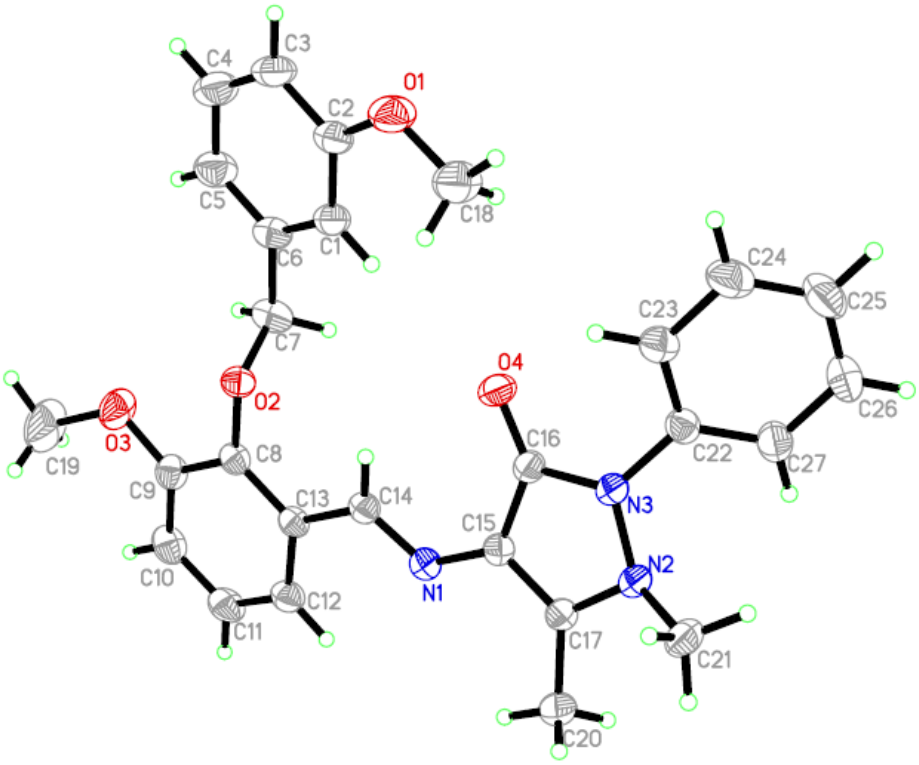

Figure 4. 3: ORTEP Drawing of 5A-9 with Atomic Numbering Scheme

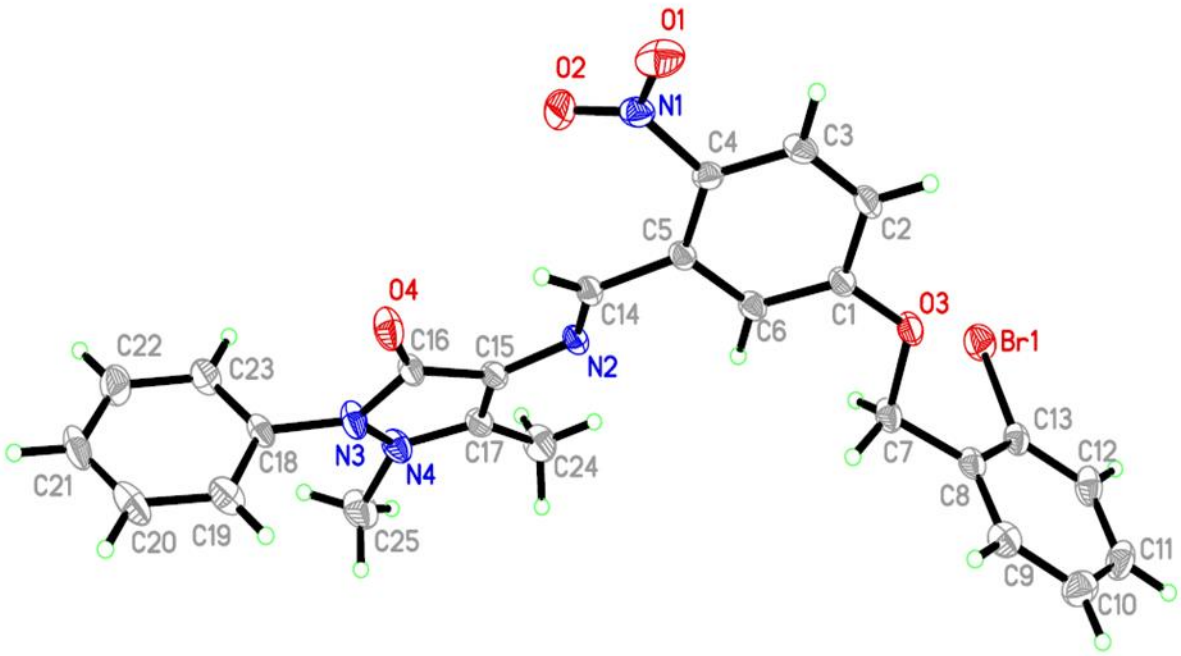

Figure 4. 4: ORTEP Drawing of 10.6 with Atomic Numbering Scheme

4.5 Biological Evaluation of Synthesised Compounds

4.5.1 Cytotoxicity of Synthesised Compounds

The percentage mortality obtained from the Brine Shrimp Lethality Assay showed that the synthesised compounds were not cytotoxic. Similarly, the percentage inhibition obtained from MTT colorimetric assay against mouse fibroblast cells indicate that the synthesised compounds were non-cytotoxic against normal cell lines.

4.5.2 Anti-inflammatory Activities of Synthesised Compounds

Anti-inflammatory activity of the synthesised compounds was done by Oxidative Burst Assay and IC_{50} value recorded (Table 4.13). Four of the synthesised compounds had anti-inflammatory activities, with compounds SB11B, SB17 and SB5 showing excellent anti-inflammatory activities with IC_{50} of 0.01±0.02, 1.50±0.03 and 1.80±0.14 µM, respectively which were higher than the standard (Ibuprofen 11.20±1.90). Compound SB19 also had a very good activity with IC_{50} of 13.40±0.12 µM, while other synthesised compounds were inactive.

The structure-activity relationship of active inflammatory compounds showed that the anti-inflammatory activity was dependent on the type and position of the substituent group. Compound SB11B which possesses a hydroxyl substituent on the ortho and meta positions of benzylidene showed excellent activity more than the standard drug. On the other hand, SB11 and SB11A which possess the same substituent but at different positions exhibited very poor activity compared to the standard drug. Compound SB5 with hydroxyl and methoxy substituent also had excellent activity. However, compounds SB5A and SB5B which possess the same substituents as SB5 but at different position did not exhibit good activity like SB5. The presence of trihydroxy substituents at benzylidene increased the anti-inflammatory activity as in the case of compound SB17. It was observed that all compounds with significant activity possess electron donating moiety (OH, OCH_3) in their structures. This suggests that activity is not only dependent on the nature of substituent but also on the position of the substituent.

Anti-inflammatory activities of most of the synthesised compounds are reported for the first time in literature. Arshad *et al.,* (2014) and Murtaza *et al.,* (2017) reported compound SB3 to be a potential anti-inflammatory agent.

4.5. 3 Antioxidant Activities of Synthesised Compounds

The antioxidant activity of the synthesised compounds was determined by DPPH free radical scavenging assay and the IC_{50} obtained. Five of the compounds possessed antioxidant activity with compound SB5 having excellent antioxidant activity with IC_{50} value of 111.10±1.80 µM when compared to the standard N-acetyl-L-Cystine (IC_{50}111.60±2.40 µM). Compound SB11B and SB17 also showed very good antioxidant activities with IC_{50} of 29.10±1.08 and 40.90±1.30 µM, respectively. Comparatively moderate antioxidant activity was observed in the case of SB11 and SB19 with IC_{50} 214.80±3.58 and 297.20±1.00 µM, respectively. Other compounds showed no activity at all (Table 4.13).

The structure-Activity Relationship of active antioxidant compounds showed that compounds with electron donating moiety (OH, OCH_3) are active antioxidants. Though compound SB11A has two hydroxyl groups as substituents like SB11B and SB11 at different positions, it did not possess activity like SB11B and SB11. Similarly, SB5A and SB5B have the same substituent group as SB5 at different positions but they did not possess activity like SB5. A similar effect has also been reported by Teran *et al.,* (2019). These observations infer that the activity of a compound does not only depend on the type or nature of the substituent but also on the position of the substituent.

4.5.4 Antiglycation Activities of Synthesised Compounds

The antiglycation activities of the synthesised compounds were carried out using human serum albumin solution. The compounds that exhibited 50% or above percent inhibition were processed for IC_{50}. Each test compound was compared with rutin the standard inhibitor. Five Schiff base and three alkyne functionalised ether compounds showed antiglycation activity. Compound SB10 showed very good activity (IC_{50} = 321.16±1.70 µM) which was very close to the standard rutin (IC_{50} = 280.50±1.50 µM). Compound SBG and SB5 also showed good activity with IC_{50} = 526.65±2.66 and IC_{50} = 575.3±1.80 µM, respectively. Comparatively moderate activity was observed in the case of SBI, SB11, SBF, SB19 and SB9B with IC_{50} value of 628.6±2.80, 638.8±02.70, 721.32±3.29, 842.51±2.40 and 856.80±01.80 µM, respectively. Compound SB9B having the least activity, while other compounds showed no activity at all (Table 4.13).

Table 4. 13. Antioxidant, Anti-inflammatory, and Antiglycation Activities of the Studied compounds

Sample code	Antioxidant (IC_{50} ± SEM (µM)	Anti-inflammation (IC_{50} ± SEM (µM)	Antiglycation (IC_{50} ± SEM (µM)
SB5	111.10±1.80	1.80±0.14	575.30±01.80
SB9B	-	-	856.80±01.80
SB10	-	-	321.16±1.70
SB11	214.80±3.58	-	638.8±02.70
SB11B	29.10±1.08	0.01±0.02	
SB17	40.90±1.30	1.50±0.03	-
SB19	297.20±1.00	13.40±0.12	842.51±2.40
SBF	-	-	721.32±3.29
SBG	-	-	526.65±2.66
SB1	-	-	628.6±2.80
N-acetyl-L-Cystine	111.60±2.40	-	-
Gallic Acid	22.80±1.35	-	-
Ibuprofen	-	11.20±1.90	-
Rutin	-	-	282.40±0.80

- = Not calculated (because of % inhibition shown was less than 50% at100 µg/mL.

4.6 Computational Studies of the Bioactive Compounds

The bioactive compounds were studied using DFT, QSAR, docking methods and ADMET screening. DFT studies were used to generate molecular descriptors, obtain theoretical spectral data, and other geometric properties of the compounds. QSAR analysis was performed to predict the biological activity obtained experimentally. Docking was done to obtain the best binding scores and the interaction of the compounds with the target. ADMET screening was done to explore their uses in clinical application.

4.6.1 Frontier Molecular Orbital of the Bioactive Compounds

The energy of HOMO (Highest Occupied Molecular Orbital) and LUMO (Lowest Unoccupied Molecular Orbitals) also known as frontier molecular orbitals are used to explain the electronic properties, chemical reactivity, stability, and bioactivity of a molecule (Zaater *et al.,* 2016; Erazua and Adeleke, 2019a). The HOMO represents the region of electron density which is associated with the electron donating ability of the molecule while the LUMO is associated with the electron accepting ability of the molecule (Odozi *et al.*, 2015). It has been established that higher value of E_{HOMO} and lower value of E_{LUMO} give the molecule a better ability to interact with other chemical species (Oyebamiji and Semire, 2021) and lead to a lower binding energy. The data for E_{Homo} and E_{Lumo} for the studied compounds are displayed on Table 4.14. Compound SB19 had the highest value of E_{HOMO} while compound SB5 had the lowest value. E_{LUMO} revealed that SB10, SB11B, SB17 and SB5 had better reactivity. This agreed with the binding energy and the experimental results. The energy difference between the HOMO and LUMO orbital known as band gap (BG), gives information on the reactivity and stability of a molecule (Obi-Egbedi and Ojo, 2017). Large BG signifies good thermodynamic stability of a molecule, whereas a small BG suggests an easy electronic transition indicating better reactivity, less stability and better protein-ligand interaction (Adebesin *et al.*, 2016; Erazua and Adeleke, 2019b; Oyebamiji and Semire, 2016). Compound SB9B with the highest BG showed least antiglycation activities and no anti-inflammatory and antioxidant potential. While compounds SB10 and SB11B with least BG show good inhibitory potential. This trend is the same for the experimental results. Figure 4.5 shows the HOMO-LUMO orbital diagram of some of the studied compound.

Table 4. 14: Selected Molecular Descriptors for the Bioactive Compounds

S/N	Code	E_{HOMO} (eV)	E_{LUMO} (eV)	BG (eV)	η	σ	μ	ω (eV)	χ	DM (Debye)	PSA	POL
1	SB5	-5.70	-2.22	3.48	1.74	0.58	-3.96	4.51	3.96	8.94	56.46	72.32
2	SB9B	-5.24	-1.18	4.06	2.03	0.49	-3.21	2.54	3.21	4.63	42.63	66.46
3	SB10	-5.23	-2.70	2.53	1.26	0.79	-3.97	6.21	3.97	9.06	76.02	68.32
4	SB11	-5.22	-1.18	3.82	1.91	0.502	-3.20	2.68	3.20	6.00	61.06	66.95
5	SB11B	-5.31	-2.64	2.67	1.34	0.75	-3.98	5.93	3.98	2.08	60.58	66.94
6	SB17	-5.67	-2.43	3.24	1.62	0.62	-4.05	5.06	4.05	6.04	72.87	67.50
7	SB19	-5.21	-1.21	4.00	2.00	0.50	-3.21	2.58	3.21	6.09	53.10	70.88
8	SBF	-5.68	-1.82	3.86	1.93	0.52	-3.75	3.64	3.75	6.15	29.09	73.14
9	SBG	-5.60	-2.20	3.40	1.70	0.59	-3.90	4.47	3.90	8.94	66.46	72.32
10	SBI	-5.13	-1.18	3.95	1.98	0.51	-3.16	2.52	3.16	3.23	35.10	75.08

η: global hardness; σ: global softness; μ: chemical potential; ω: global electrophilicity index; χ: electronegativity, PSA: polar surface area and POL: polarizability.

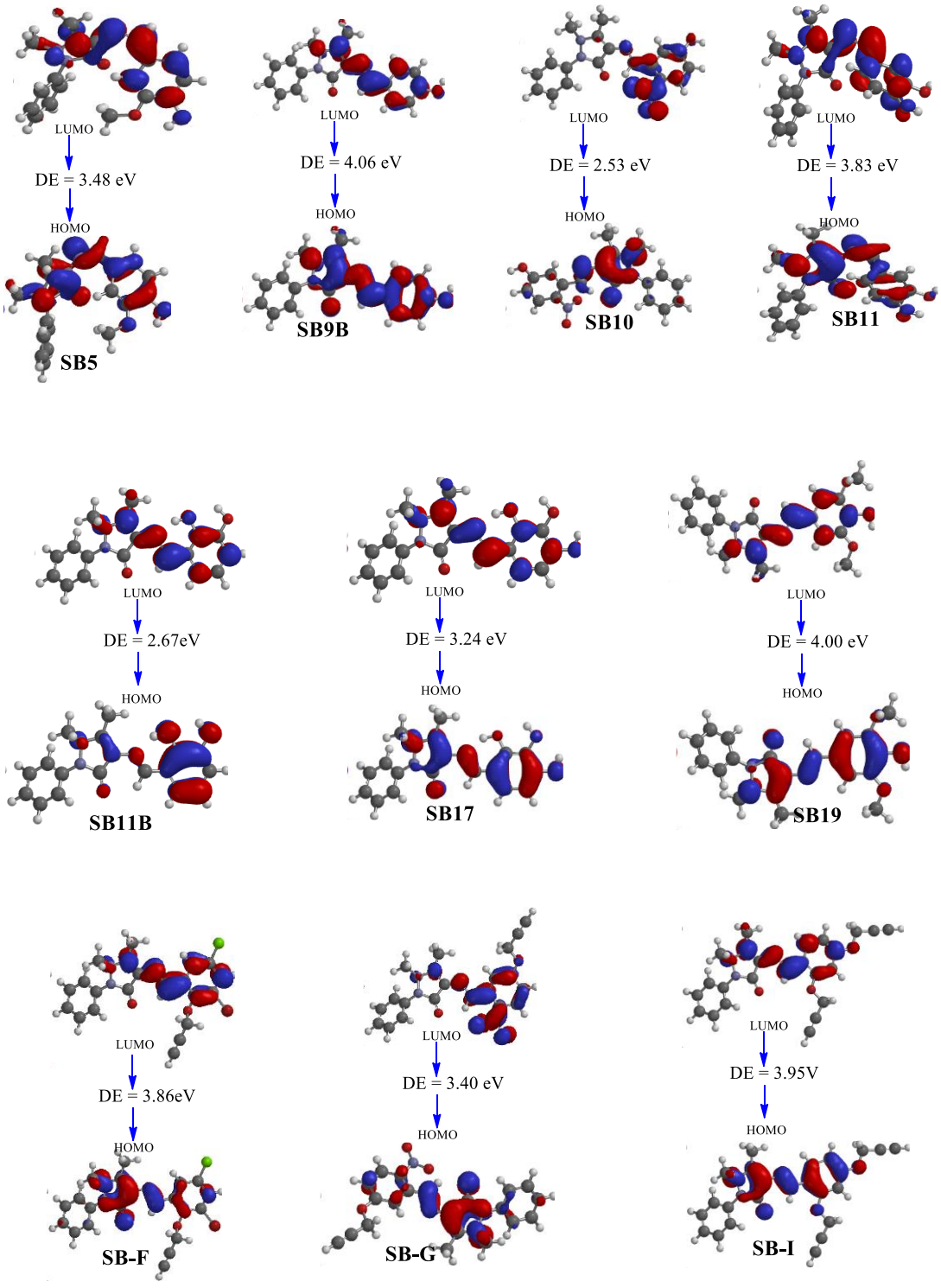

Figure 4. 5: HOMO-LUMO Orbital Diagram of the Bioactive Compounds

4.6.2 Global Reactivity Descriptors of the Bioactive Compounds

The chemical potential (μ), global hardness (η), global softness (σ), global electrophilicity index (ω) and electronegativity (χ) were obtained, using the energies of LUMO and HOMO, from Equations 3.4-3.8 and the results displayed in Table 4.14.

Chemical hardness is the resistance against electron cloud polarisation of a chemical species. It is characterised by high ionisation potential and high electronegativity, favoring the molecular stiffness with consequent chemical stability. While softness is related to basicity and electron donation with high polarisability and low electronegativity, thus favoring the molecular flexibility with consequent chemical reactivity (Costa *et al.,* 2018). A lower value of chemical hardness and greater value of softness result to higher binding affinity and consequently a better ligand-receptor interaction (Erazua and Adeleke, 2019b). There was a good correlation between Ƞ, σ and binding energy of the synthesised compounds. Compound SB9B with the least value of σ and greatest value of Ƞ possess lower bioactivity shows any least antioxidant and anti- inflammatory activity. On the other hand, compound SB10 and SB11B had the higher values of σ and had the lowest binding energy in most of the complexes formed, resulting in excellent antiglycation and anti-inflammatory activities.

Chemical potential (μ) is a measure of the ability of a molecule to cause a chemical reaction due to internal chemical energy or external energy. Since μ is being influenced by the number of atoms or molecules that are added or subtracted from the system, it can be related to binding affinity of a complex (Costa *et al.*, 2018). A lower value of μ leads to lower binding energy and better interaction. It was observed that SB17, SB11B, SB10, and SB5 with lower values of μ had significant bioactivity than compounds SB9B, SB19 and SB-I with higher values of μ.

Another global reactivity descriptor is the global electrophilicity index (ω). This describes the electron-accepting ability of the systems. A higher value of ω indicates an increase in the electron-accepting abilities of a molecule which signifies high inhibition efficiency (Erazua and Adeleke 2019b). From Table 4.14, the electron-accepting ability of the compounds are in the order of SB10 > SB11B > SB17 > SB5 > SBG > SBF > SB11 > SB19 > SB9B >SBI. It is observed that SB10, SB11B, SB17, and SB5 with high values of ω had

significant bioactivities, showing the relative importance of these descriptors in determining the activities of the compounds.

Electronegativity (χ) is used to estimate the tendency of a molecule to attract electrons from another molecule with which it performs interaction (Cunha *et al.,* 2015). A higher value of χ enhances the polarity of a molecule causing an increase in attractive forces (between receptor and other amino acid residues) in certain regions leading to more efficient receptor-ligand interaction and hence a lower binding energy. Compounds SB17, SB10, SB11B and SB5 with higher values of χ had lower binding energy, hence better bioactivities than others.

In this study, dipole moment was obtained from DFT calculation. This is a parameter that describes the interaction among atoms, and it gives information about the degree of hydrophobicity/hydrophilicity. The dipole moment of a molecule can also be described by the polarity of a system. It is the measure of the polarity of a polar covalent bond (Adejoro *et al.,* 2017). The higher the DM, the greater the polarity of the molecule and consequently the greater tendency to dissolve and interact in a polar environment (Costa *et al.,* 2018). The dipole moment for the studied compounds ranges from 2.08-9.06 Debye. These values fit perfectly in the range of values established for DM of molecular compounds (Oyewole *et al.,* 2020).

Also, Polar surface area (PSA) is a sum of surfaces of polar atoms (usually oxygen, nitrogen and attached hydrogen) in a molecule (Obi-Egbedi and Ojo, 2015). This parameter has been shown to correlate very well with the human intestinal absorption, Caco-2 monolayer permeability, and blood-brain barrier penetration. PSA is an indicator of the ligand hydrophilicity which plays an important role in shaping the protein- ligand interaction by affecting the non-bonded contribution to the binding energy (Adejoro *et al.,* 2017). It plays an important role in shaping the protein-ligand interaction by affecting the non-bonded contribution to the binding energy. According to the Veber's Rule, PSA not greater than 140 $Å^2$ are predicted to have good oral bioavailability. Molecules with a PSA greater than 140 $Å^2$ are usually believed to be poor at permeating cell membranes (Veber *et al.,* 2002). For molecules to penetrate the blood-brain barrier, PSA should be less than 60 $Å^2$ (Gupta *et al.,* 2019). PSA for the studied compounds range from 29.09-75.76-02 $Å^2$, hence they will have good oral bioavailability and have good cell permeability. The studied Schiff bases will

effectively penetrate the blood-brain barrier and can be used as drug targeted to the central nervous system except compounds SB11B, SB11, SBG, SB17 and SB10 with PSA value of 60.58, 61.06, 66.46, 72.87, and 76.02 $Å^2$, respectively.

Polarisability of a molecule characterises the capability of its electronic system to be distorted by the external field, and it plays an important role in modeling many molecular properties and biological activities (Obi-Egbedi *et al.*, 2015). Highly polarisable molecules are expected to have strong attractions with other molecules. Larger molecules in which electrons are far from the positively charged nucleus are more polarisable than smaller molecules hence polarisability increases with increase in volume and area of the molecule. From the results (Table 4.14), the most polarisable compound is SBI while compound SB9B is the least polarisable.

4.6.3 QSAR Result of the Bioactive Compounds

The developed QSAR models (equations 4.1, 4.2, and 4.3) were used to predict the observed inhibition concentration (IC_{50}) for anti-inflammatory, antioxidant and antiglycation activities, respectively. s 4.15 shows the experimental IC_{50}, predicted IC_{50} and the residual values. From this result it was observed that the developed models replicated the experimental IC_{50} values well. The low residual values between the experimental and predicted IC_{50} confirmed the models are dependable with high prediction power (Erazua *et al.*, 2021b). Figures 4.6, 4.7 and 4.8 depict the plot of predicted IC_{50} against experimental IC_{50} for the various compounds. From the plots, the distribution of projected IC_{50} and experimental IC_{50} of the various compounds along the line confirmed the developed model's dependability and efficiency. In addition, the internal validation's R^2 values and the plot's R^2 values agreed with one another, demonstrating the stability and dependability of the reported models (Grisoni *et al.*, 2018).

$$IC_{50} = -117.798 - 8.89773\ (E_{HOMO}) + 1.06647\ (Pol) \quad (4.1)$$

$$IC_{50} = -7773.26 - 518.863\ (E_{LUMO}) - 91.8124\ (DM) + 112.972\ (POL) \quad (4.2)$$

$$IC_{50} = -571045 - 0.0584913\ (DM) + 0.458413\ (E_{LUMO}) + 0.0133341\ (POL) + 0.0907915\ (PSA) \quad (4.3)$$

The result of the predicted IC_{50} showed that E_{HOMO} and polarizability of the compounds played a major role in the anti-inflammatory activity of the synthesised molecules. The antioxidant abilities of the test compounds were significantly influenced by the $E_{HOMO,}$ polarizability, and dipole moment. The antiglycation activities of the test compounds were greatly impacted by the $E_{LUMO,}$ polarizability, dipole moment and Polar Surface area.

The negative coefficients of the E_{HOMO} and DM descriptors strongly suggested that they contribute negatively to the inhibitory effects of the compounds. This implies that decreasing the amount of these independent descriptors increasing the inhibitory concentration of the examined compounds. Similarly, the positive coefficients of polarizability, and PSA in the models showed that these descriptors contributed favorably to the inhibitory effects of the ligands under investigation. It implies that the concentration of these inhibitory substances increases as the amount of these descriptors increases and vice versa (Ibrahim *et al.,* 2020; Oke *et al.*, 2022).

The anti-inflammatory activity model was statistically validated by R^2= 0.9976, = 0.9927, and $CV.R^2$ = 0.9980. The antioxidant activity model was statistically validated by R^2 = 0.9887, 0.9548, and $CV.R^2$ = 0.9940. The antiglycation activity model was also statistically validated by R^2 = 0.9871, = 0.9698, and $CV.R^2$= 0.9999 as recorded in Table 4.16. The value for calculated $CV.R^2$ for the three models developed (Table 4.16) was greater than 0.5 (standard) which indicates that the developed models were reliable, acceptable, appropriate and predictive.

Table 4. 15: Experimental and Predicted IC_{50} Values for Anti-Inflammatory, Antioxidant and Antiglycation Activities

Compounds	Observed IC_{50}	Predicted IC_{50}	Residual
anti-inflammatory activity			
SB5	1.80	1.70	0.10
SB11B	0.01	0.05	-0.04
SB17	1.50	1.52	-0.02
SB19	3.40	3.44	-0.04
Antioxidant Activity			
SB5	111.1	125.7	-14.6
SB11	214.8	211.5	3.3
SB11B	29.1	38.2	-9.1
SB17	40.9	24.2	16.7
SB19	296.2	292.5	3.7
for Antiglycation Activity			
SB5	575.30	575.30	0.00
SB-9B	856.80	857.81	0.01
SB10	321.16	321.16	0.00
SB11	638.80	638.80	0.00
SB19	842.51	842.41	-0.01
SB-F	721.32	721.22	-0.01
SB-G	526.65	526.66	0.01
SB-I	628.60	628.60	0.00

Table 4. 16: Statistical Parameters and Limit needed for the QSAR Model Assessment

Statistical parameter	Details	Accepted Value	Model 4.1	Model 4.2	Model 4.3
R^2	Correlation coefficient	≥ 0.6	0.9977	0.9743	0.9871
R^2_{adj}	Squared correlation coefficient	≥ 0.6	0.9927	0.9548	0.9698
$CV.R^2$	Cross-validation coefficient	≥ 0.5	0.9980	0.9940	0.9999
$CV.R^2$-R^2	Difference between $CV.R^2$ and R^2	≥ 0.3	0.0053	0.0392	0.0301

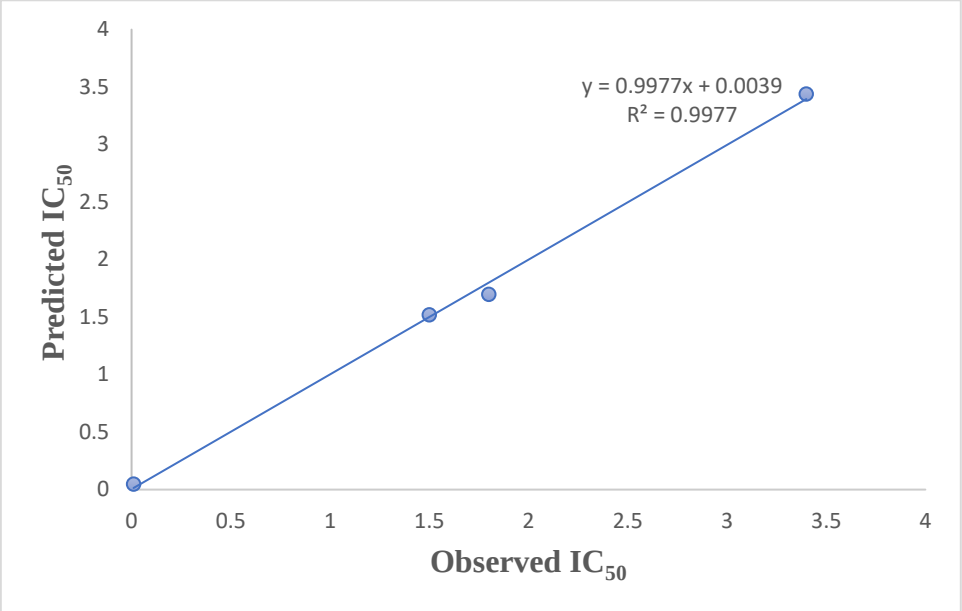

Figure 4. 6: The Predicted IC50 against the Observed IC50 for Anti-Inflammatory Activity

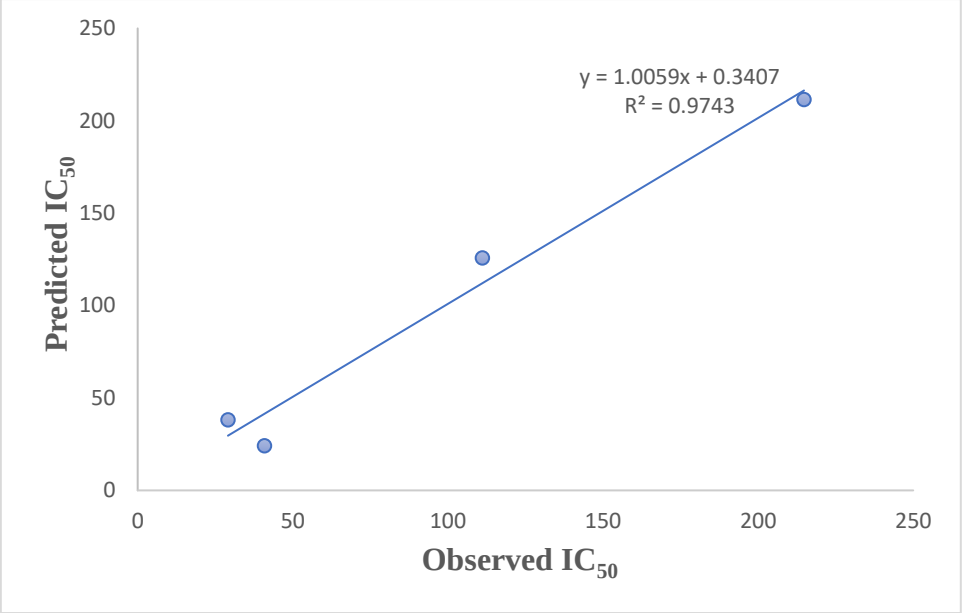

Figure 4. 7: The Predicted IC_{50} against the Observed IC_{50} for Antioxidant Activity

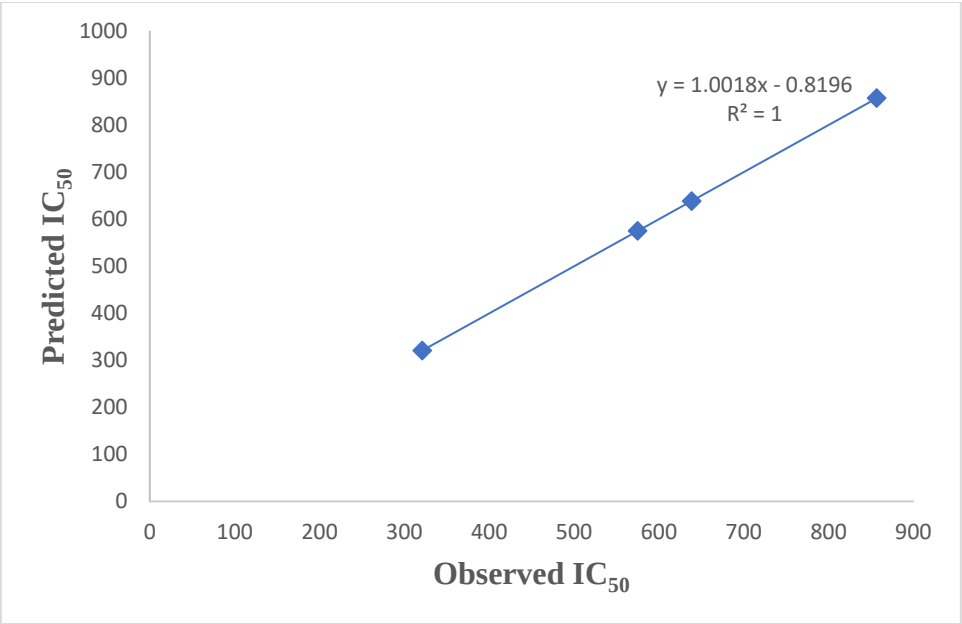

Figure 4. 8: The Predicted IC_{50} against the Observed IC_{50} for Antiglycation Activity

4.6.4 Molecular Docking Result of the Bioactive Compounds

Molecular docking is a computational technique used to recognise the structures which bind well to the enzyme pocket (Pinzi and Rastelli, 2019). The bioactive compounds and the standard drug used in each bioassay were used as ligands. These ligands were docked into the active site of the selected enzyme. To analyse the docking calculations, nine conformers were considered for each ligand-enzyme complex and the conformation with the lowest binding energy (most negative value) is identified to be the best binding mode of the docked compound to the target enzyme. The binding energy, protein residues involved in the interaction and the distance for each complex formed are displayed on Tables 4.19 to 4.26. The 2D and 3D diagrams showing protein residues involved in the interaction and type of interactions observed are also displayed in Figures 4.9 to 4.14.

Molecular Docking Result for Antioxidant Active Compounds

The interactions present in the complexes formed with HO-1 receptor (1N3U) are conventional hydrogen bond, carbon hydrogen bond, pi-alkyl, and pi-pi-T-Shaped, pi-pi-stacked and Van der Waals forces of attractions with a binding affinity which ranged from -5.2 to -7.9 Kcal/mol. It is observed that all test compounds and standards had strong binding affinity with the receptor, they perfectly snug into the active site of the receptor by interacting with the amino acid residue at the binding site (LYS-18, TYR-134, HIS-25). The high binding affinities exhibited by some of the compounds against HO-1 protein in this study is an indication of the inhibitory potential of these compounds against these biomolecules and their possible roles as therapeutic agents against oxidative stress. The tested compounds had lower binding energy than the standards used with compound SB11 and SB11B having the lowest binding energy, hence better antioxidant activities than other test compounds and standard.

The test compounds were also docked to the active site of glutathione peroxidase receptor (3KIJ) to further validate their antioxidant properties. The resulting complexes showed that the test compounds inhibit the active site of the protein with binding energy between -4.4 to -5.3 Kcal/mol, from the results, the binding energy of the compounds are in a very close range (-5.1 to -5.3) and lower than that of the standards (-4.4 and -4.5). This indicates that the compounds had better affinity to the receptor than the standards. Compound SB11B had

the best binding interaction with a binding energy of -5.3 Kcal/mol. This agrees with the result obtained for HO-1 receptor. The interactions involved in the binding are conventional hydrogen bond, Carbon hydrogen bond, pi-alkyl, and pi-pi-T-shaped, pi-anion and various Van der Waal's forces of attraction. It was observed that all ligands formed conventional hydrogen bond with ASP-83 (Table 4.18) and Van der Waal's forces of attraction with CYS-79 (active site residue). These bindings are very vital for receptor-ligand interaction and for strengthening the interaction, because of the hydrogen and hydrophobic interactions. Figure 4.9 and Figure 4.10 displayed the interaction of amino acid residues with receptor 1N3U and 3KIJ, respectively.

Table 4. 17: Binding Energy, Interactions and Distance Between the Ligands and HO-1 (1N3U) Receptor

Ligands	ΔG kcal/mol	Interactions	Distance
SB5	-7.4	(i) ARG-136 (ii) ASN-210 (iii) PHE214 (iv)THR-135 (v) GLY139 (vi) HIS-25, LIG:CH_3 (vii) LEU-138, LIG:CH_3 (viii) LYS-22 (ix) LYS-18 (x) THR-21 (xi) TYR-134 (xii) SER-142 (xiii) ALA-28 (xiv) PHE-207	(vi) 6.00, 5.64, 4.48 (viii) 4.47 (ix) 5.74 (xiv) 5.87
SB11	-7.9	(i) PHE-214 (ii) ASN-210 (iii) ARG-136 (iv) THR-135 (v) GLY-139 (vi) HIS-25 (vii)TYR-134, LIG:O (viii) THR-21, LIG:H (ix) LYS-18, LIG:H (x) LYS-22 (xi) SER-142 (xii) GLY-143 (xiii) PHE-207	(vi) 6.00, 5.57 (vii) 6.48 (viii) 3.76 (ix) 3.78, 5.76 (xiii) 5.97
SB11B	-7.9	(i) PHE-214 (ii) ASN-210 (iii) ARG-136 (iv) ALA-28 (v) THR-135 (vi) HIS-25 (vii) GLY-139 (viii) LYS-18, LIG:O (ix) LYS-22 (x) THR-21 (xi) TYR-134 (xii) SER-142	(iv) 6.60 (vi) 5.9, 5.54 (viii) 4.84
SB17	-7.8	(i) ASN-210 (ii) PHE-214 (iii) ALA-28 (iv) PHE-207 (v) LEU-138(vi) GLY-139 (vii) HIS-25 (viii) LYS-18, LIG:O (ix) LYS-22 (x) TYR-134 (xi) THR-21, LIG:O (xii) SER-142 (xiii) GLY-143 (xiv) THR-135	(iii) 6.66 (iv)5.86 (vii) 6.21, 5.82 (viii) 5.78, 5.14 (xi) 4.29
SB19	-6.8	(i) LEU-147 (ii) GLU-29 (iii) GLY-139, LIG:O (iv) HIS-25, LIG:CH_3 (v) SER-142 (vi) TYR-134, LIG:O (vii) THR-21, LIG: CH_3 (viii) LYS-18, LIG: CH_3 (ix)LYS-22 (x)THR-135 (xi) PHE-207 (xii) ASN-210 (xiii) ALA-28 (xiv) PHE-214 (xv) MET-34	(iii) 3.71 (iv) 6.08, 5.54 6.62 (v) 6.71 (vii) 4.99 (viii) 4.45 (xi) 5.81 (xiii) 5.61 (xv) 6.58
Gallic acid	-5.4	(i) HIS-25, LIG:H (ii) PHE-207 (iii) ALA-28 (iv) ASN-210 (v) THR-135 (vi) ARG-136 (vii) ASP-140, LIG:O (viii) GLY-139	(i) 4.49 (vii) 3.24
N-acetyl-L-Cystine	-5.2	(i) LYS-22 (ii) LYS-18, LIG:O, LIG:S (iii) HIS-25, LIG:S (iv) LYS-179 (v) ARG-183, LIG:O (vi) LEU-138 (vii) SER-14 (viii) THR-135 (ix) GLY-139 (x) PHE-207 (xi) TYR-134, LIG:O, LIG:H (xii) THR-21 LIG:H	(ii) 4.97, 6.19 (iii) 7.87 (v) 4.94 (xi) 5.77, 6.59 (xii) 3.31

A

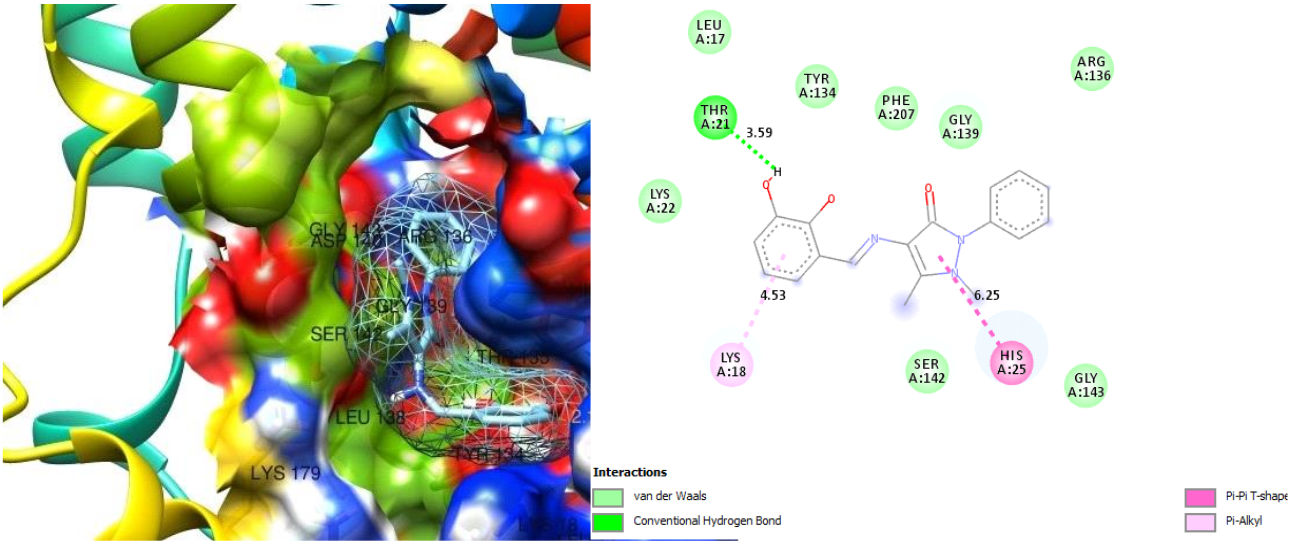

B

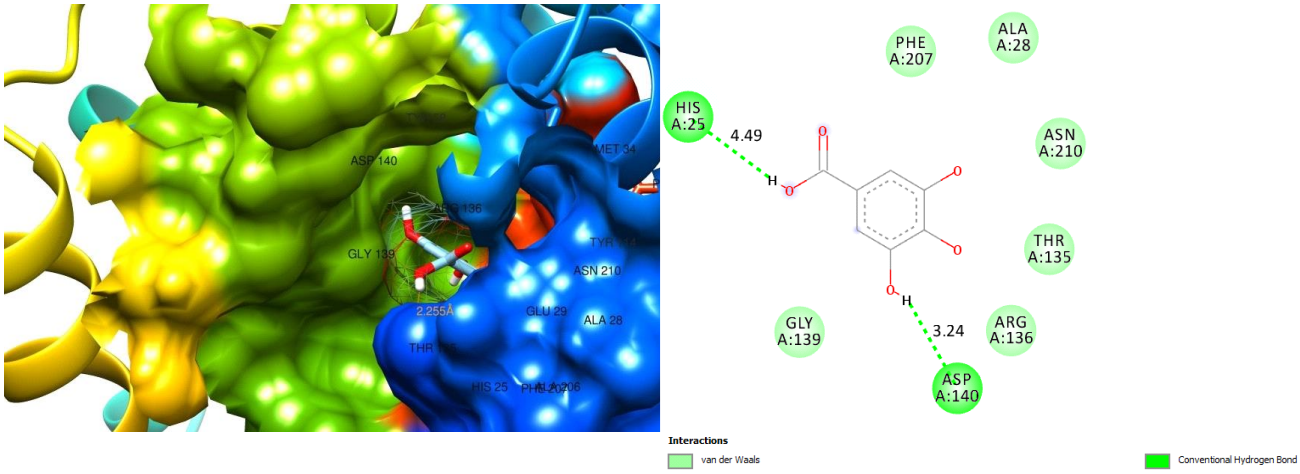

Figure 4. 9: 3D (left) and 2D (right) Views of the Molecular Interactions of Amino-Acid Residues of HO-1 (1N3U) with (A) SB11B, (B) Gallic Acid (Standard Drug)

Table 4. 18: Binding Energy, Interactions and Distance Between Ligands and Glutathione Peroxidase (3KIJ) Receptor

Ligands	ΔG kcal/mol	Interactions	Distance
SB5	-5.2	(i) ARG-84 (ii) ASP-78 (iii) SER-77 (iv) PHE-125 (v) TYR-130 (vi) CYS-79 (vii) THR-82 (viii) ASP-83, LIG:O (ix) GLN-80	(iii) 5.86 (iv) 7.06 (viii) 3.82
SB11	-5.2	(i)ARG-84 (ii) GLN-80 (iii) SER-77 (iv) THR-82 (v) TYR-130 PHE-125 (vi) ASP-78 (vii) CYS-79 (viii) ASP 83, LIG:O	(i) 5.42 (viii) 4.58, 3.69
SB11B	-5.3	(i) ASP-78 (ii) SER-77 (iii) PHE-125 (iv) TYR-130, LIG:H (v) THR-82 (vi) CYS-79 (vii) ASP-83, LIG:O (viii) GLN-80 (ix) ARG-84	(iii) 7.51 (iv) 5.86 (vii) 3.86
SB17	-5.2	(i) PHE-125 (ii) CYS-79 (iii) THR-82 (iv) GLN-80 (v) SER-77 (vi) ASP-83, LIG:O (vii) ARG-84 (viii) LEU-81 (ix) ASP-78	(vi) 3.92 (ix) 5.75
SB19	-5.1	(i) ARG-84 (ii) ASP-78 (iii) SER-77 (iv) PHE-125 (v) TYR-130 (vi) CYS-79 (vii) THR-82 (viii) GLN-80 (ix) ASP-83, LIG:O	(i) 5.15 (ix) 4.54, 3.52
Gallic acid	-4.4	(i)ASP-83, LIG: O, LIG:H (ii)THR-82 (iii)GLN-80 (iv) CYS-79, LIG:H (v)ASP-78 (vi)SER-77 (vii) PHE-125	(i) 4.07, 4.17 (iv) 3.40
N-acetyl-L-Cystine	-4.5	(i) ARG-84, LIG:H (ii) LEU-81 (iii) GLN-80, LIG:H (iv) THR-82 (v) CYS-79, LIG:O (vi) TYR-120 (vii) ASP-83, LIG:O (viii) PHE-125 (ix) SER-77 (x) ASN:85	(i) 3.1, 4.80 (iii) 3.7, 5.06 (v) 5.08 (vii) 3.56

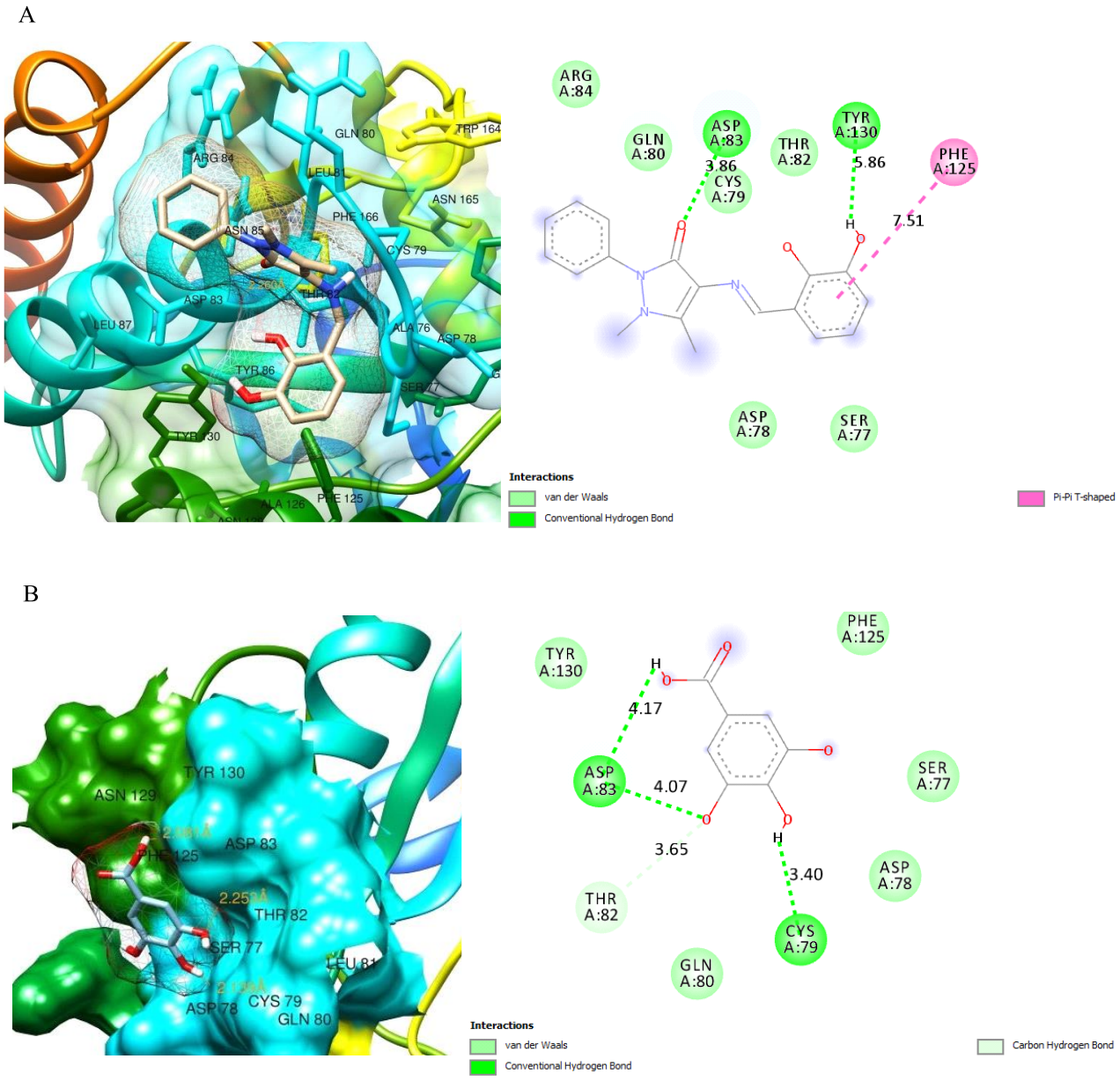

Figure 4. 10: 3D (left) and 2D (right) Views of the Molecular Interactions of amino Acid Residues of Glutathione Peroxidase (3KIJ) with (A) SB11B, (B) Gallic Acid

Molecular Docking Result for Anti-Inflammatory Active Compounds

The molecular target of many non-steroidal anti-inflammatory drugs (NSAIDs) is a member of the cyclooxygenases (COXs) family of enzymes that catalyse the rate-limiting step in the synthesis of inflammatory mediators-prostaglandins (Diederich *et al.,* 2010). Molecular interactions with critical proteins of the Cyclooxygenase-1 and cyclooxygenase-2 could modulate their activities and subsequently regulate inflammatory responses. The test compounds were docked with COX-1 and COX-2 receptors (2QGE and 1OQ5) and the results (Tables 4.19 and 4.20) indicate that the ligands can effectively inhibit the active site of both receptors.

The COX-1 receptor (2QGE) formed stable complexes with the test compounds as shown by the binding energy (Table 4.19). Compound SB11B exhibits the best binding score of -5.3 Kcal/mol. The Schiff bases had lower binding energy than the standard drug, hence they possess better anti-inflammatory activities. Conventional hydrogen bond, pi-sigma bond and Van der Waal's forces of attraction were observed in all complexes formed. They all formed alkyl bond with the active site amino acid (LYS-15). Only compound SB19 possess pi-anion bond.

The complexes formed by COX-2 receptor (1OQ5) showed lower binding energy (Table 4.20 and Figure 4.12) and more receptor-ligand interaction than the COX-1 receptor (2QGE) (Table 4.21 and Figure 4.12). The observed interactions are conventional hydrogen bond, pi-pi-T-shaped, pi-sigma, pi-alkyl, carbon hydrogen bond, unfavorable donor-donor, and Van der Waal' forces of attraction. The binding energy obtained are between -6.7 to -8.4 Kcal/mol, with compound SB11B possessing the lowest binding energy (-8.4 Kcal/mol) and hence better anti-inflammatory inhibitory activities. This agrees with the experimental results and with the result obtained for the COX-1 complexes.

From the results obtained for both receptors and from the experimental data, it is observed that compound SB11B can be a better anti-inflammatory drug than the standard if further developed.

Table 4. 19: Binding Energy, Interactions and Distance Between Ligands and (COX-1) 2QGE Receptor

Ligands	ΔG kcal/mol	Interactions	Distance
SB5	-5.2	i) MET-13 (ii) THR-106 (iii) ALA-108 (iv) LEU-17 (v) LEU-110, LIG:O (vi) ALA-109 (vii) THR-118 (viii) SER-117, LIG:H (ix) THR-119 (x) LYS-15	(iii) 6.15, 6.17 (v) 4.60, 4.56 (viii) 3.59 (x) 5.39
SB11B	-5.3	(i) ALA-109 (ii) LEU-110 (iii) ALA-108 (iv) LYS-15 (v) LEU-17 (vi) VAL-121 (vii) THR-106, LIG:O (viii) GLU-54 (ix) MET-13 (x) THR-119	(ii) 6.16 (iii) 4.94, 6.79 (iv) 5.46, (v) 5.07, 6.53 (vi) 6.76 (vii) 4.39
SB17	-5.0	(i) MET-13 (ii) THR-106 (iii) LEU-17 (iv) THR119 (v) SER-117, LIG:O, LIG:H (vi) THR-118 (vii) ALA-109 (viii) ALA-108 (ix) LEU-110 (x) LYS-15 (xi) VAL-121	(v) 4.25, 3.51 (viii) 6.16 (ix) 4.63 (x) 5.44
SB19	-4.9	(i) LEU-17 (ii) ALA-109 (iii)VAL-121 (iv) THR-106, LIG:O (v) MET-13 (vi) GLU-54 (vii) LYS-15 (viii) THR-119 (ix) ALA-108 (x) LEU-110	(i) 5.29 (iv) 4.00 (vi) 7.48 (vii) 5.62 (ix) 6.72, 5.24 (xi) 6.34
Ibuprofen	-4.9	(i) MET-13 (ii) SER-117, LIG:O (iii) THR-119, LIG:H (iv) THR-118 (v) ALA-109 (vi) LEU-110 (vii) ALA-108 (viii) LEU-17 (ix) VAL-121 (x) LYS-15, LIG:CH_3 (xi) THR- 106	(ii) 4.44 (iii) 2.75 (vii) 4.86, 6.02 (viii) 6.02 4.60, 4.63, 4.88

A

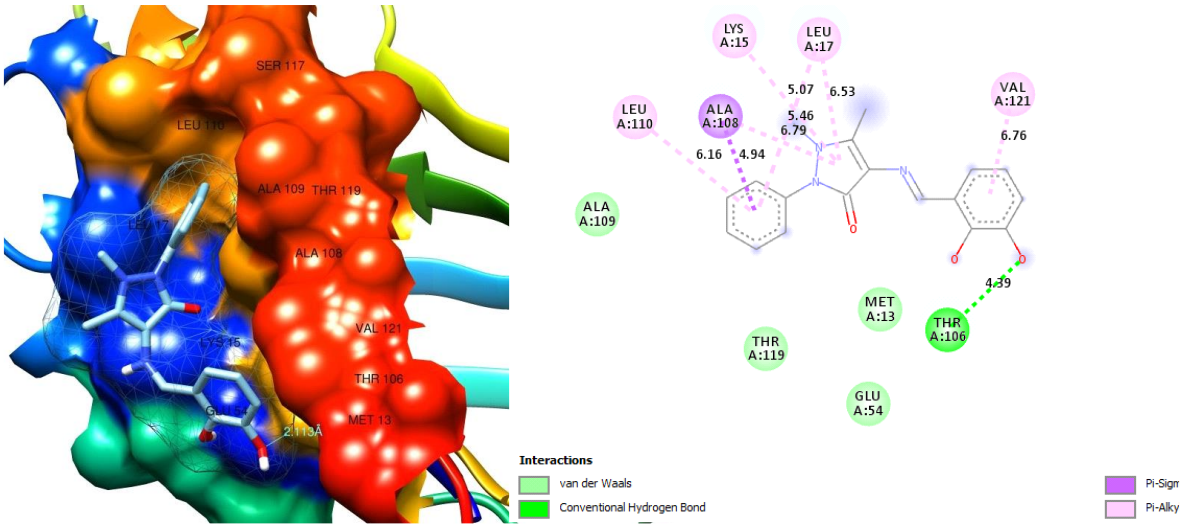

B

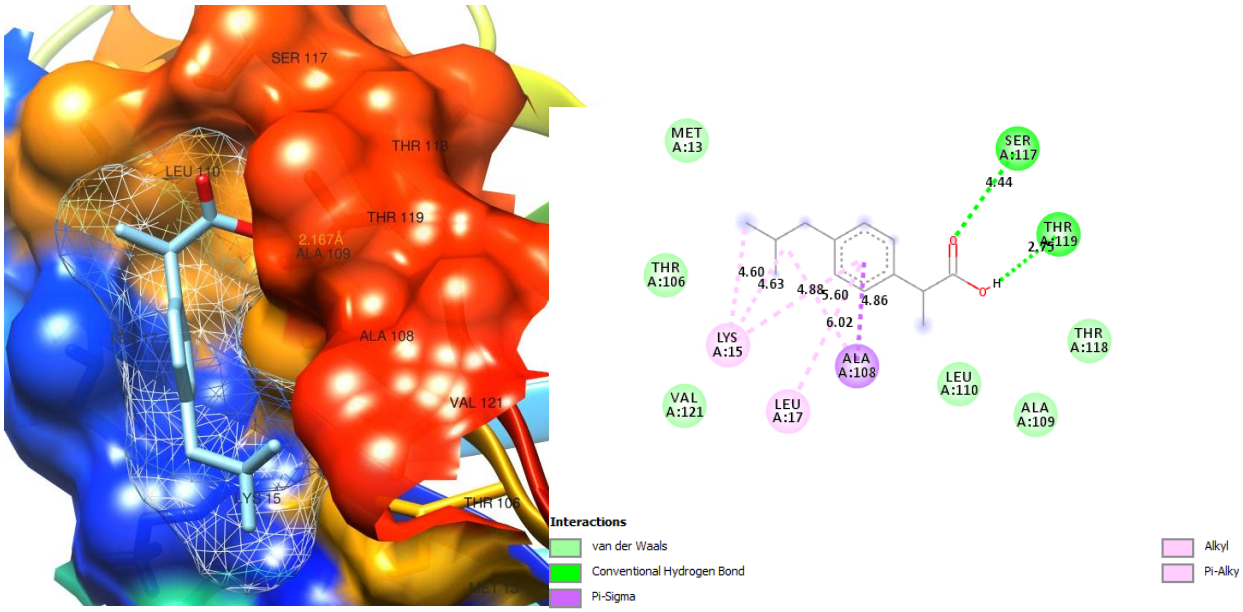

Figure 4. 11: 3D (left) and 2D (right) Views of the molecular Interactions of Amino-Acid Residues of COX-1 (2QGE) with (A) SB11B, (B) Ibuprofen

Table 4. 20: Binding Energy, Interactions and Distance Between Ligands and COX-2 (1OQ5) Receptor

Ligands	ΔG kcal/mol	Interactions	Distance
SB5	-7.6	(i) TRP-209 (ii) VAL-143 (iii) THR-199 (iv) PRO-202 (v) GLU-69, LIG:H (vi) ASN-67 (vii) LEU-60 (viii) GLN-92 (ix) ASN-62 (x) ILE-91, LIG:CH_3 (xi) PHE-131, LIG:CH_3 (xii) HIS-94, LIG:CH_3 (xiii) THR-200 (xiv) LEU-198 (xv) VAL-121	(ii) 7.43 (v) 4.17 (x) 4.32 (xi) 4.80 (xii) 5.36, 6.70 (xiv) 4.38, 6.29 (xv) 6.14
SB11B	-8.4	(i) VAL-135 (ii) PRO-202, LIG:O (iii) PRO-201 (iv) HIS-94 (v) LEU-198 (vi) VAL-207 (vii) VAL-121 (viii) SER-197 (ix) TRP-209 (x) THR-199, LIG:O (xi) HIS-199 (xii) VAL-143 (xiii) GLN-92 (xiv) HIS-96 (xv) THR-200, LIG:O (xvi) ASN-62 (xvii) PHE-131, (xviii) LEU-204	(ii) 6.58 (iii) 5.31, 5.13 (v) 4.95 (vii) 6.20 (x) 3.34, 3.66 (xii) 7.46 (xv) 3.48, 4.84
SB17	-8.2	(i) LEU-204 (ii) VAL-135 (iii) PRO-202, LIG:O (iv) PRO-201 (v) VAL-121 (vi) THR-200, LIG:O (vii) HIS-94 (viii) LEU-198 (ix) LEU-141 (x) VAL-207 (xi) VAL-143 (xii) TRP-209 (xiii) THR-199, LIG:H (xiv) HIS-96 (xv) ASN-67 (xvi) GLN-92 (xii) ASN-62 (xiii) 131	(i) 6.54 (ii) 5.23, 4.85 (v) 6.39 (vi) 4.44, 3.26 (viii) 5.39 (xiii) 2.59
SB19	-8.0	(i) GLU-69 (ii) ILE-91 (iii) VAL-121 (iv) PHE-131 (v) GLN-92, LIG:O (vi) HIS-119, LIG:CH_3 (vii) VAL-207 (viii) TRP-209, LIG:CH_3 (ix) LEU-198, LIG:CH_3 (x) VAL-143, LIG:CH_3 (xi) THR-199, LIG:O (xii) HIS-96, LIG:H (xiii) GLU-106 (xiv) HIS-94, LIG:CH_3 (xv) TRP-200 (xvi) ASN-67, LIG:CH_3 (xvii) ASN-62 (xviii) PRO-202 (xix) ALA-65	(ii) 6.34 (iv) 6.59 (v) 5.35, 5.14 (vi) 5.80 (vii) 4.59 (viii) 6.32 (ix) 4.36 (x) 5.20 (xi) 3.74 (xii) 5.52 (xiv) 4.84 (xvi) 5.99
Ibuprofen	-6.7	(i) PHE-131, LIG:CH_3 (ii) GLN-92 (iii) VAL-121 (iv) LEU-198 (v) VAL-143 (vi) HIS-94 (vii) TRP-209 (viii) HIS-119 (ix) HIS-96, LIG:H (x) THR-119 (xi) THR-200,	(i) 5.28 (iii) 6.34 (iv) 5.77 (ix) 5.30 (x) -3.19

A

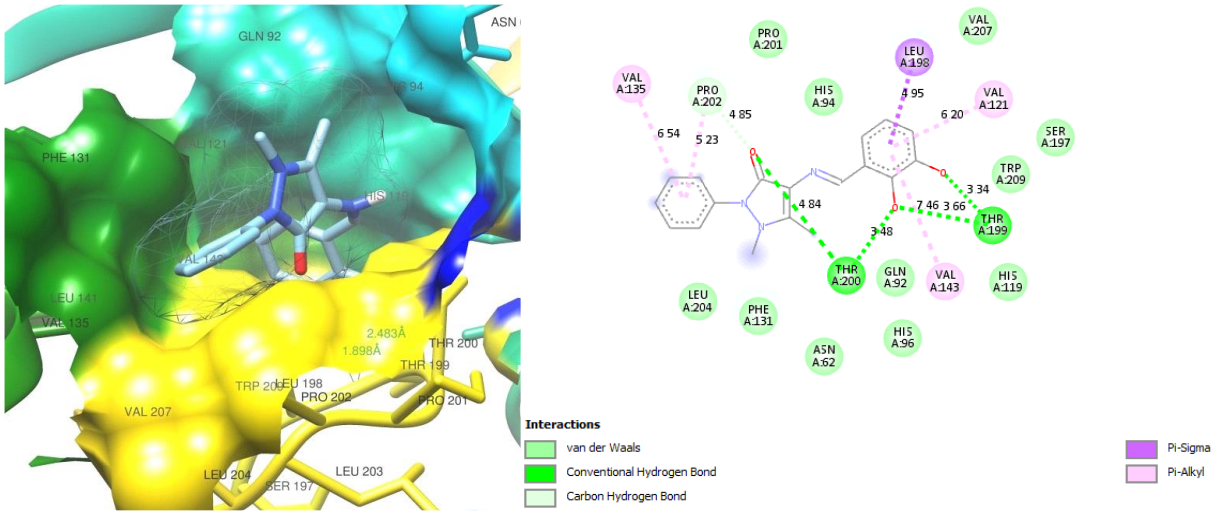

B

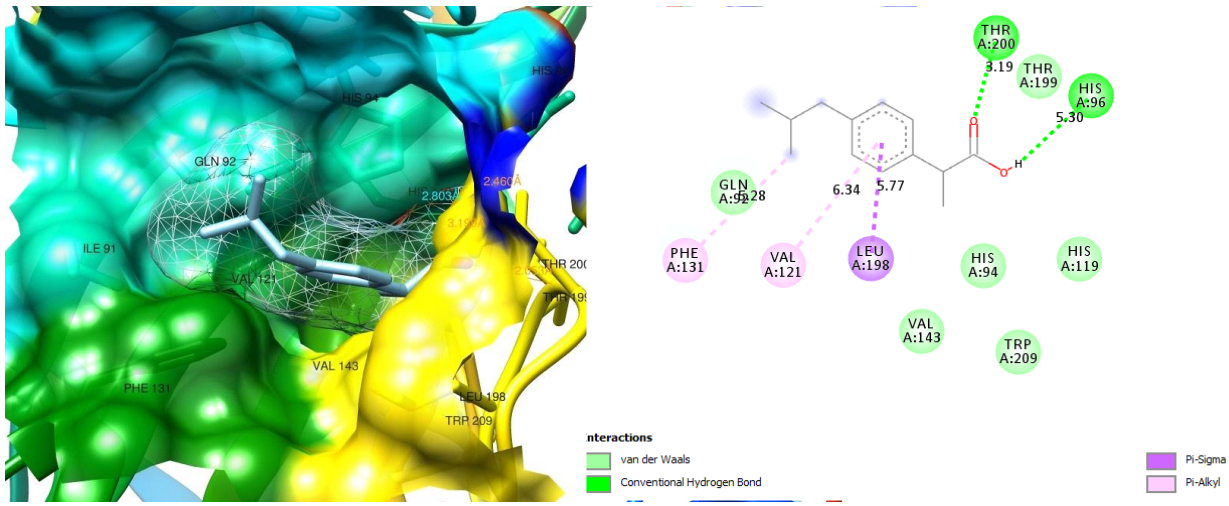

Figure 4. 12: 3D (left) and 2D (right) Views of the Molecular Interactions of Amino-Acid Residues of COX-2 (1OQ5) with (A) SB11B, (B) Ibuprofen

Molecular Docking Result for Antiglycation Active Compounds

The antiglycation activities of the studied compounds were evaluated using alpha-amylase (4GQR) and Receptor for Advanced Glycation End product (RAGE) (4LP5) as the molecular targets and the results as shown in Tables 4.21 and 4.22 revealed that the ligands could effectively inhibit the active site of both receptors.

The 4GQR receptor formed stable complexes with the test compounds as shown by the binding energy (Table 4.22 and Figure 4.13). The standard had better antiglycation activity than the investigated compounds, as shown by its lower binding energy (-7.5 Kcal/mol). This agrees with the experimental data. Among the studied compounds SB10 exhibit the best binding affinity with a binding energy of -7.4 Kcal/mol. Conventional hydrogen bond was observed in complexes formed by compound SB9B, SB10, SB11, SB19 and rutin. Carbon hydrogen bond was observed in complexes formed by compound SB5, SB10, SB19, SBF, SBG, SBI and rutin. Van der waals forces of attraction are observed in all the complexes formed. Other interactions observed are pi-anion, pi-cation, pi- stacked, pi-pi-T-shaped, pi-alkyl and alkyl. All studied compounds except SB19 showed interaction with the actual amino acid (GLU-233 and ASP-197) residue in the active site of the protein.

The complexes formed by 4LP5 receptor showed lower binding affinity (Table 4.22 and Figure 4.14) and less receptor-ligand interaction than the 4GQR. The complexes formed by the studied compound showed van der waals forces of interaction and pi-alkyl bond. They all showed hydrogen bond except compound SB5 and SBF. Other types of interaction observed in some of the complexes are carbon hydrogen bond, pi-cation, pi-sigma, pi-anion, alkyl, and halogen bond. Only compound SB19 and rutin formed vander waals forces of interaction with one of the amino acid residues (ALA-21) in the active site of the protein. The binding energy obtained are between -5.0 to -6.4 Kcal/mol, with rutin possessing the lowest binding energy (-6.4 Kcal/mol) and hence better antiglycation inhibitory activities. This agrees with the experimental result and with the result obtained for the 4GQR complexes. Among the studied compounds, SB11 had the lowest binding energy (-6.2I Kcal/mol) indicating better inhibition of the protein. From the results obtained for both receptors and from the experimental data, it is observed that compound SB10 and SB11 had good inhibitory activities when compared to the standard rutin.

Table 4. 21. Binding Energy, Interactions and Distance Between Ligands and 4GQR

Ligands	ΔG	Interactions	Distance
SB5	-7.1	(i) TYR-62 (ii) TRP-59 (iii) GLN-63 (iv) THR-163 (v) TRP-58 (vi) LYS-200, LIG:CH_3 (vii) ILE-235 (viii) HIS-201, LIG:CH_3 (ix) ASP-300, LIG:CH_3 (x) GLY-306 (xi) ARG-195 (xii) LEU-162 (xiii) GLU-233 (xiv)ALA-198 L (xv) HIS-101, LIG:CH_3	(i) 5.18 (vi) 4.24 (vii) 5.67 (viii) 5.49 (ix) 4.20 (xv) 6.20 (xvi) 5.81 (xvii) 6.34
SB9B	-7.0	(i) LYS-200 (ii) GLU-240 (iii) LEU162, LIG:O (iv) GLU 233 (v) ASP-300 (vi) PHE-256 (vii) ASN-298 (viii) ARG-195, LIG:O (ix) HIS-299, LIG:O (x) ASP-197 (xi) ALA-198 (xii) HIS-201 (xiii) ILE-235 (xiv) TYR-151	(i) 6.10 (iii) 5.42 (iv) 7.17 (v) 5.89 (viii) 6.63 (ix) 4.31 (xii) 6.22, 4.69 (xiv) 6.48
SB10	-7.4	(i) LYS-200 (ii) TRP-59 (iii) LEU-165 (iv) TYR-62 (v) TRP-58 (vi) ASP-300 (vii) ASP-197 (viii) HIS-299 (ix) ARG-195 (x) ASN-298 (xi) GLU-233, LIG:H (xii) ALA-198 (xiii) LEU-162 (xiv) HIS-201, LIG: CH_3 (xv) ILE-235 (xvi) TYR-151	(i) 6.04 (iv) 6.45 (vi) 5.89 (xi) 5.28, 7.96 (xiii) 5.57 (xiv) 5.62 (xv) 6.31, 4.55
SB11	-6.7	(i) GLU-240 (ii) LYS-200 (iii) ASP-300 LIG:H (iv) ALA-307 (v) GLU-233 (vi) PHE-256 (vii) ASN-298, LIG:O, LIG:O (viii) HIS-299 (ix) ARG-195 (x) ASP-197 (xi) ALA-198 (xii) HIS-201 (xiii) LEU-162 (xiv) ILE-235 (xv) TYR-151	(ii) 6.00 (iii) 4.21, 5.87 (v) 7.18 (vii) 5.76, 5.01 (xiii) 5.47 (xiv) 6.13, 4.64
SB19	-4.7	(i) ASN-88 (ii) THR-84, LIG:O (iii) ASN-81, LIG:O, LIG:O, (iv) ASP-77, LIG: CH_3 (v) GLU-78 (vi) ARG-80 (vii) ARG-85	(ii) 3.93 (iii) 3.13,4.24 (iv) 4.31 (vi) 5.11 (vii) 5.48
SBF	-6.6	(i)TYR-151 (ii) LYS-200 (iii) GLU240 (iv) HIS-201 (v) HIS-101 (vi) TRP-59, LIG: Cl (vii) LEU-165 (viii) TRP-58 (ix) TYR-62, LIG: Br (x) ARG-195 (xi) HIS-299, LIG: Br (xii) ASP-197 (xiii) ASP-300 (xiv) ALA-198 (xv) GLU-233 (xvi) LEU-162(xvii) GLY306 (xviii) ILE-235 (xix) ALA-307	(i) 6.78 (vi) 4.35 (ix) 4.35 (xi) 5.72 (xiv) 4.78 (xv) 6.05 (xvi) 6.94 (xviii) 6.85, 5.07
SBG	-7.2	(i) ILE-235 (ii) TYR-151 (iii) HIS-299 (iv) ALA-198 (v) TRP-58 (vi) ARG-195 (vii) ASP-197 (viii) GLU-233 (ix) LEU-162 (x) TYR-62 (xi) LEU-165 (xii) TRP-59 (xiii) THR-163 (xiv) ALA 307 (xv) ASP-300 (xvi) GLY-306 (xvii) LYS-200	(i) 4.82 (iii) 6.79 (vii) 5.20 (ix) 6.40
SBI	-4.2	(i) ALA-307 (ii) GLU-240 (iii) ARG-195 (iv) GLU-233 (v) ASP-197 (vi) LEU-165 (vii) HIS-101 (viii) ALA-198 (ix) TRP-59 (x) TYR-62 (xi) ASP-300 (xii) TRP-58 (xiii) LEU-162 (xiv) HIS-201 (xv) TYR-151 (xvi) ILE235 (xvii) LYS-200	(i) 6.53 (vii) 4.76 (viii) 4.26 (x) 4.37 (xii) 5.58 (xiii) 4.92 (xiv) 6.36 (xv) 4.70
RUTIN	-7.5	(i) ARG-80 (ii) THR-84 (iii) ASN-81, LIG:O, LIG:O (iv) ARG-85 (v) ALA-25 (vi) LEU-26 (vii) VAL-22, LIG:O (viii) GLU-78 (ix) ASP-77	(iii) 3.76, 4.68 (vii) 5.00, 6.06 (viii) 4.97 (ix) 4.12

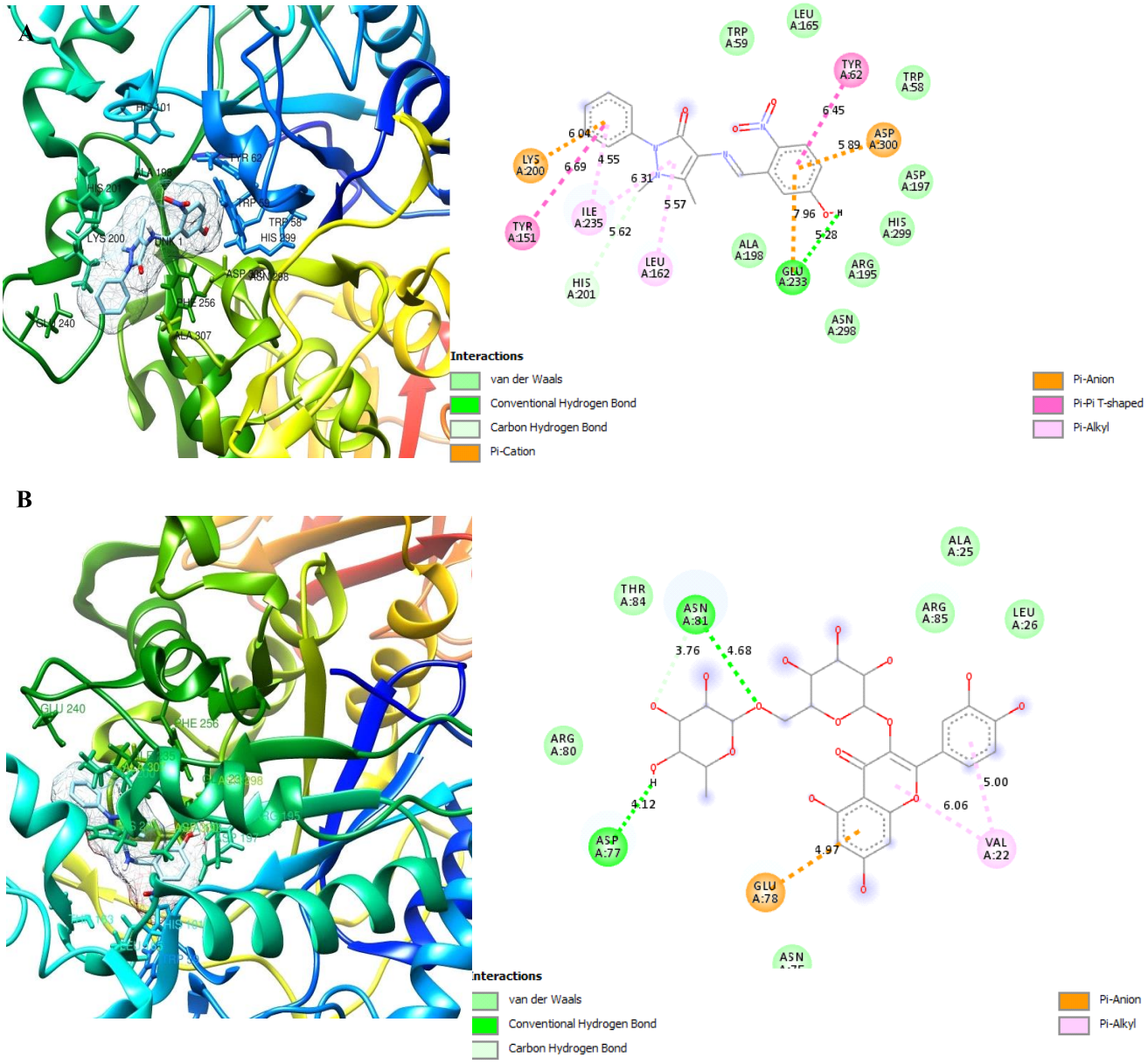

Figure 4. 13: 3D (Left) and 2D (Right) Views of The Molecular Interactions of Amino-acid Residues of α-amylase (4GQR) with (A) SB10, (B) Rutin

Table 4. 22: Binding Energy, Interactions and Distance Between Ligands and 4lp5

Ligands	ΔG	Interactions	Distance
SB5	-5.4	(i) TYR-113 (ii) LYS-37 (iii) VAL-35 (iv) LEU-34 (v) THR-27, LIG: CH_3 (vi) ARG-216 (vii) GLU-32 (viii) ARG-29 (ix) VAL-89 (x) TYR-118, LIG: CH_3 (xi) PRO-33 (xii) ALA-28, LIG: O (xiii) ILE-26	(v) 5.67 (x) 6.06 (xii) 3.72, 6.72 (xiii) 4.99
SB9B	-5.8	(i) TYR-113 (ii) LYS-37 (iii) LEU-36 (iv) LEU-34 (v) ALA-28 (vi) PRO-33, LIG:H (vii) VAL-89 (viii) ARG-29, LIG: O (ix) GLU-32 (x) TYR-118(xi) THR-27 (xii) VAL-35 (xiii) ILE-26 (xiv) GLN-24	(v) 5.06 (vi) 4.98 (viii) 6.03 (xiii) 5.15
SB10	-6.0	(i)TYR-113 (ii) LEU-36 (iii) VAL-35 (iv) ALA-28 (v) LEU34 (vi) VAL-89 (vii) GLU-32 (viii) PRO-33, LIG: H (ix) ARG-29 (x) THR-27 (xi) ILE-26 (xii) GLN-24 (xiii) LYS-37	(iv) 5.71 (v) 5.65 (viii) 4.49 (xi) 4.50 (xiii) 6.63
SB11	-6.2	(i) TYR-113 (ii) LYS-37 (iii) VAL-35 (iv) LEU-34 (v) PRO-33 (vi) GLU-32, LIG:H (vii) ARG-29 (viii) TYR-118, LIG:O (ix) THR-27 (x) ALA-28 (xi) LEU-	(vi) 3.64 (viii) 5.41 (x) (x) 6.36 (xi) 5.95 (xii) 5.08
SB19	-5.4	(i) LYS-107 (ii) GLY-40 (iii) LYS-39 (iv) GLN-24 (v) ALA-23 (vi) ASN-112, LIG:H, LIG:O (vii) SER-111 (viii) GLY-20 (ix) ALA-21 (x) MET-22 (xi) LYS-110, LIG:CH_3 (xii) THR-109	(iii) 5.20, 6.64 (vi) 3.21, 4.36 (x) 4.66 (xi) 5.27
SBF	-5.1	(i) ILE-26 (ii) THR-27 (iii) GLU-32, LIG: Cl (iv) ARG-29 (v) ALA-28, LIG: Cl (vi) LEU-34 (vii) PRO-33 (viii) VAL-35, LIG: Br (ix) GLN-24 (x) TYR-113 (xi) LYS-37	(i) ILE-26 (iii) 5.20 (v) 4.01, 6.61 (vi) 4.77 (viii) 4.48, 5.57 (xi) 5.92 (xv)
SBG	-5.2	(i) LYS-37 (ii) ILE-26 (iii) LEU-36 (iv) VAL-35 (v) LEU-34 (vi) THR-27, LIG:O (vii) PRO-33, LIG: O (viii) ALA-28 (ix) ARG-29 (x) GLU-32 (xi) TYR-118 (xii) ARG-216 (xiii) TYR-113	(ii) 5.11 (iii) 6.14 (vi) 5.88 (vii) 5.66 (x) 8.09
SBI	-5.0	(i) LYS-39 (ii) GLN-24, LIG: O (iii) ALA-28 (iv) GLU-32 (v) ARG-29 (vi) THR-27 (vii) TYR-118 (viii) ILE-26 (ix) VAL-35 (x) LEU-36 (xi) TYR113 (xii) LEU-34 (xiii) LYS-37	(ii) 5.51 (v) 5.62 (vii) 5.79 (x) 5.56 (xi) 4.59 (xii) 5.15 (xiii) 5.06
RUTIN	-6.4	(i) MET-22 (ii) GLN-24 (iii) ASN-112, LIG: O, LIG: O (iv) SER-111, LIG:O (v) ALA-121 (vi) GLY-20 (vii) LYS110 LIG:H, LIG:H (viii) THR-109, LIG:O (ix) LYS-39 LIG:H, LIG:O (x) ALA-23, LIG: H	(i) 6.32, 5.21 (iii) 3.79, 4.07 (iv) 4.36 (vii) 4.64, 4.43 (viii) 3.97 (ix) 3.84, 3.60 (x) 3.95

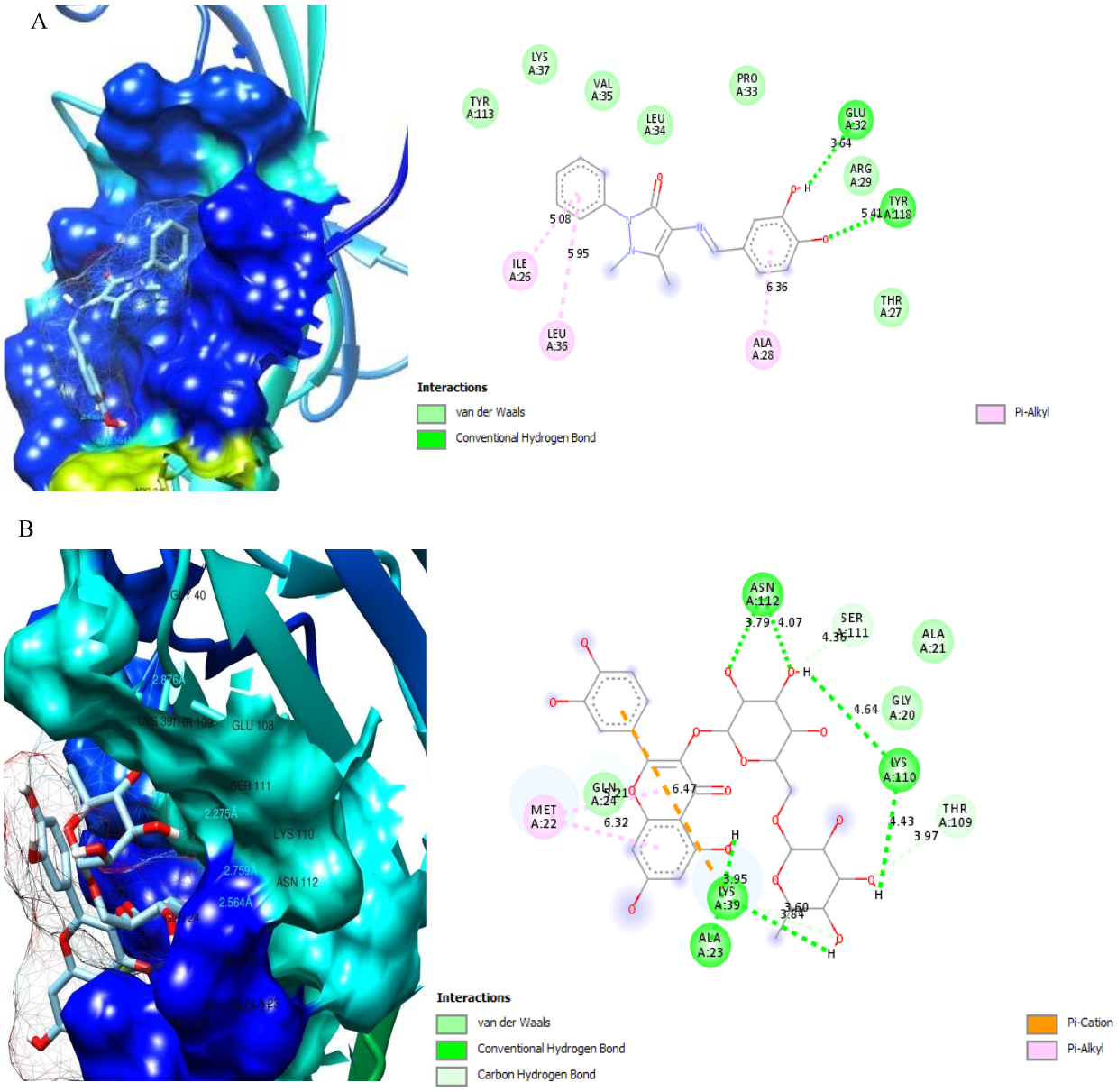

Figure 4. 14: 3D (Left) and 2D (Right) Views of The Molecular Interactions of Amino-acid Residues of RAGE (4LP5) with (A) SB11, (B) Rutin

4.6.5 ADMET Profiling of the Bioactive Compounds

Some of the investigated substances were observed to have the ability to inhibit the target proteins. To assess how well they will operate pharmacologically as medications, research on their ADMET properties is required.

In silico ADMET prediction is quick and inexpensive method to ascertain if compounds will be readily absorbed, evenly distributed to their specific site of action, favorably metabolised, and quickly removed from the body without having any negative side effects (Guan *et al.*, 2019). The prediction output for drug likeness, lipophilicity, pharmacokinetics, and toxicity profiles of the bioactive compounds are displayed on Tables 4.23, 4.24, 4. 25, and 4.26, respectively.

Drug Likeness Analysis of the Bioactive Compounds

Drug-likeness analysis is a qualitative assessment of oral bioavailability, and it is developed based on structural or physicochemical evaluation of compounds. As shown on Table 4.25, the molecular weights of the bioactive compounds are between 309 and 458, molecular weight of gallic acid, N-acetyl-L-cysteine, Ibuprofen and rutin are 170, 163, 206 and 610, respectively. The molar refractivity values ranged from 38.85 (N-acetyl-L-cysteine) to 141.38 (rutin). Number of rotatable bonds are between 1 (gallic acid) to 7 (SB-I), HBA ranged from 1-16 and HBD ranged from 0-10, The TPSA are between 37.3 (ibrubufen) and 269.43 (rutin). The higher the TPSA and molecular weight values, the less the drug candidate can penetrate and vice versa. The tested compounds have three rings and two heteroatoms (N and O) except compound SBF with four heteroatoms (N, O, Br, and Cl). Rutin has five rings and one heteroatom (O). Gallic acid and ibuprofen have one ring and one heteroatom (O). N-acetyl-L-cysteine do not have any ring but have two heteroatoms (N and O).

The test compounds and ibuprofen obeyed the Lipinski, Ghose, Veber, Egan and Muegge rules, except compound SBF which had one violation of Lipinski rule due to large number of molecular weights. Therefore, they will reflect no absorption risk if administer as oral drug. Gallic acid had one violation of Ghose and Muegge rules. N-acetyl-L-cysteine had three violations of Ghose and one violation of Muegge rules. Rutin had three violations of

Lipinski rule, four violations of Ghose rules, four violations of Muegge rules and one violation of Veber and Egan rules (Table 4.23). The test compounds demonstrated very excellent drug-likeness properties when compared side by side with the standards.

Furthermore, Lead-likeness of the test compounds was also analysised. Lead-likeness describes physicochemical boundaries defining a good lead, that is a molecular entity sui for optimization. The rule of five has been extended to the rule of three (RO3) for defining lead-like compounds (Bon *et al.,* 2022). The rule of 3states that, log P not greater than 3, MW should be less than 300 dalton, not more than 3 HBD, not more than 3 HBA and not more than 3 rotatable bonds. Interestingly, some of the test compounds had zero violation for lead likeness analysis. SB10 and SB19 had one violation each. While SB-F and SB-I had two violations each. The standard drug used as control all had one violation each (Table 4. 23). Therefore, the test compounds are suitable for further optimization.

The synthetic accessibility (SA) score is used to assess a target molecule before it is synthesised. It is a parameter used to rate the ease or difficulty of synthesizing a compound. SA Score ranges from 1 (very easy) to 10 (very difficult**)** (Swierczewska *et al.,* 2015). The studied compounds possess good SA, with SA scores ranging from 1.22 to 3.58, except rutin with higher value of 6.52 as shown on Table 4.25.

Table 4. 23: Drug-likeness Prediction Output of Test Compounds

Code	MW	RB	HBD	HBA	MR	TPSA	SA
SB5	337	4	1	4	98.47	68.75	3.14
SB9B	309	3	1	3	91.98	59.52	2.99
SB10	352	4	1	5	100.80	105.34	3.22
SB11	323	3	2	4	94.00	79.75	3.06
SB11B	323	3	2	4	94.00	79.75	3.12
SB17	339	3	3	5	96.02	99.98	3.19
SB19	357	5	5	1	104.96	77.98	3.32
SB-F	458	5	0	3	116.93	48.52	3.39
SB-G	390	6	0	5	113.04	94.34	3.46
SB-I	399	7	0	4	118.49	57.75	3.58
GAL	170	1	4	5	39.47	97.99	1.22
CYSTEINE	163	4	2	3	38.85	105.20	2.08
IBF	206	4	1	2	62.18	37.30	1.92
RUTIN	610	6	10	16	141.38	269.43	6.52

GAL: Gallic acid; Cysteine: N-acetyl-L-cysteine; IBF: Ibuprofen; MW: Molecular weight; MR: Molar refractive; HBD: Hydrogen bond donor, HBA; Hydrogen bond Acceptor, TPSA: Topological Polar Surface Area; SA: Synthetic Accessibility

Table 4. 23: Drug-Likeness Prediction Output of Test Compounds

Code	Lipinski violation	Ghose violation	Veber violation	Egan violation	Muegge violation	Lead-likeness violation
SB5	0	0	0	0	0	0
SB9B	0	0	0	0	0	0
SB10	0	0	0	0	0	1
SB11	0	0	0	0	0	0
SB11B	0	0	0	0	0	0
SB17	0	0	0	0	0	0
SB19	0	0	0	0	0	1
SB-F	1	0	0	0	0	2
SB-G	0	0	0	0	0	1
SB-I	0	0	0	0	0	2
GAL	0	1	0	0	1	1
CYSTEINE	0	3	0	0	1	1
IBF	0	0	0	0	0	1
RUTIN	3	4	1	1	4	1

GAL: Gallic acid; Cysteine: N-acetyl-L-cysteine; IBF: Ibuprofen.

Lipophilicity and Water Solubility of the Studied Compounds

The main descriptor for Lipophilicity is the partition coefficient between n-octanol and water (log Po/w). Table 4.24 displayed the lipophilicity (Log P) values, water solubility and bioavailability of the studied compounds. The partition coefficient logarithm of a drug compound in an organic or liquid phase (Log P) is termed lipophilicity. Lipophilicity and water solubility are critical physicochemical properties that determine behaviors of a drug (Zarmpi *et al.,* 2020). An orally administered drug should be sufficiently lipophilic to pass through the intestinal lining, penetrate the membrane of target cells and sufficiently hydrophilic to travel through the aqueous blood. A higher Log P value signifiles higher lipophilicity and lower water solubility (Johnson *et al.,* 2021). Log P also influences the digestion of the drug compounds in the body and increased Log P implies decreased digestion and vice-versa. The Log P values for the studied compounds ranged from -0.08 to 4.64 (Table 4.24). Gallic acid, rutin and N-acetyl-L-cysteine with very low Log P values -0.08, -1.29 and 0.21, respectively are observed to be very soluble. The synthesised compounds and Ibuprofen had Log P value of 2.24 to 4.64 and are soluble to moderately soluble. This may be due to the presence of additional polar side chains in their structure. Water solubility was estimated as the logarithm of the molar solubility in water (log S) using the SILICOS-IT predictive model. The ability of a drug compound to dissolve is impacted by its Log S value and the least value is better (Ditzinger *et al.*, 2019). The Log S values of the compounds ranged from -0.81 (very soluble (N-acetyl-L-cysteine)) to -5.89 (moderately soluble (SB-F)). This trend is perfectly in accordance with the values of Log P earlier discussed.

The bioavailability score uses the total charge, TPSA and the Lipinski filter to give a semi-quantitative estimate of the probability of the compounds to be good oral drugs (Ferreira and Andricopulo, *et al.,* 2019). The higher the TPSA and molecular weight values, the less the drug candidate can penetrate and vice versa. From the ADME results (Table 4.24), the bioavailability score of 0.55 for the synthesised compounds, 0.86 for ibuprofen, 0.56 for gallic acid and N-acetyl-L-cysteine and 0.17 for rutin were observed. The 0.55 bioavailability score signify that these compounds have about 55% probability of a minimum of 10% oral absorption in rat or human colon carcinoma (Caco-2) permeability (Xu 20 *et al.,* 2021), hence, these compounds are likely to be good as oral drugs.

Table 4. 24: Predicted Lipophilicity (Log P) Values, Water Solubility and Bioavailability of the Studied Compounds

Code	iLOGP	XLOGP3	WLOGP	MLOGP	Silicos-IT Log P	Consensus Log P	ESOL Log S	Solubility Class	BS
SB5	3.34	3.11	2.95	2.22	3.03	2.93	-4.13	M. soluble	0.55
SB9B	2.87	1.77	2.94	2.53	2.98	2.62	-3.21	soluble	0.55
SB10	2.58	2.97	3.37	1.54	1.21	2.33	-4.12	M. soluble	0.55
SB11	2.56	2.79	2.65	1.99	2.49	2.50	-3.93	Soluble	0.55
SB11B	2.65	1.41	2.65	1.99	2.49	2.24	-3.06	Soluble	0.55
SB17	3.04	2.43	2.35	1.46	2.01	2.26	-3.78	Soluble	0.55
SB19	3.53	1.71	2.96	1.91	3.09	2.64	-3.33	Soluble	0.55
SB-F	3.92	4.9	4.74	4.22	5.44	4.64	-5.89	M.soluble	0.55
SB-G	3.38	3.41	3.76	2.16	2.36	3.01	-4.45	M.soluble	0.55
SB-I	4.41	3.67	3.42	3.17	4.82	3.90	-4.59	M.soluble	0.55
GAL	2.17	0.7	0.5	0.2	-0.2	0.21	-1.64	V soluble	0.56
Cysteine	0.65	0.36	-0.49	-0.54	-0.36	-0.08	-0.81	V.soluble	0.56
IBF	2.17	3.5	3.07	3.13	3.15	3.00	-3.36	Soluble	0.86
Rutin	1.58	-0.33	-1.69	-3.89	-2.11	-1.29	-3.3	V.soluble	0.17

Pharmacokinetics Prediction of the Bioactive Compounds

Table 4.25 showed the result of pharmacokinetics prediction of the test compounds. The skin permeability (Log Kp) is a key parameter for the evaluation of molecules that might require transdermal administration (Iyer *et al.,* 2021). The more negative the log Kp, the less skin permeant is the molecule (Coderch *et al.,* 2021). Table 4.25 showed that, log Kp (cm/s) of the test compounds ranged from -10.26 (least permeant) to -5.07 (most permeant). The values indicate that the test compounds show low skin permeability. Cytochrome P450 monooxygenase is a superfamily of isoenzymes that catalyses many reactions in the phase I of drug metabolism (Sen and Stark, 2019). It has been estimated that 50-90% of drugs are substrates of five major isoforms (CYP1A2, CYP2C19, CYP2C9, CYP2D6, and CYP3A4)42 and their inhibition is a major cause of pharmacokinetics-related drug-drug interactions. The non-inhibition action against these enzymes indicates that the compounds have high probabilities of been transformed and consequently be bioavailable upon oral administration (Esteves *et al.,* 2021). All the synthesised compounds are potential inhibitor of CYP2C9 except compound SB11B. Compounds SB-F, SBG and SBI are potential inhibitor of CYP2C19. Compounds SBG, SBI and Gallic acid are potential inhibitor of CYP3A4. None of the compounds is a potential inhibitor of CYP2D6 and CYP1A2. It is worthy of note that compound SB11B, ibuprofen and N-acetyl-L-cysteine are not inhibitors to any cytochrome P450.

A well-characterised plasma membrane ATP-binding cassette transporter, known as P-glycoprotein (P-gp) is responsible for the active efflux of xenobiotics through biological membranes for the purpose of protecting the body from foreign chemicals. All synthesised compound and standard except rutin are permeability Pgp substrate. All the compounds and standard showed high probabilities of being absorbed in the gastrointestinal tract (GIT) except rutin. This suggests that these compounds have the potential to be absorbed in the GIT upon oral administration (Rathod *et al.,* 2022). The main factor for the drugs that principally focus on the brain cells is the blood brain barrier (BBB). Compounds SB5, SB9B, SB19, SB-F, SB-I and ibuprofen showed blood brain barrier (BBB) permeability, while compounds SB10, SB11, SB11B, SB17, SBG, gallic acid and N-acetyl-L-cysteine did not show BBB permeability (Table 4.25).

Table 4. 25: Pharmacokinetics Prediction Output of Test Compounds

Code	GI	BBB	P.gp	CYP 1A2	CYP2 C19	CYP 2C9	CYP2 D6	CYP 3A4	Log KP (cm/s)
SB5	High	Yes	No	No	No	Yes	No	No	-6.15
SB9B	High	Yes	No	No	No	Yes	No	No	-6.92
SB10	High	No	No	No	No	Yes	No	No	-6.34
SB11	High	No	No	No	No	Yes	No	No	-6.29
SB11B	High	No	No	No	No	No	No	No	-7.27
SB17	High	No	No	No	No	Yes	No	No	-6.64
SB19	High	Yes	No	No	No	Yes	No	No	-7.33
SB-F	High	Yes	No	No	Yes	Yes	No	No	-5.62
SB-G	High	No	No	No	Yes	Yes	No	Yes	-6.26
SB-I	High	Yes	No	No	Yes	Yes	No	Yes	-6.13
GAL	High	No	No	No	No	No	No	Yes	-6.84
Cysteine	High	No	No	No	No	No	No	No	-7.04
IBF	High	Yes	No	No	No	No	No	No	-5.07
Rutin	Low	No	Yes	No	No	No	No	No	-10.26

GAL: Gallic acid; Cysteine: N-acetyl-L-cysteine; IBF: Ibuprofen; GI: gastrointestinal; BBB: blood rain barrier and P-gp: P-glycoprotein.

Toxicity Profiles of the Bioactive Compounds

The human liver is the primary site where metabolism takes place and could be defenseless against the impacts of toxic agents and various drugs. Human hepatotoxicity (H-HT) demonstrates various kinds of harm to the liver that could cause the organ to fail (Babalola *et al.,* 2021). The mutagenicity test is used to recognise compounds that have a potential to be mutagenic causing alterations or malignant growth (Goyal *et al.,* 2022). It is important to note that the toxicity prediction of the compounds appear to be favorable, as shown in Table 4.26.

According to the ProTox II toxicity prediction all the synthesised compounds fall under the oral toxicity class 6, with LD_{50} 5600 mg/kg except SB9B (10000 mg/kg) and SBG (7500 mg/kg). Among the synthesised compounds only compounds SB10 and SB-G showed the tendency for mutagenicity. This may be due to the presence of nitro substituent in compound SB10 and SBG. Hence all synthesised compounds are relatively safe as potential therapeutic agents. Gallic acid falls under the oral toxicity class 4, with LD_{50} 2000 mg/kg. N-acetyl-L-cysteine falls under the oral toxicity class 5, with LD_{50} 4400 mg/kg and a probability of 0.76 mutagenicity. Ibuprofen falls under the oral toxicity class 3, with LD_{50} 299 mg/kg and a 0.66 probability of hepatotoxicity. While rutin falls under the oral toxicity class 5 with LD_{50} 5000 mg/kg and a probability of 0.98 immunotoxicity (Gadaleta *et al.,* 2019).

The study clearly revealed that the synthesised compound when compared with the standard drugs (control used in this study) demonstrated acceptable outcomes in the drug likeness, lipophilicity, pharmacokinetics, and toxicity prediction.

Table 4. 26. Toxicity Profiles of Test Compounds

Code	LD50 (mg/kg)	Toxicity Class	Hepato-toxicity	Carcinoge-nicity	Immune-toxicity	Mutage-nicity	Cytoto-xicity
SB5	5600	6	-	-	-	-	-
SB9B	10000	6	-	-	-	-	-
SB10	5600	6	-	-	-	+	-
SB11	5600	6	-	-	-	-	-
SB11B	5600	6	-	-	-	-	-
SB17	5600	6	-	-	-	-	-
SB19	5600	6	-	-	-	-	-
SB-F	5600	6	-	-	-	-	-
SB-G	7500	6	-	-	-	+	-
SB-I	5600	6	-	-	-	-	-
GAL	2000	4	-	-	-	-	-
Cysteine	4400	5	-	-	-	+	-
IBF	299	3	+	-	-	-	-
Rutin	5000	5	-	-	+	-	-

GAL: Gallic acid; Cysteine: N-acetyl-L-cysteine; IBF: Ibuprofen.

CHAPTER FIVE

SUMMARY, CONCLUSION AND RECOMMENDATIONS

5.1 Summary

The search for potent antioxidant, anti-inflammatory and antiglycation active compounds, fifty-eight compounds comprising of thirty Schiff bases and twenty-eight ether compounds were synthesised. There were twenty-four new compounds, while thirty-four were previously reported in literature. These compounds were of high purity and of moderate to high yields. They were synthesised majorly from 4-aminoantipyrine, different substituted benzaldehydes, benzyl halides, and propargyl bromide under varying reaction conditions. The Schiff bases obtained from 4-minontipyrine, and different substituted benzaldehydes were used as starting material for the ether compounds. All compounds were characterised with different spectroscopy techniques. All synthesised compounds were evaluated for cytotoxicity using brine shrimps lethality assay and 3T3 mouse fibroblast cell lines and none was observed to be cytotoxic. A detailed toxicity analysis was done in silico and this further confirmed that the compounds are not toxic.

The anti-inflammatory, antioxidant and antiglycation activities were evaluated *in vitro* via oxidative burst assay, DPPH, and human serum albumin solution method, respectively. Some of the compounds have not been evaluated for anti-inflammatory and antioxidant activities in literature to the best of our knowledge. None of the compounds have been reported for antiglycation activity in literature. Only the Schiff bases exhibited excellent anti-inflammatory and antioxidant activity with some of them having lower IC_{50} value (higher activity) than the standard drug. The Schiff bases and some of the ether compounds showed promising antiglycation activities.

Density Functional Theory was used to calculate molecular descriptors and it was observed that higher value of σ, ω, χ, DM, and lower value of E_{Lumo}, BG, η, μ enhanced the inhibiting strength of the compounds thereby resulting to lower binding affinity and better bioactivity. The computed geometry (bond angle, bond length and dihedral angle) and

the spectral analysis (IR, UV and 13 C NMR) gave satisfactory results which agreed with the experimental data. The QSAR models developed reproduced the experimental bioactivities of the compounds well and indicated that E_{HOMO}, E_{LUMO}, polarisability, dipole moment and PSA were critical factors for the observed biological activity. Molecular docking studies were used to complement, the experimental data, reveal the compound with the best binding affinity and the important residual interactions. Determination of the absorption, distribution, metabolism, and excretion (ADME) and toxicity properties of the compounds revealed that the synthesised compounds when compared with the standard drugs demonstrated acceptable outcomes in the druglikeness, lipophilicity, pharmacokinetics, and toxicity prediction. Therefore, the bioactive test compounds are suitable for further optimisation.

5.2. Conclusion

The results obtained showed all the synthesised compounds were not toxic, and some possessed antioxidant, anti-inflammatory and antiglycation activities. These compounds could serve as leads in the formulation of drugs for the management of inflammation, oxidative stress, and aging. It could be concluded that, the position and nature of the substituent attached to the compound can greatly affect its biological activities. It was observed that compounds which possesses -OCH_3 and OH attached to them had better biological activities. Therefore, compounds possessing these substituents should be explored more in future for the investigation of antioxidant, anti-inflammatory and antiglycation activities.

5.3 Recommendations

The efficacy of these compounds should be further determined in vivo since in vitro study may not be able to estimate the value of in vivo activity in a biological system due to some factors such as differences in bioavailability, aabsorption, and metabolism. Further, more extensive QSAR studies should be done in other to predict other similar compounds with more efficient antioxidant, anti- inflammatory and antiglycation activities. More studies should be carried out, to ultilise the bioactive compounds as efficient NSAIDs, antioxidant and antiglycating agent.

5.4 Contributions to knowledge

Twenty- four new compounds which consist of two Schiff bases and twenty-two ether compounds are added to the library of chemical compounds. This is the first report on antiglycation activity for all the synthesised compounds to the best of our knowledge. Most of the synthesised compounds are evaluated for anti-inflammatory and antioxidant property for the first time. The QSAR, Molecular docking and ADMET screening methods employed in this study have provided more insight on the inhibiting properties of the synthesised compounds.

analysis (IR, UV and 13 C NMR) gave satisfactory results which agreed with the experimental data. The QSAR models developed reproduced the experimental bioactivities of the compounds well and indicated that E_{HOMO}, E_{LUMO}, polarisability, dipole moment and PSA were critical factors for the observed biological activity. Molecular docking studies were used to complement, the experimental data, reveal the compound with the best binding affinity and the important residual interactions. Determination of the absorption, distribution, metabolism, and excretion (ADME) and toxicity properties of the compounds revealed that the synthesised compounds when compared with the standard drugs demonstrated acceptable outcomes in the druglikeness, lipophilicity, pharmacokinetics, and toxicity prediction. Therefore, the bioactive test compounds are suitable for further optimisation.

REFERENCES

Abbas, G., Alharrasi, A. S., Hussain, H., Sattar, S. A. and Choudhary, M. I. 2017. Identification of natural products and their promising inhibitors of protein glycation with non-toxic nature against mouse fibroblast 3T3 cells. *International Journal of Phytomedicine* 8: 533-539.

Abdelgawad, M. A., Labib, M. B., Ali, W. A., Kamel, G., Azouz, A. A. and EL-Shaymaa, E. N. 2018. Design, synthesis, analgesic, anti-inflammatory activity of novel pyrazolones possessing aminosulfonyl pharmacophore as inhibitors of COX-2/5-LOX enzymes. Histopathological and docking studies. *Bioorganic chemistry* 78: 103-114.

Adebesin, T. T., Oladosu, I. A., Obi-Egbedi, N. O and Odika, T. I. 2016. Demetallation, antimicrobial and computational studies of methoxy-1,3-diene substituted products from addition of natural products to tricarbonyl-2-methoxycylohexadienyl) irontetrafluoborate. *Journal of organometallic Chemistry* 819: 87-94.

Adejoro, I. A, Orodepo O. G, Adeboye, O. O and Akhigbe, F. U. 2017. Theoretical Study of the Properties of Isatin (1Hindole-2,3-dione) Based Alternating Donor-acceptor Type Conjugated Oligomers. *Physical Science International Journal* 15.4: 1-16.

Agamah, F. E., Gaston, K., Hassan, M. R., Bope, C. D., Thomford, N. E., Ghansah, A. and Chimusa, E. R. 2020. Computational/in silico methods in drug target and lead prediction. *Briefings in Bioinformatics* 21.5: 1663-1675.

Aguilar-Llanos, E., Carrera-Pacheco, S. E., González-Pastor, R., Zuniga-Miranda, J., Rodriguez-Polit, C., Romero-Benavides, J. C. and Heredia-Moya, J. 2022. Synthesis and Evaluation of Biological Activities of Schiff Base Derivatives of 4-Aminoantipyrine and Cinnamaldehydes. *Chemistry Proceedings* 12.1:43-57.

Akbari, B., Baghaei-Yazdi, N., Bahmaie, M. and Abhari, F. M. 2022. The role of plant-derived natural antioxidants in reduction of oxidative stress. *Bioctors* 48.3: 611-633.

Aktan, E. and Uyar, T. 2017. Hetarylazopyrazolone Dyes Based on Benzothiazole and Benzimidazole Ring Systems: Synthesis, Spectroscopic Investigation, and Computational Study. *Journal of Chemistry* 2017:1-10.

Alam, M. S., Choi, J. and Lee, D. 2012. Synthesis of novel Schiff base analogues of 4-amino-1,5-dimethyl-2-phenylpyrazol-3-one and their evaluation for antioxidant and anti-inflammatory activity. *Bioorganic and Medicinal Chemistry* 20: 4103-4108.

Alam, M. S., Lee, K. and Beri, M. S. 2014. Antibacterial and Cytotoxicity Activities of Schiff Base Analogues of 4-Aminoantipyrine. *Journal of Korean Society of Applied Biology, and Chemistry* 57.5: 613-619.

Alam, M. S. and Dong-Ung, L. 2016. Physicochemical Analyses of a Bioactive 4-Amino antipyrine Analogue Synthesis, Crystal Structure, Solid State Interactions, Antibacterial, Conformational and Docking Studies. *EXCLI Journal* 15: 614-629.

Ali, P., Ramakanth, P. and Meshram, J. 2010. Exploring microwave synthesis for co-ordination: synthesis, spectral characterisation, and comparative study of transition metal complexes with binuclear core derived from 4-amino-2,3-dimethyl-1-phenyl-3-pyrazolin-5-one. *Journal of Coordination Chemistry* 63.2: 323-329.

Aljeldah. M M. 2022 Antimicrobial Resistance and Its Spread Is a Global Threat. *Antibiotics*. 11.8:1082.

Al-Resayes, S. I., Warad, I., Alnuri, M. A., Choudhary, M. I., Wahab, A. and Raheed, S. 2014. Heterocyclic Schiff's bases as novel and new antiglycation agents. US20140221429.

Apotrosoaei, M., Vasincu, I., Tuchiluş, C., Lupascu, F., Constantin, S., Lupaşcu, D. and Profire, L. 2013. New Hydrazones with Pyrazolone Structure: Synthesis, Characterisation and Biological Evaluation. *Revista medico-chirurgicala a Societatii de Medici si Naturalisti din Iasi* 117.2: 538-544.

Arif, A., Alameri, A. A., Tariq, U. B., Ansari, S. A., Sakr, H. I., Qasim, M.T., Aljoborae, F. M., Ramírez-Coronel, A. A., Jabbar, S. H., Gabr, G. A., Mirzaei, R. and Karampoor, S. 2023. The functions and molecular mechanisms of Tribbles homolog 3 (TRIB3)

implicated in the pathophysiology of cancer. *International Immunopharmacology* 114: 1567-5769.

Arshad, N., Ahmad, M., Ashraf, M. Z. and Nadeem, H. 2014. Spectroscopic, electrochemical DNA binding and *in-vivo* anti-inflammatory studies on newly synthesised Schiff bases of 4-aminophenazone. *Journal of Photochemistry and Photobiology Biology* 5.138: 331-346.

Asiri, A. M. and Khan, S. A. 2010. Synthesis and Anti-Bacterial Activities of Some Novel Schiff Bases Derived from Aminophenazone. *Molecules* 15: 6850-6858.

Athira, L. S., Lakshmi, C. S. N., Balachandran, S., Dhas D. A. and Joe, H. I. 2017. Synthesis, Characterisation, Crystal Structure and theoretical Studies of 4-[(*E*)-(3-Chloro-4-Hydroxyphenyl)Diazenyl]-1,5-Dimethyl-2-Phenyl-1,2-dihydro-3*h*-Pyrazol-3-One. *Journal of Molecular Structure* 1148:185-195.

Babalola, B. A, Adetobi, T. E, Akinsuyi, O. S, Adebisi, O. and Folajimi, E. O. 2021. Computational Study of the Therapeutic Potential of Novel Heterocyclic Derivatives against SARS-CoV-2. *COVID 2021* 1: 757-774.

Baker, R. E., Mahmud, A. S., Miller, I. F., Rajeev, M., Rasambainarivo, F., Rice, B. L., Takahashi, S., Tatem, A. J., Wagner, C. E., Wang, L., Wesolowski, A. and Metcalf, C. J. 2022. Infectious disease in an era of global change. Natural Review Microbiology 20: 193-205.

Bally, M., Dendukuri, N., Rich, B., Nadeau, L., Helin-Salmivaara, A., Garbe, E. and Brophy, J. M. 2017. Risk of acute myocardial infarction with NSAIDs in real world use: bayesian meta-analysis of individual patient data. *Clinical Research Education* 357: 1909.

Baluja, S. and Chanda S. 2016. Synthesis, characterization, and antibacterial screening of some Schiff bases derived from pyrazole and 4-amino antipyrine. *Revista Colombiana de Ciencias Químico-Farmacéuticas* 45.2: 201-218.

Banti, C. N. and Hadjikakou, S. K. 2021. Evaluation of Toxicity with Brine Shrimp Assay. *Bio-protocol* 11.2: 3895-3910.

Becke, A. D. 1993. Density-functional thermochemistry. III. The role of exact exchange. *Journal of Chemical Physics* 98: 5648-5652.

Belfield, S., Firman, J. W., Enoch, S. J., Madden, J. C., Tollefsen, K. E., Mark, T. D., Cronin, A. 2023. A. review of quantitative structure-activity relationship modelling approaches to predict the toxicity of mixtures. *Computational Toxicology* 25: 2468-1113.

Bello, O. S., Alagbada, T. C., Alao, O. C. and Olatunde, A. M. 2020. Sequestering a non-steroidal anti-infammatory drug using modifed orange peels. *Applied Water Science* 10:172.

Bensaber, S. M., Allafe, H. A., Ermeli, N. B., Mohamed, S. B., Zetrini, A. A., Alsabri, S. G., Erhuma, M., Hermann, A., Jaeda, M. I. and Gbaj. A. M. 2014. Chemical synthesis, molecular modelling, and evaluation of anticancer activity of some pyrazol-3-one Schiff base derivatives. *Medicinal Chemistry Research* 23:5120-5134.

Bhatti, J. S., Sehrawat, A., Mishra, J., Sidhu, I. S., Navik, U., Khullar, N., Kumar, S., Bhatti G. K, Reddy, P. H. 2022. Oxidative stress in the pathophysiology of type 2 diabetes and related complications: Current therapeutics strategies and future perspectives. *Free Radical Biology and Medicine* 184: 114-134.

Bindu, S., Mazumder, S. and Bandyopadhyay, U. 2020. Non-steroidal anti-inflammatory drugs (NSAIDs) and organ damage: A current perspective, *Biochemical Pharmacology* 180: 114-122.

Bisht, N. and Singh, B. K. 2018. Role of Computer Aided Drug Design in Drug Development and Drug Discovery. *International Journal of Pharmaceutical Sciences and Research* 9.4: 1405-1415.

Bohm, H. J. 1992. The computer program Ludi: a new method for the *De Novo* design of enzyme inhibitors. *Journal of Computational Aided Molecular Design* 6: 61-78.

Bon, M., Bilsland, A., Bower, J. and McAulay, K. 2022. Fragment-based drug discovery-the importance of high-quality molecule libraries. *Molecular Oncology* 16.21: 3761-3777.

Borase, J. N., Mahale, R. G. and Rajput, S. S. 2021. Synthesis and Biological Evaluation of Heterocyclic Schiff Bases: A Review. *International Journal of Pharmaceutical Research* 13.2: 188-202.

Cakmak, R., Basaran, E., Boga, M., Erdogan, O., Ercan, C. and Cevik. O. 2022. Schiff Base Derivatives of 4-Aminoantipyrine as Promising Molecules: Synthesis, Structural Characterization, and Biological Activities. *Russian Journal of Bioorganic Chemistry* 48: 334-344.

Cavasotto, C. N. and Scardino, V. 2022. Machine Learning Toxicity Prediction: Latest Advances by Toxicity End Point. *ACS Omega* 7.51: 47536-47546.

Chavan, R. R. and Hosamani, K. M. 2018. Microwave-assisted synthesis, computational studies and antibacterial/anti-inflammatory activities of compounds based on coumarin-pyrazole hybrid. *Royal Society open science* 5:172435.

Chen, Y., Zhang, Y., Wang, H. and Weinan, E. 2020. Ground State Energy Functional with Hartree-Fock Efficiency and Chemical Accuracy. *The Journal of Physical Chemistry* 124.35: 7155-7165.

Chiari, L. P. A., Silva, A. P., Oliveira, A. A., Lipinski, C. L., Honorio, K. M., Alberico, B. F. and Silva, D. 2021. Drug design of new sigma-1 antagonists against neuropathic pain: A QSAR study using partial least squares and artificial neural networks. *Journal of Molecular Structure* 1223: 0022-0040.

Choi, G., Holzapfel, W. H. and Todorov, S. D. 2023. Diversity of the bacteriocins, their classification and potential applications in combat of antibiotic resistant and clinically relevant pathogens. *Critical Reviews in Microbiology* 49.5: 578-597.

Coderch, L., Collini, I., Carrer, V., Barba, C. and Alonso, C. 2021. Assessment of Finite and Infinite Dose In Vitro Experiments in Transdermal Drug Delivery. *Pharmaceutics* 13.3:364.

Costa, J. S., Ramos, R. S., Costa, K. L. S., Brasil, D. S. B., Silva, C. H. T., Ferreira, E. F. B., Borges, R. S., Campos, J. M., Macedo, W. J., and Santos, C. B. R. 2018. An In

Silico Study of the Antioxidant Ability for Two Caffeine Analogs Using Molecular Docking and Quantum Chemical Methods. *Molecules* 23: 2801-2818.

Cunha, E. L., Santos, C. F., Braga, F. S., Costa, J. S., Silva, R. C., Favacho, H. A. S., Hage-Melim, L. I. S., Carvalho, J. C. T., Silva, C. H. T. P and Santos, C. B. R. 2015. Computational investigation of antifungal compounds using molecular modeling and prediction of ADME/Tox properties. *Journal of Computational Theoretical Nanoscience* 12: 3682-3691.

Czub, N., Pacławski, A., Szlęk, J. and Mendyk, A. 2022. Do AutoML-Based QSAR Models Fulfill OECD Principles for Regulatory Assessment A 5-HT1A Receptor Case. *Pharmaceutics* 14.7:1415-1423.

Daina, A., Michielin, O. and Zoete, V. 2017. SwissADME: a free web tool to evaluate pharmacokinetics, drug-likeness and medicinal chemistry friendliness of small molecules. *Scientific Report* 7: 42717.

Defrawy, A. M., Abdallah, M. and Al-Fahemi, J. H. 2019. Electrochemical and theoretical investigation for some pyrazolone derivatives as inhibitors for the corrosion of C-steel in 0.5 M hydrochloric acid. *Journal of Molecular Liquids* 288: 110994-11117.

Ditzinger, F., Price, D. J., Ilie, A., Kohl, N. J., Jankovic, S., Tsakiridou, G., Aleandri, S., Kalantzi, L., Holm, R., Nair, A., Saal, C., Griffin, B. and Kuentz, M. 2019. Lipophilicity and hydrophobicity considerations in bio-enabling oral formulations approaches. *Journal of Pharmacy and Pharmacology* 71.4: 464-482.

Ebosie, N. P., Oonwu, M., Ogwuegbu C., Onyedika, G. and Onwumere, F. C. 2021. Biological and analytical applications of Schiff base metal complexes derived from salicylidene-4-aminoantipyrine and its derivatives. *Journal of the Iranian Chemical Society* 18: 3145-3175.

Egan, W. J., Merz, K. M. and Baldwin, J. J. 2000. Prediction of drug absorption using multivariate statistics. *Journal of Medicinal Chemistry* 43.21: 3867-77.

Erazua, E. A. and Adeleke, B. B. 2019a. DFT and Molecular Docking Investigation of Potential Anticancer Properties of Some Flavonoids. *Journal of Pure and Applied Chemistry Research* 8.3: 225-231.

Erazua, E. A. and Adeleke, B. B. 2019b. A Computational Study of Quinoline Derivatives as Corrosion Inhibitors for Mild Steel in Acidic Medium. *Journal of Applied Science and Environmental Management* 23.10: 1819-1824.

Erazua, E. A., Oyebamiji, A. K. and Adeleke, B. B. 2019. DFT-QSAR and Molecular Docking Studies on 1,2,3-Triazole-Dithiocarbamate Hybrids as Potential Anticancer Agents. *Physical Science International Journal* 20.4: 1-10.

Erazua, E. A., Oyebamiji, A. K., Akintelu, S. A., Adewole, A. D., Adelakun, A. and Adeleke, B. B. 2023. Quantitative Structure-Activity relationship, Molecular Docking and ADMET Screening of Tetrahydroquinoline Derivatives as Anti-Small Cell Lung Cancer Agents. *Eclética Química* 48.1: 55-71.

Esteves, F., Rueff, J. and Kranendonk, M. 2021. The Central Role of Cytochrome P450 in Xenobiotic Metabolism-A Brief Review on a Fascinating Enzyme Family. *Journal of Xenobiotics* 11.3: 94-114.

Fan, J., Fu, A. and Zhang, L. 2019. Progress in molecular docking. *Quantitative Biology* 7.2: 83-89.

Federica, A. and Basile, F. E. 2022. Chemistry without the Born–Oppenheimer approximation. *Philosophical Transactions of the Royal Society* A 32: 1-11.

Ferreira, L. G. and Andricopulo, A. D. 2019. ADMET modeling approaches in drug discovery. *Drug Discovery Today* 24.5:1157-1165.

Foong, W. D and McAlindon, T. M. A. 2021. Non-steroidal anti-inflammatory drugs and the gastrointestinal tract. *Clinical Medicine Journal* 21 .2: 131-134.

Forman, H. J. and Zhang, H. 2021.Targeting oxidative stress in disease: promise and limitations of antioxidant therapy. *Nature Reviews Drug Discovery* 20.8: 689-709.

Frieri, M., Kumar, K. and Boutin, A. 2017. Antibiotic resistance. *Journal of Infection and Public Health* 10.4: 369-378.

Fu, L., Yang, Z., Lu, A., Chen, X., Liu, S., Hou, T., Dong, A. and Cao, D. 2021. QSAR-assisted-MMPA to expand chemical transformation space for lead optimization. *Briefings in Bioinformatics* 22.5: 374-382.

Gadaleta, D., Vukovic, K., Toma, C., Lavado, G. J., Karmaus, A. L., Mansouri, K., Kleinstreuer, N. C., Benfenati, E. and Roncaglioni, A. 2019. SAR and QSAR modeling of a large collection of LD50 rat acute oral toxicity data. *Journal of Cheminformatics* 11.58: 1-16.

Garrick, R., Natan, A., Gould, T. and Kronik, T. 2020. Exact Generalized Kohn-Sham Theory for Hybrid Functionals. *Physical Review* 10: 021-034.

Ghorab, M. M., El-Gazzar, M. G and Alsaid, M. S. 2014. Synthesis, Characterisation and Anti-Breast Cancer Activity of New 4-Aminoantipyrine-Based Heterocycles. *International Journal of Molecular Science* 15: 539-7553.

Ghose, A. K., Viswanadhan, V. N. and Wendoloski, J. J. 1999. A knowledge-based approach in designing combinatorial or medicinal chemistry libraries for drug discovery. A qualitative and quantitative characterization of known drug databases. *Journal of Combinatorial Chemistry* 1.1: 55-68.

Goletto, L., Giovannini, T., Folkestad, S. D. and Koch, H. 2021. Combining multilevel Hartree-Fock and multilevel coupled cluster approaches with molecular mechanics: a study of electronic excitations in solutions. *Physical Chemistry Chemical Physics* 23: 4413-4425.

Goyal, K., Goel, H., Baranwal, P., Dixit, A., Khan, F., Jha, N. K., Kesari, K. K., Pandey, P., Pandey., Benjamin, M., Maurya, A., Yadav, V., Sinh, R. S., Tanwar, P., Upadhyay, T. K., and Mittan, S. 2022. Unravelling the molecular mechanism of mutagenic factors impacting human health. *Environmental Science and Pollution Research* 29:1993-62013.

Grisoni, F., Ballabio, D., Todeschini, R. and Consonni, V. 2018. Molecular descriptors for structure–activity applications: A hands-on approach. *Computational toxicology*. Nicolotti, O. Ed. Humana Press 1800: 3-53.

Grover, G., Nath, R., Bhatia, R. and Akhtar, M. J. 2020. Synthetic and therapeutic perspectives of nitrogen containing heterocycles as anti-convulsants. *Bioorganic and Medicinal Chemistry* 34: 115-125.

Guan, L., Yang, H., Cai, Y., Sun, L., Di, P., Li, W., Liu, J. and Tang, Y. 2019. ADMET-score a comprehensive scoring function for evaluation of chemical drug-likeness. *Medicinal Chemistry Communication* 10: 148-157.

Gupta, M., Lee, H. J., Barden, C. J. and Weaver, D. F. 2019. The Blood–Brain Barrier (BBB) Score. *Journal of Medicinal Chemistry* 62.21: 9824-9836.

Gupta, P., Gupta, J. K. and Halve, A. K. 2017. Synthesis and Biological Significance of Pyrazolones. *International Journal of Pharmaceutical Sciences and Research* 12.8: 2291-2310.

Herbert, J. M. 2023. Density-functional theory for electronic excited states. *Theoretical and Computational Photochemistry*. Eds. C. Garcia-Iriepa, and M. Marazzi. Elsevier. Chapter 3: 69-118.

Ho, S. and Lai-Shan. 2022. Nonsteroidal anti-inflammatory drugs and cardiovascular disease risk in spondyloarthritis-spectrum diseases. *Current Opinion in Rheumatology* 34.6: 203-208.

Homayun, B., Lin, X., Choi, H. J. 2019. Challenges and Recent Progress in Oral Drug Delivery Systems for Biopharmaceuticals. *Pharmaceutics* 11.3: 129-144.

Ibrahim, M. T., Uzairu, A., Uba, S. and Shallangwa, G. A. 2020. Quantitative structure-activity relationship, molecular docking, drug-likeness, and pharmacokinetic studies of some non-small cell lung cancer therapeutic agents. Beni-Suef *University Journal for Basic and Applied Science* 9: 49-65.

Ireland, R. and McKemmish, R. K. 2023. On the specialization of Gaussian basis sets for core-dependent properties. *Journal of Chemical Physics* 159: 064102-064129.

Irfan, M. 2020. Selective cyclooxygenase-2 inhibitors: A review of recent chemical scaffolds with promising anti-inflammatory and COX-2 inhibitory activities. *Medicinal Chemistry Research* 84: 1-22.

Isert, C., Atz, K. and Schneider, G. 2023. Structure-based drug design with geometric deep learning. *Current Opinion in Structural Biology* 79: 102-118.

Ivanova, L. and Karelson, M. 2022. The Impact of Software Used and the Type of Target Protein on Molecular Docking Accuracy. *Molecules* 27.24: 9041-9054.

Iyer, A., Jyothi, V. G., Agrawal, A., Khatri, D. K., Srivastava, S., Singh, S. B. and Madan, J. 2021. Does skin permeation kinetics influence efficacy of topical dermal drug delivery system: Assessment, prediction, utilization, and integration of chitosan biomacromolecule for augmenting topical dermal drug delivery in skin. *Journal of Advanced Pharmaceutical Technology and Research* 12.4: 345-355.

Jahnavi, K., Reddy, P., Vasudha, B. and Narender, B. 2019. Non-steroidal anti-inflammatory drugs: an overview. *Journal of Drug Delivery and Therapeutics* 9.1: 442-448.

Jia, P., Pei, J., Wang, G., Pan, X., Zhu, Y., Wu, Y. and Ouyang, L. 2022. The roles of computer-aided drug synthesis in drug development. *Green Synthesis and Catalysis* 3.1: 11-24.

Kabir, M. and Uzzaman, M. 2022. A review on biological and medicinal impact of heterocyclic compounds. *Results in Chemistry* 4: 100606-100617.

Kang, Q. and Yang, C. 2020. Oxidative stress, and diabetic retinopathy. Molecular mechanisms, pathogenetic role and therapeutic implications. *Redox Biology* 37: 2213-2317.

Karatas, M. O., Tekin, S., Alici, B. and Sandal, S. 2019. Cytotoxic effects of coumarin substituted benzimidazolium salts against human prostate and ovarian cancer cells. *The Journal of Chemical Sciences* 131.69;1647-1659.

Kasare, M. S., Dhavan, P. P., Shaikh, A. H., Jadhav, B. L. and Pawar, D. L, 2022. Novel Schiff base scaffolds derived from 4-aminoantipyrine and 2-hydroxy-3-methoxy-5-(phenyldiazenyl) benzaldehyde: Synthesis, antibacterial, antioxidant and anti-inflammatory. *Journal of Molecular Recognit*ion 35.9: 2976-2985.

Kashyap, S., Kumar, S., Ramasamy, K., Lim., S. M., Ali Shah, S. A., Om, H. and Narasimhan, B. 2018. Synthesis, biological evaluation, and corrosion inhibition studies of transition metal complexes of Schiff base. *Chemistry Central Journal* 12:117.

Khalid, M., Petroianu, G. and Adem, A. 2022. Advanced Glycation End Products and Diabetes Mellitus: Mechanisms and Perspectives. *Biomolecules* 12.4: 542-557.

Khan, K. M., Ali, M., Taha, M., Rasheed, S., Perveen, S. and Choudhary. 2009. Synthesis of bis-Schiff bases of isatins and their antiglycation activity. *Bioorganic and Medicinal Chemistry* 17: 7795-7801.

Kovacs, D., Kiraly, P and Toth, G. 2021. Sample-size dependence of validation parameters in linear regression models and in QSAR. *SAR and QSAR in Environmental Research* 32.4: 247-268.

Kshatriya, R., Shelke, P., Mali, S., Yashwantrao, G., Pratap, A. and Saha, S. 2021. Synthesis and evaluation of anticancer activity of pyrazolone appended triarylmethanes (TRAMs). *ChemistrySelect* 6: 6230-6239.

Kurdekar, G. S., Sathisha, M. P., Budagumpi, S., Kulkarni, N. V., Revankar, V. K. and Suresh, D. K. 2012. 4-Aminoantipyrine based Schiff base transition metal complexes as potent anticonvulsant agents. *Medicinal Chemistry Research* 21: 2273-2279.

Kumar, M., Padmini, T. and Ponnuve, T. 2017. Synthesis, characterisation, and antioxidant activities of Schiff bases are of cholesterol. *Journal of Saudi Chemical Society* 21: S322-S328.

Kumar, S. and Kumar, S. 2019. Molecular Docking: A Structure-Based Approach for Drug Repurposing. *In Silico Drug Design*. Academic Press Ed. K Roy, Chater 6:161-189.

Leah, Q., Scott, K. R., Finn, S. P., Hayes, M. and Gray, S. G. 2020. An In Vitro Study Determining the anti-inflammatory activities of sinapinic acid-containing extracts generated from Irish rapeseed meal. *Medical Research Archives* 8.10: 2375-2394.

Li, Y., Liu, Y, Wang, H., Xiong, X., Wei, P. and Li, F. 2013. Synthesis, Crystal Structure, Vibration Spectral, and DFT Studies of 4-Aminoantipyrine and Its Derivatives. *Molecules* 18: 877-893.

Liang, Z., Chen, X., Yang, Z., Liu, Y., Qiu, X., Zeng, Z., Lu, S. and Liu, Y. 2022. Sodium Ions Affect Pyrraline Formation in the Maillard Reaction with Lys-Containing Dipeptides and Tripeptides. *Frontiers in nutrition* 9.2: 874-883.

Lipinski, C. A., Lombardo, F., Dominy, B. W. and Feeney, P. J. 2001. Experimental and computational approaches to estimate solubility and permeability in drug discovery and development settings. *Advance Drug Delivery Review* 46.1-3: 3-26.

Lomas, J. S. 2019. Relationships between NMR shifts and interaction energies in biphenyls, alkanes, aza-alkanes, and oxa-alkanes with X-H…H-Y and X-H…Z (X, Y = C or N; Z = N or O) hydrogen bonding. *Analytical science journal* 57.12: 1121-1135.

Mahajan, N. D. and Jain, N. 2021. Heterocyclic Compounds and Their Applications in The Field of Biology. *Natural, Volatiles and Essential Oils* 8.4: 1223-1229.

Mahdaviara, M., Menad, N.A., Ghazanfari, M. H. and Hemmati-Sarapardeh, A. 2020. Modeling relative permeability of gas condensate reservoirs: Advanced computational frameworks. *Journal of Petroleum Science and Engineering* 189: 0920-0935.

Mahmud, S. and Rosen, N. 2019. History of NSAID Use in the Treatment of Headaches Pre and Post-industrial Revolution in the United States: the Rise and Fall of

Antipyrine, Salicylic Acid, and Acetanilide. *Current Pain and Headache Report* 23.6:1-13.

Martemucci, G., Portincasa, P., Ciaula, A. D., Mariano, M., Centonze, V. and Alessandro, A. G. 2022. Oxidative stress, aging, antioxidant supplementation and their impact on human health: An overview. *Mechanisms of Ageing and Development* 206: 111-127.

Mesbah, M., Douadi, T., Sahli, T., Issaadi, S., Boukazoula, S. and Chafaa, S. 2018. Synthesis, characterisation, spectroscopic studies, and antimicrobial activity of three new Schiff bases derived from Heterocyclic moiety. *Journal of Molecular Structure* 115: 41-48.

Muegge, I. and Rarey, M. 2001. Small molecule docking and scoring. *Review Computational Chemistry* 17: 1-60.

Muntha, P. 2016. Drug discovery and development. *Journal of Pharmacy and Pharmaceutical Sciences* 51: 135-142.

Murtaza, S., Akhtar, M. S., Kanwal, F., Abbas, A., Ashiq, S. and Shamam, S. 2017. Synthesis and biological evaluation of Schiff base of 4-aminophenazone as anti-inflammatory, analgesic, and antipyretic agents. *Journal of Saudi Chemical Society* 21: S359-S372.

Nagai, R., Akashi, R. and Sugino, O. 2020. Completing density functional theory by machine learning hidden messages from molecules. *npj Computational Materials* 6: 43-57.

Nowotny, K., Jung, T., Hohn, A., Weber, D. and Grune, T. 2015. Advanced glycation end products and oxidative stress in type 2 diabetes mellitus. *Biomolecules* 5.1: 194-222.

Obasi, L. N., Kaior, G. U., Rhyman, L., Ibrahim, A. A., Hoong-Kun, F. and Ramasami, P. 2016. Synthesis, characterisation, antimicrobial screening, and computational studies of 4-[3-(4-methoxy-phenyl)-allylideneamino]-1,5-dimethyl-2-phenyl-1,2-dihydro-pyrazol-3-one *Journal of Molecular Structure* 1120: 180-186 Obi-Egbedi,

N. O. and Ojo, N. D. 2015. Computational studies of the corrosion inhibition potentials of some derivatives of 1H-Imidazo [4, 5-F] [1, 10] phenanthroline. *Journal of Science Research* 14: 50-56.

Obi-Egbedi, N. O., Targema, M., Adeoye, M. D and Gbangban, S. T. 2015. Calculation of Electronic Properties of Some 4-Nitroaniline Derivatives: Molecular Structure and Solvent Effects. *International Research Journal of Pure and Applied Chemistry* 8.3: 165-174.

Odozi, N. W., Babalola, J. O., Ituen, E. B. and Eseola, A. O. 2015. Imidazole derivative as novel effective inhibitor of mild steel corrosion in aqueous sulphuric acid. *American Journal of Physical Chemistry* 4.1: 1-9.

Oguntibeju, O. O. 2019. Type 2 diabetes mellitus, oxidative stress, and inflammation: examining the links. *International Journal of Physiology* 1511.3: 45-63.

Oke, A. M., Adelakun, A. O., Akintelu, S. A., Soetan, E. A., Oyebamiji, A. K. and Ewemoje, T. A. 2022. Inhibition of angiotensin converting enzyme by phytochemicals in *Cucurbita pepo* L. *In silico Approach*. *Pharmacological Research - Modern Chinese Medicine* 4: 100142.

Orabi, E. A., Orabi, M. A. A., Mahross and kaud Abdel-Hakim, A. F. M. 2018. Computational investigation of the structure and antioxidant activity of some pyrazole and pyrazolone derivatives. *Journal of Saudi Chemical Society* 22.6: 705-714.

Osang, J. E., Adedokun, I. O., Isreal-Cookey, C. 1., Egor, A. O., Uquetan, U. I., Ekpo, C. M. and Umuji, J. I. 2020. Review of Mathematical Modelling of the Time Dependent Schrodinger Wave Equation using Different methods Specialty. *Journal of Engineering and Applied Science* 5.1: 10-27.

Oyebamiji., K. A. and Semire, B. 2016. Studies of 1, 4-Dihydropyridine Derivatives for Anti-Breast Cancer (MCF-7) Activities: Combinations of DFT-QSAR and Docking Methods. *New York Science Journal* 9.6: 58-66.

Oyebamiji, A. K. and Semire, B. 2021. In-Silico Study on Anti-bacteria and Anti-fungal Activities of 3,4-Dihydropyrimidin-2(1*H*) One Urea Derivatives. *Chemistry Africa* 4:149159.

Oyewole, R. O., Oyebamiji, A. K. and Semire. B. 2020. Theoretical calculations of molecular descriptors for anticancer activities of 1, 2, 3-triazole-pyrimidine derivatives against gastric cancer cell line (MGC-803): DFT, QSAR and docking approaches. *Heliyon* 6: 0326-0342.

Paredes, A., Olivieri, D. N. and Michinel, H. 2020. From optics to dark matter: A review on nonlinear Schrodinger-Poisson systems, Physica D: Nonlinear Phenomena 403: 0167-0178. Wu, F., Zhou, Y., Li, L., Shen, X., Chen, G., Wang, X., Liang, X., Tan, M. and Huang, Z. 2020. Computational Approaches in Preclinical Studies on Drug Discovery and Development. *Frontiers in Chemistry* 8.2: 1-32.

Parikh, P. H., Timaniya, J. B., Patel, M. J. and Patel, K. P. 2022. Microwave-assisted synthesis of pyrano[2,3-c]-pyrazole derivatives and their anti-microbial, anti-malarial, anti-tubercular, and anti-cancer activities. *Journal of Molecular Structure* 1249: 022-038.

Parmar, N., Teraiya, S., Patel, R., Barad, R., Jajda, H. V. Thakkar, H. 2015. Synthesis, antimicrobial and antioxidant activities of some 5-pyrazolone based Schiff bases. *Journal of Saudi Chemical Society* 19: 36-41.

Parr, R. G., Szentpaly, L. and Liu, S. 1999. Electrophilicity index. *Journal of the America Chemical Society* 121:1922-1924.

Parvarinezhad, S., Salehi, M., Malekshah, R. E., Kubicki, M. and Khaleghian, A. 2022. Synthesis, characterization, spectral studies two new transition metal complexes derived from pyrazolone by theoretical studies and investigate anti-proliferative activity. *Applied Organometallic Chemistry* 36: 6563-6572.

Pauling, L. 1960. The nature of the chemical bond and the structure of molecules and crystals: an introduction to modern structural chemistry. Cornell university press. 1-10.

Pinzi, L. and Rastelli, G. 2019. Molecular Docking: Shifting Paradigms in Drug Discovery. *International Journal of Molecular Sciences* 20.18: 4331.

Pisoschi, A. M., Pop, A., Iordache, F., Stanca, L., Predoi, G. and Serban, A. I. 2021. Oxidative stress mitigation by antioxidants - An overview on their chemistry and influences on health status. *European Journal of Medicinal Chemistry* 209.1: 112891-112910.

Prajapat, P. 2018. Utility of Synthetic, Medicinal and Pharmaceutical Chemistry in Drug Design. *Modern Chemistry and Applications* 6.2:1-11.

Pradeepkiran, J. A., Sainath, S.B. and Shrikanya, K.V.L. 2021. In silico validation and ADMET analysis for the best lead molecules. Eds. J.A. Pradeepkiran, S.B. Sainath, B. Melitensis. Academic Press. Chapter 5: 133-176.

Puzyn, T., Leszczynski, J. and Cronin, M. 2010. *Recent Advances in QSAR Studies*: Methods and applications. Vol. 8; Springer Dordrecht.

Qian, H. F., Geng, J., Xu, D. and Huang W. 2019. Hydrazone to deprotonated azo/azo-enol transformation for isomeric pyrazolone based heterocyclic dyes via metal-ion complexation Dye. *Pigment* 160: 853-862.

Qin, X., Chen, J., Luo, Li, J., Jia, S., Zhang, Z., Jiang, Q., Hu, W., An, H. and Yang, T. 2023. High performance computing for first-principles Kohn-Sham density functional theory towards exascale supercomputers. *CCF Transactions on High Performance Computing* 5: 26-42.

Quadri, T. W., Olasunkanmi, L. O., Akpan, E. D., Fayemi, E. O, Lee, H., Lgaz, H., Verma, C., Guo, L., Kaya, S. and Ebenso, E. E. 2022. Development of QSAR-based (MLR/ANN) predictive models for effective design of pyridazine corrosion inhibitors. *Materials Today Communications* 30: 103-133.

Raczuk, E., Dmochowska, B., Samaszko-Fiertek, J. and Madaj, J. 2022. Different Schiff Bases-Structure, Importance and Classification. *Molecules* 27.3: 787-799.

Radha, V. P., Chitra, S., Jonekirubavathi, S., Chung, I., Kim, S. and Prabakaran, M., 2020. Transition metal complexes of novel binuclear Schiff base derived from 3,3′-diaminobenzidine: synthesis, characterization, thermal behavior, DFT, antimicrobial and molecular docking studies. *Journal of Coordination Chemistry* 73.6: 1009-1027.

Ramadan, A. M., Alshehri, A. A. and Bondock, S. 2019. Synthesis, physico-chemical studies, and biological evaluation of new metal complexes with some pyrazolone derivatives. *Journal of Saudi Chemical Society* 23.8: 1192-1205.

Ramajayam, R., Tan, K. P., Liu, H. G. and Liang, P. H. 2010. Synthesis and evaluation of pyrazolone compounds as SARS-coronavirus 3C-like protease inhibitors. *Bioorganic Medical Chemistry* 18: 7849-7854.

Rathod, S., Desai, H., Patil, R. and Sarolia, J. 2022. Non-ionic Surfactants as a P-Glycoprotein(P-gp) Efflux Inhibitor for Optimal Drug Delivery-A Concise Outlook. *Journal of the American Association of Pharmaceutical Scientists* 23.1: 55-69.

Remes, C., Paun, A., Zarafu, I., Tudose, M., Caproiu, M. T., Ionita, G., Bleotuz, C., Matei, L. and Ionita, P. 2012. Chemical and biological evaluation of some new antipyrine derivatives with properties. *Bioorganic Chemistry* 41-42: 6-12.

Rensburg, R. V. and Reuter, H. 2019. An overview of analgesics: NSAIDs, paracetamol, and topical analgesics Part 1. *South African Family Practice* 61.1: S4-S10.

Reygaert, W. C. 2018. An overview of the antimicrobial resistance mechanisms of bacteria. *AIMS Microbiology* 4.3: 482-501.

Rungratanawanich, W., Qu, Y., Wang, X., Essa, M., M. and Song, B. 2021 Advanced glycation end products (AGEs) and other adducts in aging-related diseases and alcohol-mediated tissue injury. *Experimental and Molecular Medicine* 53: 168-188.

Sak, K. and Everaus, H. 2017. Established Human Cell Lines as Models to Study Anti-leukemic Effects of Flavonoids. *Current Genomics* 18.1: 3-26.

Sakthivel, K., Jeyasubramanian, B., Thangagiri, J. and Raja, D. 2020. Recent advances in schiff base metal complexes derived from 4-aminoantipyrine derivatives and their potential applications. *Journal of Molecular Structure* 1222.2: 128-135.

Salam, M. A., Al-Amin, M. Y., Salam, M. T., Pawar, J. S., Akhter, N., Rabaan, A. A. and Alqumber, M. A. A. 2023. Antimicrobial Resistance: A Growing Serious Threat for Global Public Health. *Healthc*are 11.13: 1946-1954.

Scamps, G., Goriely, S., Olsen, E., Bender, M and Skyrme, W. R. 2021. Hartree-Fock-Bogoliubov mass models on a 3D mesh: effect of triaxial shape. *The European Physical Journal A* 57: 333-347.

Sen, A. and Stark, H. 2019. Role of cytochrome P450 polymorphisms and functions in development of ulcerative colitis. *World Journal of Gastroenterology* 25.23: 2846-2862.

Senbagam, R., Vijayakumar, R., Rajarajan, M., Balaji, S., Manikandan, V., Vanangamudi, G. and Thirunarayanan, G. 2016. Synthesis, assessment of substituent effect and antimicrobial activities of (4E)-4-benzylideneamino)-1,2-dihydro-2,3-dimethyl-1-phenylpyrazol-5-one compounds. *Karbala International Journal of Modern Science* 16.2: 56-62.

Sethi, S., Joshi, A., Arora, B., Bhowmik, A., Sharma, R. R. and Kumar, P. 2020. Significance of FRAP, DPPH, and CUPRAC assays for antioxidant activity determination in apple fruit extracts. *European Food Research and Technology* 246: 591-598.

Shaw, R. A. 2020. The completeness properties of Gaussian-type orbitals in quantum chemistry. *International journal for quantum chemistry* 120.17: 6264-6256.

Shen, C. Y., Lu, C. H., Wu, CH., Li, K. J., Kuo, Y. M., Hsieh, S. C. and Yu, C. L. 2020. The Development of Maillard Reaction, and Advanced Glycation End Product (AGE)-Receptor for AGE (RAGE) Signaling Inhibitors as Novel Therapeutic Strategies for Patients with AGE-Related Diseases. *Molecules* 27.25:5591-5599.

Shoaib, M., Rahman, G., Ali, S. W. and Naveed, M. U. 2015. Synthesis of 4-aminoantipyrine derived Schiff bases and their evaluation for antibacterial, cytotoxic, and free radical scavenging activity. *Bangladesh Journal of Pharmacology* 10: 332-336.

Siegel, R. L., Miller., K. D., Wagle, N. K. and Jemal, A. 2023. Cancer statistics, 2023. *A Cancer Journal for Clinicians* 73:17-48.

Singh, G., Satija, P., Singh, B., Sinha, S., Sehgal, R. and Sahoo, S. C. 2020. Design, crystal structures and sustainable synthesis of family of antipyrine derivatives: Abolish to bacterial and parasitic infection. *Journal of Molecular Structure* 1199: 127-139.

Singh, G., Suman, Diksha, Pawan, Mohit, Sushma, Priyanka, Saini, P. and Satija, P. 2022. Design and synthesis of 4-aminoantipyrine appended triazole linked bis-organosilane and their silica nanoparticles for selective recognition of Fe3+ ions. *Journal of Molecular Structure* 1250. 2: 131766-131768.

Sinniah, A.,Yazid, S. and Flower, R. J. 2021. From NSAIDs to Glucocorticoids and Beyond. *Cells* 10: 3524-3539.

Somarouthu, D., Thota, V. and PrakashKamma, B. 2020. Severe Acute Respiratory Syndrome (SARS). *World Journal of Pharmaceutical Research* 9.12: 324-337.

Sonia, G., Thachil, K. K., Parameswaran, M. K. and Kochupappy, P. T. 2013. Synthesis of some Benzoxazinyl Pyrazolone Arylidenes as Potent Antimicrobials and Antioxidants. *Medicinal Chemistry Research* 23: 1320-1241.

Soroceanu, A. and Bargan, A. 2022 Advanced and Biomedical Applications of Schiff-Base Ligands and Their Metal Complexes: A Review. *Crystals* 12.10: 1436-1453.

Suhane, S., Nerkar, A. G., Modi, K., Sanjay, D. and Sawan. T. 2019. 2D and 3D-Qsar Analysis of Amino (3-((3,5-Difluoro-4-Methyl-6-Phenoxypyridine-2- Yl)Oxy) Phenyl)Methaniminium Derivatives as Factor Xa Inhibitor. *International Journal of Pharmacy and Pharmaceutical Sciences* 11.2: 104-114.

Starowicz, M. and Zielinski, H. 2019. Inhibition of Advanced Glycation End-Product Formation by High Antioxidant-Leveled Spices Commonly Used in European Cuisine. *Antioxidants* 8.4:100-113.

Stohr, M., Voorhis, T. V., and Tkatchenko, A., 2019. Theory and practice of modeling van der Waals interactions in electronic-structure calculations. *Chemical Society Review* 48: 4118-4154.

Stojkovic, D., Petrovic, J., Carevic, T., Sokovic, M. and Liaras, K. 2023. Synthetic and Semisynthetic Compounds as Antibacterials Targeting Virulence Traits in Resistant Strains: A Narrative Updated Review. *Antibiotics* 12.6: 963-977.

Suryawanshi, V. S., Yadav, A. R., Mohite, S, K. and Magdum, C. S. 2020. Toxicological Assessment using Brine Shrimp Lethality Assay and Antimicrobial activity of Capparis Grandis. *Journal of University of Shanghai for Science and Technology* 22.11: 746-759.

Swierczewska, M., Lee, K. C. and Lee, S. 2015. What is the future of PEGylated therapies. *Expert Opinion on Emerging Drugs* 20.4: 531-539.

Teran, R., Guevara, R., Mora, J., Dobronski, L., Barreiro-Costa, O., Beske, T. Pérez-Barrera, J., Araya Maturana, R., Rojas-Silva, P., Poveda, A. and Heredia-Moya, J. 2019. Characterization of Antimicrobial, Antioxidant, and Leishmanicidal Activities of Schiff Base Derivatives of 4-Aminoantipyrine. *Molecules* 24: 2696-2978.

Tok, F., Kocyigit-Kaymakcıoglua, B., Saglıkb, N., Levent, S., Ozkay, Y. and Kaplancıklı, Z. A. 2019. Synthesis and biological evaluation of new pyrazolone Schiff bases as monoamine oxidase and cholinesterase inhibitors. *Bioorganic Chemistry* 84: 41-50.

Tomar, V. 2022. A Review on Procedure of QSAR Assessment in Organic Compounds as a Measure of Antioxidant Potentiality. *International Journal for Global Academic and Scientific Research* 1.1: 7-12.

Tran, T. N. and Henary, M. 2022. Synthesis and Applications of Nitrogen-Containing Heterocycles as Antiviral Agents. *Molecules* 27.9: 2700-2711.

Trott, O. and Olson, A. J. 2010. AutoDock Vina: Improving the Speed and Accuracy of Docking with a New Scoring Function, Efficient Optimisation and Multithreading. *Journal of Computational Chemistry* 31: 455-461.

Veber, D. F., Johnson, S. R., Cheng, H. Y., Smith, B. R., Ward, K. W. and Kopple, K. D. 2002. Molecular properties that influence the oral bioavailability of drug candidates. *Journal of medicinal chemistry*. 45.12: 2615-2623.

Veerasamy, R. 2022. QSAR-An Important In-Silico Tool in Drug Design and Discovery. *Advances in Computational Modeling and Simulation*. Eds. R. Srinivas, R. Kumar, and Dutta, M. Springer, 978-981.

Velazquez-Meza, M. E., Galarde-Lopez, M., Carrillo-Quiroz, B. and Alpuche-Aranda, C. M. 2022. Antimicrobial resistance: One Health approach. *Veterinary World* 15.3: 743-749.

Vemula, D., Jayasurya, P., Sushmitha, V., Kumar, Y. N. and Bhandari, V. 2023. CADD, AI, and ML in drug discovery: A comprehensive review. *European Journal of Pharmaceutical Sciences* 181: 0928-0987.

Wang, Y. 2022. When Quantum Computation Meets Data Science: Making Data Science Quantum. *Harvard Data Science Review* 4.1: 1162-124.

Wong, R. S. Y. 2019. Role of Nonsteroidal Anti-Inflammatory Drugs (NSAIDs) in Cancer Prevention and Cancer Promotion. Advances in Pharmacological Sciences 34:1-10.

Wu, F., Zhou, Y., Li, L., Shen, X., Chen, G., Wang, X., Liang, X., Tan, M. and Huang, Z. 2020. Computational Approaches in Preclinical Studies on Drug Discovery and Development. *Frontiers in Chemistry* 8.2: 1-32.

Xi, P., Xu, Z., Liu, X., Chen, F., Zeng, Z., Zhang, X. and Liu, Y. 2009. Synthesis, Characterisation, Antioxidant Activity and DNA-Binding Studies of Three Rare Earth (III) Complexes with 1-(4-Aminoantipyrine)-3-tosylurea Ligand. *Journal of Fluoresence* 19: 63-72.

Xu, Y., Li, Y., Xie, J., Xie, L., Mo, J. and Chen. W. 2021. Bioavailability, Absorption, and Metabolism of Pelargonidin-Based Anthocyanins Using Sprague-Dawley Rats and Caco-2 Cell Monolayers. *Journal of Agricultural and Food Chemistry* 69.28: 7841-7850.

Yang, L., Feng, J. and Ren, A. 2005. Theoretical studies on the electronic and optical properties of two thiophene-fluorene based π-conjugated copolymers. *Polymer* 46:10970-10982.

Yasar, Z. and Zaheer, Z. 2021. 4-Aminoantipyrine Analogs as Anti-inflammatory and Antioxidant agents: Synthesis, Biological Evaluation and Molecular Docking. *International Journal of Pharmaceutical Investigation*. 11.1: 14-22.

Yeung, E., Kundu, S. and Hodas, N. 2019. Learning Deep Neural Network Representations for Koopman Operators of Nonlinear Dynamical Systems. *American Control Conference* 4832-4839.

Yuan, T., Chen, H., Fu, D., Hu, Wang, J., Yuan, Q., Yu, H., Xu, W. and Xie, X. 2019. New insights into oxidative stress and inflammation during diabetes mellitus-accelerated atherosclerosis. *Redox Biology* 20: 247-260.

Zaater, S., Bouchoucha, A., Djebbar, S. and Brahimi, M. 2016. Structure, vibrational analysis, electronic properties, and chemical reactivity of two benzoxazole derivatives: functional density theory study. *Journal of Molecular Structure* 1123: 344-354.

Zarmpi, P., Flanagan, T., Meehan, E., Mann, J. and Fotaki, N. 2020. Impact of Magnesium Stearate Presence and Variability on Drug Apparent Solubility Based on Drug Physicochemical Properties. *American Association of Pharmaceutical Scientists* 22.4: 75-93.

Zgutka, K., Tkacz, M., Tomasiak, P. and Tarnowski, M. 2023. A Role for Advanced Glycation End Products in Molecular Ageing. *International Journal of Molecular Sciences* 24.12: 9881-9894.

Zhao, L., Tao, Z., Pavosevic, F., Wildman, A., Hammes-Schiffer, S. and Li, X. 2020 Real-Time Time-Dependent Nuclear-Electronic Orbital Approach: Dynamics beyond the Born-Oppenheimer Approximation. *The Journal of Physical Chemistry Letters* 11.10: 4052-4058.

Zhang, J. and Lu, T. 2021. Efficient evaluation of electrostatic potential with computerized optimized code. *Physical Chemistry Chemical Physics* 23: 20323-20328.